Research Topics

Modern advances in direct reactions for nuclear structure

Edited by
Alan Wuosmaa, Benjamin Kay and
Sean J. Freeman

Published in
Frontiers in Physics

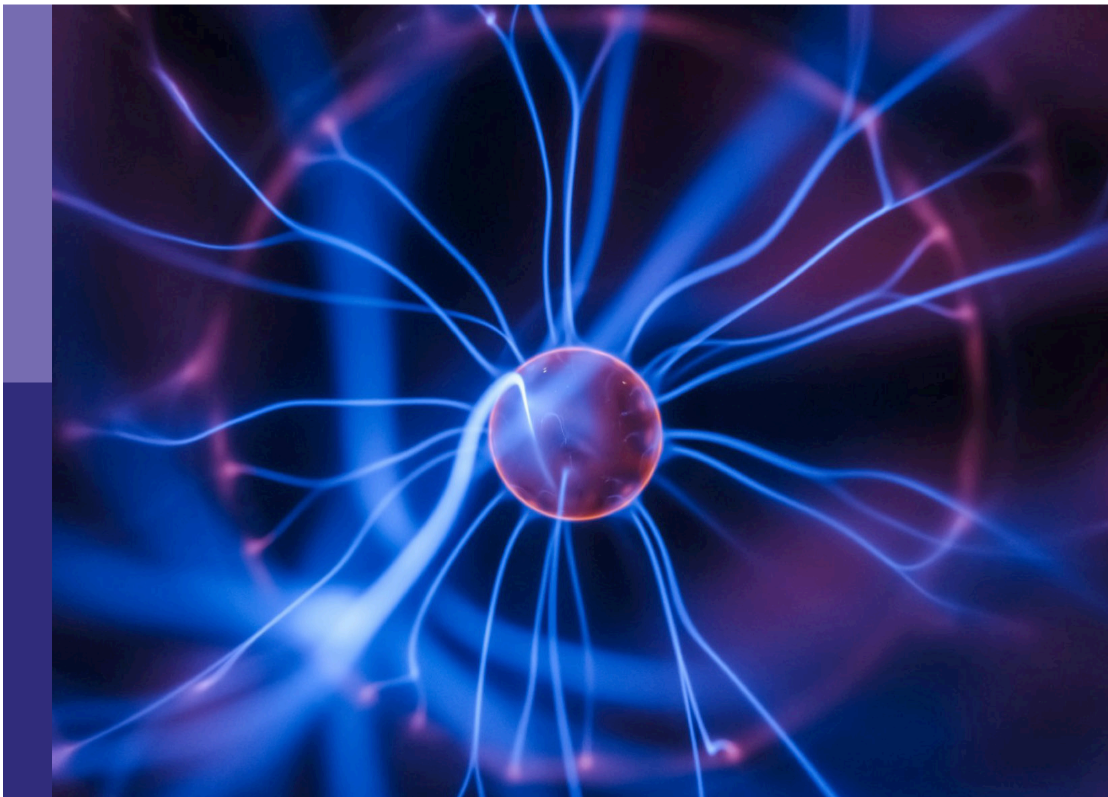

ISSN 1664-8714
ISBN 978-2-8325-6535-3
DOI 10.3389/978-2-8325-6535-3

Generative AI statement
Any alternative text (Alt text) provided alongside figures in the articles in this ebook has been generated by Frontiers with the support of artificial intelligence and reasonable efforts have been made to ensure accuracy, including review by the authors wherever possible. If you identify any issues, please contact us.

About Frontiers

Frontiers is more than just an open access publisher of scholarly articles: it is a pioneering approach to the world of academia, radically improving the way scholarly research is managed. The grand vision of Frontiers is a world where all people have an equal opportunity to seek, share and generate knowledge. Frontiers provides immediate and permanent online open access to all its publications, but this alone is not enough to realize our grand goals.

Frontiers journal series

The Frontiers journal series is a multi-tier and interdisciplinary set of open-access, online journals, promising a paradigm shift from the current review, selection and dissemination processes in academic publishing. All Frontiers journals are driven by researchers for researchers; therefore, they constitute a service to the scholarly community. At the same time, the *Frontiers journal series* operates on a revolutionary invention, the tiered publishing system, initially addressing specific communities of scholars, and gradually climbing up to broader public understanding, thus serving the interests of the lay society, too.

Dedication to quality

Each Frontiers article is a landmark of the highest quality, thanks to genuinely collaborative interactions between authors and review editors, who include some of the world's best academicians. Research must be certified by peers before entering a stream of knowledge that may eventually reach the public - and shape society; therefore, Frontiers only applies the most rigorous and unbiased reviews. Frontiers revolutionizes research publishing by freely delivering the most outstanding research, evaluated with no bias from both the academic and social point of view. By applying the most advanced information technologies, Frontiers is catapulting scholarly publishing into a new generation.

What are Frontiers Research Topics?

Frontiers Research Topics are very popular trademarks of the *Frontiers journals series*: they are collections of at least ten articles, all centered on a particular subject. With their unique mix of varied contributions from Original Research to Review Articles, Frontiers Research Topics unify the most influential researchers, the latest key findings and historical advances in a hot research area.

Find out more on how to host your own Frontiers Research Topic or contribute to one as an author by contacting the Frontiers editorial office: frontiersin.org/about/contact

Modern advances in direct reactions for nuclear structure

Topic editors
Alan Wuosmaa — University of Connecticut, United States
Benjamin Kay — Argonne National Laboratory (DOE), United States
Sean J. Freeman — European Organization for Nuclear Research (CERN), Switzerland

Citation
Wuosmaa, A., Kay, B., Freeman, S. J., eds. (2025). *Modern advances in direct reactions for nuclear structure*. Lausanne: Frontiers Media SA.
doi: 10.3389/978-2-8325-6535-3

Table of contents

frontiers | Frontiers in Physics

TYPE Editorial
PUBLISHED 20 June 2025
DOI 10.3389/fphy.2025.1643501

Editorial: Modern advances in direct reactions for nuclear structure

A. H. Wuosmaa[1]*, S. J. Freeman[2,3] and B. P. Kay[4]

[1]Department of Physics, University of Connecticut, Storrs, CT, United States, [2]EP Department, Conseil Européen pour la Recherche Nucléaire (CERN), Genève, Switzerland, [3]Schuster Laboratory, University of Manchester, Manchester, United Kingdom, [4]Physics Division, Argonne National Laboratory, Lemont, IL, United States

Check for updates

OPEN ACCESS

EDITED AND REVIEWED BY
Jie Meng,
Peking University, China

*CORRESPONDENCE
A. H. Wuosmaa,
✉ alan.wuosmaa@uconn.edu

RECEIVED 09 June 2025
ACCEPTED 12 June 2025
PUBLISHED 20 June 2025

CITATION
Wuosmaa AH, Freeman SJ and Kay BP (2025) Editorial: Modern advances in direct reactions for nuclear structure.
Front. Phys. 13:1643501.
doi: 10.3389/fphy.2025.1643501

KEYWORDS

direct nuclear reactions, exotic beams, instrumentation, nuclear structure, nuclear reaction theory, accelerator facilities

Editorial on the Research Topic
Modern advances in direct reactions for nuclear structure

1 Introduction

The study of nuclei far away from stability, with large imbalances between the number of protons and neutrons, is a central Research Topic in modern nuclear physics today. New experimental facilities now provide access to nuclei that were previously inaccessible, revealing new and unexpected behaviors. Older models of nuclear structure fail to explain the properties of such nuclei, spurring major new theoretical developments. Key to testing these new theories are new data. Direct reactions have, for decades supplied the underpinnings of nuclear structure models. The necessity to use radioactive beams from the new facilities introduces a host of technical difficulties, including experiment count rates, and complicated kinematics that adversely affect experimental resolutions.

In this Research Topic, we draw together works from experimentalists and theorists that show just some of the many new developments in detector and spectrometer technology, experimental approaches, and structure and reaction theory to confront the challenges that will drive studies in the field into the next decade and beyond. These collected papers illustrate how modern experimental techniques can yield data on nuclei far from stability, and how modern theory can help understand those data.

New instrumentation is key to addressing the physics of exotic isotopes, and modern methods can access data that were previously inaccessible. Ayyad et al. describe advances using the Active-Target Time-Projection Chamber (ATTPC), a highly sensitive device that is both a thick gaseous target and a detector capable of untangling complex multi-particle final states with good resolution. The ATTPC permits sensitive measurements with beams of very low intensity, extending the reach of direct-reaction studies. Silicon detectors have long been a workhorse for direct-reaction measurements, and new, complex multi-segmented arrays play an important role. In his paper, Pain describes the ORRUBA, GODDESS and associated instruments used for a wide variety of measurements, for both nuclear structure and nuclear astrophysics. The coupling of the silicon-detector array with large, modern arrays of germanium gamma-ray detectors adds to the capabilities. Many direct-reaction studies involve nucleon transfer between a light ion, typically ^{1,2}H or ^{3,4}He, and a heavier nucleus; with unstable nuclei, the heavy nucleus is the beam, and the light species is often in the form of a solid plastic or metal foil. Such targets have impurities that can complicate the measurements, but a high-purity gas-jet target that can alleviate such problems. Chipps describes a powerful alternative to solid targets, the JENSA device, which has facilitated a number of high-resolution studies of hydrogen- and helium-induced reactions.

With new instruments come exciting new measurement techniques. Sobotka and Charity have pioneered a groundbreaking approach to studying a wide range of nuclear phenomena using Invariant-Mass Spectroscopy. They apply this powerful method to light proton-rich nuclei to study the nature of the proton dripline, and exotic unbound systems beyond that dripline. The data characterize unbound states that can help understand the shell structure of exotic nuclei. Another aspect key to the evolution of shell structure in neutron-rich systems is the nature of the spin-orbit interaction. In her contribution, Chen examines the trends in spin-orbit splitting for neutron-rich silicon and tin nuclei. Her analysis can distinguish between effects of the spin-orbit potential itself, and from the wave functions of weakly bound nucleons. The data she describes for the ^{32}Si(d,p)^{33}Si reaction were obtained using the SOLARIS spectrometer, one of three spectrometers that exist worldwide with a novel design based on a solenoidal magnetic field. The helical motion of the light ions emitted in two-body reactions within the magnetic field provide an innovative way to avoid kinematical factors that degrade the Q-value resolution obtained when making such measurements with radioactive beams in inverse kinematics with more conventional techniques.

The data from direct-reaction measurements do not immediately yield information about nuclear structure; they must be understood in the context of theoretical analyses of the reactions. Reaction theory has made significant advances in recent years, and our Research Topic includes two examples highlighting these developments. Any experimental result needs a measure of the uncertainty, and in the case of direct reactions, uncertainties associated with theoretical analyses are often neglected. The contribution by Hebborn and Nunes seeks to address the problem by describing sources of uncertainty from optical-model analyses of reaction data and their propagation in the determination of direct-reaction observables. A key ingredient in the analysis of direct reaction data involves predicting the reaction cross section from Distorted-Wave Born or Distorted-Wave Impulse Approximation (DWBA or DWIA) calculations. Central to those calculations are the optical-model parameters used to understand the scattering states. Typically, those parameters are the product of empirical fits to scattering data, but Atkinson and Dickhoff present a different approach, the Dispersive Optical Model (DOM) that uses dispersion relations to connect continuum and bound states, developing data driven predictions for nucleon knockout reactions.

New structure data inspire new theoretical interpretations. Correlations in nuclei are the focus of many current investigations. Macchiavelli et al. address the connection between correlations and the well-known quenching of spectroscopic factors. They consider the case of electron-induced proton knockout from ^{48}Ca, one also addressed by Atkinson and Dickhoff, and discuss the implications of correlations on other features of nuclear structure.

Finally, no experiments are possible without facilities able to provide the necessary beams. While FRIB, CERN/ISOLDE, and FAIR are well known, smaller facilities also play a crucial role in modern nuclear experimental science. The J. D. Fox Superconducting Linear Accelerator Laboratory at Florida State University, described by Spieker and Almaraz-Calderon, is an excellent example of what can be done on a scale smaller than the major national laboratories. They provide a tour of the laboratory, presenting examples of high-resolution spectrometer results, as well as data from sophisticated particle, gamma-ray and neutron detector arrays.

We hope that this Research Topic provides a glimpse into just a few of the many diverse efforts marking current progress in the field of direct nuclear reactions.

Author contributions

AW: Writing – original draft, Writing – review and editing, Conceptualization. SF: Conceptualization, Writing – review and editing. BK: Conceptualization, Writing – review and editing.

Funding

The author(s) declare that financial support was received for the research and/or publication of this article. This material is based upon work supported by the U. S. Department of Energy, Office of Science, Office of Nuclear Physics, under Contract Numbers DE-SC0014552 (AHW) and DE-AC02-6CH11357 (BPK), and the UK Science and Technology Facilities Council under Grant Refs ST/V001116/1 and ST/Y000323/1 (SJF).

Conflict of interest

The authors declare that the research was conducted in the absence of any commercial or financial relationships that could be construed as a potential conflict of interest.

The author(s) declared that they were an editorial board member of Frontiers, at the time of submission. This had no impact on the peer review process and the final decision.

Generative AI statement

The author(s) declare that no Generative AI was used in the creation of this manuscript.

Publisher's note

frontiers | Frontiers in Physics

TYPE Original Research
PUBLISHED 20 December 2024
DOI 10.3389/fphy.2024.1511394

Nuclear structure and direct reaction studies in particle-γ coincidence experiments at the FSU John D. Fox superconducting linear accelerator laboratory

Mark-Christoph Spieker* and Sergio Almaraz-Calderon*

Department of Physics, Florida State University, Tallahassee, FL, United States

OPEN ACCESS

EDITED BY
Benjamin Kay,
Argonne National Laboratory (DOE),
United States

REVIEWED BY
Praveen C. Srivastava,
Indian Institute of Technology Roorkee, India
AJ Mitchell,
Australian National University, Australia

*CORRESPONDENCE
Mark-Christoph Spieker,
✉ mspieker@fsu.edu
Sergio Almaraz-Calderon,
✉ salmarazcalderon@fsu.edu

RECEIVED 14 October 2024
ACCEPTED 20 November 2024
PUBLISHED 20 December 2024

CITATION
Spieker M-C and Almaraz-Calderon S (2024) Nuclear structure and direct reaction studies in particle-γ coincidence experiments at the FSU John D. Fox superconducting linear accelerator laboratory.
Front. Phys. 12:1511394.
doi: 10.3389/fphy.2024.1511394

Since its foundation in the 1960s, the John D. Fox Superconducting Linear Accelerator Laboratory at Florida State University (FSU) pursued research at the forefront of nuclear science. In this contribution, we present recent highlights from nuclear structure and reaction studies conducted at the John D. Fox Superconducting Linear Accelerator Laboratory, also featuring the general experimental capabilities at the laboratory for particle-γ coincidence experiments. Specifically, we focus on light-ion induced reactions measured with the Super-Enge Split-Pole Spectrograph (SE-SPS) and the CATRiNA neutron detectors, respectively. Some results obtained with the CeBrA demonstrator for particle-γ coincidence experiments at the SE-SPS are presented. A highlight from the first experimental campaigns with the combined CLARION2-TRINITY setup, showing that weak reaction channels can be selected, is discussed as well.

KEYWORDS

nuclear structure, direct reactions, magnetic spectrograph, γ-ray detection, particle-γ coincidence experiments, neutron detection, angular distributions, particle-g angular correlations

1 Introduction

Nuclear physics has entered a new exciting era with next-generation rare isotope beam facilities like the Facility for Rare Isotope Beams (FRIB) coming online and enabling experiments with atomic nuclei, which were previously inaccessible, to study their structure and a multitude of reactions with them. These experiments are expected to inform, *e.g.*, *r*-process nucleosynthesis and to test fundamental symmetries by using nuclei as laboratories enhancing signals to investigate beyond standard model physics. In this new era, stable-beam facilities continue to play an important role by allowing detailed, high-statistics experiments with modern spectroscopy setups and provide complementary information for rare-isotope studies by, *e.g.*, studying structure phenomena of stable nuclei close to the particle-emission thresholds and by investigating details of different nuclear reactions, thus, testing reaction theory. Modern coincidence experiments, that combine multiple detector systems, can also address open questions in stable nuclei providing important pieces to solving the nuclear many-body problem and quality data to guide the development of *ab-initio*-type theories for the spectroscopy of atomic nuclei. Since its foundation in the 1960s, the John D. Fox Superconducting Linear Accelerator Laboratory at Florida State University [1] has continued to pursue research at the forefront of nuclear science. New experimental setups, which were recently commissioned at the Fox Laboratory and which will be presented in this article, enable detailed studies of atomic nuclei close to the valley of β stability through modern spectroscopy experiments that detect particles and γ rays in coincidence.

1.1 History of the John D. Fox laboratory

The Florida State University (FSU) Accelerator Laboratory began operation in 1960 following the installation of an EN Tandem Van de Graaf accelerator. It was the second of its type in the United States. Since its dedication in March 1960, the FSU Accelerator Laboratory has been recognized for several scientific and technical achievements. Examples of the early days of operation are the first useful acceleration of negatively-charged helium ions at FSU in 1961 [2] and the experimental identification of isobaric analogue resonances in proton-induced reactions in 1963 [3].

The laboratory entered its second development stage in 1970 with the installation of a Super-FN Tandem Van de Graaff accelerator. As a third major stage of evolution, a superconducting linear post-accelerator based on ATLAS technology was funded by the U.S. National Science Foundation in the mid-1980s [4], with the first experiment on the completed facility run in 1987 [5, 6]. The Super-FN Tandem Van de Graaff and superconducting linear post-accelerator are still being used at the FSU Accelerator Laboratory today. In combination with two SNICS sources and an RF-discharge source, they provide a variety of accelerated beams, ranging from protons to accelerated titanium ions, for experiments relevant for nuclear science. In March 2007, FSU's Superconducting Linear Accelerator Laboratory was named for John D. Fox, a longtime FSU faculty member who was instrumental in its development.

Today, the local group operates in addition to the two accelerators a number of experimental end stations allowing experiments at the forefront of low-energy nuclear physics. The present layout of the FSU laboratory is shown in Figure 1. Experiments with light radioactive ion beams, which are produced in-flight, can be performed at the RESOLUT facility [7]. The Array for Nuclear Astrophysics Studies with Exotic Nuclei, ANASEN [8], and the RESONEUT detector setup for resonance spectroscopy after (d,n) reactions [9] are major detector setups available for experiments at the RESOLUT beamline. The laboratory further added to its experimental capabilities by introducing the CATRINA neutron detector array [31], the MUSIC-type active target detector ENCORE [10], and by installing the Super-Enge Split-Pole Spectrograph (SE-SPS) in collaboration with Louisiana State University, including its first new ancillary detector systems SABRE [11] and CEBRA [12] for coincidence experiments. Recently, the FSU group also installed the high-resolution γ-ray array CLARION2 and the TRINITY particle detector [13] in collaboration with Oak Ridge National Laboratory. This array consists of up to 16 Compton-suppressed, Clover-type High-Purity Germanium (HPGe) detectors.

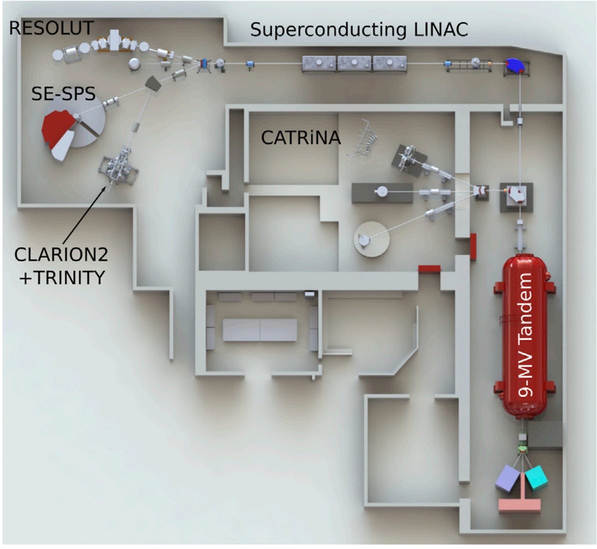

FIGURE 1
Model of the FSU John D. Fox Superconducting Linear Accelerator Laboratory as of fall 2024. Experimental setups featured in this article are highlighted.

2 Featured experimental setups and capabilities

2.1 The Super-Enge Split-Pole Spectrograph (SE-SPS)

The Super-Enge Split-Pole Spectrograph (SE-SPS) has been moved to FSU after the Wright Nuclear Structure Laboratory (WNSL) at Yale University ceased operation. Like any spectrograph of the split-pole design [14], the SE-SPS consists of two pole sections used to momentum-analyze reaction products and focus them at the magnetic focal plane to identify nuclear reactions and excited states. The split-pole design allows to accomplish approximate transverse focusing as well as to maintain second-order corrections in the polar angle θ and azimuthal angle ϕ, i.e., $(x/\theta^2) \approx 0$ and $(x/\phi^2) \approx 0$, over the entire horizontal range [14]. H. Enge specifically designed the SE-SPS spectrograph as a large-acceptance modification to the traditional split-pole design for the WNSL. The increase in solid angle from 2.8 to 12.8 msr was achieved by doubling the pole-gap, making the SE-SPS well-suited for coincidence experiments. At FSU, the SE-SPS was commissioned in 2018. The design resolution of ~ 20 keV was achieved in June 2019 during a $^{12}C(d,p)^{13}C$ experiment with a thin natural Carbon target after improvements to the accelerator optics, the dedicated beamline by adding a focusing quadrupole magnet in front of the scattering chamber, and the new CAEN digital data acquisition [15]. Figure 2 shows the SE-SPS in target room 2 of the FSU John D. Fox Laboratory.

In singles experiments, i.e., stand-alone mode, the SE-SPS with its current light-ion with its current light-ion focal plane detection system [16] (see Figure 2) can be used to study the population of excited states in light-ion induced reactions, determine (differential) cross sections and measure the corresponding angular distributions. Currently, laboratory scattering angles of up to 60°

FIGURE 2
The FSU Super-Enge Split-Pole Spectrograph (SE-SPS) (left). The sliding seal scattering chamber is installed here. Parts of the rail system to measure angular distributions can be seen. The beam enters from the lower left corner. The position sensitive focal plane detector (right). The proportional-counter (tracking) section of the detector is shown and opened. The field cage and cathode plate, and some of the delay-line chips above the field-cage section can be seen on the green circuit board. One position sensitive anode wire section is taken out to show the pick-up pad structure, which is coupled to the delay-line chips and angled at 45°.

can be covered. The focal-plane detector consists of a position-sensitive proportional counter with two anode wires (see Figure 2), separated by about 4.3 cm, to measure position, angle, and energy loss, and a large plastic scintillator to determine the rest energy of the residual particles passing through the detector. The focal-plane detector has an active length of about 60 cm. A sample particle identification plot with the energy loss measured by the front-anode wire and the rest energy measured by the scintillator is shown in Figure 3. Unambiguous particle identification is achieved. Under favorable conditions, the detector can be operated at rates as high as two kilocounts/s (kcps). A sample position spectrum measured with the delay lines of the SE-SPS focal plane detector is also shown in Figure 4. As the resolution depends on the solid angle, target thickness and beam-spot size, it may vary from experiment to experiment. See also comments in [14, 17]. In standard operation and with a global kinematic correction, i.e., assuming a vertical shift of the real focal plane with respect to the two position-sensitive sections of the detector, a full width at half maximum of 30–70 keV has been routinely achieved. This corresponds to a position resolution of about 2 mm. This resolution can be improved further with position-dependent offline corrections. An example for such a correction, taking into account the position dependence of the z shift for obtaining the true focal-plane position relative to the two anode wires and assuming that it depends linearly $z(x) = m^{*}x + z_0$ on the focal-plane position x, has been added to Figure 4. A slope of $m = 0$ would correspond to the standard correction of calculating the real focal plane from a "vertical" shift relative to the two focal-plane wires and is shown with a red line in Figures 4B, C. As can be seen in Figures 4B, C, there is a region with $m > 0$, where the "tracks" mostly corresponding to excited states of ^{48}Ti populated in ^{49}Ti(d,t) get narrower after the correction, thus improving the position resolution along the focal plane. The improved focal-plane spectrum is shown in Figure 4D. The magnetic field is 11.2 kG and the solid-angle acceptance $\Delta\Omega$ was kept at 4.6 msr for this experiment. The necessity of kinematic corrections for magnetic spectrographs and how to calculate the vertical z shift for, *e.g.*, the split-pole design were also discussed in [14].

Angular distributions provide direct information on the angular momentum, l, transfer and, for one-nucleon transfer reactions, information on the involved single-particle levels. For the set of (d,p) experiments performed with the SE-SPS up to date, very good to excellent agreement has been observed between the experimental data and the reaction calculations using the conventional Distorted Wave Born Approximation (DWBA) and the adiabatic distorted wave (ADW) method with input from global optical model potentials. Further details were discussed in [18–23]. Some examples for ^{52}Cr$(d,p)^{53}$Cr are shown in Figure 7 and will be discussed further in the next section in the context of particle-γ coincidence experiments with the SE-SPS and CeBrA.

2.1.1 The CeBrA demonstrator for particle-γ coincidence experiments at the SE-SPS

The Cerium Bromide Array (CeBrA) demonstrator for particle-γ coincidence experiments at the SE-SPS has recently been commissioned at the John D. Fox Laboratory [12]. It has been extended since with four 3 × 3 inch detectors on temporary loan from Mississippi State University (see Figure 5). This extended demonstrator has a combined full energy peak (FEP) efficiency of about 3.5 % at 1.3 MeV. For comparison, the five-detector demonstrator had an FEP efficiency of about 1.5 % at 1.3 MeV [12]. The comparison underscores the significant gain when adding larger volume detectors. Over the next years, a 14-detector array will be built in collaboration with Ursinus College and Ohio University through funding from the U.S. National Science Foundation, combining the existing detectors (four 2 × 2 inch and one 3 × 4 inch) of the demonstrator with five additional 3 × 4 inch and four 3 × 6 inch CeBr$_3$ detectors.

An example for a particle-γ coincidence matrix, measured in ^{52}Cr$(d,p\gamma)^{53}$Cr with the five-detector demonstrator, is shown in Figure 6. Using diagonal gates, γ decays leading to specific (excited) states can be selected. In Figure 6, γ decays to the ground state of ^{53}Cr were selected. Three states stand out as they are also strongly populated in (d,p) [21]. They are the excited states at 2,321 keV, 3,617 keV, and 4,690 keV. The decay of the 4690-keV state is, to our knowledge, observed for the first time. No information on its γ decay is adopted [24]. The γ ray at ~2.6 MeV indicates that, different from previous conclusions [21], both the 2657-keV and 2670-keV states might have been populated in (d,p). The ground-state branch of the $J^{\pi} = 5/2^{-}$, 2657-keV state is too small to explain the excess of counts. More details will be discussed in a forthcoming publication [25], which will also highlight the significant value added from performing complementary singles and coincidence experiments with the SE-SPS. A feature, which can be immediately appreciated

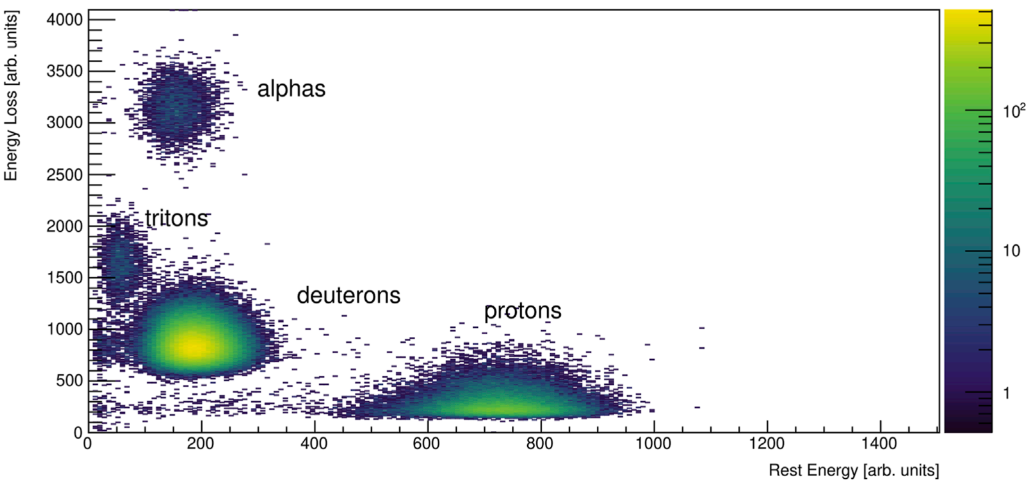

FIGURE 3
Particle identification with the FSU SE-SPS. The example of deuteron-induced reactions (d,X) on ^{49}Ti has been chosen. Here, protons, deuterons, tritons, and α particles fall within the momentum acceptance of the SE-SPS and can be clearly distinguished. The rest energy is measured with the plastic scintillator at the end of the focal-plane detector. The energy loss can be determined using one of the anode-wire signals. Here, the energy loss measured with the front-anode wire is shown.

from Figure 6, is that the energy resolution of the SE-SPS barely changes over the length of the focal plane, while the $CeBr_3$ energy resolution shows the expected dependence on γ-ray energy [12]. Using the additional γ-ray information and projecting onto the excitation-energy axis will allow us to distinguish close-lying states, which might be too close in energy to do so in SE-SPS singles experiments or where particle spectroscopy alone does not provide conclusive results. For this, differences in γ-decay behavior can be used. As an example, see the very different γ-decay behavior of the 3617-keV, $J^\pi = 1/2^-$ and the 3707-keV, $J^\pi = 9/2^+$ states of ^{53}Cr in Figure 6. For the 3,617-keV state, the 3,617-keV $1/2^- \rightarrow 3/2^-_1$ ground-state transition is the strongest, while it is the 2,417-keV $9/2^+ \rightarrow 7/2^-_1$ transition for the 3,707-keV state. Another example, using different diagonal gates for the $^{61}\mathrm{Ni}(d,p\gamma)^{62}\mathrm{Ni}$ reaction and, thus, selecting γ decays leading to different final states with different J^π as "spin filter", was featured in Ref. [12].

The coincidently detected γ rays also provide access to important complementary information such as γ-decay branching ratios and particle-γ angular correlations for spin-parity assignments, as well as the possibility to determine nuclear level lifetimes via fast-timing techniques and excluding feeding due to gates on the excitation energy [12]. For the latter, the smaller detectors are better suited because of their better intrinsic timing resolution as also discussed in Ref. [12]. For dedicated fast-timing measurements, two 1×1 inch $CeBr_3$ detectors are available at FSU in addition to the four 2×2 inch detectors. These have an even better timing resolution than the 2×2 inch detectors, however, at the cost of a significantly lower FEP efficiency. A careful analysis of their timing properties and FEP efficiencies is ongoing.

We will briefly highlight some particle-γ angular correlations measured with the five detector CeBrA demonstrator. Particularly, we will discuss how these can be used to make spin-parity assignments and to determine multipole mixing ratios δ. Figure 7 shows three proton-γ angular correlations measured in $^{52}\mathrm{Cr}(d,p\gamma)^{53}\mathrm{Cr}$ and with all five $CeBr_3$ detectors placed in a common plane with an azimuthal angle $\phi_\gamma = 0°$. In addition to the experimental data, predictions from combined ADW calculations with CHUCK3 [26] yielding scattering amplitudes and ANGCOR [27] calculations using these scattering amplitudes to generate the angular correlations are shown. The associated density matrices, $\rho_{mm'}$, needed to calculate the proton-γ angular correlations with the formalism presented in Ref. [28] and which are connected to the scattering amplitudes for the different m substates, were added, too. As all the γ-ray transitions of Figure 7 are primary transitions, the multipole mixing ratio δ is the only free parameter. It was determined via χ^2 minimization. Excellent agreement is observed between the experimentally measured and the calculated distributions for the excited states at $E_x = 564$ keV, 1,006 keV, and 2,320 keV of ^{53}Cr. For the 564-keV state, a one-neutron transfer to the $2p_{1/2}$ neutron orbital was assumed [red, longer dashed line in Figure 7A]. For the 2320-keV state, the neutron was transferred into the $2p_{3/2}$ orbital (blue, shorter dashed line). For the 1,006-keV state, the neutron was transferred into the $1f_{5/2}$ orbital (green, shorter dashed line). For the 2,320-keV and 1,006-keV states, transfers to their corresponding spin-orbit partner are also shown in Figure 7. In panels (c) and (f), predictions for a neutron transfer into the $1f_{7/2}$ orbital are shown with orange, longer dashed lines.

As expected for the 564-keV, $1/2^-_1 \rightarrow 3/2^-_1$ ground-state transition, the negligible alignment [see Figure 7G] leads to an isotropic angular distribution. We note that this is true for any value of δ. For the 2320-keV, $3/2^- \rightarrow 3/2^-_1$ and 1,006-keV, $5/2^-_1 \rightarrow 3/2^-_1$ ground-state transitions, the m-substate population (alignment) [see Figures 7H, I] results in observable angular distributions. In both cases, the multipole mixing ratio indicates that the transition is dominantly of $E2$ character. A more in depth discussion will be provided in a forthcoming publication [25]. Figures 7D, E show clearly that $J^\pi = 1/2^-$ and $J^\pi = 3/2^-$ states can be distinguished based on their observed proton-γ angular correlation. (d,p)

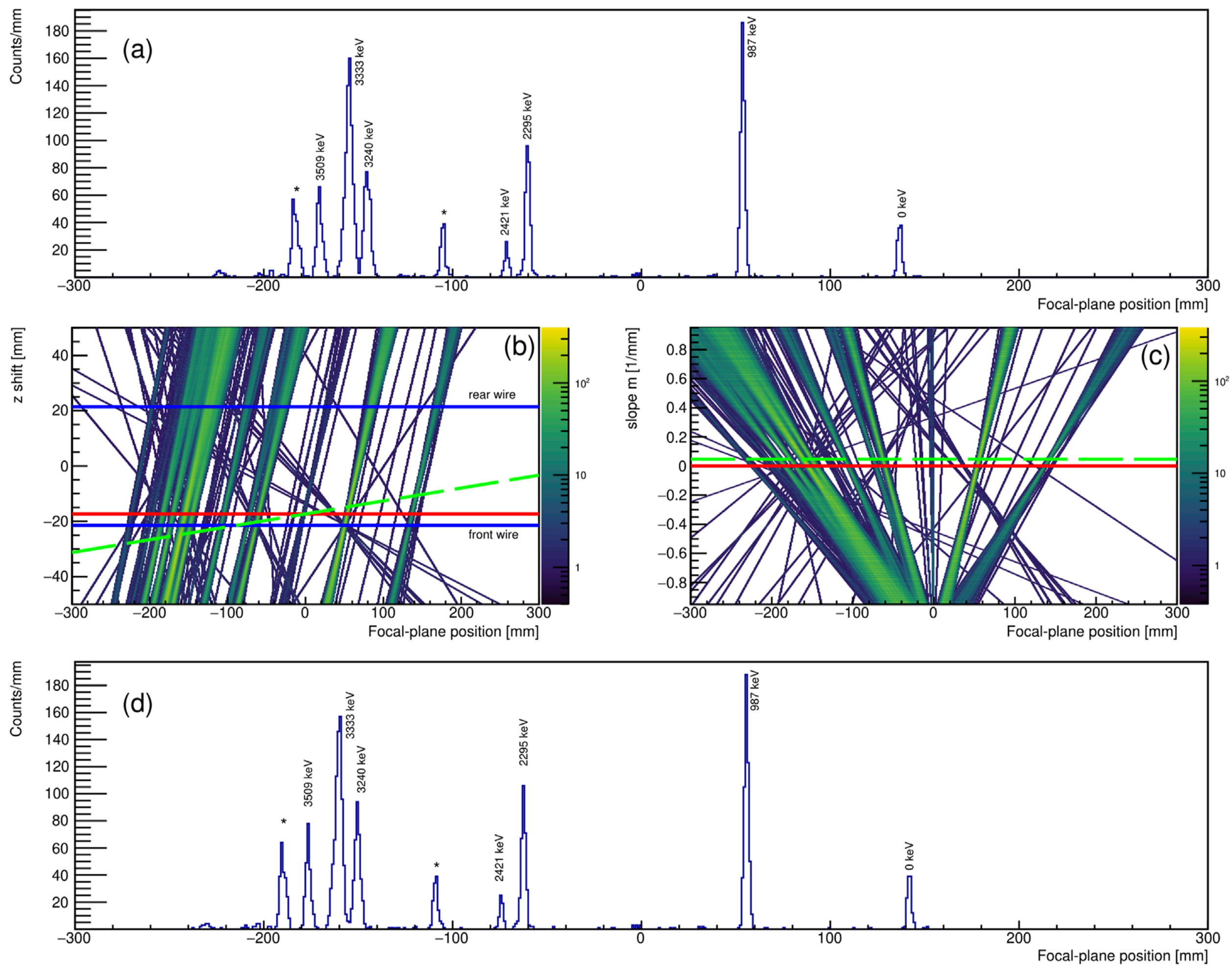

FIGURE 4
(A) Triton spectrum measured in ^{49}Ti$(d,t)^{48}$Ti with the SE-SPS placed at a laboratory scattering angle of 30°. Excited states of ^{48}Ti are marked with their excitation energy. Contaminants stemming from other Ti isotopes in the target are identified with asterisks. A vertical shift of the real focal plane relative to the front and back wire of the focal-plane detector was assumed [shown as red line in panels **(B)** and **(C)**]. **(B)** and **(C)** possible correction when assuming that the z shift of the focal plane depends on the focal-plane position according to $z(x) = m^{*}x + z_0$, i.e., a linear tilt. The position of the front and rear wires are highlighted with blue lines and labeled, respectively. **(D)** Focal-plane spectrum when the linear correction of panels **(B)** and **(C)** is applied.

singles experiments with an unpolarized deuteron beam cannot discriminate between these states since both are populated via an $l = 1$ angular momentum transfer [see Figures 7A, B]. The situation appears more complex for the f orbitals, where the predicted proton-γ angular correlations are not sufficiently different to discriminate between a $7/2^- \rightarrow 3/2^-$ and $5/2^- \rightarrow 3/2^-$ transition [see Figure 7F]. For the known 1,006-keV, $J^\pi = 5/2^-$ state, the calculation assuming a neutron transfer into the $1f_{5/2}$ orbital does provide the slightly better χ^2 value though. For completeness, we added the proton-γ angular correlation for the $5/2^- \rightarrow 3/2^-$ transition calculated with the currently adopted multipole-mixing ratio to Figure 7F. As discussed in [12], the adopted ratio appears to be incorrect. However, different sign conventions for the multipole mixing ratios could also be the origin of the disagreement.

With more detectors, which will be added to the full CeBrA array within the next couple of years, statistics will increase and particle-γ angular correlation measurements can be performed in planes with varying ϕ_γ. Four "rings" will be available in the standard configuration, where three of them have at least four detectors (see Figure 5). The full setup will allow to further test details of different transfer reactions and the predicted alignment. Measuring particle-γ angular correlations in planes with different θ_γ could potentially help to better discriminate between spin-orbit partners, like $1f_{5/2}$ and $1f_{7/2}$, too. Another example of how different angular correlations can look for the $2d_{5/2}$ and $2d_{3/2}$ spin-orbit partners will be shown in Section. 3.2.

2.2 The CATRiNA neutron detector array

The CATRiNA neutron detector array currently consists of 32 deuterated-benzene (C_6D_6) liquid scintillator neutron detectors. There are two sizes of CATRiNA detectors: 16 "small" detectors and 16 "large" detectors. The "small" CATRiNA detectors encapsulate

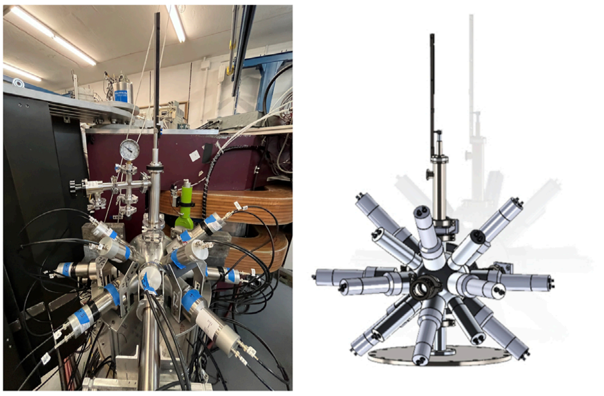

FIGURE 5
The extended CeBrA demonstrator in front of the SE-SPS (left). The array consists of four 2 × 2 inch, four 3 × 3 inch, and one 3 × 4 inch $CeBr_3$ detectors. The 3 × 3 inch detectors are temporary loans from Mississippi State University. The detectors are installed around the dedicated scattering chamber. Some of the lead bricks, used to shield background coming from the Faraday cup and the SE-SPS entrance slits, can be seen. See Ref. [12] for more details on the five-detector CeBrA demonstrator. A CAD drawing of the geometry planned for the 14-detector array including four 2 × 2 inch, six 3 × 4 inch, and four 3 × 6 inch $CeBr_3$ detectors is also shown (right).

the deuterated scintillating material in a 2″ diameter × 2″ deep cylindrical aluminum cell, while the "large" detectors encapsulate the scintillating material in a 4″ diameter × 2″ deep cylindrical aluminum cell [30, 31].

The use of deuterated scintillating material for neutron detection, rather than traditional hydrogen-based scintillating material, is due to unique features produced in the light-output spectrum. Neutrons scattered off the deuterium in the scintillator will produce a characteristic forward recoil peak and low valley in the light-output spectrum. This feature is due to the asymmetry of the cross section for $n-d$ scattering, which peaks at backwards angles and extends across a large range of neutron energies. As an example, Figure 8 shows a DWBA calculation made with the FRESCO computer program [29] for the elastic scattering cross sections of 5-MeV neutrons off the deuteron ^2H and proton ^1H as a function of the center-of-mass (CM) angle. The difference between the angular distributions can be clearly seen. The characteristic light-output spectra of deuterated scintillators is then used for the extraction of neutron energies using spectrum-unfolding methods. Determining neutron energies from spectrum unfolding is an alternative to fully relying on time-of-flight (ToF) information for neutron energies. This alternative is particularly beneficial if a compact neutron detector system like CATRiNA is used, which efficiently optimizes solid angle coverage and the size of the detector array for neutron studies. The CATRiNA detectors have equivalent properties of organic scintillators for neutron detection such as large scattering cross section for neutrons with the scintillating material, fast response time, and pulse shape discrimination capabilities that allow separation of neutron (n) and gamma-ray (γ) events.

To highlight the capabilities of the CATRiNA neutron detectors, a (d,n) proton-transfer experiment was conducted on a solid deuterated-polyethylene, CD_2, target of 400-μg/cm^2 thickness and a set of "large" CATRiNA detectors placed in target room #1 of the Fox Laboratory. The FN Tandem accelerator provided deuteron beams with energy $E_d = 5-8$ MeV. The deuteron beam was bunched to 2-ns width with intervals of 82.5 ns for time-of-flight (ToF) measurements using the accelerator's radiofrequency (RF) as reference signal. The CATRiNA detectors were placed at 1-m distance from the CD_2 target. A thick graphite disk was placed 2 m downstream from the target and used as a beam stop to minimize beam-induced background. The graphite beam stop was held inside a 30 cm × 30 cm × 30 cm borated-polyethylene block, which was surrounded with 5-cm thick lead bricks and thin lead sheets to reduce background from beam-induced neutrons and γ rays from the beamstop, respectively. The experimental setup is shown in Figure 8. The characterization of the CATRiNA detectors and the description of the unfolding method can be found in Refs. [30, 31]. Neutrons from the interaction of the deuterium beam with the carbon and deuterium in the CD_2 target were used to compare neutron energies measured with ToF and extracted with the unfolding methods.

In the following, the pulse-shape discrimination (PSD) properties of the CATRiNA detectors have been used to separate neutron and γ-ray interactions in the detectors. For the ToF measurements, the time difference was measured between the prompt-gamma signal and the neutron peaks coming from the interaction of the beam with the target. The accelerator's RF signal was used as a "stop" signal while the "start" signal was provided by an "or" of any events registered in the CATRiNA detectors. The energy of the neutrons was then calculated using non-relativistic kinematics taking into account the target to detector distance and the measured time of flight.

For the extraction of neutron energies via unfolding, the pulse height spectrum was analyzed. The raw pulse-height spectra of the detectors are obtained by gating the neutron events in the PSD plots and projecting onto the long-integration axis. A correlation matrix, ToF vs pulse height, of neutron events from interaction of an 8-MeV deuteron beam with the CD_2 target is shown in Figure 9. It can be seen that the most energetic neutrons have the highest pulse-height values. The raw pulse-height spectra show distinctive shoulders that shift to the right as the neutron energy increases and can be attributed to separate states populated in the reaction. A typical raw pulse height spectrum is shown in Figure 9.

To unfold the neutron energies, a response matrix needs to be created. The response matrix correlates the light-output (or pulse-height) spectra of the detectors with the neutron energies and the detector efficiencies. A statistical method is then employed to extract energies of incident neutrons by comparing to the response matrix of the detector in an iterative process. The present data were analyzed using a response matrix simulated with the Monte Carlo neutron-particle transport code MCNP6 [32] and validated using selected mono-energetic neutrons from the $^7Li(p,n)$ reaction [30, 33]. The response matrix for one of the "large" CATRiNA detectors is shown in Figure 9. The neutron energies extracted via unfolding method were obtained using a statistical algorithm with the Maximum-Likelihood Expectation Method (MLEM) [30, 33]. Neutron energies obtained by the described spectrum unfolding method were compared with the neutron energies obtained from the ToF method. States in ^{13}N were populated by the ^{12}C (d,n)^{13}N reaction. At $E_d = 5$ MeV, the energy of neutrons corresponding to the population of the $1/2^-$ ground state in ^{13}N is around 4 MeV for the angles measured. Similarly, the $1/2^+$ ground state in ^3He populated

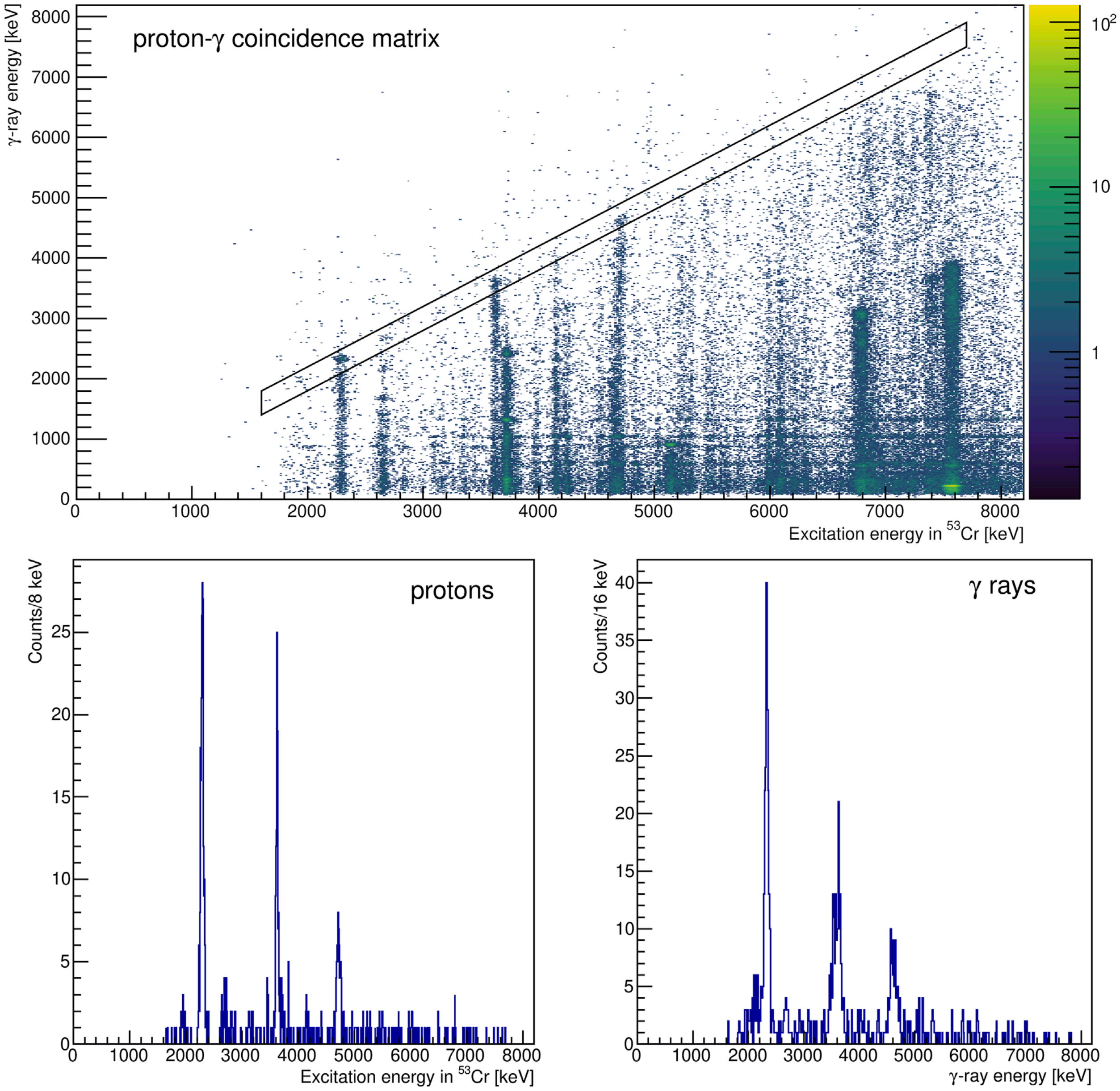

FIGURE 6
Proton-γ coincidence matrix measured in ^{52}Cr($d,p\gamma$)^{53}Cr (top panel). In addition, projections onto the excitation-energy axis (protons) and onto the "γ-ray energy" axis (γ rays) are shown in the two bottom panels. These spectra were obtained by applying the diagonal gate shown in the top panel to the proton-γ coincidence matrix. This specific gate selects γ decays to the ground state of ^{53}Cr. At higher energies, excited states of ^{13}C populated through the ^{12}C(d,p) reaction on the Carbon target backing can be seen (top panel).

by the ^{2}H(d,n)^{3}He reaction is visible at ~7 MeV. A software threshold cut of around 2 MeV was placed on the neutron energies to minimize neutron background and obtain a clean n/γ separation with the CATRiNA detectors. The neutron spectra for a detector placed at 34° obtained by both methods is shown in Figure 10. As the beam energy was increased, other features of the spectrum became visible. At $E_d = 8$ MeV, neutrons corresponding to the $J^\pi = 1/2^-$ g.s in ^{13}N have neutron energies of around 7.2 MeV. In addition, neutrons corresponding to the population of the $1/2^+$ first excited state in ^{13}N at $E_{ex} = 2.36$ MeV are detected at 4.8 MeV, and a doublet with spin-parity assignments of $3/2^-$ and $5/2^+$, respectively, and $E_x \approx 3.5$ MeV is observed at 3.6 MeV. The $1/2^+$ ground state in ^{3}He is now visible at around 9.5 MeV.

The direct comparison of neutron spectra obtained by ToF and by unfolding procedures in Figure 10 shows the potential of the CATRiNA detectors. Since the commissioning experiment reported here, the unfolding method has been improved with better experimental response matrices, which initially limited the resolution of the CATRiNA detectors. A Novel Unfolding algorithm Using Bayesian Iterative Statistics (ANUBIS) was developed. ANUBIS takes into account uncertainties associated with the unfolding algorithm and determines stopping criteria to optimize the

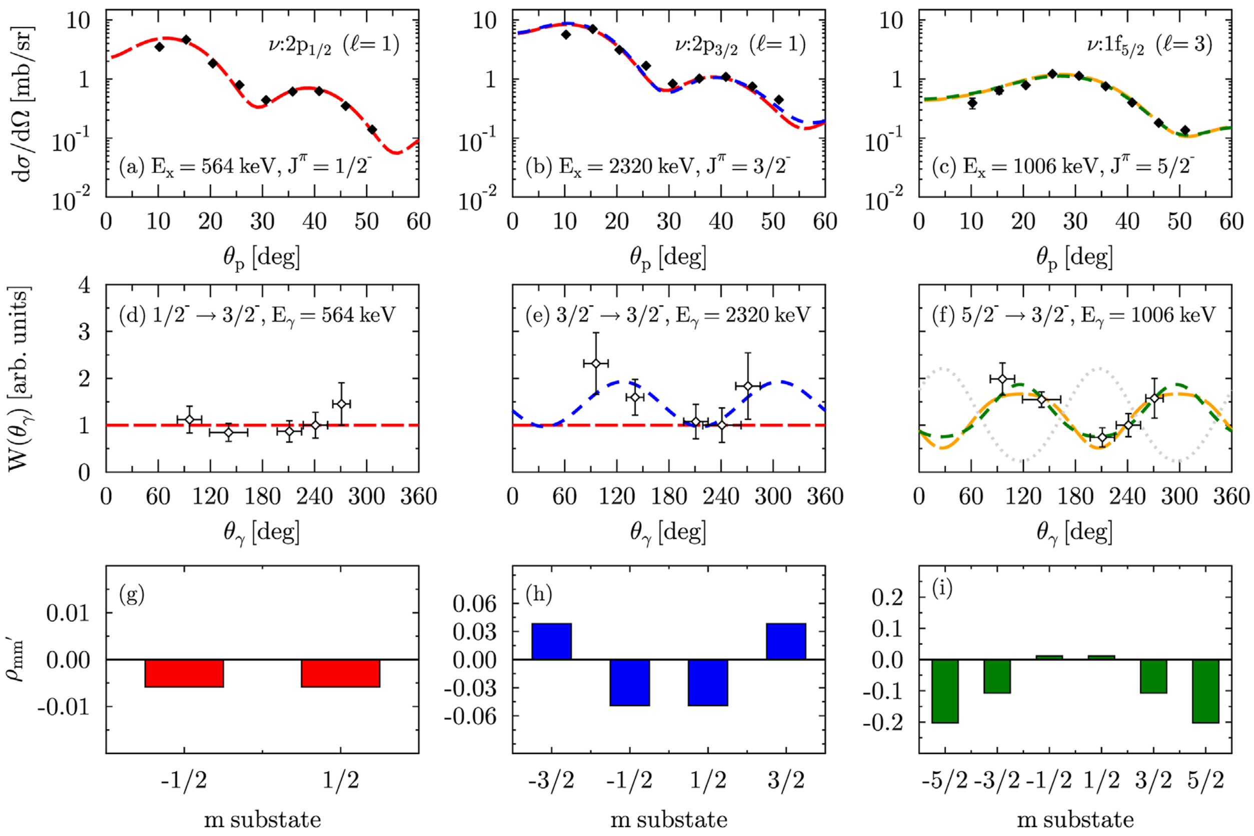

FIGURE 7
(A–C) ^{52}Cr(d,p)^{53}Cr angular distributions and **(D–F)** proton-γ angular correlations measured in ^{52}Cr($d,p\gamma$)^{53}Cr for the 564-keV, $J^\pi = 1/2^-$ state, the 2,320-keV, $J^\pi = 3/2^-$ state, and the 1,006-keV, $J^\pi = 5/2^-$ state. The angular correlations for **(D)** the 564-keV, $1/2^- \rightarrow 3/2^-_1$, **(E)** 2,320-keV, $3/2^- \rightarrow 3/2^-_1$, and **(F)** 1,006-keV, $5/2^- \rightarrow 3/2^-_1$ γ-ray ground-state transitions are shown, respectively. In addition, predictions from **(A–C)** ADW calculations with CHUCK3 [26], and **(E–F)** combined ADW calculations and ANGCOR [27] calculations to generate the angular correlations are shown for each transition (lines). **(G–I)** Density matrices $\rho_{mm'}$ as defined in, *e.g.*, Ref. [28]. The proton-γ angular correlation for the $5/2^- \rightarrow 3/2^-$ transition calculated with the currently adopted multipole-mixing ratio of $\delta = 0.36(2)$ was added to **(F)** [gray, dotted line]. Different sign conventions for the multipole mixing ratios are likely the origin of the disagreement. Note that the y-scale in panels **(D–F)** is the same.

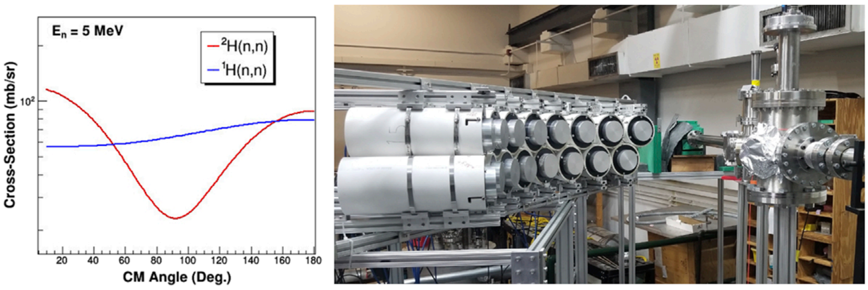

FIGURE 8
(left) DWBA calculations made with the FRESCO computer program [29] for $n-d$, and $n-p$ elastic scattering showing the difference between the isotropic angular distribution for $n-p$ scattering and the non-isotropic angular distribution for $n-d$ scattering. (right) The CATRiNA neutron detector array in target room #1 at the John D. Fox Laboratory.

procedure [31]. Angular distributions from the ^{12}C(d,n)^{13}N$_{gs}$ and from the ^{2}H(d,n)^{3}He reactions using a 5-MeV deuteron beam are shown in Figure 11. Comparison between the angular distributions with ToF and unfolding methods are in very good agreement, additionally validating the two independent approaches.

CATRiNA is envisioned to play a central role at the John D. Fox Laboratory for neutron spectroscopy studies as well as for coincidence measurements between neutrons, γ rays, and charged particles using the different detector systems available at the laboratory.

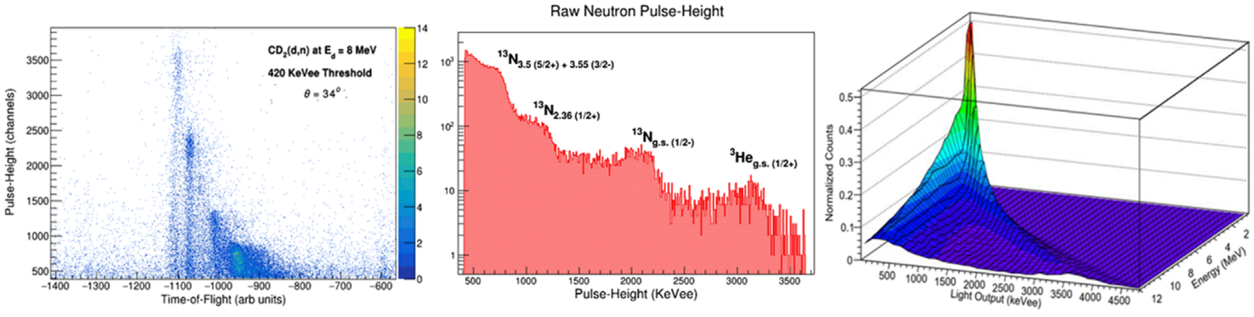

FIGURE 9
(left) Pulse-height vs ToF correlation for neutrons from the interaction of an 8-MeV deuteron beam with a 400-μm/cm^2 thick CD$_2$ target. (middle) Raw pulse-height spectrum obtained from projecting neutron events in a PSD plot on the long integration axis. Different neutron groups can be identified. (right) Simulated response matrix for the CATRiNA detectors. The simulation was performed using the Monte Carlo neutron transfer code MCNP6 [32].

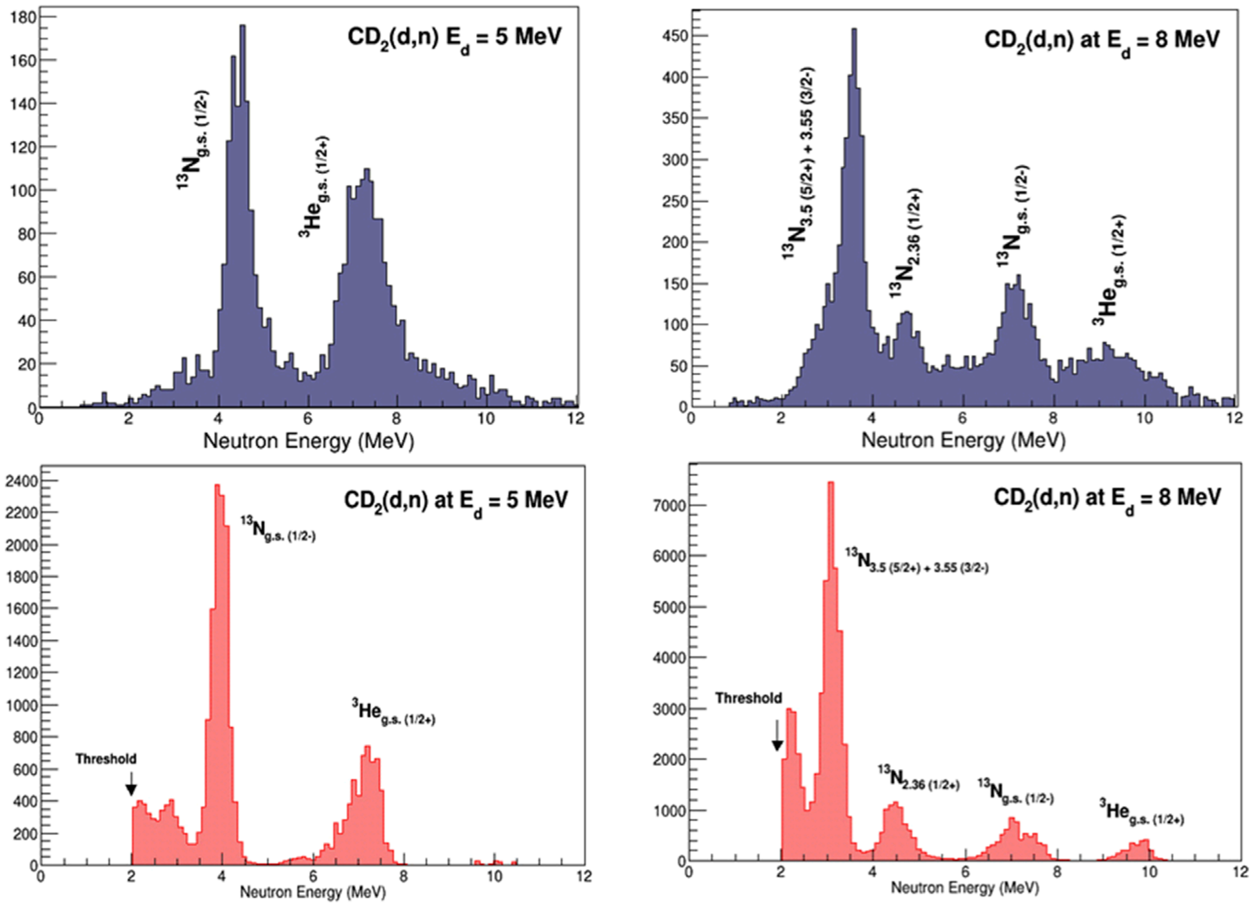

FIGURE 10
Direct comparison of the neutron-energy spectra obtained *via* time-of-flight (top panels) *versus* those obtained with an unfolding method (bottom panels). Data obtained from (d,n) reactions with deuteron-beam energies of $E_d = 5$ MeV and 8 MeV are shown.

2.3 The CLARION2+TRINITY array for high-resolution γ-ray spectroscopy and reaction-channel selection

CLARION2-TRINITY is a new setup at the John D. Fox Laboratory for high-resolution γ-ray spectroscopy in conjunction with charged particle detection [13]. The γ rays are recorded by Clover-type High-Purity Germanium detectors (HPGe) detectors. The geometry is chosen to be non-Archimedian and detectors are arranged such that no detectors have a separation of $\Delta\theta = 180°$ to suppress coincident detection of 511-keV γ rays from pair production. The TRINITY particle detector uses a relatively

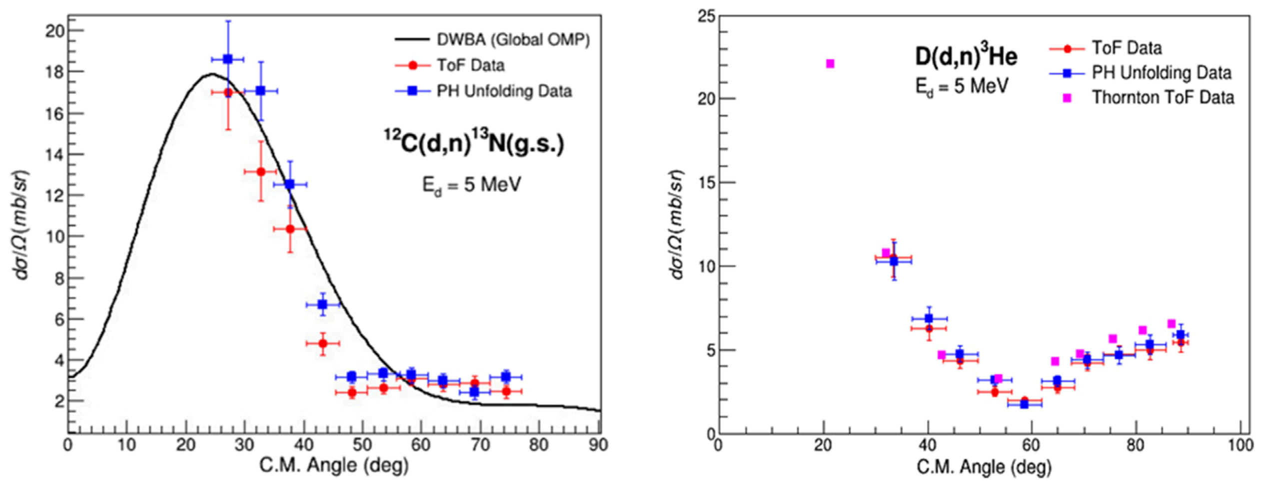

FIGURE 11
Angular distributions obtained from the interaction of a 5-MeV deuteron beam with the CD_2 target. DWBA calculations were made with FRESCO [29]. Angular distributions obtained with the ToF and unfolding method are compared showing excellent agreement.

new type of scintillator, Gadolinium Aluminum Gallium Garnet ($Gd_3Al_2Ga_3O_{12}$) doped with Cerium (GAGG:Ce). This scintillator has intrinsic particle discrimination capabilities through two decay components with different decay times and varying relative amplitudes. The particle identification with the GAGG:Ce is obtained by comparing waveform integrals of the fast "peak" and the delayed "tail". The ratio of these two quantities allows to discriminate between protons, α particles, and heavier ions. The array was commissioned in December 2021 with nine clover-type HPGe detectors and two rings of GAGG:Ce scintillators [13]. This initial setup has now been augmented with a tenth clover-type HPGe detector and all five GAGG:Ce rings of TRINITY installed. More details on the combined setup including a description of energy-loss and contaminant measurements with the zero-degree GAGG:Ce detector can be found in [13]. The first science publication from the array features results from the safe Coulomb excitation of Ti isotopes and focuses on the suppression of quadrupole collectivity in ^{49}Ti [34].

The setup has also been used to study unstable ^{32}Si in the $^{16}\text{O}(^{18}\text{O},2p)^{32}\text{Si}$ fusion-evaporation reaction. The weak $2p$ evaporation channel could be isolated selectively by detecting both protons with TRINITY. For this reaction, triple coincidences between the two protons and γ rays were detected with CLARION2+TRINITY. As the beam energy is precisely known and the setup allows to measure the energies and angles of the outgoing protons, the excitation energy in ^{32}Si, from which γ rays were emitted, as well as the velocity and direction of the ^{32}Si recoil at the time of emission of the γ ray could be reconstructed. As the "complete" kinematics of the reaction are known, excitation-energy gated γ-ray spectra as well as γ-transition gated excitation-energy spectra could be generated (see Figure 12 for an example). As can be seen in Figure 12, the combined CLARION2+TRINITY system provides high resolution for γ rays and moderate resolution in the excitation-energy spectra, mainly due to the target thickness and limited energy resolution of the GAGG:Ce scintillators of TRINITY. For the $^{16}\text{O}(^{18}\text{O},2p)^{32}\text{Si}$ reaction, which is a weak reaction channel, excitation-energy gating provided considerably better statistics for angular distribution and polarization analysis of γ-ray transitions than a conventional $\gamma\gamma$-coincidence analysis. Some details of the reaction-channel selection were already discussed in [13]. More details and results will be presented in a forthcoming publication.

3 Selected science highlights (2020–2024)

3.1 Single-particle strengths around $N = 28$ measured with the SE-SPS

Spectroscopic factors obtained from one-nucleon adding and removal reactions have been critically discussed in recent years, especially for rare isotopes with large proton to neutron separation energy asymmetries (see, *e.g.*, Refs. [35–37] and references therein). In stable nuclei, it is commonly accepted that only about 60 % of the predicted spectroscopic strengths are observed experimentally (see, *e.g.*, compilations in Refs. [36–40]). Often, systematics are, however, only available for a few selected nuclei, a few isotopic or isotonic chains, and for the spectroscopic strength of a specific single-particle orbit.

In Figure 13, we show a systematic study of the running sum for the neutron spectroscopic factors $\text{SF} = \sigma_{exp.}/\sigma_{s.p.}$ for the even-Z, $N = 29$ isotones; $\sigma_{s.p.}$ is the single particle cross section predicted for an excited state with excitation energy E_x from ADW calculations. The $N = 29$ isotones were studied at the FSU SE-SPS in (d,p) experiments [18, 19, 21]. As can be seen, about $50-70$ % of the expected strength are exhausted in all three nuclei and for all three single-particle orbitals. However, it is also quite clear that it is not sufficient to just study the first few excited states. Significant parts of the $2p_{3/2}$, $2p_{1/2}$ and $1f_{5/2}$ spectroscopic strengths are fragmented to excited states with higher excitation energies. Especially for the $2p_{1/2}$ and $1f_{5/2}$ strengths, the strength is fragmented among excited states up to the neutron-separation energy, S_n. Studying the fragmentation of

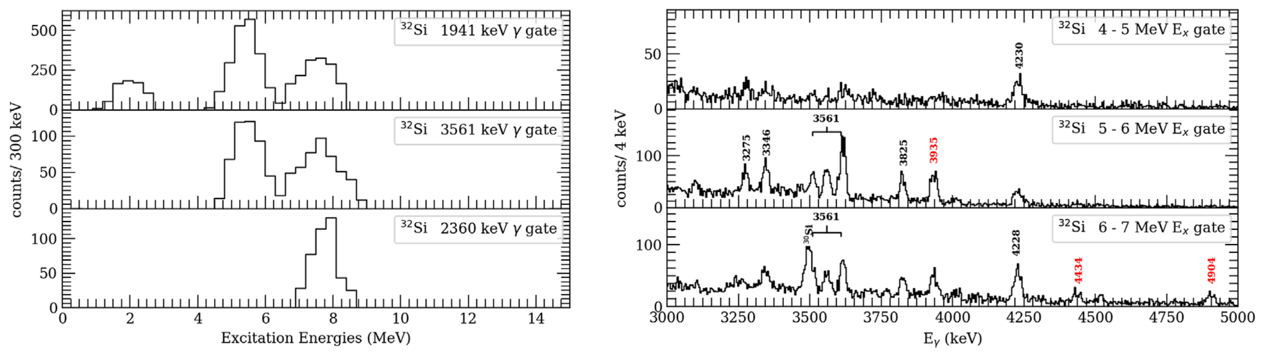

FIGURE 12
^{16}O(^{18}O,$2p$)^{32}Si reaction measured with CLARION2+TRINITY and a beam energy of 30 MeV. (left) Reconstructed excitation energy spectra of ^{32}Si when gating on specific γ-ray transitions deteced with the CLARION2 Clover detectors. (right) Excitation energy gated γ-ray spectra for three 1-MeV wide, excitation-energy windows. γ-ray transitions marked in red were observed for the first time. See text for more information.

the spectroscopic strengths in (d,p) experiments up to such high energies allows for a more reliable extraction of the centroid energies of the neutron single-particle orbitals. It should be noted though, that, if orbitals were partially filled, one would in general need to perform both the adding and removal reactions to experimentally determine occupancies and the real single-particle orbital energies (see, *e.g.* [41, 42], and comments therein).

With our new data on the energies of the single-particle orbitals, we could address the disappearance of the $N = 32$ and $N = 34$ subshell gaps in the heavier isotones. The $N = 32$ subshell gap for Ca and Ti isotopes, and its disappearance in Cr and Fe isotopes were discussed previously (see, *e.g.* [43, 44], and references therein). In Ref. [18], it was stated that the closure of the $N = 32$ subshell gap in the transition from Ti to Cr would need to be explained by the placement of the $1f_{5/2}$ neutron orbit relative to the $2p_{1/2}$ orbit. Within the remaining uncertainties discussed in [18, 19, 21], our recent (d,p) studies indeed support that the gap between these two orbits shrinks with increasing proton number (see Figure 13), possibly explaining the closing of the $N = 32$ subshell gap in heavier isotones. The data do, however, also show that rather than the $1f_{5/2}$ centroid coming significantly down in energy, it is the $2p_{1/2}$ orbital's centroid energy which increases. This is different from the initial hypothesis [18] and underlines the importance of performing systematic studies of spectroscopic strengths along isotopic and isotonic chains. The disappearance of the gap between the $1f_{5/2}$ and $2p_{1/2}$ neutron orbits with increasing proton number might also explain the possibly very localized occurrence of the $N = 34$ subshell gap (see [45] and references therein).

3.2 The neutron one-particle-one-hole structure of the pygmy dipole resonance

The pygmy dipole resonance (PDR) has been observed on the low-energy tail of the isovector giant dipole resonance (IVGDR) below and above the neutron-separation threshold. While the additional strength is recognized as a feature of the electric dipole response of many nuclei with neutron excess [46–48], its microscopic structure, which intimately determines its contribution to the overall strength, is still poorly understood making reliable predictions of the PDR in neutron-rich nuclei far off stability difficult. It has been shown that the coupling to complex configurations drives the strength fragmentation for both the IVGDR and the PDR, and that more strength gets fragmented to lower energies when including such configurations (see the review article [48]). The wavefunctions of $J^\pi = 1^-$ states belonging to the PDR are, however, expected to be dominated by one-particle-one-hole (1p-1h) excitations of the excess neutrons. First experiments were performed to access these parts of the wavefunction via inelastic proton scattering through isobaric analog resonances and via one-neutron transfer (d,p) experiments. The experimental results were compared to predictions from large scale shell model calculations including up to two-particle-two-hole (2p-2h) excitations for both protons and neutrons, and to quasiparticle phonon model (QPM) calculations including up to 3-phonon excitations. The comparison of experiment and theory for doubly-magic ^{208}Pb [49] and semi-magic ^{120}Sn [50] indicates that PDR states' wavefunctions are indeed largely dominated by 1p-1h excitations of the excess neutrons. It is important to note that (d,p) experiments are not able to access all relevant neutron 1p-1h configurations within one even-even nucleus as only those can be populated that can be reached from the ground state of the even-odd target nucleus. Therefore, (d,p) experiments performed along isotopic and isotonic chains are instructive. While these probe neutron configurations above the Fermi surface, (p,d) and (d,t) reactions can be used to study some of the relevant configurations below the Fermi surface.

First (d,p) experiments were performed with the SE-SPS to study the emergence of the PDR around the $N = 28$ shell closure. Results for ^{62}Ni have been published [20]. A complimentary real photon scattering (γ,γ') experiment was performed to aid the identification of the PDR $J^\pi = 1^-$ states up to an excitation energy of $E_x = 8.5$ MeV. As (d,p) data are available up to S_n, a follow-up (γ,γ') experiment was performed at the high intensity γ-ray source (HIγS) of the Triangle Universities Nuclear Laboratory (TUNL), which is currently being analyzed. As discussed in [20], the combined data allowed us to exclude a significant contribution of the $(2p_{3/2})^{-1}(3s_{1/2})^{+1}$ neutron 1p-1h configuration to the wavefunctions

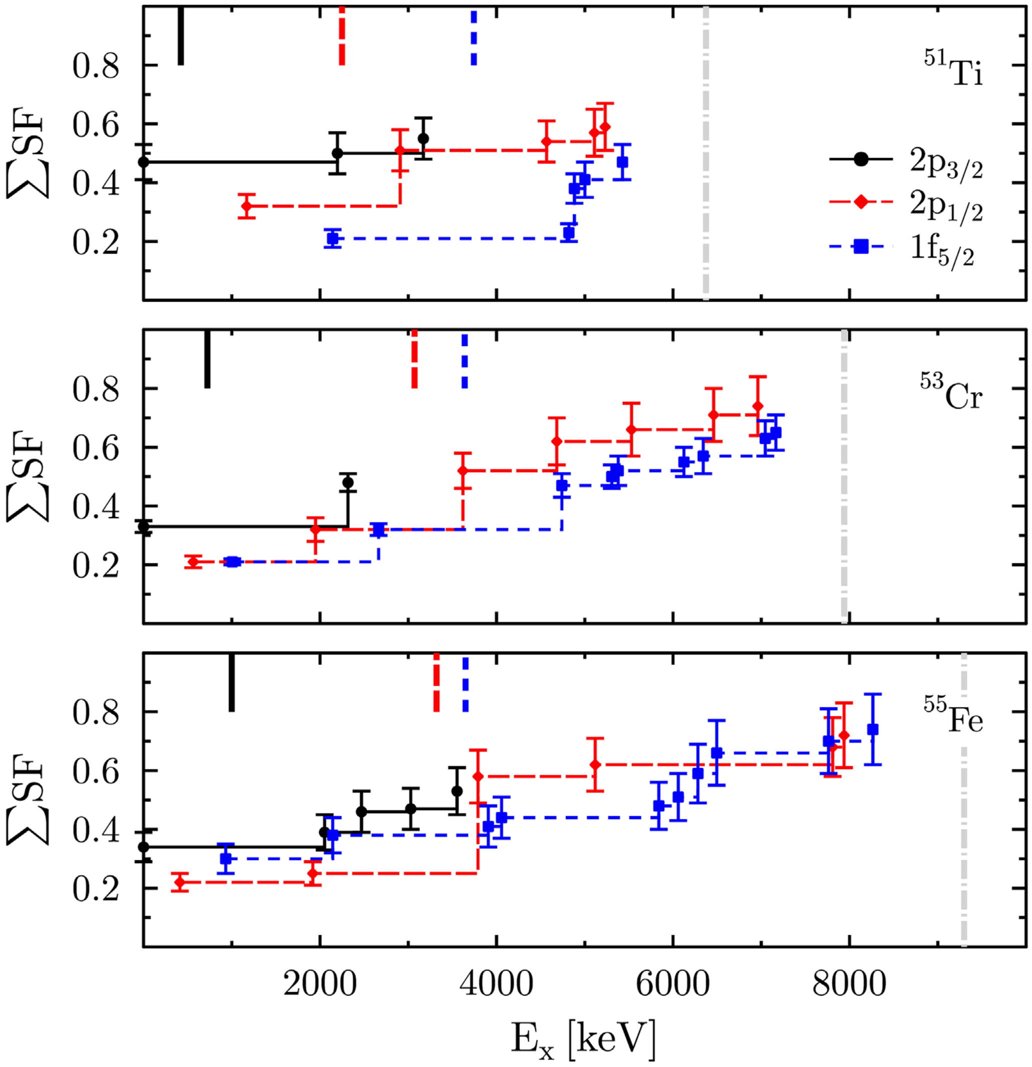

FIGURE 13
Running sum of the spectroscopic strengths for the neutron $2p_{3/2}$ (black circles), $2p_{1/2}$ (red triangles), and $1f_{5/2}$ (blue squares) orbitals measured for the even-Z, $N = 29$ isotopes ^{51}Ti [18], ^{55}Fe [19], and ^{53}Cr [21]. The centroid energies reported in Refs. [18, 19, 21] are also shown with vertical bars of the corresponding colors. Uncertainties were discussed in [18, 19, 21]. The gray dashed line corresponds to the neutron-separation energy of the corresponding nucleus. Measurements were performed up to that energy.

below S_n and, thus, to conclude that any strength increase beyond $N = 28$ would need to be linked to either the $(2p_{3/2})^{-1}(2d_{5/2})^{+1}$ or $(2p_{3/2})^{-1}(2d_{3/2})^{+1}$ configurations if the predictions of Inakura *et al.* were correct [51].

While l transfers can be easily determined through (d,p) angular distributions, the $(2p_{3/2})^{-1}(2d_{5/2})^{+1}$ and $(2p_{3/2})^{-1}(2d_{3/2})^{+1}$ neutron 1p-1h configurations cannot be distinguished in SE-SPS singles experiments with an unpolarized deuteron beam (see Figure 14A for the (d,p) angular distributions calculated with CHUCK3 [26]). Particle-γ correlations provide, however, the means to discriminate between spin-orbit partners. See Figures 14B, C for the particle-γ angular correlations calculated with ANGCOR [27] for a fixed polar angle and two different azimuthal angles. The correlations are expected to look quite different for varying azimuthal angles θ_γ and, thus, provide additional sensitivity for discriminating between the spin-orbit partners. As mentioned in Section. 2.1.1, the full CeBrA array will enable measurements at different θ_γ angles.

$(d,p\gamma)$ experiments have already been performed for nuclei close to $N = 28$ with the extended CeBrA demonstrator (see Figure 5) to study the γ-ray strength function (γSF) via the surrogate reaction method (SRM). As can be seen in Figure 6, the energy resolution of the $CeBr_3$ detectors is sufficient to resolve several low-energy γ-ray transitions resulting from the deexcitation of low-lying excited states fed by higher-lying states. Therefore, the normalized γ-ray yields can be determined as a function of excitation energy providing the data for the SRM to constrain the γSF [52]. The SE-SPS allows to perform these experiments well past the neutron-separation energy. The indirectly extracted γSF from $(d,p\gamma)$ can then be compared to the ground-state γSF measured in real-photon scattering, possibly helping to understand whether the PDR is only a feature of the ground state γSF. The complimentary (d,p) singles data provide the

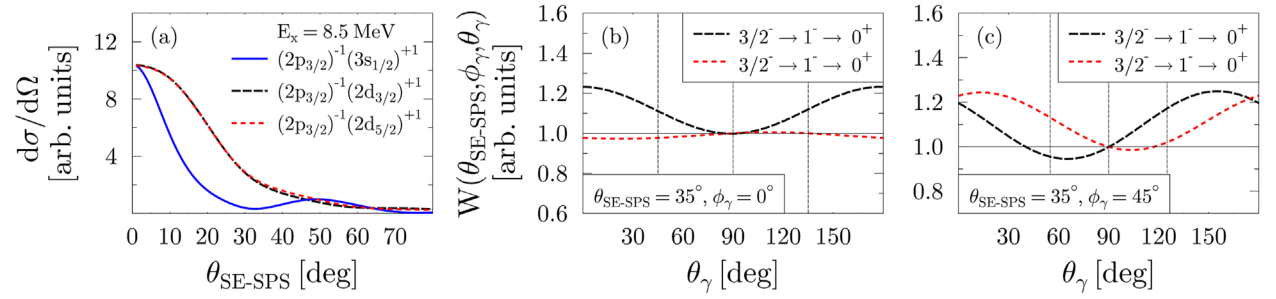

FIGURE 14
(A) Theoretical angular distributions for 1p-1h configurations populating an arbitrary $J^{\pi} = 1^{-}$ state at $E_x = 8.5$ MeV in ^{53}Cr$(d,p)^{54}$Cr and calculated with CHUCK3 [26] **(B, C)** Predicted proton-γ angular correlations in $(d,p\gamma)$ shown for two rings of CeBrA and calculated with ANGCOR [27]. Some of the detectors in those rings are highlighted with vertical, dashed lines.

means to test the microscopic details of wavefunctions predicted by theoretical models that mean to describe the γSF as also discussed in [49, 50].

3.3 Nuclear astrophysics studies with CATRiNA

The CATRiNA neutron detectors are aimed to be used in coincidence with other detector systems at the John D. Fox Laboratory. For instance, we recently performed a resonance spectroscopy study to constrain the ^{25}Al$(p,\gamma)^{26}$Si reaction rate via a very selective n/γ coincidence measurement [53].

The detection of the long-lived radioisotope ^{26}Al (5^{+}, $T_{1/2} = 7.17 \times 10^{5}$ yr) in the Galaxy via the satellite based observation of its characteristic 1.809-MeV γ-ray line is of paramount relevance in nuclear astrophysics [54]. This observation is recognized as direct evidence that nucleosynthesis is an ongoing process in the Galaxy, explaining earlier measurements of the excess of ^{26}Mg found in meteorites and presolar dust grains [55, 56]. The COMPTEL [57] and INTEGRAL [58] space missions have mapped the intensity distribution of the 1.809-MeV γ-ray line and inferred an equilibrium mass of $2-3$ solar masses of ^{26}Al in the Milky Way, with most of its mass accumulated in regions of star formation co-rotating with the plane of the Galaxy [59]. To understand the stellar nucleosynthesis of ^{26}Al, one needs to understand all the reactions that produce and destroy ^{26}Al in the relevant astrophysical scenarios. An additional complication to the accurate modeling and calculation of its nucleosynthesis comes from the short-lived isomeric state in ^{26}Al (0^{+}, $T_{1/2} = 6.4$ s) located 228 keV above the long-lived ground state [60].

At nova burning temperatures of $T \sim 0.1 - 0.5$ GK, the ^{25}Al$(p,\gamma)^{26}$Si reaction and the subsequent β-decay of ^{26}Si leads predominantly to the population of ^{26}Al in its short-lived isomeric state (^{26}Al^{m}) rather than its ground state (^{26}Al^{g}). The isomeric ^{26}Al^{m} (0^{+}) state directly β-decays to the ground state of ^{26}Mg (0^{+}), bypassing the emission of the 1.809-MeV γ-ray line. Therefore, ^{26}Al could contribute to the ^{26}Mg abundance measured in meteorites and pre-solar grains without space telescopes observing its associated γ ray.

A high-resolution measurement at the John D. Fox Laboratory was conducted to populate low-lying proton resonances in ^{26}Si using the ^{24}Mg$(^{3}$He$,n\gamma)^{26}$Si reaction to resolve outstanding discrepancies on the properties of the resonances relevant for the calculation of the ^{25}Al$(p,\gamma)^{26}$Si reaction rate. Specifically, we focused on five low-lying resonances within the Gamow window of this reaction [61]. For the experiment, a stable 10-MeV ^{3}He beam from the FN Tandem accelerator was used to bombard an enriched 492-μg/cm^{2} self-supporting ^{24}Mg target. The ^{3}He beam was bunched to 1.7-ns width with intervals of 82.5 ns. The unreacted beam was sent into a thick graphite disk acting as beam-stop located 2 m downstream from the target position. Neutrons from the ^{24}Mg$(^{3}$He$,n\gamma)^{26}$Si reaction were measured with a set of 16 CATRiNA neutron detectors placed at a distance of 1 m from the reaction target covering an angular range of $\Delta\theta_{lab} = \pm 40°$. A set of three FSU, Clover-type HPGe γ-ray detectors, placed at 90° from the target, were used to measure γ rays from deexcitations of populated states in ^{26}Si in coincidence. The PSD capabilities of CATRiNA were used to separate neutron from γ events detected in the CATRiNA detectors. The neutron gate in the PSD plots were then applied to the raw ToF spectra to obtain neutron-ToF spectra for all the CATRiNA detectors as shown in Figure 15.

The ToF spectrum of each detector cannot be easily added together since neutrons arriving at each detector from a given populated state in ^{26}Si have different energies due to the reaction kinematics. The neutron events for all 16 CATRiNA detectors were added together in a Q-value plot of the reaction. Given that the Q-value of the reaction for the ground-state is small ($Q_{gs} = 70$ keV), the Q-value plot can be read as the negative excitation energy of ^{26}Si. The states of interest, low-lying proton resonances in ^{26}Si, are located below $Q - 5.5$,MeV ($S_P = 5.513$ MeV). A Q-value vs. γ-ray energy correlation matrix was then built for events in coincidence between CATRiNA detectors and the FSU Clover-type HPGe detectors. Several transitions from resonant states are well resolved due to the high resolution of the γ-ray detectors. An example of this 2D correlation matrix is shown in Figure 15, expanded on states above the proton-separation threshold (states below the red dotted line) in coincidence with γ rays between $2.8-4.5$ MeV. One can clearly identify transitions corresponding to deexcitation of the 0^{+}_{4} and the 1^{+}_{1} states, respectively. Using the extracted spectroscopic information of relevant resonances in ^{26}Si, we calculated the rate

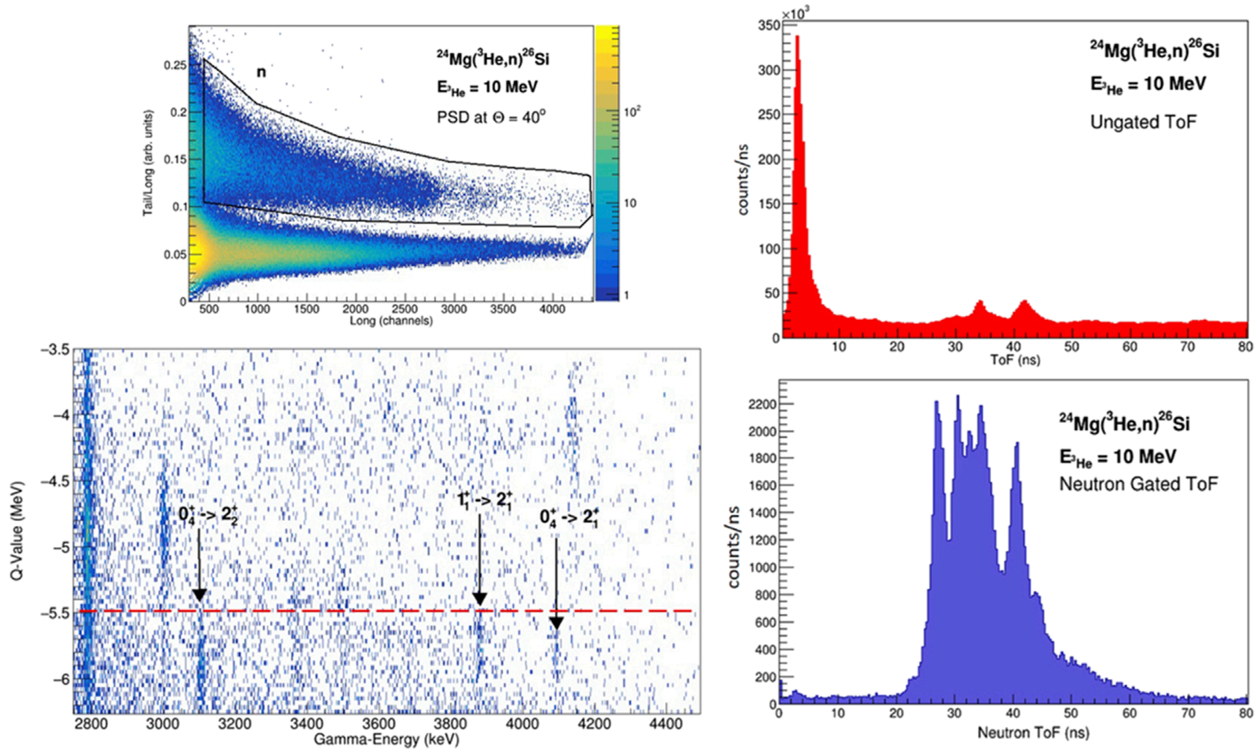

FIGURE 15
A pulse-shape discrimination (PSD) plot for one of the CATRiNA detectors is shown at the top left. Neutron events are clearly separated from γ-ray events. A raw time-of-flight (ToF) plot of CATRiNA is shown in the top right. A ToF plot gated on neutron events is shown in the bottom right. States in ^{26}Si are identified by their ToF relative to the prompt γ ray from the reaction. A zoomed-in portion of a Q-value vs. γ-ray energy correlation matrix, built from coincident neutron events and γ-ray events, is shown in the bottom left. States of interest are below the horizontal, dotted line which indicates the proton-separation energy (S_p) in ^{26}Si. Transitions corresponding to deexcitations of the 0_4^+ and 1_1^+ are clearly visible.

of the ^{25}Al$(p,\gamma)^{26}$Si reaction over nova temperatures resolving long standing discrepancies in the literature. See [53] for more details.

4 Summary and outlook

This article highlighted recently commissioned setups for particle-γ coincidence experiments at the FSU John D. Fox Superconducting Linear Accelerator Laboratory. Particularly, the combined CeBrA + SE-SPS setup for light-ion transfer experiments and coincident γ-ray detection, the coupling of the CATRiNA neutron detectors with HPGe detectors measuring neutron-γ coincidences for reaction-channel selection, and the combined CLARION2+TRINITY setup for high resolution γ-ray spectroscopy were featured. These setups allow to perform selective experiments addressing open questions in nuclear structure, nuclear reactions, and nuclear astrophysics. (d,p) studies of single-particle orbitals close to the $N = 28$ neutron-shell closure, of the pygmy dipole resonance (PDR), and of the ^{24}Mg$(^3$He$,n\gamma)^{26}$Si reaction to resolve outstanding discrepancies on the properties of the resonances relevant for the calculation of the ^{25}Al$(p,\gamma)^{26}$Si reaction rate were discussed. In the next couple of years, the full CeBrA array consisting of 14 CeBr$_3$ detectors will be completed. For the SE-SPS, plans are also in place to design a new focal-plane detector with increased position resolution and higher count rate capabilities based on the multi-layer thick gaseous electron multiplier (M-THGEM) technology [62–64], which also allows for the detection of heavier ions opening new possibilities for experimental studies. In addition, the design of a compact mini-orange conversion electron spectrometer for particle-electron coincidence experiments at the SE-SPS is nearly completed. In the near future, the CATRiNA detectors will be coupled with the CLARION2 HPGe detectors increasing the γ-ray efficiency significantly compared to previous experiments described in this article. Opportunities for coupling CATRiNA with the SE-SPS for charged-particle-neutron coincidence measurements are also being explored.

Data availability statement

The raw data supporting the conclusions of this article will be made available by the authors, without undue reservation.

Author contributions

M-CS: Conceptualization, Data curation, Formal Analysis, Funding acquisition, Investigation, Methodology, Project administration, Resources, Software, Supervision, Validation, Visualization, Writing–original draft, Writing–review and editing.

SA-C: Conceptualization, Data curation, Formal Analysis, Funding acquisition, Investigation, Methodology, Project administration, Resources, Software, Supervision, Validation, Visualization, Writing–original draft, Writing–review and editing.

Funding

The author(s) declare that financial support was received for the research, authorship, and/or publication of this article. The FSU group acknowledges support by the U.S. National Science Foundation (NSF) under Grant Nos. PHY-2012522 (WoU-MMA: Studies of Nuclear Structure and Nuclear Astrophysics) and PHY-2412808 (Studies of Nuclear Structure and Nuclear Astrophysics), and by the U.S. Department of Energy, National Nuclear Security Administration (NNSA) under Grant No. DE-NA0004150 [Center for Excellence in Nuclear Training And University-based Research (CENTAUR)] as part of the Stewardship Science Academic Alliances Centers of Excellence Program. Support by Florida State University is also gratefully acknowledged.

Acknowledgments

M-CS and SA.C. express their gratitude to the staff at the John D. Fox Laboratory for their continued support of the research program. Input from Samuel L. Tabor and Vandana Tripathi for the description of CLARION2+TRINITY, and from John D. Fox Laboratory Director Ingo Wiedenhöver is gratefully acknowledged. The authors thank Kirby W. Kemper for input for the history of the laboratory. M-CS thanks Ben Crider from Mississippi State University for the temporary loan of his 3 × 3 inch $CeBr_3$ detectors, and Lewis A. Riley from Ursinus College as well as Paul D. Cottle from Florida State University for the continuing and productive collaboration. SA.C. thanks former FSU graduate students Jesus Perello and Ashton Morelock for the contributions to the development of CATRiNA during their graduate work. M-CS also thanks FSU graduate students Alex L. Conley, Dennis Houlihan, and Bryan Kelly for their contributions to the presented work.

Conflict of interest

The authors declare that the research was conducted in the absence of any commercial or financial relationships that could be construed as a potential conflict of interest.

Generative AI statement

The author(s) declare that no Generative AI was used in the creation of this manuscript.

Publisher's note

References

1. John D. *Fox superconducting linear accelerator laboratory*. Florida State University (2024). Available from: https://fsunuc.physics.fsu.edu (Accessed December, 2024).

2. Carter E, Davis R. He-H_2-and other negative ion beams available from a duoplasmatron ion source with gas charge exchange. *Rev Scientific Instr* (1963) 34:93–6. doi:10.1063/1.1718134

3. Fox J, Moore C, Robson D. Excitation of isobaric analog states in $_{89}$Y and ^{90}Zr. *Phys Rev Lett* (1964) 12:198–200. doi:10.1103/PhysRevLett.12.198

4. Chapman K. Florida State University superconducting booster. *Nucl Instr Methods* (1981) 184:239–45. doi:10.1016/0029-554X(81)90875-2

5. Fox J, Frawley A, Myers E, Wright L, Chapman K, Smith D, et al. The Florida State University superconducting heavy ion linear accelerator — recent progress. *Nucl Instr Methods Phys Res Section B: Beam Interactions Mater Atoms* (1987) 24-25:757–8. doi:10.1016/S0168-583X(87)80240-9

6. Myers E, Chapman K, Fox J, Frawley A, Allen P, Faragasso J, et al. Status of the Florida State University superconducting linear accelerator. *Nucl Instr Methods Phys Res Section B: Beam Interactions Mater Atoms* (1989) 40-41:904–7. doi:10.1016/0168-583X(89)90504-1

7. Wiedenhoever I, Baby LT, Santiago-Gonzales D, Rojas A, Blackmon JC, Rogachev GV, et al. Studies of exotic nuclei at the RESOLUT facility of Florida state university. In: JH Hamilton, AV Ramayya, editors. *Fission and properties of neutron-rich nuclei - proceedings of the fifth international conference on ICFN5*. World Scientific Publishing Co. Pte. Ltd. (2013). p. 144–51. doi:10.1142/9789814525435_0015

8. Koshchiy E, Blackmon J, Rogachev G, Wiedenhöver I, Baby L, Barber P, et al. ANASEN: the array for nuclear astrophysics and structure with exotic nuclei. *Nucl Instr Methods Phys Res Section A: Acc Spectrometers, Detectors Associated Equipment* (2017) 870:1–11. doi:10.1016/j.nima.2017.07.030

9. Baby L, Kuvin S, Wiedenhöver I, Anastasiou M, Caussyn D, Colbert K, et al. RESONEUT: a detector system for spectroscopy with (d,n) reactions in inverse kinematicsn reactions in inverse kinematics. *Nucl Instr Methods Phys Res Section A: Acc Spectrometers, Detectors Associated Equipment* (2018) 877:34–43. doi:10.1016/j.nima.2017.09.019

10. Asher B, Almaraz-Calderon S, Baby L, Gerken N, Lopez-Saavedra E, Morelock A, et al. The encore active target detector: a multi-sampling ionization chamber. *Nucl Instr Methods Phys Res Section A: Acc Spectrometers, Detectors Associated Equipment* (2021) 1014:165724. doi:10.1016/j.nima.2021.165724

11. Good E, Sudarsan B, Macon K, Deibel C, Baby L, Blackmon J, et al. SABRE: the silicon array for branching ratio experiments. *Nucl Instr Methods Phys Res Section A: Acc Spectrometers, Detectors Associated Equipment* (2021) 1003:165299. doi:10.1016/j.nima.2021.165299

12. Conley A, Kelly B, Spieker M, Aggarwal R, Ajayi S, Baby L, et al. The CeBrA demonstrator for particle-γ coincidence experiments at the FSU Super-Enge Split-Pole Spectrograph. *Nucl Instr Methods Phys Res Section A: Acc Spectrometers, Detectors Associated Equipment* (2024) 1058:168827. doi:10.1016/j.nima.2023.168827

13. Gray T, Allmond J, Dowling D, Febbraro M, King T, Pain S, et al. CLARION2-TRINITY: a Compton-suppressed HPGe and GAGG: Ce-Si-Si array for absolute cross-section measurements with heavy ions. *Nucl Instr Methods Phys Res Section A: Acc Spectrometers, Detectors Associated Equipment* (2022) 1041:167392. doi:10.1016/j.nima.2022.167392

14. Enge HA. Magnetic spectrographs for nuclear reaction studies. *Nucl Instr Methods* (1979) 162:161–80. doi:10.1016/0029-554X(79)90711-0

15. CAEN. Digitizer families (2024). Available from: https://www.caen.it/sections/digitizer-families/ (Accessed December, 2024).

16. Good EC. *A study of* ^{26}*Al (p, γ)*^{27}*Si with the silicon array for branching ratio experiments (SABRE)*. Ph.D. thesis, Louisiana State University (2020).

17. DeVries R, Shapira D, Clover M. Increasing a spectrometer's solid angle without loss of resolution. *Nucl Instr Methods* (1977) 140:479–80. doi:10.1016/0029-554X(77)90364-0

18. Riley LA, Nebel-Crosson JM, Macon KT, McCann GW, Baby LT, Caussyn D, et al. ^{50}Ti(*d, p*)^{51}Ti: single-neutron energies in the *N*=29 isotones, and the *N*=32 subshell closure. *Phys Rev C* (2021) 103:064309. doi:10.1103/PhysRevC.103.064309

19. Riley LA, Hay ICS, Baby LT, Conley AL, Cottle PD, Esparza J, et al. ^{54}Fe(*d, p*)^{55}Fe and the evolution of single neutron energies in the *N*=29 isotones. *Phys Rev C* (2022) 106:064308. doi:10.1103/PhysRevC.106.064308

20. Spieker M, Baby LT, Conley AL, Kelly B, Müscher M, Renom R, et al. Experimental study of excited states of ^{62}Ni via one-neutron (*d, p*) transfer up to the neutron-separation threshold and characteristics of the pygmy dipole resonance states. *Phys Rev C* (2023) 108:014311. doi:10.1103/PhysRevC.108.014311

21. Riley LA, Simms DT, Baby LT, Conley AL, Cottle PD, Esparza J, et al. $g_{9/2}$ neutron strength in the N=29 isotones and the ^{52}Cr(*d, p*)^{53}Cr reaction. *Phys Rev C* (2023) 108:044306. doi:10.1103/PhysRevC.108.044306

22. Hay ICS, Cottle PD, Riley LA, Baby LT, Baker S, Conley AL, et al. Measurement of $g_{9/2}$ strength in the stretched 8^- state and other negative parity states via the ^{51}V(*d, p*)^{52}V reaction. *Phys Rev C* (2024) 109:024302. doi:10.1103/PhysRevC.109.024302

23. Kuchera AN, Hoffman CR, Ryan G, D'Amato IB, Guarinello OM, Kielb PS, et al. Single-neutron adding on ^{34}S. *The Eur Phys J A* (2024) 60:176. doi:10.1140/epja/s10050-024-01399-z

24. NNDC Online Data Service. ENSDF database (2024). Available from: http://wwwnndcbnlgov/ensdf/ (Accessed December, 2024).

25. Riley LA, Spieker M, Cottle PD, et al. *A study of the ^{52}Cr^{53}(d, pγ)^{53}Cr reaction with the CeBrA demonstrator* (2024).

26. Kunz PD, Comfort JR. Extended version (unpublished). *Program CHUCK3* (1978).

27. Harakeh MN, Put LW. KVI internal report 67i, (unpublished). *Program ANGCOR* (1979).

28. Rybicki F, Tamura T, Satchler G. Particle-gamma angular correlations following nuclear reactions. *Nucl Phys A* (1970) 146:659–76. doi:10.1016/0375-9474(70)90748-7

29. Thompson IJ. Coupled reaction channels calculations in nuclear physics. *Comput Phys Rep* (1988) 7:167–212. doi:10.1016/0167-7977(88)90005-6

30. Perello J, Almaraz-Calderon S, Asher B, Baby L, Gerken N, Hanselman K. Characterization of the CATRiNA neutron detector system. *Nucl Instr Methods Phys Res Section A: Acc Spectrometers, Detectors Associated Equipment* (2019) 930:196–202. doi:10.1016/j.nima.2019.03.084

31. Morelock A, Perello J, Almaraz-Calderon S, Asher B, Brandenburg K, Derkin J, et al. Characterization and description of a spectrum unfolding method for the CATRiNA neutron detector array. *Nucl Instr Methods Phys Res Section A: Acc Spectrometers, Detectors Associated Equipment* (2022) 1034:166759. doi:10.1016/j.nima.2022.166759

32. Goorley T, James M, Booth T, Brown F, Bull J, Cox L, et al. Initial MCNP6 release overview. *Nucl Technol* (2012) 180:298–315. doi:10.13182/NT11-135

33. Perello Izaguirre J. *Study of low-lying proton resonances in ^{26}Si and neutron spectroscopic studies with CATRiNA*. Ph.D. thesis, Florida State University (2021).

34. Gray T, Allmond J, Benetti C, Wibisono C, Baby L, Gargano A, et al. Suppressed electric quadrupole collectivity in ^{49}ti. *Phys Lett B* (2024) 855:138856. doi:10.1016/j.physletb.2024.138856

35. Lee J, Tsang MB, Bazin D, Coupland D, Henzl V, Henzlova D, et al. Neutron-proton asymmetry dependence of spectroscopic factors in Ar isotopes. *Phys Rev Lett* (2010) 104:112701. doi:10.1103/PhysRevLett.104.112701

36. Tostevin JA, Gade A. Updated systematics of intermediate-energy single-nucleon removal cross sections. *Phys Rev C* (2021) 103:054610. doi:10.1103/PhysRevC.103.054610

37. Kay BP, Tang TL, Tolstukhin IA, Roderick GB, Mitchell AJ, Ayyad Y, et al. Quenching of single-particle strength in A=15 nuclei. *Phys Rev Lett* (2022) 129:152501. doi:10.1103/PhysRevLett.129.152501

38. Lee J, Tsang MB, Lynch WG. Neutron spectroscopic factors from transfer reactions. *Phys Rev C* (2007) 75:064320. doi:10.1103/PhysRevC.75.064320

39. Lee J, Tsang MB, Lynch WG, Horoi M, Su SC. Neutron spectroscopic factors of ni isotopes from transfer reactions. *Phys Rev C* (2009) 79:054611. doi:10.1103/PhysRevC.79.054611

40. Tsang MB, Lee J, Su SC, Dai JY, Horoi M, Liu H, et al. Survey of excited state neutron spectroscopic factors for Z=8−28 nuclei. *Phys Rev Lett* (2009) 102:062501. doi:10.1103/PhysRevLett.102.062501

41. Schiffer JP, Hoffman CR, Kay BP, Clark JA, Deibel CM, Freeman SJ, et al. Test of sum rules in nucleon transfer reactions. *Phys Rev Lett* (2012) 108:022501. doi:10.1103/PhysRevLett.108.022501

42. Schiffer JP, Hoffman CR, Kay BP, Clark JA, Deibel CM, Freeman SJ, et al. Valence nucleon populations in the Ni isotopes. *Phys Rev C* (2013) 87:034306. doi:10.1103/PhysRevC.87.034306

43. Prisciandaro J, Mantica P, Brown B, Anthony D, Cooper M, Garcia A, et al. New evidence for a subshell gap at N=32. *Phys Lett B* (2001) 510:17–23. doi:10.1016/S0370-2693(01)00565-2

44. Leistenschneider E, Reiter MP, Ayet San Andrés S, Kootte B, Holt JD, Navrátil P, et al. Dawning of the *N*=32 shell closure seen through precision mass measurements of neutron-rich titanium isotopes. *Phys Rev Lett* (2018) 120:062503. doi:10.1103/PhysRevLett.120.062503

45. Liu HN, Obertelli A, Doornenbal P, Bertulani CA, Hagen G, Holt JD, et al. How robust is the *N*=34 subshell closure? First spectroscopy of ^{52}Ar. *Phys Rev Lett* (2019) 122:072502. doi:10.1103/physrevlett.122.072502

46. Savran D, Aumann T, Zilges A. Experimental studies of the pygmy dipole resonance. *Prog Part Nucl Phys* (2013) 70:210–45. doi:10.1016/j.ppnp.2013.02.003

47. Bracco A, Lanza E, Tamii A. Isoscalar and isovector dipole excitations: nuclear properties from low-lying states and from the isovector giant dipole resonance. *Prog Part Nucl Phys* (2019) 106:360–433. doi:10.1016/j.ppnp.2019.02.001

48. Lanza E, Pellegri L, Vitturi A, Andrés M. Theoretical studies of pygmy resonances. *Prog Part Nucl Phys* (2023) 129:104006. doi:10.1016/j.ppnp.2022.104006

49. Spieker M, Heusler A, Brown BA, Faestermann T, Hertenberger R, Potel G, et al. Accessing the single-particle structure of the pygmy dipole resonance in ^{208}Pb. *Phys Rev Lett* (2020) 125:102503. doi:10.1103/PhysRevLett.125.102503

50. Weinert M, Spieker M, Potel G, Tsoneva N, Müscher M, Wilhelmy J, et al. Microscopic structure of the low-energy electric dipole response of ^{120}Sn. *Phys Rev Lett* (2021) 127:242501. doi:10.1103/PhysRevLett.127.242501

51. Inakura T, Nakatsukasa T, Yabana K. Emergence of pygmy dipole resonances: magic numbers and neutron skins. *Phys Rev C* (2011) 84:021302. doi:10.1103/PhysRevC.84.021302

52. Ratkiewicz A, Cizewski JA, Escher JE, Potel G, Harke JT, Casperson RJ, et al. Towards neutron capture on exotic nuclei: demonstrating (*d,pγ*) as a surrogate reaction for (*n*, γ). *Phys Rev Lett* (2019) 122:052502. doi:10.1103/PhysRevLett.122.052502

53. Perello JF, Almaraz-Calderon S, Asher BW, Baby LT, Benetti C, Kemper KW, et al. Low-lying resonances in ^{26}Si relevant for the determination of the astrophysical ^{25}Al(*p*, γ)^{26}Si reaction rate. *Phys Rev C* (2022) 105:035805. doi:10.1103/PhysRevC.105.035805

54. Prantzos N, Diehl R. Radioactive ^{26}Al in the galaxy: observations versus theory. *Phys Rep* (1996) 267:1–69. doi:10.1016/0370-1573(95)00055-0

55. Lee T, Papanastassiou DA, Wasserburg GJ. Aluminum-26 in the early solar system: fossil or fuel? *Astrophysical J Lett* (1977) 211:L107–L110. doi:10.1086/182351

56. José J, Hernanz M, Amari S, Lodders K, Zinner E. The imprint of nova nucleosynthesis in presolar grains. *Astrophysical J* (2004) 612:414–28. doi:10.1086/422569

57. Diehl R, Dupraz C, Bennett K, Bloemen H, Hermsen W, Knoedlseder J, et al. COMPTEL observations of Galactic 26Âl emission. *Astron Astrophysics* (1995) 298:445.

58. Laurent Bouchet JPR Elisabeth Jourdain. Observation of the ^{26}al emission distribution throughout the galaxy with integral/spi. *PoS ICRC2015* (2015) 896. doi:10.22323/1.236.0896

59. Diehl R, Halloin H, Kretschmer K, Lichti GG, Schönfelder V, Strong AW, et al. Radioactive ^{26}al from massive stars in the galaxy. *Nature* (2006) 439:45–7. doi:10.1038/nature04364

60. Iliadis C, Champagne A, Chieffi A, Limongi M. The effects of thermonuclear reaction rate variations on ^{26}Al production in massive stars: a sensitivity study. *Astrophysical J Suppl Ser* (2011) 193:16. doi:10.1088/0067-0049/193/1/16

61. Chipps KA. Resonances above the proton threshold in ^{26}Si. *Phys Rev C* (2016) 93:035801. doi:10.1103/PhysRevC.93.035801

62. de Olivera R, Cortesi M. First performance evaluation of a multi-layer thick gaseous electron multiplier with in-built electrode meshes—MM-THGEM. *J Instrumentation* (2018) 13:P06019. doi:10.1088/1748-0221/13/06/P06019

63. Cortesi M, Pereira J, Bazin D, Ayyad Y, Cerizza G, Fox R, et al. Development of a novel MPGD-based drift chamber for the NSCL/FRIB S800 spectrometer. *J Instrumentation* (2020) 15:P03025. doi:10.1088/1748-0221/15/03/P03025

64. Ciraldo I, Brischetto G, Torresi D, Cavallaro M, Agodi C, Boiano A, et al. Characterization of a gas detector prototype based on Thick-GEM for the MAGNEX focal plane detector. *Nucl Instr Methods Phys Res Section A: Acc Spectrometers, Detectors Associated Equipment* (2023) 1048:167893. doi:10.1016/j.nima.2022.167893

frontiers | Frontiers in Physics

TYPE Review
PUBLISHED 03 January 2025
DOI 10.3389/fphy.2024.1511402

OPEN ACCESS

EDITED BY
Alan Wuosmaa,
University of Connecticut, United States

REVIEWED BY
Linda Hlophe,
Michigan State University, United States
Andres Arazi,
National Atomic Energy
Commission, Argentina

*CORRESPONDENCE
L. G. Sobotka,
✉ lgs@wustl.edu

RECEIVED 14 October 2024
ACCEPTED 29 November 2024
PUBLISHED 03 January 2025

CITATION
Sobotka LG and Charity RJ (2025) Using intermediate energy knockout, pickup, and charge exchange reactions with invariant mass spectroscopy for investigating nuclear structure beyond the proton drip line.
Front. Phys. 12:1511402.
doi: 10.3389/fphy.2024.1511402

Using intermediate energy knockout, pickup, and charge exchange reactions with invariant mass spectroscopy for investigating nuclear structure beyond the proton drip line

L. G. Sobotka[1,2]* and R. J. Charity[1]

[1]Department of Chemistry, Washington University, St. Louis, MO, United States, [2]Department of Physics, Washington University, St. Louis, MO, United States

The continuum structure of light p-rich elements has been extensively studied in recent years by invariant-mass spectroscopy. The feeble Coulomb barrier for light proton-rich nuclei makes proton decay an essential tool in this region not unlike alpha decay is in the trans-Pb region and neutron-deficient rare earths. Unlike binary alpha decay, the part of the Chart of the Nuclides this mini review will focus on can undergo decay into many-particle final states and invariant-mass spectroscopy is the frame-invariant and multi-particle replacement for simple binary alpha-particle spectroscopy. Here we highlight how pairing is reflected in the zig-zaggy pattern of the drip line, the decay of nuclides beyond the drip lines, and what the masses of nuclides exterior to the p-drip line have taught us about shell structure. In this context, the subtlety of removing the Wigner, or n-p congruence, energy when interpreting nucleon separation-energy systematics is discussed. We also present examples of where isospin symmetry is maintained in the continuum and where it is not.

KEYWORDS

invariant mass, Wigner energy, intermediate energy, shell structure, reactions

1 Introduction

For medium and heavy nuclei, the large Coulomb barriers for fission, alpha, and proton decay retard these decays and allow weak decay modes to dominate over large regions of the nuclear chart. As the Coulomb barrier reduces with decreasing atomic number (Z), the proton decay rate increases becoming the dominate decay mode in the South-West part of the chart. Until one reaches decay rates commensurate with nucleon transit times across a nucleus, the nuclei that p-decay are no less real than those with positive Q-values for alpha decay, or for that matter, positive fission Q-values. These metastable nuclei exhibit structure and are amenable to study by a technique that is at its essence no different than what is done with alpha-particle spectroscopy. This technique is called invariant-mass spectroscopy (IMS) and is the tool employed for extracting the results reported here.

This mini-review presents some selected results which have employed IMS operating on knockout, charge exchange, and pickup reaction products. As soon will become clear, the primary utility of using the different reaction types is that the continuum structure of several nuclei in the region of a single secondary beam can be studied in one experiment. Some confirmation of the reaction mechanism can often be found in the velocity of the reconstructed decaying parent nucleus, e.g., a product of a simple knockout reaction will have a velocity close to that of the beam while pickup and charge-exchange products are notably slower [1]. The angular momentum mismatch in intermediate energy pick-up reactions favors population of high-spin states. This feature may, or may not, be advantageous, but cognizance of this bias is certainly required [1, 2].

We will start by showing how pairing is reflected in the zig-zaggy pattern of the drip line and in the total number and type (1p or prompt 2p) proton-decay steps. The second selected topic is a presentation of how the masses of some of the newly discovered light p-rich nuclei have informed us about the evolution of nuclear structure far from stability. In this exercise the subtlety of removing the Wigner, or n-p congruence, energy must be considered as the cases transit through $N \sim Z$. We then present examples where isospin symmetry is maintained, with textbook clarity, in the continuum. The first of these is two mated pairs of 2-proton decay from analog T = 2 to T = 1 states. One of each pair is from the ground-state of the $T_z = T$ nuclide and the decay of the mate from the excited analog in the $T_z = T - 1$ nuclide. In both mated pairs, i.e., all 4 decays, 2p decay occurs as there is no 1p decay that is both energy and isospin allowed. The second isospin symmetry demonstration is paired rotational bands embedded in the continuum. We finish our selected topics with some counter balance to the above examples with selected cases of isospin symmetry breaking induced by asymmetric decay thresholds between the isospin partners. Not presented in this work are the many subtleties of employing IMS for complex nuclear decays, e.g., constructing backgrounds. For this technical detail the interested reader is directed elsewhere, e.g., [3].

2 Experimental methods

The invariant-mass technique requires an accurate determination of the energy-momentum 4-vectors of all the products in the final state. From this information, the decay energy (E_T) of the parent relative to the multifragmented final state can be determined. The technique is not different in its base form from what is used in high-energy physics to, for example, determine the mass of the Higgs boson from detecting the final-state photon and the pairs of either electrons or muons that the Z boson decays into [4]. In fact, this example is similar to many nuclear IMS studies where the decay is concatenated and the intermediate is identified by correlations within a sub-event. In cases relevant to this mini-review, a decay that ultimately produces two protons and a residue can emit two protons at the same time, likely because there is no intermediate state, or sequentially emit two protons. In the latter case the intermediate can be identified because the invariant mass of one of the protons and the residue, one of two sub-events in this case, reconstruct the mass of a known resonance in the intermediate nucleus [5]. However, in another sense IMS is just an inversion of what is done in α-particle spectroscopy where measuring the energy of the α particle provides an excitation spectrum of the daughter. As indicated in the introduction, there is another connection between α-particle spectroscopy and the IMS employed to study p-rich nuclei. In both cases, the parents are energetically metastable and kinetically trapped by a Coulomb barrier.

A typical experiment is diagrammed in Figure 1A. The emitted light particles, residue, and any γ ray from the deexcitation of the residue must be detected. If there are neutrons emitted they must be detected, but this review will not deal with such cases as the focus is on studies of p-rich nuclei. Some non-obvious subtleties are worth pointing out. The ultimate resolution is often limited by the undetermined energy losses in a finite-thickness target. The choice of target thickness is fixed by the width of the parent state one is seeking to study. (The wider this state, the thicker the target one can tolerate.) There is one - fortunate - case where the target thickness is usually not a significant contributor to the resolution. If there is no heavy residue and all the decay fragments have the same energy loss per unit mass, e.g., the decay of ^{10}C into 2α's and $2p'$s or the decay of ^{8}C into one α and $4p'$s, there is no differential velocity loss in the target. The transverse position of the reaction vertex in the target is a higher-order correction in that the IMS logic only requires a common vertex.

At intermediate energy, stopping of light charged particles requires rather thick scintillators. These scintillators have far inferior energy resolution as compared to double-sided Si detectors that are typically employed for the ΔE measurement and to fix the position of the light-charged particles. This difference in resolution translates into the general result that decays transverse to the beam, where the IMS resolution is largely fixed by the position, have superior resolution compared to longitudinal decays for which the IMS resolution is largely determined by the resolution of the scintillator and relative energy-loss considerations [10].

Related to the common vertex assumption, and the determination of the relative momentum vectors, an accurate position of the residue, should it exist, is important. All our recent work has employed some version of a 2-dimensional scintillating-fiber array positioned close the plane of the position determining Si detector, to fix the residue trajectory. This position fix of the residue that is ultimately detected in either a spectrometer [7] or in the Si array itself [6] comes at the cost of some modest efficiency loss (~15 %) as the fibers have inactive cladding [11–14].

Finally, if the heavy daughter is produced in a bound excited state, the value of the decay energy E_T determined by the particles alone will be that in reference to the excited daughter. To reconstruct the actual mass-difference relative to the ultimate (perhaps multi-particle) final ground state, the emitted gamma's must be detected. This can be done in high efficiency, but not high resolution, with scintillation-based γ-ray detectors that surround the target [8]. These considerations have lead to several systems of which the schematic setup shown in Figure 1A is one.

3 Selected results

3.1 Decays beyond the drip lines

We start by showing a decays-eye view of the lower portion of the nuclear chart in Figure 1B. The zig-zaggy drip lines are defined in this part of the chart and these lines display easily understood pairing features. Namely, even atomic number (Z) elements have proton drip lines more removed from stability and the neutron-drip

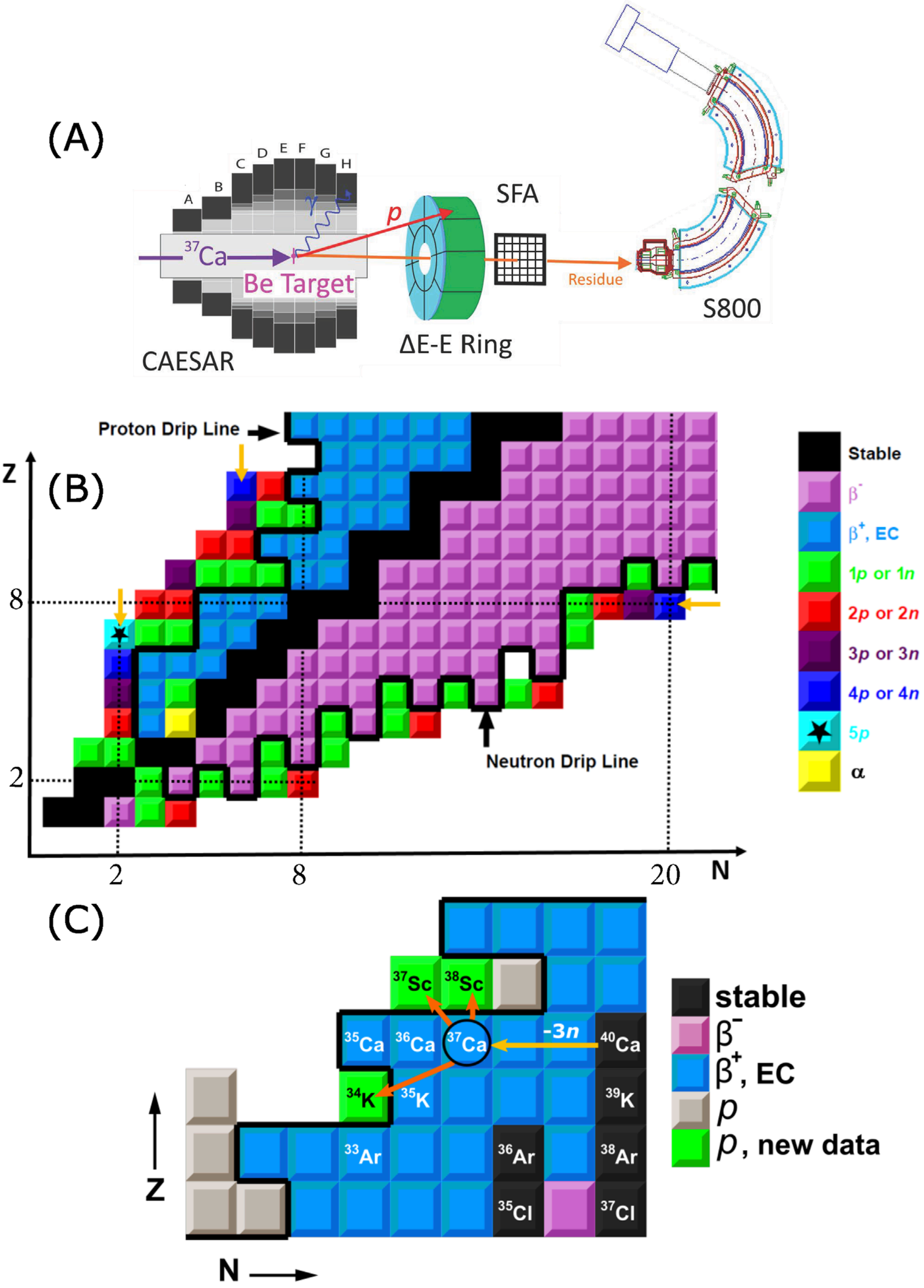

FIGURE 1
(A) Schematic of an invariant-mass experiment utilizing a position-sensitive ΔE-E [Si-CsI(Tl)] telescope for light charged-particle detection [6, 15], a spectrometer for identification and energy determination of the heavy residue (S800) [7], a scintillating fiber array (SFA) for an accurate determination of the position of the residue [15], and an array for detecting γ rays from excited residues (CAESAR) [8]. **(B)** Lower portion of the Chart of the Nuclides where the drip lines, multi-nucleon decays, and the standard magic numbers (2, 8 and, for neutrons only, 20) are indicated, the latter by dotted lines. The orange arrows are decay sequences mentioned in the text **(C)**. Starting from a primary beam of ^{40}Ca, the selected secondary, ^{37}Ca, produces the indicated products upon collisions with ^{9}Be nuclei in the secondary target. Among the produced nuclei are three (^{34}K, ^{37}Sc, and ^{38}Sc, shown in lime) previously unobserved and for which ground-state masses were determined [9].

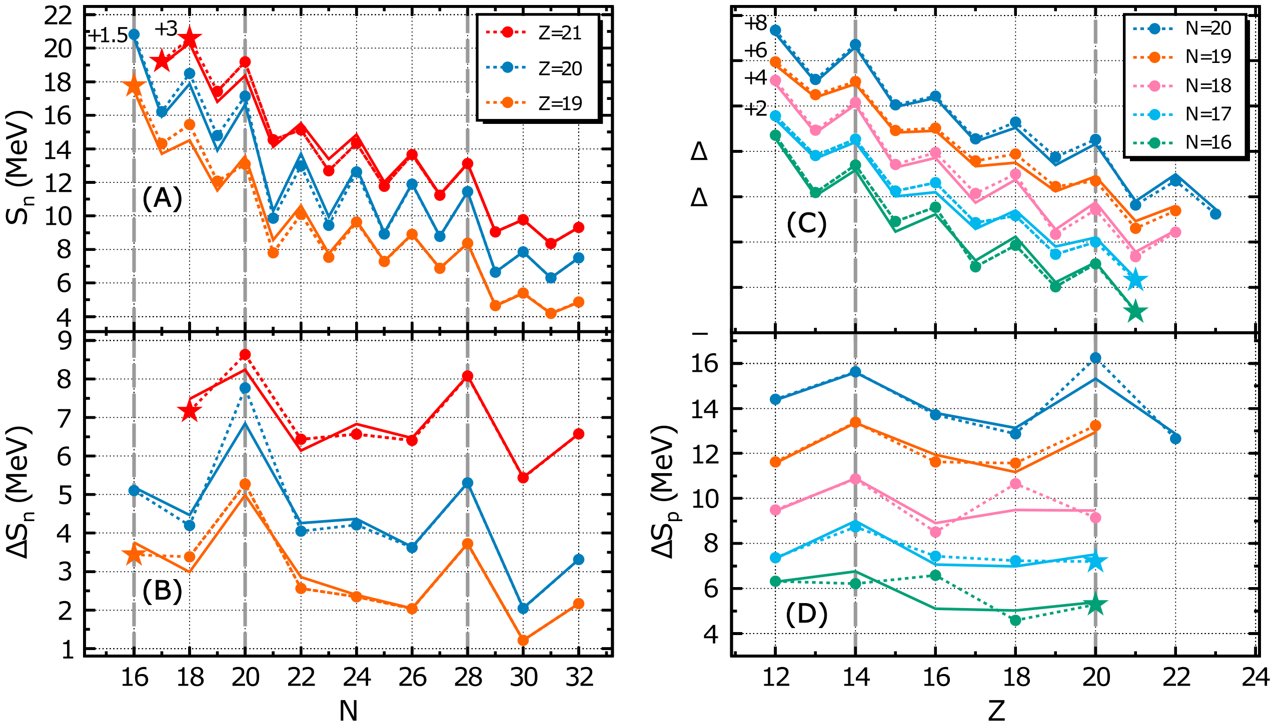

FIGURE 2
Experimental neutron **(A)** and proton **(C)** separation energies and changes in neutron **(B)** and proton **(D)** separation energies for even-*N* isotopes and even *Z* isotones. Data are represented by points (or stars for new values) connected by dashed lines and are shifted, as indicated, for visual clarity. Removing the Wigner energy results in the solid lines.

line is scalloped with even neutron number (N) isotopes inside and odd N isotopes outside the drip line. As required by the energetics, the number of nucleons emitted is that required to land inside the drip line. The N = 6 isotones, note upper orange arrow, extend from 1 to 4 protons emitted from ^{15}F to ^{18}Mg [14] (with the residue in each being ^{14}O). The N = 2 isotones extend from ^{5}Li up to ^{9}N with the latter (see star) exhibiting the record length decay chain of 5 protons [15]. By examination of the subevents, it is often possible to reconstruct the kinetic decay chain, see, for example, [5]. If Z = odd, the first decay step is always emission of a single proton and long decay sequences are concatenations of 1p and prompt 2p decay steps. The latter principally, but not exclusively, occurs when there is no energy and isospin allowed 1p decay path.

3.2 Wigner-removed separation energies

Using a secondary beam of ^{37}Ca impinging on a ^{9}Be target, resonances corresponding to the ground states of ^{34}K and ^{37,38}Sc were found, see Figure 1C. Using the IMS determined decay energies and the known mass excesses of the daughters, three new masses were determined [9]. These mass measurements allow for an extended look at neutron and proton separation-energy trends, which are shown in the upper panels of Figure 2 (The new masses allowed for calculation of the data represented by stars.) The lower panels in this figure show the separation energy differences defined by $\Delta S_n(N,Z) = S_n(N,Z) - S_n(N+1,Z) = [\Delta M(N+1,Z) + \Delta M(N-1,Z)] - 2\Delta M(N,Z)$ and an equivalent expression for protons.

First, take note of the expected behavior. The jumps in ΔS_n at $N = 20$ and $N = 28$ illustrate the classic neutron shell closures. The reduced increase in ΔS_n for $^{41}_{21}\mathrm{Sc}_{20}$ (red, top data sequence) should be noted and we shall return to this observation. Next, note that at $N = 16$, the raw data (points connected with dotted lines) suggest a neutron shell closure for ^{36}Ca (blue). (The word "suggest" is used as one expects a general increase in neutron separation energy with decreasing neutron number.) This had previously been noted [16]. However, the new data point, for $Z = 19$ (orange star), indicates that the enhanced binding for $N = 16$ has largely diminished. Again, we shall return to this observation. Finishing on what is, more-or-less, expected; note that the change in proton separation energies exhibit a clear peak for ^{40}Ca (Figure 2D, blue points and dotted line). One observes a diminution of ΔS_p and the apparent loss of the enhancement of the proton removal energy when N recedes below 20.

Before proceeding to the explore the not-so-obvious trends, for which some inklings were provided above, we have to appreciate that there are three structure issues at play in these mass derived quantities. Two of these are the standard issues of nuclear shells and pairing of like nucleons. The remaining issue, unimportant for heavier nuclei or neutron-rich nuclei, is the so-called Wigner or n-p congruence energy [17, 18]. The latter, included early on in macroscopic mass models, results in extra stabilization near

$N = Z$ and arises from $T = 0$ (but not necessarily $J = 1$) neutron-proton pairing correlations [19]. The real separation energies are enhanced if the parent N/Z asymmetry is smaller, suppressing its mass, than that of the daughter. If one desires to focus only the impact of nuclear shells, pseudo separation energies should be constructed which remove congruence-energy effects. Such Wigner-"corrected" separation energies, are not observables as they remove, in a model-dependent way, one structure effect. As the Wigner energy rapidly reduces away from $N = Z$, Wigner-removed pseudo values of $\Delta S_n(N, Z)$ are strongly reduced if the central nucleus has $N = Z$ (as the actual separation energies are inflated by n/p congruence) and will increase this quantity if either of the nuclei corresponding to one nucleon added or removed has $N = Z$. To generate the Wigner-removed pseudo-separation energies we employ the procedure suggested by Goriely *et al* [20]. The results are shown as solid lines, without points, in Figure 2. The shading between the solid and dashed lines highlights the Wigner-energy contribution.

We are now ready to return to the not-so-obvious trends. The Wigner-energy-removed pseudo-separation energies confirm the suggestion of a $N = 16$ subshell closure as one observes that $\Delta S_n(N, Z)$ increases from $N = 18$ to $N = 16$ for potassium ($Z = 19$) isotopes similar to the trend observed for calcium isotopes, compare orange and blue solid lines *without dots* in Figure 2B. (Removing the Wigner energy suppresses the pseudo-separation energy for $^{37}_{19}K_{18}$ more than for $^{35}_{19}K_{16}$, as the former is closer to $N = Z$.)

A $Z = 14$ subshell closure is most clearly seen as a peak in ΔS_p between $N = 20$ and $N = 17$, see Figure 2D. At $N = 16$, there is no evidence for this feature. With 16 neutrons, the $\nu 0d_{5/2}$ and $\nu 1s_{1/2}$ orbitals are nominally filled, so adding another neutron starts filling the $\nu 0d_{3/2}$ orbital. Through the tensor interaction [21], neutrons occupying the $\nu 0d_{3/2}$ will stabilize the $\pi 0d_{5/2}$, increasing the energy gap between it and the higher lying $\pi 1s_{1/2}$. This effect explains the observed low proton occupation of the $\pi 1s_{1/2}$ orbit in $^{34}_{14}Si_{20}$, which lead to the suggestion that this nucleus is doubly magic [22]. More insight into this topic can be found in the paper by J. Chen found in the present issue [23]. Finding the mirror of this effect in $^{34}_{20}Ca_{14}$ is a future research opportunity.

Neither the real nor the Wigner-removed pseudo-proton-separation energy differences show an increase at $Z = 20$ for $N < 19$ (The recent invariant-mass work added data allowing for the calculation of the values for $N = 17$ and $N = 16$, stars in Figure 2D.) In these cases, the Wigner modification is of little consequence. This analysis confirms that $Z = 20$ has lost its "magicity" for $N < 19$. This conclusion had previously been reached through the two-nucleon removal cross section for ^{38}Ca [24] and measurement of the B (E2) for ^{36}Ca [25]. This enfeebling of the $Z = 20$ shell for neutron deficient isotopes has also been mentioned in a recent global examination of shell gaps over the whole chart of nuclides [26]. However, with some introspection, data from ^{40}Ca (e,e'p) [27] told us three decades ago that even ^{40}Ca had a somewhat open proton sd shell and an appreciable cross-shell $f_{7/2}$ spectroscopic factor of about 1/3, (results confirmed by (d,^{3}He) proton knockout studies [28].) Another point of heuristic value deduced from panels (B) and (D) of Figure 2, is that congruence is a non-negligible contributor to the stability of ^{40}Ca.

Finally, we return to an observation made above from Figure 2B - the reduced increase in ΔS_n for $^{41}_{21}Sc_{20}$ (red) compared to the two other isotones plotted (either $^{40}_{20}Ca_{20}$ or $^{39}_{19}K_{20}$). The Wigner-energy-removal modification only amplifies this observation and therefore we must also conclude that the $N = 20$ shell is significantly weakened for $Z > N$.

3.3 Isospin symmetry

One example of isospin symmetry found in the continuum is mated pairs of 2p emitters. Figure 3 shows two such cases [29, 30]. The schemes on the top show the ground-state 2p decay of Z = even, T = 2 nuclei. These decays are characterized by each proton removing 1/2 of the total available decay energy, a characteristic of decays unperturbed by intermediates and thus indicating "direct" 2p decay. (Experience has taught that if a potential intermediate is broad, it leaves no "finger print" on the decay.) The lower decay schemes show the same T = 2 to T = 1 decays rotated in isospace into the $T_z = T - 1$ nuclei, i.e., the decays of the analogs. In these cases, while there are single-proton energetically-allowed narrow intermediates, there are no energetically *and* isospin allowed intermediates. (These potential intermediate states are T = 1/2.) As in the $T_z = 2$ cases (top), the two protons share the decay energy equally. In the A = 8 analog decay, the charged-particle IMS was coupled with the gamma detection to confirm that the 2p decay populated the isobaric analog state in ^{6}Li [31] (In the other case, the addition of excitation energy of the 2p daughter's T = 1 gamma-decaying analog state to the measured 2p decay energy yielded the energy of the previously unobserved T = 2 state in ^{12}N [30].) One would also expect another mated pair for A = 16, i.e. $^{16}Ne_{gs}$ and its T = 2 analog in ^{16}F. Despite considerable effort, no clear evidence for the second of this pair has been found. We suspect that the resolution of the riddle lies in the failure of isospin allowed 2p decay to effectively compete (at Z = 9) with isospin violating 1p decay.

Another beautiful example of isospin symmetry in the continuum is the mated rotational bands in the A = 10 nuclei ^{10}Be and ^{10}C. These nuclei become unbound (to n and 2p emission) at 6.812 and 3.821 MeV, respectively. The ground and 2^+_1 states are particle bound in both cases and have been known for decades. Other than the 0^+_2 state in ^{10}Be, all other states in either the ground rotational band or those built on the second 0^+ state are in the continuum. Tentative, but highly plausible, reconstructions of the ground and excited rotational bands in these two nuclei, as well as the analog of the excited (T = 1) band in the intermediate odd-odd ^{10}B nucleus, are shown in Figure 4. All of the states for ^{10}Be shown in this standard rotational (excitation energy vs. spin) plot have been known for years. Only the spin of what is now assigned as 4^+_1 was uncertain, although it was known to be T = 1 [32]. (Note that in the assignments made in Figure 4, 4^+_1 belongs to the excited, but much lower moment-of-inertia, excited band while 4^+_2 belongs to the ground-state band.). The spin assignments made for ^{10}C only became possible when a highly plausible assignment could be made for 0^+_2, the search for which was rather tortuous but for which the final chapters were IMS studies, one with an incorrect assignment [33] which prompted another study which lead to the assignment used in Figure 4 [34]. The correct assignment was made based on the similarity of the 3-body correlations for this state with those for other 0^+ 2p decays. Using similar logic, the higher spin states could

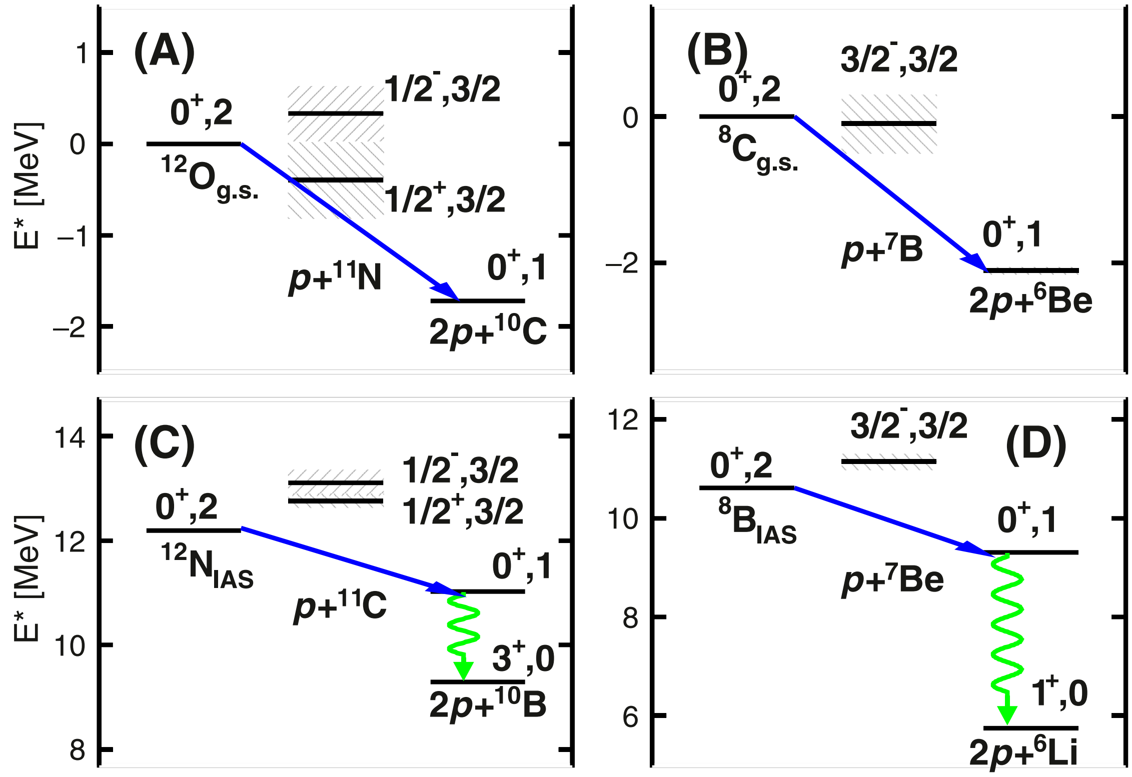

FIGURE 3
Decay schemes for two mated pairs, A = 12 Left and A = 8 Right, of T = 2 to T = 1 2p decays. **(A,B)** shows the $T_z = T$ cases and **(C,D)** shows the $T_z = T - 1$ cases. Note that the former are ground-state 2p emitters and the latter are the highly excited analogs which decay to T = 1 analog states in the $T_z = 0$ daughters that gamma decay to the respective ground states.

be given tentative assignments [34]. While this spin assignment method is novel and should be viewed with some measure of skepticism, confidence in the assignments is generated by the fact that the apparent moments-of-inertia are constant and the same in the two bands independent of isospin projection. (In three cases for the excited band.) While these assignments must be considered tentative, the results, taken at face value, show that the rotational structures in these clustered nuclei show remarkable insensitivity to decay thresholds.

3.4 Breaking isospin symmetry

Isospin symmetry can be broken by asymmetric coupling to the continuum. The classic case, considered by both Ehrman [35] and Thomas [36] is for the A = 13 pair ^{13}C and ^{13}N, see Figure 5C, where the ground and first three excited states of the former are bound to neutron decay while for the latter all but the ground state are unbound to proton decay. The excitation energies of the $3/2^-$ and $5/2^+$ states are similar in the two nuclei while the excitation energy of the unbound $1/2^+$ state in ^{13}N is downshifted by 0.73 MeV relative to its mirror state. The base explanation is simply that, for states unconfined by an angular momentum barrier, the Coulomb energy for the proton-rich case is less, i.e., the wave functions are slightly expanded, for states coupled to the continuum.

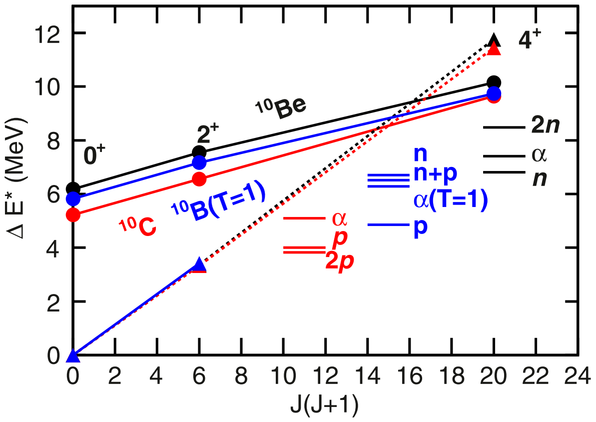

FIGURE 4
Comparison of analog rotational bands in ^{10}C, ^{10}B, and ^{10}Be. The quantity ΔE^* is the excitation energy relative to the first $T = 1$, $J^\pi = 0^+$ state. The rotation bands built on the excited 0^+ states have smaller moments of inertia compared to those built on the first 0^+ states. The decay thresholds are indicated. The indicated α threshold for ^{10}B (blue) is for decay to the T = 1 IAS in ^{6}Li.

While several examples of what has been come to be known as "Thomas-Ehrman" (TE) shifts have been known for decades, the study of proton-rich nuclei by IMS has extended the list of known

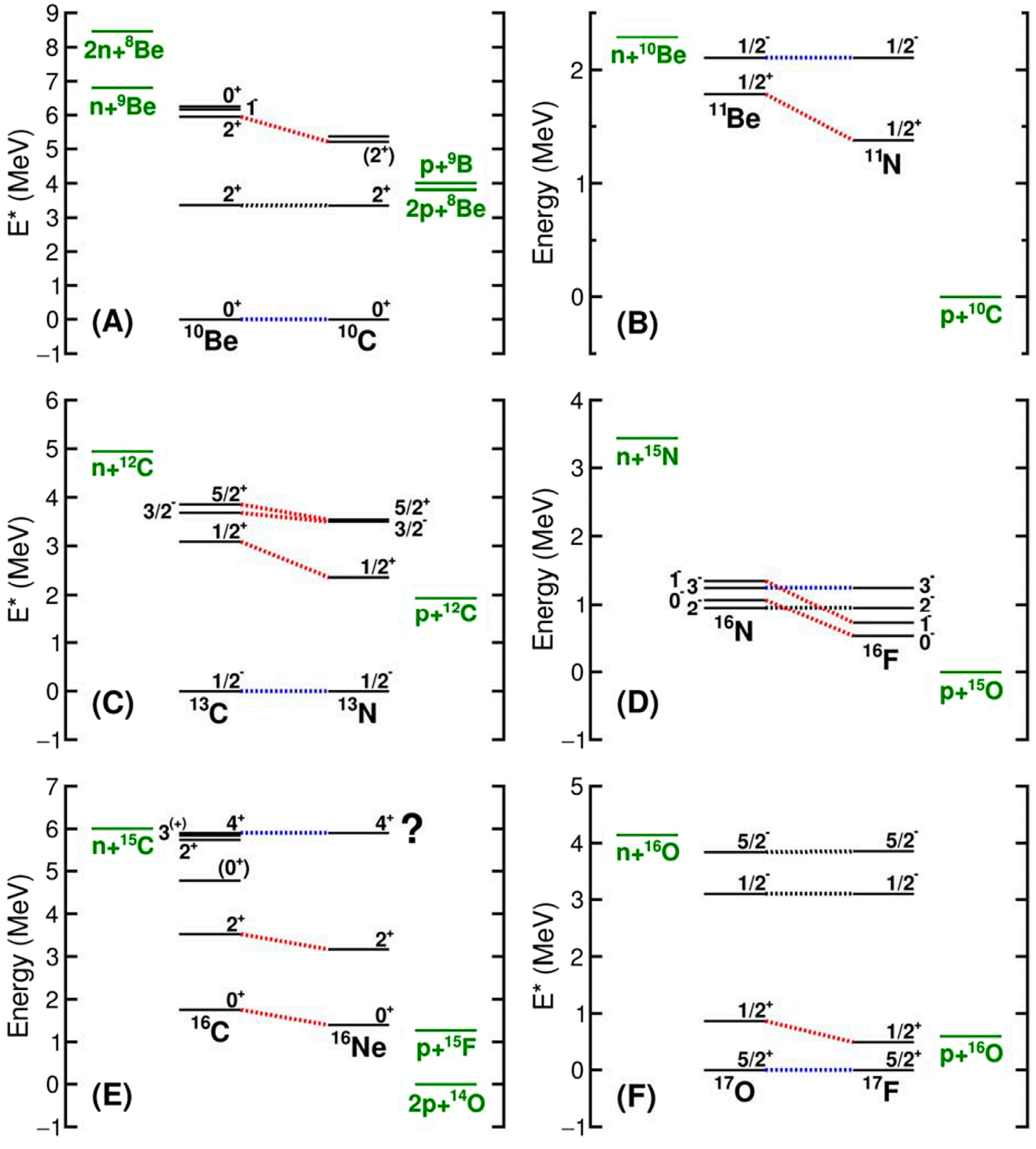

FIGURE 5
Selection of mirror nuclei which exhibit (or in one case - expected to exhibit) Thomas-Ehrman shifts. In each of the panels analog levels are connected by dotted lines and the relevant decay thresholds are indicated (in green) exterior to the level schemes. The analog levels connected by blue dotted lines are the reference level and those connected by red dotted lines are those with a downward shift for the p-rich nuclide suggesting a substantial s-wave component. When the ground state is the reference state, the ordinate is the actual excitation energy otherwise the ordinate zero is taken as the relevant p-decay threshold. The data for **(A–D,F)** are taken from ref. 32. The same is true for ^{16}C in **(E)**. However, as the reference (4^{+}) level in ^{16}Ne has not be observed, the positions of the lower levels and thresholds with respect to this level are not fixed.

examples several of which are shown in the other panels of Figure 5. The A = 11 and A = 17 cases, 5 (B) and (F) are similar to the A = 13 case (C) in that the 1/2^{+} state is down shifted relative to the 1/2^{-}, and the 5/2^{-} state in (F). In the A = 17 case (F), the ground states are used as references and the ordinate is again (as in (C)) the excitation energy. However, to display the shift in the A = 11 case (B), we have chosen to fix the energy ordinate zero to the p + ^{10}C decay threshold, the decay products of ^{11}N, and reference the mirror schemes to one another using levels with finite ℓ composition, blue dotted lines. For A = 16 (D), all the levels in the p-rich ^{16}F are unbound while none of those in the mirror are. Using the graphical tool employed in (B), one notes that, if the two high-spin levels are used to align the level schemes, the two levels that can decay by s-wave emission are down shifted.

The ground and first excited states for both ^{10}Be and ^{10}C (A) are bound, however there are two levels in ^{10}C well below the third excited state in ^{10}Be but above both the 1p and 2p decay thresholds (The mirror 1n and 2n thresholds for ^{10}Be are above all levels in question.) One of these levels is 0^+_2, the band head of the second rotational band, see Figure 4, and the other, which decays to p + ^{9}B, has been assigned $J^\pi = 2^+$, see [37] and references cited therein, an assignment consistent with direct reaction data. (This state is not part of either of the rotational bands shown in Figure 4).

The remaining panel of Figure 5E represents a research opportunity. All the levels shown are known [32] except the 4^+ in ^{16}Ne. While states with $J^\pi \le 3$ can be reached with contributions from the second proton s orbit, $J^\pi = 4^+$ states cannot. Finding this state, allows for an assessment of the actual downshifts of the lower levels, including the ground state, and thus estimates of the contribution from the second s orbit.

4 Conclusion

The lower portion of the Chart of the Nuclides is now mapped out to where nuclei convert from metastable to unstable and thus cease to exist. The pattern of nucleon decays, like the drip-lines themselves, reflect the strong influence of like-nucleon pairing. Sequences of single- and double-proton decay have been mapped out on the p-rich side with the longest chain starting with ^{9}N emitting a single proton to the even Z and well studied ^{8}C, which decays by two steps of 2p emission ending with an alpha-core residue.

As with any Fermion system, the punctuation of structure is the irregularity of single-particle levels. However, in the nuclear two-Fermion system, shell structure is conflated with n-p congruence effects. While generally not important, this latter structure effect is important in p-rich light nuclei [26]. Employing a reasonable prescription for removing n-p congruence effects, it was found that a $N = 16$ subshell is a meaningful concept for both ^{36}Ca and ^{35}K. Another finding of note is a weakening of the $Z = 20$ shell closure when $N < 19$.

Two examples of isospin symmetry were presented. One of these, presented in duplicate, is mated pairs of two-proton decay, both T = 2 to T = 1, one from the ground state of the $T_Z = 2$ nucleus and the other from its analog. Another example is the mated rotational bands, both ground and excited, in A = 10 systems. Finally, a selection of cases of isospin symmetry breaking, induced by differing decay thresholds, was presented. Generating a catalog of such cases, and explaining the systematics therein, presents a research opportunity.

In our view, the most interesting unresolved questions concerning the structure-reactions (they are intimately spliced) of nuclei near the proton-drip line are related to cases for which multiple open channels exist. Such cases are often found near the drip line but are exceedingly important at high excitation energy near stability, e.g., the ^{13}C $(\alpha,n)^{16}$O reaction which provides neutrons to the s-process. Advances in theory which allow for treatment of multiple open channels, especially when one of the channels is a cluster, should be a high priority for the field.

Author contributions

LS: Funding acquisition, Investigation, Methodology, Project administration, Resources, Supervision, Writing–original draft, Writing–review and editing, Conceptualization, Data curation, Validation. RC: Conceptualization, Formal Analysis, Investigation, Software, Supervision, Visualization, Writing–review and editing, Data curation, Methodology, Validation.

Funding

The author(s) declare that financial support was received for the research, authorship, and/or publication of this article. The work presented in this report is based upon work supported by the U.S. Department of Energy, Office of Science, Office of Nuclear Physics under Awards No. DE-FG02-87ER-40316.

Acknowledgments

The results presented here on the separation energies beyond the proton drip line are part of the thesis work of Nicolas Dronchi who, of course, did the hard analysis work on that project [38].

Conflict of interest

The authors declare that the research was conducted in the absence of any commercial or financial relationships that could be construed as a potential conflict of interest.

Generative AI statement

The author(s) declare that no Generative AI was used in the creation of this manuscript.

Publisher's note

References

1. Charity RJ, Brown K, Webb T, Sobotka LG. Invariant-mass spectroscopy of ^{10}B,^{11}C, ^{14}F, ^{16}F, and ^{18}Na. *Phys Rev C* (2023) 107:054301. doi:10.1103/PhysRevC.107.054301

2. Brink D. Kinematical effects in heavy-ion reactions. *Phys Lett B* (1972) 40:37–40. doi:10.1016/0370-2693(72)90274-2

3. Charity RJ, Sobotka LG. Invariant-mass spectroscopy in projectile fragmentation reactions. *Phys Rev C* (2023) 108:044318. doi:10.1103/PhysRevC.108.044318

4. Aad G, the ATLAS collaboration. A detailed map of Higgs boson interactions by the ATLAS experiment ten years after the discovery. *Nature* (2022) 607:52–9. doi:10.1016/S0168-9002(98)00960-7

5. Mercurio K, Charity RJ, Shane R, Sobotka LG, Elson JM, Famiano M, et al. Correlated two-proton decay from ^{10}C. *Phys Rev C* (2008) 78:031602. doi:10.1103/PhysRevC.78.031602

6. Wallace M, Famiano M, van Goethem MJ, Rogers A, Lynch W, Clifford J, et al. The high resolution array (HiRA) for rare isotope beam experiments. *Nucl Instrum Methods A* (2007) 583:302–12. doi:10.1016/j.nima.2007.08.248

7. Yurkon J, Bazin D, Benenson W, Morrissey D, Sherrill B, Swan D, et al.Focal plane detector for the S800 high-resolution spectrometer. *Nucl Instrum Methods A* (1999) 422:291–5. doi:10.1016/S0168-9002(98)00960-7

8. Weisshaar D, Gade A, Glasmacher T, Grinyer GF, Bazin D, Adrich P, et al. CAESAR-A high-efficiency CsI(Na) scintillator array for in-beam γ ray spectroscopy with fast rare-isotope beams. *Nucl Instrum Methods A* (2010) 624:615–23. doi:10.1016/j.nima.2010.09.148

9. Dronchi N, Charity RJ, Sobotka LG, Brown BA, Weisshaar D, Gade A, et al. Evolution of shell gaps in the neutron-poor calcium region from invariant-mass spectroscopy of ^{37,38}Sc, ^{35}Ca, and ^{34}K. *Phys Rev C* (2024) 110:L031302. doi:10.1103/PhysRevC.110.L031302

10. Charity RJ, Brown KW, Elson J, Reviol W, Sobotka LG, Buhro WW, et al. Invariant-mass spectroscopy of ^{18}Ne, ^{16}O, and ^{10}C excited states formed in neutron-transfer reactions. *Phys Rev C* (2019) 99:044304. doi:10.1103/PhysRevC.99.044304

11. Binns W, Connell J, Dowkontt P, Epstein J, Israel M, Klarmann J. A scintillating optical fiber track imaging detector. *Nucl Instr Methods Phys Res Section A: Acc Spectrometers, Detectors Associated Equipment* (1986) 251:402–6. doi:10.1016/0168-9002(86)90808-9

12. Ruchti R. Tracking with scintillating fibers. *Nucl Phys B - Proc Supplements* (1995) 44:308–19. doi:10.1016/S0920-5632(95)80049-2

13. Back B, Betts R, Gillitzer A, Henning W, Hofman D, Nanal V A beam vertex detector using scintillating fibers. *Nucl Instr Methods Phys Res Section A: Acc Spectrometers, Detectors Associated Equipment* (1998) 412:191–9. doi:10.1016/S0168-9002(98)00096-5

14. Jin Y, Niu CY, Brown KW, Li ZH, Hua H, Anthony AK, et al. First observation of the four-proton unbound nucleus ^{18}Mg. *Phys Rev Lett* (2021) 127:262502. doi:10.1103/PhysRevLett.127.262502

15. Charity RJ, Wylie J, Wang SM, Webb TB, Brown KW, Cerizza G, et al. Strong evidence for ^{9}N and the limits of existence of atomic nuclei. *Phys Rev Lett* (2023) 131:172501. doi:10.1103/PhysRevLett.131.172501

16. Lalanne L, Sorlin O, Poves A, Assié M, Hammache F, Koyama S, et al. N=16 magicity revealed at the proton drip line through the study of ^{35}Ca. *Phys Rev Lett* (2023) 131:092501. doi:10.1103/PhysRevLett.131.092501

17. Garvey GT, Gerace WJ, Jaffe RL, Talmi I, Kelson I. Set of nuclear-mass relations and a resultant mass table. *Rev Mod Phys* (1969) 41:S1–S80. doi:10.1103/RevModPhys.41.S1

18. Myers WD. *Droplet model of atomic nuclei*. New York: Plenum (1977).

19. Satuła W, Dean D, Gary J, Mizutori S, Nazarewicz W. On the origin of the Wigner energy. *Phys Lett B* (1997) 407:103–9. doi:10.1016/S0370-2693(97)00711-9

20. Goriely S, Chamel N, Pearson JM. Further explorations of skyrme-Hartree-Fock-Bogoliubov mass formulas. xiii. the 2012 atomic mass evaluation and the symmetry coefficient. *Phys Rev C* (2013) 88:024308. doi:10.1103/PhysRevC.88.024308

21. Otsuka T, Fujimoto R, Utsuno Y, Brown BA, Honma M, Mizusaki T. Magic numbers in exotic nuclei and spin-isospin properties of the *NN* interaction. *Phys Rev Lett* (2001) 87:082502. doi:10.1103/PhysRevLett.87.082502

22. Mutschler A, Lemasson A, Sorlin O, Bazin D, Borcea C, Borcea R A proton density bubble in the doubly magic ^{34}Si nucleus. *Nat Phys* (2017) 13:152–6. doi:10.1038/nphys3916

23. Chen J. Systematic trends in the spin-orbit splitting towards weak-binding. *Front Phys.* (2024).

24. Beck T, Gade A, Brown BA, Tostevin JA, Weisshaar D, Bazin D, et al. Probing proton cross-shell excitations through the two-neutron removal from ^{38}Ca. *Phys Rev C* (2023) 108:L061301. doi:10.1103/PhysRevC.108.L061301

25. Dronchi N, Weisshaar D, Brown BA, Gade A, Charity RJ, Sobotka LG, et al. Measurement of the B(E2↑) strengths of ^{36}Ca and ^{38}Ca. *Phys Rev C* (2023) 107:034306. doi:10.1103/PhysRevC.107.034306

26. Buskirk L, Godbey K, Nazarewicz W, Satuła W. Nucleonic shells and nuclear masses. *Phys Rev C* (2024) 109:044311. doi:10.1103/PhysRevC.109.044311

27. Kramer G, Blok H, Van Den Brand J, Bulten H, Ent R, Jans E, et al. Proton ground-state correlations in ^{40}Ca studied with the reaction ^{40}Ca(e,e'p)^{39}K. *Phys Lett B* (1989) 227:199–203. doi:10.1016/S0370-2693(89)80022-X

28. Chen J. Nuclear data sheets for A = 39. *Nucl Data Sheets* (2018) 149:1–251. doi:10.1016/j.nds.2018.03.001

29. Charity RJ, Elson JM, Manfredi J, Shane R, Sobotka LG, Chajecki Z, et al. 2p-2p decay of ^{8}C and isospin-allowed 2p decay of the isobaric-analog state in ^{8}B. *Phys Rev C* (2010) 82:041304. doi:10.1103/PhysRevC.82.041304

30. Jager MF, Charity RJ, Elson JM, Manfredi J, Mahzoon MH, Sobotka LG, et al. Two-proton decay of ^{12}O and its isobaric analog state in ^{12}N. *Phys Rev C* (2012) 86:011304. doi:10.1103/PhysRevC.86.011304

31. Brown KW, Buhro WW, Charity RJ, Elson JM, Reviol W, Sobotka LG, et al. Two-proton decay from the isobaric analog state in ^{8}B. *Phys Rev C* (2014) 90:027304. doi:10.1103/PhysRevC.90.027304

32. NNDC. Evaluated nuclear structure data file (ENSDF) (2024). Available from: https://www.nndc.bnl.gov/ensdf/ (Accessed September, 2024).

33. Curtis N, Achouri NL, Ashwood NI, Bohlen HG, Catford WN, Clarke NM, et al. Breakup reaction study of the brunnian nucleus ^{10}C. *Phys Rev C* (2008) 77:021301. doi:10.1103/PhysRevC.77.021301

34. Charity RJ, Sobotka LG, Webb TB, Brown KW. Two-proton decay from α-cluster states in ^{10}C and ^{11}N. *Phys Rev C* (2022) 105:014314. doi:10.1103/PhysRevC.105.014314

35. Ehrman JB. On the displacement of corresponding energy levels of ^{13}C and ^{13}N. *Phys Rev* (1951) 81:412–6. doi:10.1103/PhysRev.81.412

36. Thomas RG. An analysis of the energy levels of the mirror nuclei, ^{13}C and ^{13}N. *Phys Rev* (1952) 88:1109–25. doi:10.1103/PhysRev.88.1109

37. Charity RJ, Wiser TD, Mercurio K, Shane R, Sobotka LG, Wuosmaa AH, et al. Continuum spectroscopy with a ^{10}C beam: cluster structure and three-body decay. *Phys Rev C* (2009) 80:024306. doi:10.1103/PhysRevC.80.024306

38. Dronchi ND. *Proton-decay branches and structures in ^{7}Li and neutron-poor nuclides around calcium. Phd thesis*. Saint Louis, MO: Washington University (2024). Available from: https://openscholarship.wustl.edu/art_sci_etds/3277/.

frontiers | Frontiers in Physics

TYPE Review
PUBLISHED 06 January 2025
DOI 10.3389/fphy.2024.1505982

Learning from knockout reactions using a dispersive optical model

M. C. Atkinson[1]* and W. H. Dickhoff[2]

[1]Nuclear Data and Theory Group, Lawrence Livermore National Laboratory, Livermore, CA, United States, [2]Department of Physics, Washington University in St. Louis, St. Louis, MO, United States

OPEN ACCESS

EDITED BY
Alan Wuosmaa,
University of Connecticut, United States

REVIEWED BY
Angela Bonaccorso,
National Institute of Nuclear Physics of Pisa, Italy
Theocharis S. Kosmas,
University of Ioannina, Greece

*CORRESPONDENCE
M. C. Atkinson,
✉ mackenzie.c.atkinson@gmail.com

RECEIVED 04 October 2024
ACCEPTED 04 December 2024
PUBLISHED 06 January 2025

CITATION
Atkinson MC and Dickhoff WH (2025) Learning from knockout reactions using a dispersive optical model.
Front. Phys. 12:1505982.
doi: 10.3389/fphy.2024.1505982

We present the empirical dispersive optical model (DOM) as applied to direct nuclear reactions. The DOM links both scattering and bound-state experimental data through a dispersion relation, which allows for fully consistent, data-informed predictions for nuclei where such data exist. In particular, we review investigations of the electron-induced proton knockout reaction from both ^{40}Ca and ^{48}Ca in a distorted-wave impulse approximation (DWIA) utilizing the DOM for a fully consistent description. Viewing these reactions through the lens of the DOM allows us to connect the documented quenching of spectroscopic factors with the increased high-momentum proton content in neutron-rich nuclei. A similar DOM-DWIA description of the proton-induced knockout from ^{40}Ca, however, does not currently fit in the consistent story of its electron-induced counterpart. With the main difference in the proton-induced case being the use of an effective proton–proton interaction, we suggest that a more sophisticated in-medium interaction would produce consistent results.

KEYWORDS

nuclear structure, knockout reactions, optical potential, Green's function, distorted-wave impulse approximation

1 Introduction

Independent particle models (IPMs) provide a simplified view of the nucleus in which correlations are neglected and all orbitals are completely filled up to the Fermi level according to the Pauli principle. However, due to residual interactions, orbitals below the Fermi energy are depleted, while those above it are filled. Knockout reactions, in which a nucleon is removed from a nuclear target after collision with a projectile, are suitable for studying this distortion of the Fermi sea. The importance of the $(e,e'p)$ reaction in clarifying the details of this rearrangement near the Fermi energy is well-established and initially reviewed in [1]. Subsequent high-resolution work at the Nikhef facility in Amsterdam then provided a detailed view of the limitations of the IPMs in describing closed-shell nuclei [2–10]. The primary interaction in this reaction is electromagnetic and well-understood so that at sufficient high-electron beam energy, a distorted-wave impulse approximation (DWIA) provides an excellent reaction model [11–14].

In the traditional application of the DWIA to $(e,e'p)$ cross sections, the Nikhef group typically utilized a global optical potential at the energy of the outgoing proton to describe the distorted wave. The overlap function from the ground state to the relevant state in the nucleus with one proton removed was obtained from a standard Woods–Saxon potential, with the depth adjusted to the separation energy and the radius constrained by the momentum dependence of the observed cross section. The cross sections obtained for targets consisting of closed shell nuclei then typically require a scaling factor of 0.6–0.7 to generate an accurate description of the data [9]. This scaling factor, usually referred to as the (reduced) spectroscopic factor, corresponds to the normalization of the overlap function between the target ground state and the excited state of the recoiling $A-1$ nucleus. A spectroscopic factor less than 1 indicates a divergence from the IPM. Furthermore, the data show that additional removal strength with essentially the same overlap function is located at nearby energies, providing clear evidence of the fragmentation of the single-particle strength [5, 15].

It has been argued in the literature that spectroscopic factors, while representing a useful concept, are not observables [16]. No doubt the $(e,e'p)$ reaction provides the cleanest probe of removal probabilities. A similar approach in atoms for the $(e,2e)$ reaction supports this claim (see [17]). Apart from assessing the accuracy of the DWIA method for the $(e,e'p)$ reaction, it is also necessary to clarify the validity of the chosen nuclear wave functions of the Nikhef analysis. We note that separate structure wave functions (phenomenological overlap function) and unrelated distorted scattering waves obtained from local optical potentials were employed. The dispersive optical model (DOM), which was first proposed by Mahaux and reviewed in [18], provides an approach to clarify these issues. In this article, we review the application of the DOM to DWIA calculations of knockout reactions [19–21]. Recent implementations of the DOM have introduced fully nonlocal dispersive potentials [22, 23], allowing additional data to be included in the description, like the particle number and the nuclear charge density, which were not considered in [18]. It is thus possible to extract all nuclear ingredients needed for a DWIA calculation of $(e,e'p)$ from a DOM that is constrained by all available elastic nucleon scattering data, as well as separation energies, particle number, ground-state binding energy, charge radius, and the nuclear charge density for ^{40}Ca and ^{48}Ca in our case. Indeed, the distorted outgoing proton wave and the overlap function with its implied normalization are all provided by the DOM to allow for a consistent description of both $^{40}\text{Ca}(e,e'p)\ ^{39}\text{K}$ and $^{48}\text{Ca}(e,e'p)\ ^{47}\text{K}$ cross sections. The states analyzed for this reaction are the ground and first excited states of ^{39}K and ^{47}K, which correspond to the 0d3/2 and 1s1/2 valence hole states in the IPSM.

Although stable targets corresponding to closed-shell nuclei have been investigated using the $(e,e'p)$ reaction, corresponding results for exotic nuclei are not available and may never be. Alternative reactions have been explored in inverse kinematics at rare isotope facilities. For example, the heavy-ion nucleon knockout reaction was employed by the researchers of the National Superconducting Cyclotron Laboratory at Michigan State University [24, 25]. The results suggested a strong dependence of the removal probability on the difference in separation energies between minority and majority species. The analysis of these data for open-shell nuclei relies on small model space shell model calculations, which already allow for partial orbital occupancy. The resulting reduction factors for overlap functions similarly generated as for the $(e,e'p)$ reaction yield values close to 1 for the removal of valence majority nucleons and a strong suppression for the corresponding minority nucleons. The obtained results for closed-shell nuclei, with respect to the IPM description, are consistent with the $(e,e'p)$ results mentioned above. This dependence on nucleon asymmetry is not consistent with the corresponding results of transfer reactions reviewed in [26] or the single-nucleon removal experiments recently reported in [27, 28]. At this time, no clear consensus has been reached on this intriguing difference. A comprehensive status report of these different approaches containing a theoretical background was reported in [29]. We provide an additional perspective on this situation based on our DOM analyses of $^{40}\text{Ca}(e,e'p)\ ^{39}\text{K}$ and $^{48}\text{Ca}(e,e'p)\ ^{47}\text{K}$.

The electron-induced proton knockout reaction, $(e,e'p)$, has been considered the cleanest spectroscopic method for decades. An alternative approach is proton-induced knockout or $(p,2p)$, which, despite some concerns about uncertainties [29–36], has been established as a complementary spectroscopic tool to $(e,e'p)$ with approximately 15% uncertainty for incident energy above 200 MeV [36]. Although the $(e,e'p)$ reaction involves one proton distorted wave, there are three such components in the $(p,2p)$ reaction. In addition, the interaction responsible for the transition to the final state, apart from being fundamentally two-body in nature, involves an in-medium proton–proton (pp) interaction. The pp interaction is not nearly as well-understood as the electromagnetic transition operator (ep) in the $(e,e'p)$ reaction, which is a predominantly one-body operator.

Using the same DOM bound-state and scattering wave functions that were employed in the DWIA analysis of $^{40}\text{Ca}(e,e'p)^{39}\text{K}$, we performed a DWIA calculation of $^{40}\text{Ca}(p,2p)^{39}\text{K}$ in [21]. This was not only the first DWIA calculation of $^{40}\text{Ca}(p,2p)^{39}\text{K}$ to utilize consistent nuclear ingredients but also the first time that the distorted waves of the incoming and outgoing protons were generated by a nonlocal optical potential. The resulting analysis pointed to an inconsistency between the electron-induced and proton-induced knockout reactions; although the DOM-provided spectroscopic factor of 0.71 reproduces the $(e,e'p)$ data, this factor had to be further reduced to 0.56 to reproduce the $(p,2p)$ data. Since the only difference between the descriptions of these two reactions is the ep interaction vs the pp interaction, the inevitable conclusion is that a further study of the in-medium pp interaction is required. We note that transfer reactions have also been studied with DOM ingredients [37–39], but such studies require additional analysis of the reaction model, although applying current nonlocal DOM potentials may provide useful insights.

The underlying Green's function formalism of the single-particle propagator is presented in Section 2.1, while the DOM framework is introduced in Section 2.2. The application of the DOM to the $(e,e'p)$ reactions is described in Section 3. Results for the $^{40}\text{Ca}(e,e'p)$ and $^{48}\text{Ca}(e,e'p)$ reactions are presented in Sections 3.1, 3.2, respectively. A discussion of the $(p,2p)$ results employing DOM ingredients is provided in Section 4. Conclusions and some outlook are presented in Section 5.

2 Theory

This section is organized to provide brief introductions into the underlying theory of the DOM.

2.1 Single-particle propagator

The single-particle propagator describes the probability amplitude for adding (removing) a particle in state α at one time to (from) the non-degenerate ground state and propagating on top of that state until a later time when it is removed (added) in state β [17]. In addition to the conserved orbital and total angular momentum (ℓ and j, respectively), the labels α and β in Equation 1 refer to a suitably chosen single-particle basis. We employed a coordinate-space basis in our original ^{48}Ca calculation in [40], but we have switched to a Lagrange basis [41] in all subsequent calculations (including that of ^{208}Pb from [42]). It is convenient to work with the Fourier-transformed propagator in the energy domain:

$$G_{\ell j}(\alpha,\beta;E) = \langle\Psi_0^A|a_{\alpha\ell j}\frac{1}{E-\left(\widehat{H}-E_0^A\right)+i\eta}a^\dagger_{\beta\ell j}|\Psi_0^A\rangle + \langle\Psi_0^A|a^\dagger_{\beta\ell j}\frac{1}{E-\left(E_0^A-\widehat{H}\right)-i\eta}a_{\alpha\ell j}|\Psi_0^A\rangle, \quad (1)$$

with E_0^A representing the energy of the non-degenerate ground state $|\Psi_0^A\rangle$. Many interactions can occur between the addition and removal of the particle (or *vice versa*), all of which need to be considered to calculate the propagator. No assumptions about the detailed form of the Hamiltonian $\widehat{H}$ need be made for the present discussion, but it is assumed that a meaningful Hamiltonian exists that contains two-body and three-body contributions. The application of perturbation theory then leads to the Dyson equation [17], which is given by

$$G_{\ell j}(\alpha,\beta;E) = G_\ell^{(0)}(\alpha,\beta;E) + \sum_{\gamma,\delta}G_\ell^{(0)}(\alpha,\gamma;E)\,\Sigma^*_{\ell j}(\gamma,\delta;E)\,G_{\ell j}(\delta,\beta;E), \quad (2)$$

where $G_\ell^{(0)}(\alpha,\beta;E)$ corresponds to the unperturbed propagator (the propagator derived from the unperturbed Hamiltonian, H_0, which in the DOM corresponds to the kinetic energy) and $\Sigma^*_{\ell j}(\gamma,\delta;E)$ is the irreducible self-energy [17]. The hole spectral density for energies below ε_F is obtained from:

$$S^h_{\ell j}(\alpha,\beta;E) = \frac{1}{\pi}\mathrm{Im}\ G_{\ell j}(\alpha,\beta;E), \quad (3)$$

where the h superscript signifies it as the hole spectral amplitude. For brevity, we drop this superscript for the rest of this review. The diagonal element of Equation 3 is known as the (hole) spectral function identifying the probability density for the removal of a single-particle state with the quantum number $\alpha\ell j$ at energy E. The single-particle density distribution can be calculated from the hole spectral function as

$$\rho^{(p,n)}_{\ell j}(r) = \sum_{\ell j}(2j+1)\int_{-\infty}^{\varepsilon_F}dE\ S^{(p,n)}_{\ell j}(r,r;E), \quad (4)$$

where the (p,n) superscript refers to protons or neutrons and $\varepsilon_F = \frac{1}{2}(E_0^{A+1}-E_0^{A-1})$ is the average Fermi energy, which separates the particle and hole domains [17]. The number of protons and neutrons (Z,N) is calculated by integrating $\rho^{(p,n)}_{\ell j}(r)$ over all spaces. In addition to the particle number, the total binding energy can be calculated from the hole spectral function using the Migdal–Galitski sum rule [17]:

$$E_0^{N,Z} = \frac{1}{2}\sum_{\alpha\beta}\int_0^{\varepsilon_F}dE\left[\langle\alpha|\widehat{T}|\beta\rangle S^h(\alpha,\beta;E) + \delta_{\alpha\beta}ES^h(\alpha,\alpha;E)\right]. \quad (5)$$

The expression in Equation 5 assumes that the dominant contribution involves the two-nucleon interaction [43, 44].

To visualize the spectral function of Equation 3, it is useful to sum (or integrate) over the basis variables, α so that only energy dependence, $S_{\ell j}(E)$, remains. The spectral strength $S_{\ell j}(E)$ is the contribution at energy E to the occupation from all orbitals with the angular momentum ℓj. It reveals that the strength for a shell can be fragmented rather than isolated at the independent-particle model (IPM) energy levels. Figure 1 shows the spectral strength of a representative set of proton (panel (a)) and neutron (panel (b)) orbits in ^{48}Ca that would be considered bound in the IPM. The locations of the peaks shown in Figure 1 correspond to the energies of discrete bound states with one nucleon removed. For example, the s1/2 spectral function shown in Figure 1 has two peaks below ε_F that correspond to the 0s1/2 and 1s1/2 quasihole states, while the f7/2 spectral function has a peak below (neutrons) and above (protons) ε_F that corresponds to the 0f7/2 quasihole/particle state. The wave functions of these quasihole/particle states can be obtained by transforming the Dyson equation into a nonlocal Schrödinger-like equation by disregarding the imaginary part of $\Sigma^*(\alpha,\beta;E)$:

$$\sum_\gamma\langle\alpha|T_\ell + \mathrm{Re}\ \Sigma^*_{\ell j}\left(\varepsilon^n_{\ell j}\right)|\gamma\rangle\psi^n_{\ell j}(\gamma) = \varepsilon^n_{\ell j}\psi^n_{\ell j}(\alpha), \quad (6)$$

where $\langle\alpha|T_\ell|\gamma\rangle$ is the kinetic-energy matrix element, including the centrifugal term. The wave function, $\psi^n_{\ell j}(\alpha)$, is the overlap between the A and $A-1$ systems and the corresponding energy, $\varepsilon^n_{\ell j}$, is the energy required to remove a nucleon with the particular quantum numbers $n\ell j$:

$$\psi^n_{\ell j}(\alpha) = \langle\Psi_n^{A-1}|a_{\alpha\ell j}|\Psi_0^A\rangle, \qquad \varepsilon^n_{\ell j} = E_0^A - E_n^{A-1}. \quad (7)$$

When solutions to Equations 6, 7 are found near the Fermi energy, where there is naturally no imaginary part of the self-energy, the normalization of the quasihole is well-defined as the spectroscopic factor:

$$Z^n_{\ell j} = \left(1 - \frac{\partial\Sigma^*_{\ell j}\left(\alpha_{qh},\alpha_{qh};E\right)}{\partial E}\Big|_{\varepsilon^n_{\ell j}}\right)^{-1}, \quad (8)$$

where α_{qh} corresponds to the quasihole state that solves Equation 6. The quasihole peaks in shown Figure 1 become narrower as the levels approach ε_F, which is a consequence of the imaginary part of the irreducible self-energy decreasing when approaching ε_F. The last mostly occupied neutron level in panel (b) of Figure 1 (0f7/2) has a spectral function that is essentially a delta function peaked at its energy level, where the imaginary part of the self-energy vanishes. Valence proton hole orbits (1s1/2 and 0 days 3/2) exhibit the same behavior. For these orbitals, the strength of the spectral function at the peak corresponds to the spectroscopic factor shown in Equation 8. This spectroscopic factor is the very same we employ in the $(e,e'p)$ calculations, which is discussed in Section 3.1 (see also [19, 20]).

2.2 Dispersive optical model

The Dyson equation, Equation 2, simplifies the complicated task of calculating $G_{\ell j}(\alpha,\beta;E)$ from Equation 1 to find a suitable $\Sigma^*(\alpha,\beta;E)$ to invert. It was recognized long ago that $\Sigma^*(\alpha,\beta;E)$

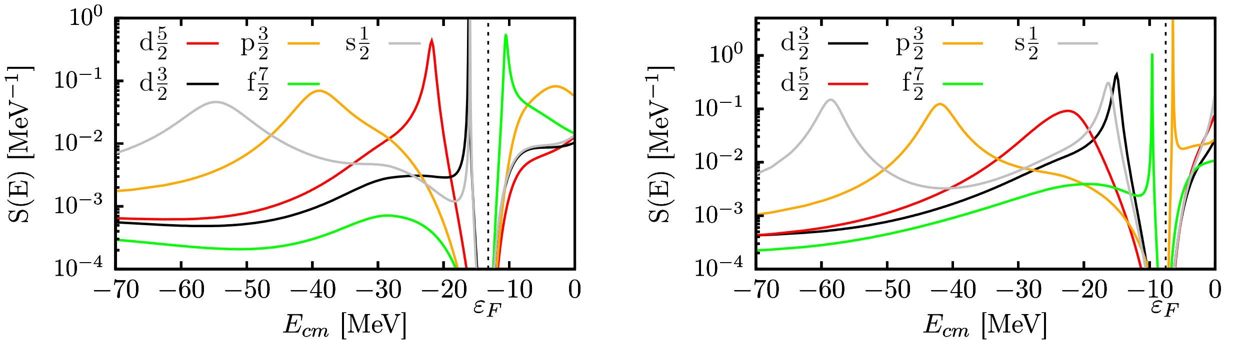

FIGURE 1
Proton (left) and neutron (right) spectral functions of a representative set of ℓj shells in ^{48}Ca. The particle states are differentiated from the hole states by the dotted line representing ε_F. Figure adapted from [20].

represents the potential that describes elastic-scattering observables [45]. The link with the potential at negative energy is then provided by the Green's function framework, as realized by Mahaux and Sartor, who introduced the DOM, as reviewed in [18]. The analytic structure of the nucleon self-energy allows one to apply the dispersion relation, which relates the real part of the self-energy at a given energy to a dispersion integral of its imaginary part over all energies. The energy-independent correlated Hartree–Fock (HF) contribution [17] is removed by employing a subtracted dispersion relation with the Fermi energy used as the subtraction point [18]. The subtracted form has the additional advantage of focusing on energies closer to the Fermi energy, for which more experimental data are available. We still refer to the energy-independent part of our potential as the HF term, and is sufficiently attractive to bind the relevant levels at exactly the correct energies. In practice, the imaginary part is assumed to reach the Fermi energy on both sides while being extremely small in its vicinity. The subtracted form of the dispersion relation employed in this work is given by

$$\begin{aligned}\text{Re }\Sigma^*(\alpha,\beta;E) = \text{Re }\Sigma^*(\alpha,\beta;\varepsilon_F) &- P\int_{\varepsilon_F}^{\infty}\frac{dE'}{\pi}\text{Im }\Sigma^*(\alpha,\beta;E')\left[\frac{1}{E-E'}-\frac{1}{\varepsilon_F-E'}\right]\\ &+ P\int_{-\infty}^{\varepsilon_F}\frac{dE'}{\pi}\text{Im }\Sigma^*(\alpha,\beta;E')\left[\frac{1}{E-E'}-\frac{1}{\varepsilon_F-E'}\right],\end{aligned} \tag{9}$$

where P is the principal value. The static term, $\text{Re}\Sigma^*(\alpha,\beta;\varepsilon_F)$, is denoted by Σ_{HF} from here on. Equation 9 constrains the real part of $\Sigma^*(\alpha,\beta;E)$ by empirical information on the HF and imaginary parts, which are closely tied to experimental data. Initially, standard functional forms for these terms were introduced by Mahaux and Sartor, who also cast the DOM potential in a local form by a standard transformation, which turns a nonlocal static HF potential into an energy-dependent local potential [46]. Such an analysis was extended in [47, 48] to a sequence of Ca isotopes and in [49] to semi-closed-shell nuclei heavier than Ca. The transformation to the exclusive use of local potentials precludes a proper calculation of the nucleon particle number and expectation values of the one-body operators, like the charge density in the ground state (see Equation 4). This obstacle was eliminated in [50], but it was shown that the introduction of nonlocality in the imaginary part was still necessary in order to accurately account for the particle number and the charge density [22]. Theoretical work provided further support for this introduction of a nonlocal representation of the imaginary part of the self-energy [51, 52]. A review detailing these developments was published in [23].

2.2.1 Functional form of the DOM self-energy

We employ a nonlocal representation of the self-energy, following [22], where $\Sigma_{\text{HF}}(\boldsymbol{r},\boldsymbol{r}')$ and $\text{Im }\Sigma(\boldsymbol{r},\boldsymbol{r}';E)$ are parametrized, and the energy dependence of the real part, $\text{Re }\Sigma(\boldsymbol{r},\boldsymbol{r}';E)$, is generated from the dispersion relation shown in Equation 9. The HF term consists of a volume term, spin-orbit term, and a wine-bottle-shape generating term [53]:

$$\Sigma_{HF}(\boldsymbol{r},\boldsymbol{r}') = V_{\text{vol}}(\boldsymbol{r},\boldsymbol{r}') + V_{\text{so}}(\boldsymbol{r},\boldsymbol{r}') + V_{\text{wb}}(\boldsymbol{r},\boldsymbol{r}') + \delta(\boldsymbol{r}-\boldsymbol{r}')\,V_C(r), \tag{10}$$

where the Coulomb potential, $V_C(r)$, is also included. The radial part of the potentials in Equation 10 takes the following form:

$$V_{\text{vol}}(\boldsymbol{r},\boldsymbol{r}') = V^{\text{vol}} f\left(\tilde{r}, r^{\text{HF}}_{(p,n)}, a^{\text{HF}}\right) H\left(\boldsymbol{s};\beta^{\text{HF}}\right), \tag{11}$$

where V^{vol} is a parameter that determines the depth of the potential and $r^{\text{HF}}_{(p,n)}$, a^{HF}, and β^{HF} are parameters that control the shape of the Woods–Saxon form factor f and Perey–Buck-shaped [46] nonlocality H:

$$\begin{gathered} f(r,r_i,a_i) = \left[1+\exp\left(\frac{r-r_iA^{1/3}}{a_i}\right)\right]^{-1} \\ H(\boldsymbol{s};\beta) = \exp\left(-\boldsymbol{s}^2/\beta^2\right)/\left(\pi^{3/2}\beta^3\right) \end{gathered} \tag{12}$$

and

$$\tilde{r} = \frac{r+r'}{2} \qquad \boldsymbol{s} = \boldsymbol{r}-\boldsymbol{r}'. \tag{13}$$

The radial form of V_{wb} and V_{so} are similar to those expressed in Equations 11–13; their explicit forms can be found in [54]. The imaginary self-energy consists of the volume, surface, and spin-orbit terms:

$$\begin{aligned}\mathrm{Im}\Sigma\left(\boldsymbol{r},\boldsymbol{r}';E\right) = -W^{vol}_{0\pm}(E)\, f\left(\tilde{r};r^{vol}_{\pm};a^{vol}_{\pm}\right) H\left(\boldsymbol{s};\beta^{vol}\right) \\ + 4a^{sur}_{\pm} W^{sur}_{\pm}(E)\, H\left(\boldsymbol{s};\beta^{sur}\right) \frac{d}{d\tilde{r}} f\left(\tilde{r},r^{sur}_{\pm},a^{sur}_{\pm}\right) + \mathrm{Im}\Sigma_{so}\left(\boldsymbol{r},\boldsymbol{r}';E\right),\end{aligned} \tag{14}$$

where $W^{vol}_{0\pm}(E)$ and $W^{sur}_{\pm}(E)$ are energy-dependent depths of the volume and surface potentials, respectively, and the ± subscript indicates that there are different forms used above and below the Fermi energy (see [54] for the exact forms of the potentials in Equation 14). When considering asymmetric nuclei, such as ^{48}Ca, additional terms proportional to the asymmetry, $\alpha_{\mathrm{asy}} = \frac{N-Z}{A}$, are added to $\Sigma_{\mathrm{HF}}(\boldsymbol{r},\boldsymbol{r}')$ and $\mathrm{Im}\Sigma(\boldsymbol{r},\boldsymbol{r}';E)$ for a Lane-like representation [55]. These asymmetric terms introduce additional parameters describing both their radial shape and energy-dependent depths [54]. For the full list of parameters used in ^{48}Ca, see [20, 54].

As mentioned previously, it was typical in the past to replace nonlocal potentials by local, energy-dependent potentials [17, 18, 46, 56]. The introduction of an energy dependence alters the dispersive correction from Equation 9 and distorts normalization, leading to incorrect spectral functions and related quantities [50]. Thus, a nonlocal implementation permits the self-energy to accurately reproduce important observables such as charge density, particle number, and ground-state binding energy.

To use the DOM self-energy for predictions, the parameters of the self-energy are constrained through weighted χ^2 minimization (using Powell's method [57]) by measurements of elastic differential cross sections ($\frac{d\sigma}{d\Omega}$), analyzing powers (A_θ), reaction cross sections (σ_{react}), total cross sections (σ_{tot}), charge density (ρ_{ch}), energy levels ($\varepsilon_{n\ell j}$), particle number, and the root mean square charge radius (R_{ch}). The angular dependence of $\Sigma(\boldsymbol{r},\boldsymbol{r}';E)$ is represented in a partial-wave basis, and the radial component is represented in a Lagrange basis using Legendre and Laguerre polynomials for scattering and bound states, respectively. The bound states are found by diagonalizing the Hamiltonian in Equation 6, the propagator is found by inverting the Dyson equation, Equation 2, while all scattering calculations are done in the framework of R-matrix theory [41].

The reproduction of all available experimental data (see [19, 20, 22, 40] for comparisons to training data) indicates that we have realistic self-energies of ^{40}Ca and ^{48}Ca capable of describing both bound-state and scattering processes. A parallel DOM analysis of these and other nuclei was conducted using Markov chain Monte Carlo (MCMC) methods to optimize the potential parameters employing the same experimental data and a very similar functional form but with a reduced number of parameters. All observables from this MCMC fit fell within one standard deviation of those presented above [58, 59].

3 DWIA description of the $(e,e'p)$ cross section

In the past, $(e,e'p)$ cross sections obtained at Nikhef in Amsterdam have been successfully described by utilizing the DWIA. This description is expected to be particularly good when kinematics that emphasize the longitudinal coupling of the excitation operator, which is dominated by a one-body operator, are used. The Nikhef group was able to fulfill this condition by choosing kinematic conditions, in which the removed proton carried momentum parallel or antiparallel to the momentum of the virtual photon. Under these conditions, the transverse contribution involving the spin and possible two-body currents is suppressed. Therefore, the process can be interpreted as requiring an accurate description of the transition amplitude from the resulting excited state to the ground state by a known one-body operator. This transition amplitude is contained in the polarization propagator, which can be analyzed with a many-body description involving a linear response [17]. Such an analysis demonstrates that the polarization propagator contains two contributions. The first term describes the propagation of a particle and a hole as they interact with the medium but not with each other. The other term involves their interaction. The latter term dominates at low energy when the proton that absorbs the photon participates in collective excitations like surface modes and giant resonances.

When the proton receives energy on the order of 100 MeV, it is expected that the resulting excited state can be well-approximated by the dressed particle and dressed hole excitation [60]. When strong transitions are considered, like in the present work, two-step processes have only minor influence [2, 5]. This interpretation forms the basis of the DWIA applied to exclusive $(e,e'p)$ cross sections obtained by the Nikhef group. The ingredients of the DWIA, therefore, require a proton distorted wave describing the outgoing proton at the appropriate energy and an overlap function with its normalization for the removed proton. The distorted wave was typically obtained from a standard (local) global optical potential shown in [61] for ^{40}Ca. The overlap function was obtained by adjusting the radius of a local Woods–Saxon potential to the shape of the $(e,e'p)$ cross section while adjusting its depth to the separation energy of the hole. Its normalization was obtained by adjusting the calculated DWIA cross section to the actual data [9]. Standard nonlocality corrections were applied to both the outgoing and removed proton wave functions [62], effectively making the bound-state wave function the solution of a nonlocal potential. We observe that such corrections are ℓ-independent and, therefore, different from the nonlocal DOM implementation.

In order to describe the $(e,e'p)$ reaction, the incoming electron, the electron–proton interaction, the outgoing electron, and the outgoing proton must be addressed. The cross section is calculated from the hadron tensor, $W^{\mu\nu}$, which contains matrix elements of the nuclear charge-current density, J^μ [14]. Using DWIA, which assumes that the virtual photon exchanged by the electron couples to the same proton that is detected [11, 13], the nuclear current can be written as

$$J^\mu(\boldsymbol{q}) = \int d\boldsymbol{r} e^{i\boldsymbol{q}\cdot\boldsymbol{r}} \chi^{(-)*}_{E\ell j}(\boldsymbol{r}) \left(\hat{J}^\mu_{\mathrm{eff}}\right)_{E\ell j}(\boldsymbol{r})\, \psi^n_{\ell j}(\boldsymbol{r}) \sqrt{\mathcal{Z}^n_{\ell j}}, \tag{15}$$

where $\chi^{(-)^*}_{E}(\boldsymbol{r})$ is the outgoing proton distorted wave [14], $\psi^n_{\ell j}$ is the overlap function, $Z^n_{\ell j}$ is its normalization, $\boldsymbol{q} = \boldsymbol{k_f} - \boldsymbol{k_i}$ is the electron three-momentum transfer, and $\hat{J}^\mu_{\mathrm{eff}}$ is the effective current operator [14]. The incoming and outgoing electron waves are treated within the effective momentum approximation, where the waves are represented by plane waves with effective momenta to account for distortion from the interaction with the target nucleus [12].

$$k^{\mathrm{eff}}_{i(f)} = k_{i(f)} + \int d\boldsymbol{r}\, V_c(\boldsymbol{r})\, \phi^2_{\ell j}(\boldsymbol{r}), \tag{16}$$

where $V_c(\boldsymbol{r})$ is the Coulomb potential of the target nucleus. This alters Equation 15 by replacing $\boldsymbol{q}$ with the $\boldsymbol{q}_{\mathrm{eff}}$ in Equation 16.

In the plane-wave impulse approximation (PWIA), in which the outgoing proton wave is approximated by a free scattering (plane) wave, the $(e,e'p)$ cross section can be factorized into an off-shell electron–proton cross section and the spectral function [14]:

$$S(E_m, \boldsymbol{p}_m) = \frac{1}{k\sigma_{ep}} \frac{d^6\sigma}{dE_{e'}\, d\Omega_{e'}\, dE_p\, d\Omega_p}. \tag{17}$$

The off-shell electron–proton cross section, σ_{ep}, is approximated from the on-shell electron–proton cross section using the σ_{cc1} model, as proposed in [63]. The factorization shown in Equation 17 does not hold true for the DWIA, but $(e,e'p)$ cross sections, both experimental and theoretical, are typically divided by σ_{cc1} when displayed. In principle, corrections due to two-step processes could be considered, but they are estimated to make negligible contributions for the transitions considered in this study [5].

The calculations of the $(e,e'p)$ cross sections in [19] were performed by employing DOM ingredients that were constrained by the experimental data discussed in Section 2.2. Appropriate distorted waves and overlap functions with their normalization were thus generated that allow for a DWIA description of the exclusive $(e,e'p)$ cross section for valence holes in ^{40}Ca. An agreement with cross sections, therefore, not only supports the description of the reaction in a DWIA framework but also confirms the overall consistency of the DOM approach including its interpretation of the normalization of the overlap functions as spectroscopic factors that can be confronted with data.

3.1 ^{40}Ca$(e,e'p)^{39}$K

The first nonlocal DOM description of ^{40}Ca data is presented in [22]. Meanwhile, additional experimental higher-energy proton reaction cross sections [64] had been incorporated, which caused some adjustments of the DOM parameters compared to [22]. The updated parameters are collected in App. A of [19]. Adjusting the parameters from the previous values [22] to describe these additional experimental results leads to an equivalent description for all data except these reaction cross sections. These higher-energy data dictate that the proton reaction cross section remain flat for energies in the region of approximately 150 MeV, as shown in Figure 2. This means there is more absorption at higher energies than in the previous fit, leading to increased strength in the imaginary part of the self-energy. Due to the dispersion relation, Equation 9, this increases the spectral strength at positive energies when the Dyson equation is solved. The sum rule discussed in detail in [65], which relates to the integral over all energies of the strength of the valence holes, implies that strength is transferred from below the Fermi energy to the energies with an increased imaginary part. This resulting loss of strength below the Fermi energy reduces the spectroscopic factors by approximately 0.05 compared to the results reported in [22].

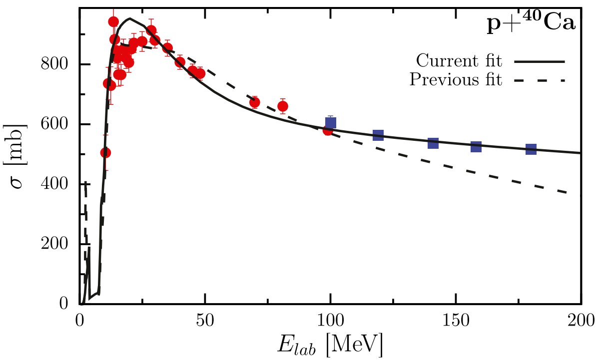

FIGURE 2
Proton reaction cross section for ^{40}Ca. The solid line represents the newest fit [19], while the dashed line depicts the original fit [22]. The circular data points were included in the original fit, while the square data points [64] were added in the newest fit. Figure adapted from [19].

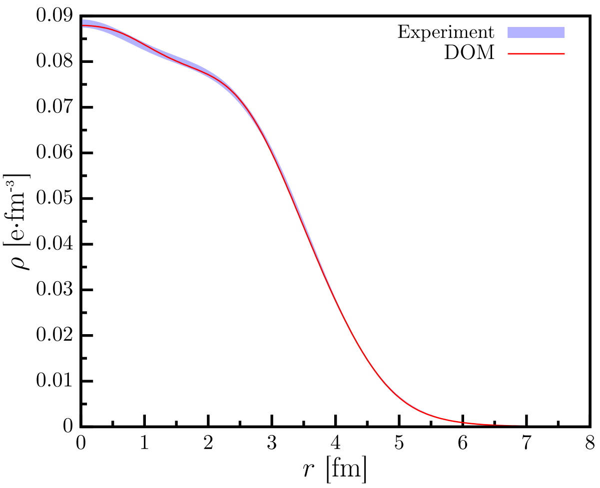

FIGURE 3
Experimental and fitted ^{40}Ca charge density. The solid line is calculated using the DOM propagator, while the experimental band represents the 1% error associated with the extracted charge density from elastic electron scattering experiments [66, 67]. Figure adapted from Ref. [19].

To accurately calculate the $(e,e'p)$ cross section in the DWIA, it is imperative that the DOM self-energy not only precisely generates available elastic scattering data but also bound-state information. This is due to the fact that the shape of the cross section is primarily determined by the bound-state overlap function [5]. Thus, not only should the experimental charge radius be reproduced but also the charge density should match the experimental data, as shown in Figure 3, where the DOM charge density is shown as the solid line and compared with the deduced charge density (Fourier–Bessel parametrization) obtained from [66] with the band representing the 1% error.

The ^{40}Ca DOM self-energy leads to the spectral strength distributions shown in Figure 4. The experimental bars are the results of an angular-momentum decomposition of the experimental spectral function at T_p = 100 MeV, as described in [15]. The

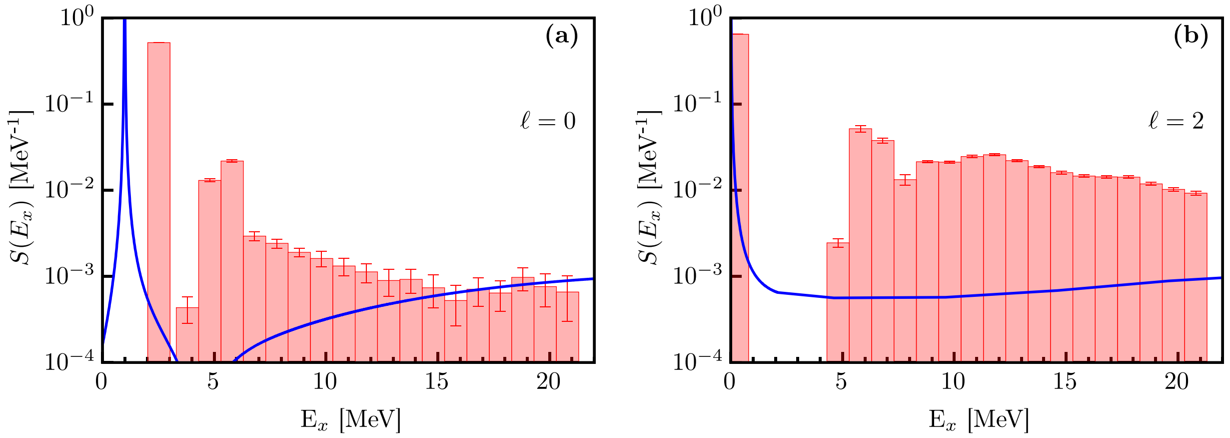

FIGURE 4
Spectral strength as a function of excitation energy for **(A)** the 1s1/2and **(B)** the 0d3/2proton orbitals, calculated from the DOM using Equation (3)) (solid line) and extracted from the ^{40}Ca$(e,e'p)$ ^{39}K experiment [5, 15] (bars). The peaks in the DOM curves and experimental data correspond to the energies of the quasihole protons in ^{40}Ca. Notably, the experimental fragments in **(B)** above 4 MeV mostly correspond to 0d5/2strength. Figure adapted from [19].

experimental distributions for $\ell = 0, 2$ clearly show that the strength is already strongly fragmented at low energies. The main peak in each case represents the valence hole transition of interest. This fragmentation is smeared in the DOM via the non-zero imaginary component of the self-energy, which is why the DOM curves shown in Figure 4 are continuous rather than discrete. The imaginary part of the self-energy approaches 0 near ε_F, which results in the sharp peaks of the DOM curve shown in Figure 4 (analogous to what is observed in Figure 1). The DOM, therefore, does not yet include the details of the low-energy fragmentation of the valence hole states, which requires the introduction of pole structure in the self-energy [68]. The spectroscopic factor of Equation 8 corresponds to the main peak of each distribution shown in Figure 4. It is calculated directly from the ^{40}Ca DOM self-energy, which results in values of 0.71 and 0.74 for the 0d3/2 and 1s1/2 peaks, respectively. The results are probed in more detail by analyzing the momentum distributions of the ^{40}Ca$(e,e'p)$ ^{39}K reaction.

In the past, the DWIA calculations by the Nikhef group have been performed using the DWEEPY code [13]. The momentum distributions in [19] are calculated by adapting a recent version of the DWEEPY code [69] to use the DOM-bound states, distorted waves, and spectroscopic factors as inputs. Before confronting the DOM calculations with the experimental cross sections, it is necessary to consider the consequences of the low-energy fragmentation shown in Figure 4. For the 0d3/2 ground-state transition (panel (b) of Figure 4), there is a clear separation with higher-lying fragments, the majority of which cannot be distinguished from 0d5/2 contributions as the experiments did not provide the necessary polarization information. In addition, these higher-lying fragments appear to carry little 0d3/2 strength [70], so the DOM spectroscopic factor can, therefore, be directly used to calculate the cross section of the ground-state peak.

The situation is different for the 1s1/2 distribution, which, while dominated by the large fragment at 2.522 MeV, exhibits substantial surrounding strength, as shown in Figure 4a. These contributions come from other discrete poles in the propagator, reflecting the mixing of the 1s1/2 orbit to more complicated excitations nearby in energy. The origin of these additional discrete poles is not explicitly included in the DOM, although there is a smooth energy-dependent imaginary term in the self-energy to approximate their effect on the spectral strength [17]. This approximation is sufficient for discussing integrated values such as the charge density and particle number, but it falls short when considering the details of the low-energy fragmentation into discrete energies, as in the present situation. The calculated DOM spectroscopic factor, therefore, includes strength in the neighborhood of the quasihole energy, resulting in an inflated value. This effect is only noticeable in the $\ell = 0$ case because there is a non-negligible amount of strength in the region near the peak. We turn to experimental data to account for this effect by enforcing that the ratio between the strength of the peak to the total spectral strength shown in the energy domain of Figure 4 is the same between the data as for the DOM:

$$\frac{\mathcal{Z}_F^{\mathrm{DOM}}}{\int dE\ S^{\mathrm{DOM}}(E)} = \frac{\mathcal{Z}_F^{\mathrm{exp}}}{\int dE\ S^{\mathrm{exp}}(E)}. \tag{18}$$

Accounting for the contributions to the momentum distribution from different energies by scaling the DOM spectroscopic factor is justified by observing that the shape of the momentum distribution calculated at similar energies is identical, with the strength being the only difference [5]. The scaling of the spectroscopic factor leads to a reduction from 0.74 to 0.60. As mentioned, no correction is needed for the 0d3/2 spectroscopic factor. The resulting momentum distributions are shown in Figure 5. The previous analysis of the Nikhef group at $T_p = 100$ MeV [5] produced a comparable reproduction of the data with somewhat smaller spectroscopic factors, as shown in Table 1.

In order to estimate the uncertainty for the DOM spectroscopic factors, we followed the bootstrap method from [71], which was also employed in [40] to assess the uncertainty for the neutron skin in ^{48}Ca. New modified datasets were created from the original data by randomly renormalizing each angular distribution or excitation function within the experimental error to incorporate

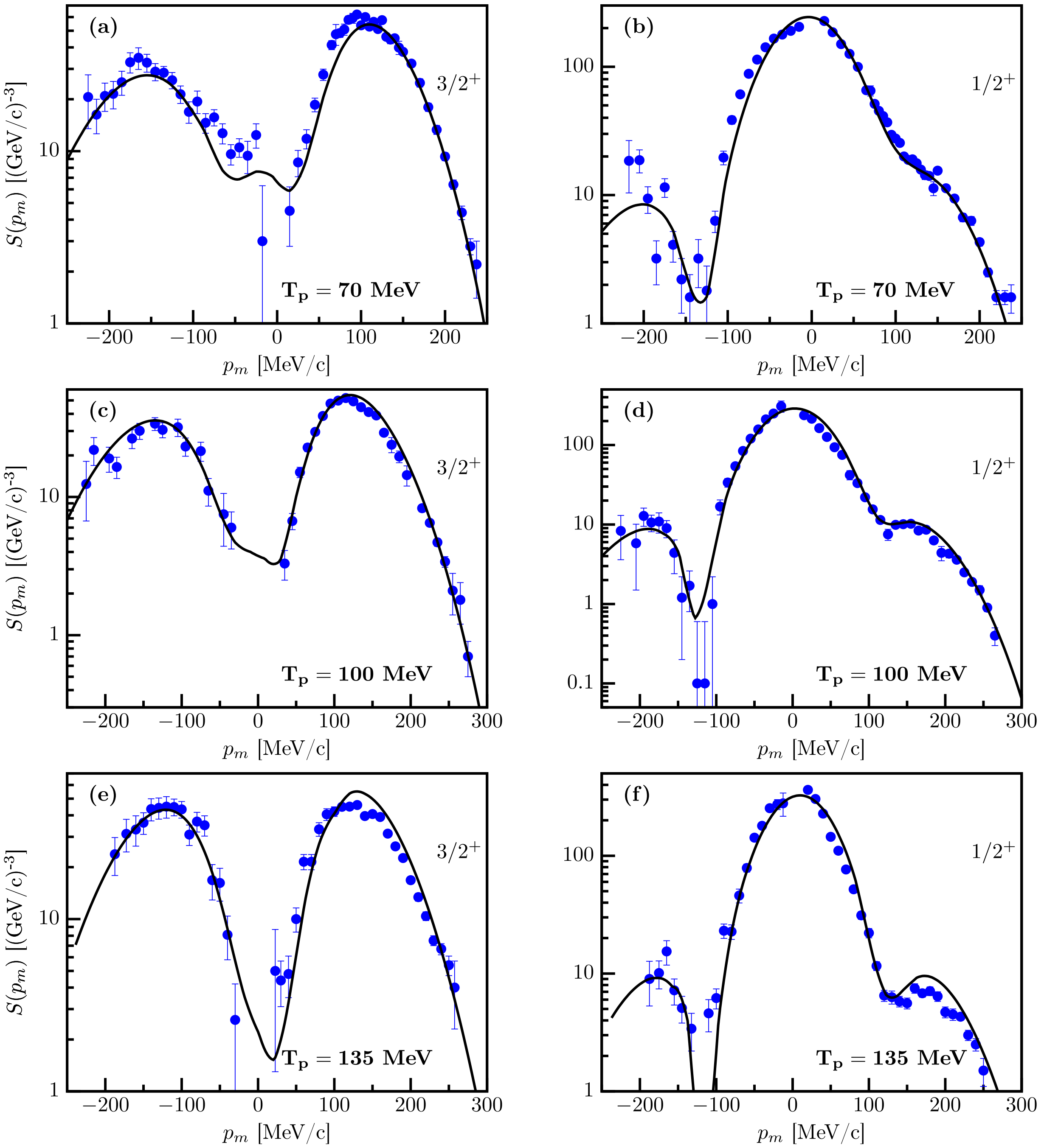

FIGURE 5
^{40}Ca(e,$e'p$) ^{39}K spectral functions in parallel kinematics at an outgoing proton kinetic energies of 70, 100, and 135 MeV. The solid line is the calculation employing the DOM, while the points from the experiment are detailed in [5]. **(A)** Distribution for the removal of the 0d3/2. The curve contains the DWIA for the 3/2$^+$ ground state including a spectroscopic factor of 0.71. **(B)** Distribution for the removal of the 1s1/2 proton with a spectroscopic factor of 0.60 for the 1/2$^+$ excited state at 2.522 MeV. Panels **(C)** and **(E)** are the same as **(A)** except the outgoing proton energy is 100 MeV and 135 MeV, respectively. Panels **(D)** and **(F)** are the same as **(A)** except that the outgoing proton energy is 100 MeV and 135 MeV, respectively. Figure adapted from [19].

fluctuations from the systematic errors. The resulting uncertainties are listed in Table 1.

The DOM results yield at least as good agreement with the data as the standard analysis of [5] for the 100-MeV outgoing protons. The main difference in the description can be pinpointed to the use of nonlocal potentials to describe the distorted waves. Nonlocal potentials tend to somewhat suppress interior wave functions of scattering states and introduce an additional ℓ dependence, as compared to local potentials. We, therefore, concluded that this consistent treatment clarifies that spectroscopic factors will be

TABLE 1 Comparison of spectroscopic factors deduced from the previous analysis [5] using the Schwandt optical potential [61] to the normalization of the corresponding overlap functions obtained in the present analysis from the DOM including an error estimate, as described in the text.

$\mathcal{Z}$	0d3/2	1s1/2
Reference [5]	0.65 ± 0.06	0.51 ± 0.05
DOM	0.71 ± 0.04	0.60 ± 0.03

larger by approximately 0.05 when the proper nonlocal dispersive potentials are employed.

The DOM treatment of experimental data associated with both the particle and hole aspects of the single-particle propagator further allows for an assessment of the quality of the DWIA to describe exclusive $(e,e'p)$ cross sections with outgoing proton energies of approximately 100 MeV. It is, therefore, fortunate that additional data were obtained at 70 and 135 MeV to further delineate the domain of validity for the DWIA description of the reaction. Figures 5A, B show the results when the DOM is employed at this lower energy for the two valence hole states in ^{39}K. The only difference in the DOM calculations for these cases is the energy of the outgoing proton wave function; the overlap functions and spectroscopic factors remain the same.

The agreement with the data at 135 MeV shown in Figures 5E, F is slightly worse but still acceptable. At this energy (and the corresponding value of the electron three-momentum transfer), the contribution of the transverse component of the excitation operator, where other mechanisms contribute in addition to those included in the present operator, will be larger. Given these results, it seems that parallel kinematics, with the longitudinal part of the operator dominating and proton energy of approximately 100 MeV, as chosen by the Nikhef group, is optimal for probing the removal probability of valence protons. We note that this can only be achieved if an analysis is conducted in which all nuclear constituents are provided by a nucleon self-energy constrained by all relevant available data, as in the DOM. The excellent agreement found here, therefore, supports the validity of the DOM approach, which can automatically account for the DWIA cross section in the domain where this approximation is expected to be valid.

The DOM results also generate the complete spectral distribution for the 0d3/2 and 1s1/2 orbits according to

$$S^{n-}_{\ell j}(E) = \sum_{\alpha,\beta} \psi^n_{\ell j}(\alpha)\, S^h_{\ell j}(\alpha,\beta;E)\, \psi^n_{\ell j}(\beta) \tag{19}$$

and similarly for the strength above the Fermi surface [65]

$$S^{n+}_{\ell j}(E) = \int drr^2 \int dr' r'^2 \psi^n_{\ell j}(r)\, S^p_{\ell j}(r,r';E)\, \psi^n_{\ell j}(r'), \tag{20}$$

where the actual procedure involves a double integral in coordinate space over the particle spectral amplitude. Distributions calculated using Equations 19, 20 are displayed in Figure 6 from −100 to 100 MeV. The energy axis refers to the $A-1$ system below the Fermi energy and the $A+1$ system above it. For clarity, a small imaginary strength in the self-energy near the Fermi energy was employed, providing the peaks a small width. The occupation probabilities are obtained from

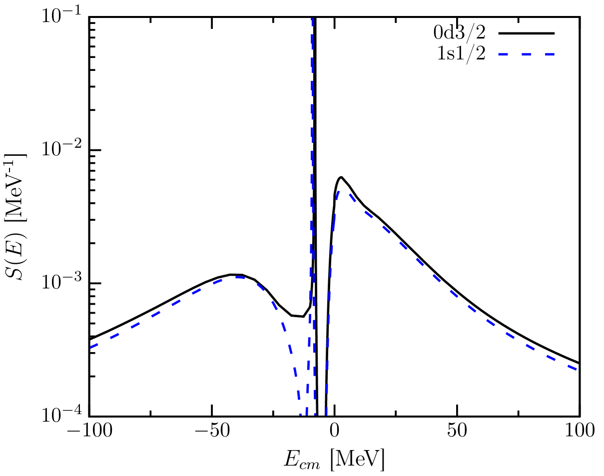

FIGURE 6
Spectral distribution of the 0d3/2 and 1s1/2 orbits as a function of energy. Additional strength outside this domain is not shown. Figure adapted from [19].

$$n^n_{\ell j} = \int_{-\infty}^{\epsilon_F} dE S^{n-}_{\ell j}(E). \tag{21}$$

For the 0d3/2 and 1s1/2 orbits, Equation 21 results in 0.80 and 0.82, respectively. The strength at negative energy not residing in the DOM peak, therefore, corresponds to 9% and 7%, respectively. This information is constrained by the proton particle number and the charge density. The strength above the Fermi energy is constrained by the elastic-scattering data and generates 0.17 and 0.15 for the 0d3/2 and 1s1/2 orbits, respectively, when Equation 22,

$$d^n_{\ell j} = \int_{\varepsilon_F}^{\infty} dE\; S^{n+}_{\ell j}(E), \tag{22}$$

is employed up to 200 MeV. The sum rule given by Equation 23

$$1 = n^n_{\ell j} + d^n_{\ell j} = \langle \Psi^A_0 | a^\dagger_{n\ell j} a_{n\ell j} + a_{n\ell j} a^\dagger_{n\ell j} | \Psi^A_0 \rangle, \tag{23}$$

associated with the anticommutation relation of the fermion operators, therefore, suggests that an additional 3% of the strength resides above 200 MeV, which is similar to what was found in [65]. Strength above the energy, where surface physics dominates, can be ascribed to the effects of short-range and tensor correlations. The main characterization of the strength distribution shown in Fig. 55 of [68] is therefore confirmed for ^{40}Ca. The present results, thus, suggest that it is possible to generate a consistent view of the strength distributions of these orbits while employing all the available experimental constraints. We, therefore, conclude that it is indeed quite meaningful to employ concepts like spectroscopic factors and occupation probabilities when discussing correlations in nuclei.

3.2 ^{48}Ca$(e,e'p)^{47}$K

The first DOM fit of ^{48}Ca was published in [40]. However, just as in the case of ^{40}Ca in [19, 22], the proton reaction cross section is

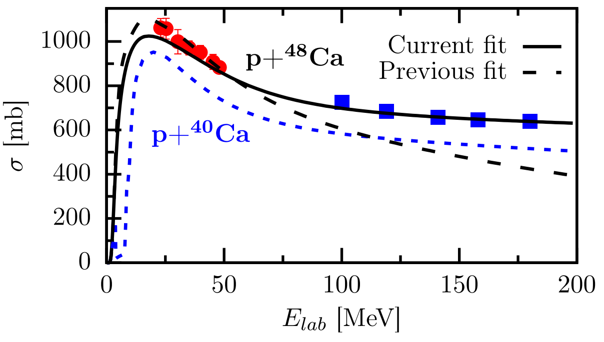

FIGURE 7
Proton reaction cross sections for ^{48}Ca and ^{40}Ca. The solid line represents the current ^{48}Ca fit [20], while the dashed line depicts the previous ^{48}Ca fit [40]. The dotted line represents the ^{40}Ca fit from [19]. The circular points are the same ^{48}Ca experimental data used in [49] and were included in the previous fit. The square points are extrapolated from the $\sigma^{40}_{\text{react}}(E)$ experimental data points at the corresponding energies and included in the current ^{48}Ca fit. Figure adapted from [20].

underestimated by approximately 200 MeV. Although there are no experimental data for ^{48}Ca at these energies, there is a data point at 700 MeV of the proton reaction cross section for ^{40}Ca and ^{48}Ca [72]. Comparing the available data for $\sigma^{40}_{\text{react}}(E)$ at 200 MeV and 700 MeV reveals that the reaction cross section essentially remains flat between these energies. It is reasonable to expect that $\sigma^{48}_{\text{react}}(E)$ assumes the same shape as $\sigma^{40}_{\text{react}}(E)$ at high energies. Thus, data points are extrapolated from the ^{40}Ca experimental data at energies above 100 MeV by applying the ratio that is seen in the 700 MeV data for $\sigma^{48}_{\text{react}}(E)/\sigma^{40}_{\text{react}}(E)$ [20]. The extrapolated points are shown as blue squares in Figure 7, while the updated fit is represented with the solid curve. The remainder of the fit did not change significantly from [40].

To analyze the proton spectroscopic factors, the ^{48}Ca$(e,e'p)^{47}$K cross section is calculated using the DWIA, following the same procedure detailed in Section 3.1 for ^{40}Ca. The experimental data on the ^{48}Ca$(e,e'p)^{47}$K reaction were obtained in parallel kinematics for outgoing proton kinetic energies of $T_p = 100$ MeV at Nikhef and previously published in [70]. As shown in [19], the DOM spectroscopic factors need to be renormalized by incorporating the observed experimental fragmentation of the strength near the Fermi energy that is not yet included in the DOM self-energy. The experimental strength distributions for $\ell = 0$ and the $\ell = 2$ excitations of ^{47}K are shown in Figure 8, which are overlaid with the corresponding DOM spectral functions calculated from Equation 3. Similar to the ^{40}Ca calculation, the distributions shown in Figure 8 are used to renormalize the DOM spectroscopic factors using Equation 18. This scaling results in a reduction from 0.64 to 0.55 for the 1s1/2 orbital and 0.60 to 0.58 for the 0d3/2 orbital. These values are in good agreement with the originally published spectroscopic factors [70], as shown in Table 2. The uncertainties in the values of the spectroscopic factors were determined using the same bootstrap method discussed in Section 3.1.

Employing the resulting renormalized spectroscopic factors leads to quantitative agreement with the experimental momentum distributions shown in Figure 9. The comparison of the spectroscopic factors in ^{48}Ca and ^{40}Ca, Z_{48} and Z_{40}, shown in Table 3 reveals that both orbitals experience a reduction with the addition of eight neutrons. This indicates that strength from the spectroscopic factors is pulled to the continuum in $S(E)$ when eight neutrons are added to ^{40}Ca. Thus, the stronger coupling to surface excitations in ^{48}Ca, demonstrated by the larger proton reaction cross section when compared to ^{40}Ca (see Figure 7), strongly contributes to the quenching of the proton spectroscopic factor. It is important to note how crucial the extrapolated high-energy proton reaction cross-section data are in drawing these conclusions. Without them, there is no constraint for the strength of the spectral function at large positive energies, which could result in no quenching of the spectroscopic factors of ^{48}Ca due to the sum rule, Equation 23, that requires the strength to integrate to one when all energies are considered [17, 65].

In addition to the depletion of the spectroscopic factor due to long-range correlations, strength is also pulled to continuum energies due to SRC. A large portion of high-momentum content is caused by the tensor force in the nucleon–nucleon (NN) interaction. In particular, the tensor force preferentially acts on pairs of neutrons and protons (np pairs) with the total spin $S = 1$. This phenomenon is known as np dominance [73] and is demonstrated by a factor of 20 difference between the number of observed np SRC pairs and the number of observed pp and nn SRC pairs in exclusive $(e,e'pp)$ and $(e,e'p)$ cross-section measurements of ^{12}C, ^{27}Al, ^{56}Fe, and ^{208} Pb [73]. The dominance of np SRC pairs would imply that the number of high-momentum protons observed in a nucleus is dependent on how many neutrons it contains. More specifically, one would expect that the high-momentum content of protons would increase with neutron excess since there are more neutrons available to make np SRC pairs. The CLAS collaboration confirmed this asymmetry dependence by measuring the high-momentum content of protons and neutrons from $(e,e'p)$ and $(e,e'n)$ cross-section measurements in ^{12}C, ^{27}Al, ^{56}Fe, and ^{208}Pb [74].

This effect can be studied by comparing the DOM-generated momentum distributions for ^{40}Ca and ^{48}Ca since the only difference between them is the eight additional neutrons in ^{48}Ca that mainly fill the 0f7/2 shell. It is clearly shown in Figure 10 that the ^{48}Ca proton momentum distribution (solid blue line) has more high-momentum content than the ^{40}Ca proton momentum distribution (dashed blue line). Since the number of protons does not change between ^{40}Ca and ^{48}Ca, the added high-momentum content in the tail of ^{48}Ca is accounted for by a reduction in the distribution of the $k < k_F$ region. Focusing on the neutrons shown in Figure 10 (red lines), the ^{48}Ca momentum distribution is significantly greater than the ^{40}Ca distribution for $k < k_F$. This is not surprising since there are now eight more neutrons that are dominated by a low-momentum content. The high-momentum content of the neutrons in ^{40}Ca decreases from 14.7% to 12.6% when eight neutrons are added to form ^{48}Ca, while the high-momentum content of the protons increases from 14.0% to 14.6%. The effects of the asymmetry of ^{48}Ca on the high-momentum content are evident in the fact that there are more high-momentum protons than neutrons. Both the increase in the proton high-momentum content and the decrease in the neutron high-momentum content are qualitatively consistent with the CLAS measurements of neutron-rich nuclei [74] and support the np-dominance picture, as predicted in [75, 76]. Notably, at this stage of the DOM development, no attempt has been made to

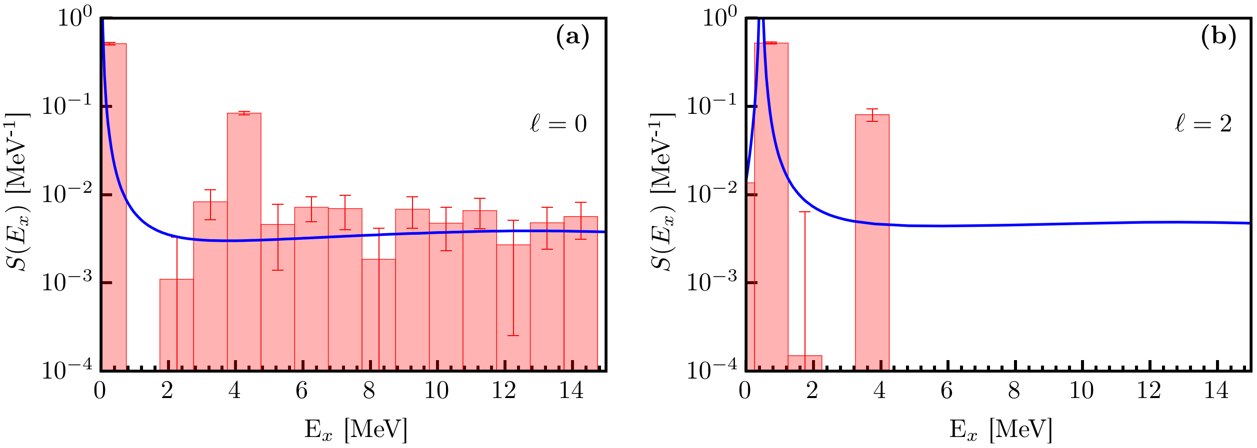

FIGURE 8
Spectral strength as a function of excitation energy in ^{48}Ca. The solid lines are DOM spectral functions for **(A)** the 1s1/2 and **(B)** the 0d3/2 proton orbitals. The histograms are the excitation energy spectra in ^{47}K extracted from the ^{48}Ca$(e,e'p)$ ^{47}K experiment [15, 70]. The peaks in the DOM curves and experimental data correspond to the quasihole energies of the protons in ^{48}Ca. The experimental spectrum in **(B)** is the isolated 0d3/2 orbital. Figure adapted from [20].

TABLE 2 Comparison of spectroscopic factors in ^{48}Ca deduced from the previous analysis [70] using the Schwandt optical potential [61] to the normalization of the corresponding overlap functions obtained in the text present analysis from the DOM including an error estimate, as described in the text.

$\mathcal{Z}$	0d3/2	1s1/2
Reference [70]	0.57 ± 0.04	0.54 ± 0.04
DOM	0.58 ± 0.03	0.55 ± 0.03

quantitatively account (i.e., introduce additional constraints) for the CLAS observations.

Another manifestation of the more correlated protons can be seen in the spectral functions of Figure 1. The broader peaks of the proton spectral functions shown in Figure 1A, compared to those of the neutrons in Figure 1B, indicate that the protons are more correlated. Furthermore, the increased proton high-momentum content in ^{48}Ca is a result from the added strength in the continuum of the hole spectral function when compared to that of ^{40}Ca. To conserve the proton number (and preserve the sum rule of Equation 23), an increase in strength at continuum energies in $S_{\ell j}(E)$ of ^{48}Ca must be compensated by a decrease in strength from energies close to the proton Fermi energy in ^{48}Ca. In particular, this contributes to the quenching of the spectroscopic factors of the 0d3/2 and 1s1/2 orbitals, before renormalization (see Equation 18), in ^{48}Ca from the values for ^{40}Ca, as shown in Table 3. In this way, the spectroscopic factor provides a link between the low-momentum-knockout experiments done at Nikhef and the high-momentum-knockout experiments done at JLAB by the CLAS collaboration.

The success of the DOM in describing both ^{40}Ca$(e,e'p)^{39}$K and ^{48}Ca$(e,e'p)^{47}$K results has provided a foothold for understanding the quenching of spectroscopic factors. A DOM investigation across the nuclear chart would deepen our understanding as a data-informed spectroscopic factor could be generated for each nucleus using Equation 8. This would require a global parametrization of the DOM, which is currently in development. Meanwhile, we note that for ^{208}Pb (see [54] for fit), the DOM values of the valence spectroscopic factors are consistent with the observations of [77] and the interpretation of [78]. The past extraction of spectroscopic factors using the ^{208}Pb$(e,e'p)^{207}$Tl reaction yielded a value of approximately 0.65 for the valence 2s$_{1/2}$ orbit [8] based on the results of [79, 80]. Although the use of nonlocal optical potentials may slightly increase this value, as shown in [19], it may be concluded that the value of 0.69 obtained from the DOM analysis is consistent with the past result. Nikhef data obtained in a large missing energy and momentum domain [81] can now be consistently analyzed, employing the complete DOM spectral functions.

4 Proton-induced knockouts

As discussed in Section 1, knockout reactions can be induced by nuclear projectiles such as protons. Although these reactions are not as clean due to the probe interacting through the nuclear *pp* force rather than the electromagnetic *ep* force, the DWIA description does a fairly good job of reproducing experimental data. Furthermore, these reactions are not limited to forward kinematics like their electron-induced counterparts; the proton can act as both the beam and the target. This is useful because it allows for the study of nuclei far from stability by utilizing rare isotope beams in laboratories such as the DOE flagship facility for rare isotope beams (FRIBs).

Since we have an accurate description of ^{40}Ca$(e,e'p)^{39}$K using the DOM, we are in a good position to investigate the reaction description of the analogous ^{40}Ca$(p,2p)^{39}$K reaction. The kinematics of the $(p,2p)$ experiment are setup in a similar manner to those of the $(e,e'p)$ experiment, and the outgoing proton energy is 100 MeV, which we showed is an optimal energy for a good DWIA description of knockout [19]. While the experiment we compare to was performed using a proton beam on a stable

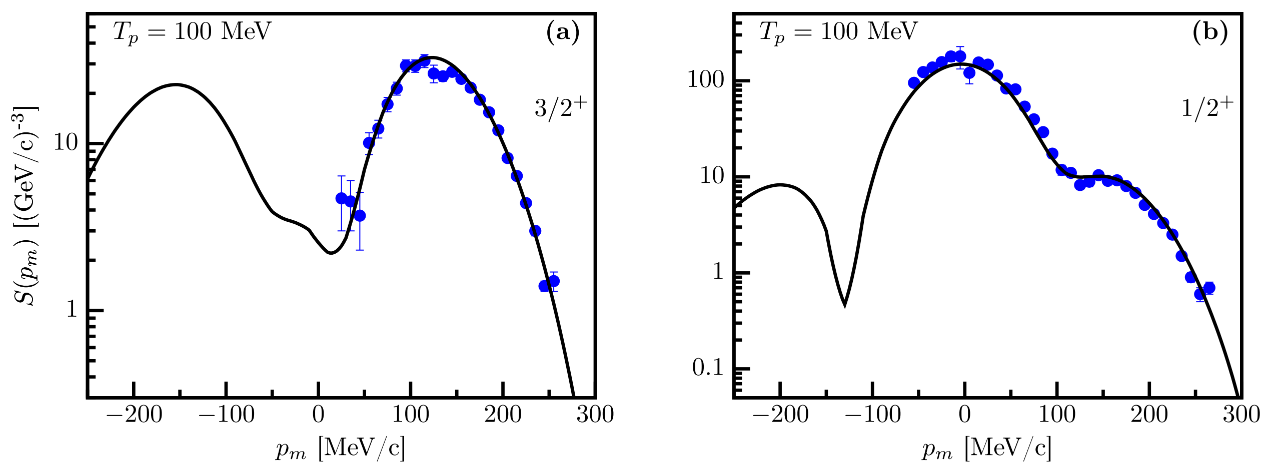

FIGURE 9
^{48}Ca($e,e'p$) ^{47}K spectral functions in parallel kinematics at an outgoing proton kinetic energy of 100 MeV. The solid line is the calculation employing the DOM, while the points are from the experiment detailed in [70]. **(A)** Distribution for the removal of the 1s1/2 proton. The curve contains the DWIA for the 1/2$^+$ ground state using the DOM-generated spectroscopic factor of 0.55 (renormalized using Equation (18)). **(B)** Distribution for the removal of the 0d3/2 with a DOM-generated spectroscopic factor of 0.58 (renormalized using Equation (18)) for the 3/2$^+$ excited state at 0.36 MeV. Figure adapted from [20].

TABLE 3 Comparison of DOM spectroscopic factors in ^{48}Ca and ^{40}Ca. These factors have not been renormalized and represent the aggregate strength near the Fermi energy.

$\mathcal{Z}$	0d3/2	1s1/2
^{40}Ca	0.71 ± 0.04	0.74 ± 0.03
^{48}Ca	0.60 ± 0.03	0.64 ± 0.03

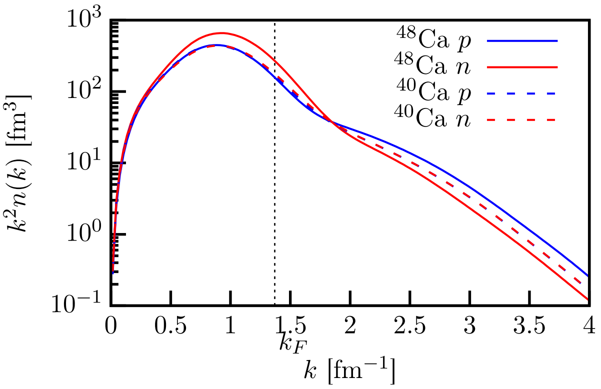

FIGURE 10
Comparison of DOM-calculated momentum distributions of protons (blue) and neutrons (red) in ^{48}Ca (solid) and ^{40}Ca (dashed). The dotted line marks the value used for k_F. Figure adapted from [20].

^{40}Ca target [82], it serves as a benchmark for the DWIA description of proton-induced knockout, allowing it to be applied in more exotic cases where protons are used as targets for rare isotope beams.

4.1 DWIA in (p, 2p)

In [21], the factorized form of the nonrelativistic DWIA with the spin degrees of freedom is employed. The transition matrix T within the distorted wave impulse approximation framework is given by

$$T_{\mu_1\mu_2\mu_0\mu_j} = \sum_{\mu_1'\mu_2'\mu_0'\mu_p} \tilde{t}_{\mu_1'\mu_2'\mu_0'\mu_p} \int d\boldsymbol{R}\, \chi^{(-)*}_{1,\mu_1'\mu_1}(\boldsymbol{R})\, \chi^{(-)*}_{2,\mu_2'\mu_2}(\boldsymbol{R})\, \chi^{(+)}_{0,\mu_0'\mu_0}(\boldsymbol{R})\, e^{-i\alpha_R \boldsymbol{K}_0\cdot\boldsymbol{R}}$$

$$\times \sum_m \left(\ell m s_p \mu_p | j \mu_j\right) \psi^n_{\ell jm}(\boldsymbol{R}). \qquad (24)$$

In Equation 24, the incident and two emitted protons are labeled as particle 0–2, while the bound proton in the initial state is labeled as p. $\chi_{i,\mu_i'\mu_i}$ is a distorted wave of particle $i = 0, 1, 2$ having the asymptotic (local) third component μ_i (μ_i') of its spin $s_i = 1/2$. The outgoing and incoming boundary conditions of the distorted waves are denoted by superscripts (+) and (−), respectively. $\boldsymbol{K}_0$ is the momentum (wave number) of the incident proton, and α_R is the mass ratio of the struck particle and the target. n is the radial quantum number, and ℓ, j, m are the single-particle orbital angular momentum, total angular momentum, and third component of ℓ, respectively. $\psi^n_{\ell jm}$ is the single-particle wave function (SPWF) normalized to unity. $\tilde{t}_{\mu_1'\mu_2'\mu_0'\mu_p}$ is the matrix element of the pp effective interaction t_{pp}:

$$\tilde{t}_{\mu_1'\mu_2'\mu_0'\mu_p} = \left\langle \boldsymbol{\kappa}', \mu_1'\mu_2' | t_{pp} | \boldsymbol{\kappa}, \mu_0'\mu_p \right\rangle, \qquad (25)$$

where $\boldsymbol{\kappa}$ and $\boldsymbol{\kappa}'$ are relative momenta of two protons in the initial and the final states, respectively. The factorization procedure of t_{pp} is explained using the local semi-classical approximation (LSCA) and the asymptotic momentum approximation (AMA) in the appendix of [21]. It should be noted that the factorized DWIA is often regarded as a result of the zero-range approximation, but t_{pp} is a finite-range interaction.

The triple differential cross section (TDX) with respect to the emitted proton energy T_1^{lab} and emission angles Ω_1^{lab} and Ω_2^{lab} is given as

$$\frac{d^3\sigma^{\mathrm{lab}}}{dT_1^{\mathrm{lab}}d\Omega_1^{\mathrm{lab}}d\Omega_2^{\mathrm{lab}}} = \mathcal{Z}_{lj}^n J_{\mathrm{lab}G} F_{\mathrm{kin}} \frac{(2\pi)^4}{\hbar v_\alpha} \frac{1}{(2s_0+1)(2j+1)} \sum_{\mu_1\mu_2\mu_0\mu_j} \left| T_{\mu_1\mu_2\mu_0\mu_j} \right|^2, \tag{26}$$

with $\mathcal{Z}_{lj}^n$, $J_{\mathrm{lab}G}$, F_{kin}, and v_α being the spectroscopic factor, the Jacobian from the center-of-mass frame to the laboratory frame, kinetic factor, and the relative velocity of the incident proton and the target, respectively. Quantities in Equation 26 with the superscript lab are evaluated in the laboratory frame, while the others are in the center-of-mass frame. For details, see Section 3.1 of [36].

Equations 15, 25, 26 for electron- and proton-induced knockout, respectively, have many similarities. They both employ the same spectroscopic factor, bound-state wave function, and 100-MeV outgoing proton distorted wave. The proton-induced expression includes two additional proton distorted waves to account for the incoming and outgoing projectile proton, but the main difference between these two equations is the appearance of the *pp* interaction in the form of $\tilde{t}_{\mu_1'\mu_2'\mu_0'\mu_p}$ in Equation 25. In the electron case, this is factorized outside of the hadronic part of the cross section, which is not possible in the proton-induced case. We probe this difference by employing the same DOM wave functions between $(e,e'p)$ and $(p,2p)$ cases.

4.2 Results and discussion

Theoretical knockout cross sections are calculated using the DWIA framework with the DOM SPWF and distorted waves. The reaction kinematics is in a coplanar kinematics, and the opening angles of the emitted protons are fixed at the same angle: $\phi_1^{\mathrm{L}} = 0°$, $\phi_2^{\mathrm{L}} = 180°$, and $\theta_1^{\mathrm{L}} = \theta_2^{\mathrm{L}} = 42.0°$ in the Madison convention [83]. The kinematics of the three particles is then uniquely determined by T_1^{L}. The DOM-DWIA result is compared with those of the phenomenological SPWF and the optical potential in panel (a) of Figure 11. For this comparison, the DOM-DWIA cross section is adjusted to the data rather than employing the DOM-generated spectroscopic factor from Equation 8. The phenomenological SPWF suggested by [70], the Koning–Delaroche optical potential parameter set (KD) [84], and the Dirac phenomenology (DP) [85–87] are also considered. Spectroscopic factors are, therefore, extracted from the ratio of the present calculations and the experimental data taken by the E258 experiment at the RCNP [82] by minimizing

$$\chi^2\left(\mathcal{Z}_{0d_{3/2}}\right) = \sum_i \frac{\left(\mathcal{Z}_{0d_{3/2}}\sigma_i^{\mathrm{DWIA}} - \sigma_i\right)^2}{\delta_i^2}, \tag{27}$$

where σ_i^{DWIA} and σ_i are theoretical and experimental cross sections at data points i, respectively, and δ_i is the associated error of the experimental data. Obtained spectroscopic factors are summarized in Table 1. Following [36], only the data points around the peak, larger than $25\,\mu$b/(MeV sr^2), are fit to reduce the uncertainty.

The spectroscopic factors obtained from the phenomenological $(p,2p)$ analysis (the first two rows of Table 4) are consistent with the phenomenological $(e,e'p)$ analysis, which resulted in 0.65 ± 0.06 [5]. On the other hand, the spectroscopic factor obtained using the DOM wave functions to reproduce the $(p,2p)$ cross section is in disagreement with the DOM value (using Equation 8) of 0.71 ± 0.04. Since the spectroscopic factor is a property of the quasihole bound state, it should not depend on the reaction mechanism or beam energy [90]. As shown in [36], the spectroscopic factors for the valence levels near the Fermi energies of stable nuclei extracted from $(p,2p)$ reactions above 200 MeV, using the DWIA with local potentials, are consistent with those from $(e,e'p)$ with uncertainties ranging from 10% to 15%. The nonlocality correction to the SPWF and distorted waves is considered to be a primary source of uncertainty in determining these spectroscopic factors [36].

Employing different potentials to generate the proton scattering and bound-state wave functions complicates the interpretation of these results. However, the DOM bound-state and scattering wave functions are both fully consistent within the DWIA framework and equivalent between the $(e,e'p)$ and $(p,2p)$ reactions. Nevertheless, $\mathcal{Z}_{0\mathrm{d}3/2}$ obtained with the DOM-DWIA analysis of the ^{40}Ca$(p,2p)$ data at 200 MeV, in which the nonlocality is treated in a sophisticated manner, differs by at least 21% from the value used to reproduce $(e,e'p)$ data utilizing the same DOM. With the nucleus-dependent ingredients of the DWIA description eliminated as causes for this discrepancy (because the same DOM ingredients are used in both the $(e,e'p)$ and $(p,2p)$ cases), we explore differences in the reaction descriptions to uncover the source of discrepancy.

We first consider the consequences of using three distorted proton waves in the $(p,2p)$ reaction, as compared to just one in $(e,e'p)$. There is an uncertainty associated with the DOM distorted waves due to the experimental data points used in the DOM fit. Recalling the strong correlation between the proton reaction cross sections and the $(e,e'p)$ cross sections demonstrated in Section 3, we look to uncertainties in the experimental proton reaction cross-section data points in energy regions corresponding to those of the distorted proton waves to get a rough estimate of the uncertainty associated with the DOM distorted waves. The proton reaction cross-section data points from [91, 92] suggest an uncertainty in the corresponding DOM distorted waves of approximately 3%. Furthermore, due to the kinematics of the reaction, one of the proton energies is as low as 36 MeV. In the DOM analysis of ^{40}Ca$(e,e'p)^{39}$K, the description of the experimental cross section for outgoing proton energies of 70 MeV, the lowest of the considered proton energies, is somewhat less satisfactory [19]. This indicates that the impulse approximation may not be applicable at proton energies of 70 MeV and below. Since one of the outgoing proton energies in this ^{40}Ca$(p,2p)^{39}$K reaction is even less than 70 MeV, it is reasonable to expect some discrepancy in the ^{40}Ca$(p,2p)^{39}$K TDX. This discrepancy may be reduced when higher proton beam energies are considered, but this implies that the DOM analysis has to be extended to higher energies. Noting that previous analyses of $(p,2p)$ and $(e,e'p)$ resulted in consistent spectroscopic factors, we conclude that any inaccuracies caused by low-energy protons do not explain the high 21% discrepancy we are observing between DOM descriptions of $(e,e'p)$ and $(p,2p)$. We also investigated the uncertainty arising from a different choice of the *pp* effective interactions when employing the DOM in the DWIA. Three different types of *pp* effective interaction were utilized: the Franey–Love effective interaction (FL) [88], the Melbourne

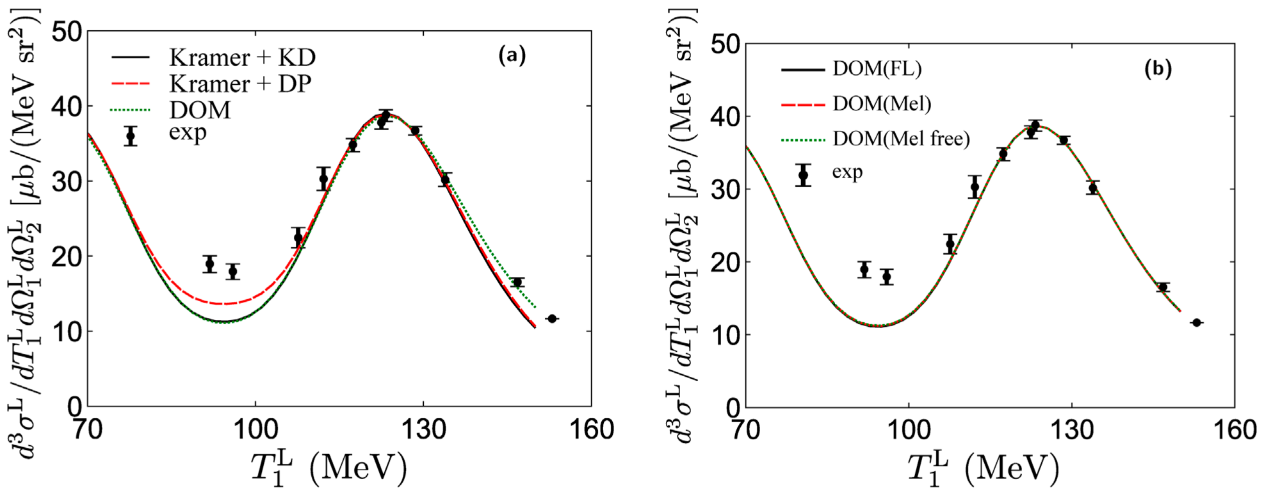

FIGURE 11
(A) TDX with different optical potentials. The solid and dashed lines are TDXs with the Koning–Delaroche optical potential (KD) and Dirac phenomenology (DP), respectively. The result with the DOM is also shown as the dotted line. All results reflect cross sections that are normalized with the spectroscopic factors shown in Table 1. **(B)** TDX calculated using the DOM with different *pp* effective interactions. The solid, dashed, and dotted lines are TDXs with the Franey–Love effective interaction [88] (FL), Melbourne *g*–matrix interaction at mean density [89] (Mel), and that at zero density (Mel free), respectively. See Table 1 for corresponding normalization (spectroscopic) factors. The experimental data taken by the E258 experiment at RCNP [82] are also shown. Figure adapted from [21].

TABLE 4 Normalization (spectroscopic) factors extracted in ^{40}Ca(p,2p)^{39}K using Equation (27).

SPWF	Optical pot	*pp* int	$\mathcal{Z}_{0d_{3/2}}$
Kramer	KD	FL	0.623 ± 0.006
Kramer	Dirac	FL	0.672 ± 0.006
DOM	DOM	FL	0.560 ± 0.005
DOM	DOM	Mel	0.489 ± 0.005
DOM	DOM	Mel (free)	0.515 ± 0.005

g–matrix interaction at mean density (Mel) [89], and that at zero density (Mel free) were utilized. The Franey–Love interaction is a free-space *t*-matrix aimed at reproducing high-energy *pp* scattering cross sections. The Melbourne interactions utilize the so-called *g*-matrix, which is an approximation to account for the fact that the *pp* interaction in $(p,2p)$ takes place in a nucleus rather than a vacuum. The *g*-matrix is typically calculated from the *pp* interaction via ladder diagrams in infinite nuclear matter and mapped to finite nuclei using the density [89]. The mean density of the $(p,2p)$ reaction is defined in Section 6.1. of [36]. The choice of the *pp* effective interaction does not change the form of the TDX(see panel (b) of Figure 11), but it does change the magnitude of the TDX, causing the normalization factor to reproduce experimental data to vary (see Table 4).

The uncertainty due to the choice of the *pp* effective interaction results in $Z_{0d_{3/2}} = 0.489–0.560$, which is still inconsistent with the DOM $(e,e'p)$ results [19]. However, the variation in the spectroscopic factors using the different interactions (see Table 1) indicates that the $(p,2p)$ reaction is sensitive to the chosen effective *pp* interaction. We note that the main difference between $(e,e'p)$ and $(p,2p)$ is the need to employ an in-medium *pp* interaction, which is not well-constrained. We, therefore, hypothesize that the $(p,2p)$ reaction must be investigated with a more sophisticated treatment of the *pp* interaction beyond the standard *t*- or *g*-matrix approach. One immediate concern is that present treatments of this effective interaction do not allow for energy transfer in the elementary process. Since a substantial excitation energy is involved in the $(p,2p)$ reaction, it implies that the mediators of the strong interaction, in particular the pion, must be allowed to propagate [93]. The in-medium effective *pp* interaction should be calculated in finite nuclei, which can be achieved by utilizing DOM propagators. The formalism for this nucleus-dressed interaction is analogous to that of the *g*-matrix, but instead of mapping the infinite nuclear matter propagator to ^{40}Ca via the density, we can explicitly employ the DOM propagator (Equation 2) of ^{40}Ca. The incorporation of the ^{40}Ca DOM propagator in the effective *pp* interaction should contribute to improving the reaction description such that the DOM spectroscopic factor of $Z_{0d_{3/2}} = 0.71$ will ultimately describe both ^{40}Ca$(e,e'p)^{39}$K and ^{40}Ca$(p,2p)^{39}$K cross sections.

5 Conclusion and outlook

We have reviewed a nonlocal dispersive optical-model analysis of ^{40}Ca and ^{48}Ca, in which we fit elastic-scattering angular distributions, absorption and total cross sections, single-particle energies, charge densities, ground-state binding energies, and particle numbers. When sufficient data are available to constrain the self-energy, the DOM can provide accurate predictions. In particular, the unique capability of the DOM to simultaneously describe bound-state and scattering wave functions leads to fully consistent DWIA descriptions of knockout reactions. After updating the high-energy reaction cross sections used to constrain the DOM self-energies in ^{40}Ca and ^{48}Ca, the predictions ^{40}Ca$(e,e'p)^{39}$K and ^{48}Ca$(e,e'p)^{47}$K reproduced the Nikhef experimental data, resulting in the updated spectroscopic factors for both ^{40}Ca and ^{48}Ca (see Table 3) [19, 20]. Furthermore, we observe a reduction in the spectroscopic factors from ^{40}Ca to ^{48}Ca, which is consistent with the quenching observed in the systematic analysis of [29]. Through the spectral function picture of the nucleus provided by the DOM, we connect the quenching of spectroscopic factors to the increase in the high-momentum content of protons when eight neutrons are added to ^{40}Ca to form ^{48}Ca.

The DOM-DWIA description of the proton-induced knockout from ^{40}Ca, however, does not currently fit in the consistent story of its electron-induced counterpart. Indeed, the DOM-DWIA overestimates the ^{40}Ca$(p,2p)^{39}$K by 21% even though the same DOM wave functions (bound and scattering) are employed, which were so successful in describing the ^{40}Ca$(e,e'p)^{39}$K reaction. We hypothesize that the main cause of this discrepancy is the fact that the probe in $(p,2p)$ interacts with the nucleus through the nuclear pp interaction rather than the electromagnetic ep interaction in $(e,e'p)$. We are, therefore, working on improving the $(p,2p)$ description by utilizing DOM propagators to explicitly treat the pp interaction as scattering inside ^{40}Ca rather than in free-space (t-matrix) or infinite nuclear matter (g-matrix). The ability of the DOM to provide both bound and scattering nucleon wave functions is opening the door to a new research opportunity for the nucleon–nucleon scattering process in many-body systems. This is of particular importance as nucleus-induced reactions, which utilize the NN interaction in their theoretical description (including $(p,2p)$), can be employed in inverse kinematics to study nuclei off stability at RIB facilities [27, 28]. There is, therefore, a definite need to improve the description of the effective interaction in the medium, which will also be influenced by the nucleon asymmetry studied in exotic systems.

Author contributions

MA: conceptualization, formal analysis, resources, visualization, writing–original draft, and writing–review and editing. WD: conceptualization, formal analysis, writing–original draft, and writing–review and editing.

Funding

The author(s) declare that financial support was received for the research, authorship, and/or publication of this article. This work was performed under the auspices of the U.S. Department of Energy by Lawrence Livermore National Laboratory under contract DE-AC52-07NA27344 and was supported by the LLNL-LDRD Program under Project No. 24-LW-062. This work was also supported by the U.S. National Science Foundation under grants PHY-1912643 and PHY-2207756.

Acknowledgments

The authors acknowledge the important contributions to some of this research from Henk Blok, Bob Charity, Louk Lapikás, Kazuyuki Ogata, and Kazuki Yoshida.

Conflict of interest

The authors declare that the research was conducted in the absence of any commercial or financial relationships that could be construed as a potential conflict of interest.

Generative AI statement

The authors declare that no Generative AI was used in the creation of this manuscript.

Publisher's note

References

1. Frullani S, Mougey J. *Advances in nuclear physics, volume 14*. New York: Plenum Press (1984).

2. van der Steenhoven G, Blok HP, den Herder JWA, Jans E, Keizer PHM, Lapikás L, et al. Two-step processes in the quasi-free (e,e'p) reaction. *Phys Rev C* (1985) 32:1787–8. doi:10.1103/physrevc.32.1787

3. den Herder JWA, Blok HP, Jans E, Keizer PHM, Lapikás L, Quint ENM, et al. Single-particle properties of ^{51}V and ^{90}Zr studied with the reaction. *Nucl Phys A* (1988) 490:507–55. doi:10.1016/0375-9474(88)90012-7

4. Steenhoven GVD, Blok H, Jans E, Jong MD, Lapikás L, Quint E, et al. Knockout of protons from 12C induced by the reaction. *Nucl Phys A* (1988) 480:547–72. doi:10.1016/0375-9474(88)90463-0

5. Kramer GJ, Blok HP, van den Brand JFJ, Bulten HJ, Ent R, Jans E, et al. Proton ground-state correlations in ^{40}ca studied with the reaction ^{40}CaK. *Phys Lett B* (1989) 227:199–203. doi:10.1016/S0370-2693(89)80022-X

6. de Witt Huberts PKA. Proton spectral functions and momentum distributions in nuclei from high-resolution experiments. *J Phys G: Nucl Part Phys* (1990) 16:507–44. doi:10.1088/0954-3899/16/4/004

7. Dieperink AEL, Huberts PKA. *Ann Rev Nuc Part S* (1990) 40:239–84. doi:10.1146/annurev.ns.40.120190.001323

8. Sick I, de Witt Huberts PKA. *Comm Nucl Part Phys* (1991) 20:177.

9. Lapikás L. Quasi-elastic electron scattering off nuclei. *Nucl Phys A* (1993) 553:297–308. doi:10.1016/0375-9474(93)90630-G

10. Pandharipande VR, Sick I, Pkad H. Independent particle motion and correlations in fermion systems. *Rev Mod Phys* (1997) 69:981–91. doi:10.1103/RevModPhys.69.981

11. Boffi S, Giusti C, Pacati FD. Electron-nucleon interaction in quasi-free scattering. *Nucl Phys A* (1980) 336:416–26. doi:10.1016/0375-9474(80)90218-3

12. Giusti C, Pacati FD. Electron distortion in quasifree (e,e'p) reactions. *Nucl Phys A* (1987) 473:717–35. doi:10.1016/0375-9474(87)90276-4

13. Giusti C, Pacati FD. Separation of structure functions and electron distortion in quasifree (e, ep) reactions. *Nucl Phys A* (1988) 485:461–80. doi:10.1016/0375-9474(88)90548-9

14. Boffi S, Giusti C, Pacati FD, Radici M. *Electromagnetic response of atomic nuclei*. New York: Oxford (1996).

15. Kramer GJ. *Ph.D. thesis*. Amsterdam: Universiteit van Amsterdam (1990).

16. Furnstahl RJ, Hammer H. *Phys Lett B* (2002) 531:203–8. doi:10.1016/s0370-2693(01)01504-0

17. Dickhoff WH, Van Neck D. *Many-body theory exposed!, 2nd edition*. New Jersey: World Scientific (2008).

18. Mahaux C, Sartor R. *Single-particle motion in nuclei*. Boston, MA: Springer (1991) p. 1–223. doi:10.1007/978-1-4613-9910-0_1

19. Atkinson MC, Blok HP, Lapikás L, Charity RJ, Dickhoff WH. Validity of the distorted-wave impulse-approximation description of Ca40(e,e′p)K39 data using only ingredients from a nonlocal dispersive optical model. *Phys Rev C* (2018) 98:044627. doi:10.1103/PhysRevC.98.044627

20. Atkinson MC, Dickhoff WH. Investigating the link between proton reaction cross sections and the quenching of proton spectroscopic factors in 48ca. *Phys Lett B* (2019) 798:135027. doi:10.1016/j.physletb.2019.135027

21. Yoshida K, Atkinson MC, Ogata K, Dickhoff WH. First application of the dispersive optical model to reaction analysis within the distorted-wave impulse approximation framework. *Phys Rev C* (2022) 105:014622. doi:10.1103/PhysRevC.105.014622

22. Mahzoon MH, Charity RJ, Dickhoff WH, Dussan H, Waldecker SJ. Forging the link between nuclear reactions and nuclear structure. *Phys Rev Lett* (2014) 112:162503. doi:10.1103/PhysRevLett.112.162503

23. Dickhoff WH, Charity RJ, Mahzoon MH. Novel applications of the dispersive optical model. *J Phys G: Nucl Part Phys* (2017) 44:033001. doi:10.1088/1361-6471/44/3/033001

24. Gade A, Adrich P, Bazin D, Bowen MD, Brown BA, Campbell CM, et al. Reduction of spectroscopic strength: weakly-bound and strongly-bound single-particle states studied using one-nucleon knockout reactions. *Phys Rev C* (2008) 77:044306. doi:10.1103/PhysRevC.77.044306

25. Tostevin JA, Gade A. Systematics of intermediate-energy single-nucleon removal cross sections. *Phys Rev C* (2014) 90:057602. doi:10.1103/PhysRevC.90.057602

26. Dickhoff WH, Charity RJ. Recent developments for the optical model of nuclei. *Prog Part Nucl Phys* (2019) 105:252–99. doi:10.1016/j.ppnp.2018.11.002

27. Atar L, Paschalis S, Barbieri C, Bertulani C, Díaz Fernández P, Holl M, et al. Quasifree reactions on oxygen isotopes: observation of isospin independence of the reduced single-particle strength. *Phys Rev Lett* (2018) 120:052501. doi:10.1103/PhysRevLett.120.052501

28. Kawase S, Uesaka T, Tang TL, Beaumel D, Dozono M, Fukunaga T, et al. Exclusive quasi-free proton knockout from oxygen isotopes at intermediate energies. *Prog Theor Exp Phys* (2018) 2018. doi:10.1093/ptep/pty011.021D01

29. Aumann T, Barbieri C, Bazin D, Bertulani CA, Bonaccorso A, Dickhoff WH, et al. Quenching of single-particle strength from direct reactions with stable and rare-isotope beams. *Prog Part Nucl Phys* (2021) 118:103847. doi:10.1016/j.ppnp.2021.103847

30. Jacob G, Maris TAJ. Quasi-free scattering and nuclear structure. *Rev Mod Phys* (1966) 38:121–42. doi:10.1103/RevModPhys.38.121

31. Jacob G, Maris TAJ. Quasi-free scattering and nuclear structure. ii. *Rev Mod Phys* (1973) 45:6–21. doi:10.1103/RevModPhys.45.6

32. Chant NS, Roos PG. Distorted-wave impulse-approximation calculations for quasifree cluster knockout reactions. *Phys Rev C* (1977) 15:57–68. doi:10.1103/PhysRevC.15.57

33. Chant NS, Roos PG. Spin orbit effects in quasifree knockout reactions. *Phys Rev C* (1983) 27:1060–72. doi:10.1103/PhysRevC.27.1060

34. Samanta C, Chant NS, Roos PG, Nadasen A, Wesick J, Cowley AA. Tests of the factorized distorted wave impulse approximation for reactions. *Phys Rev C* (1986) 34:1610–9. doi:10.1103/PhysRevC.34.1610

35. Cowley AA, Lawrie JJ, Hillhouse GC, Whittal DM, Förtsch SV, Pilcher JV, et al. Quasifree knockout in 16O15N at an incident energy of 151 MeV. *Phys Rev C* (1991) 44:329–35. doi:10.1103/PhysRevC.44.329

36. Wakasa T, Ogata K, Noro T. Proton-induced knockout reactions with polarized and unpolarized beams. *Prog Part Nucl Phys* (2017) 96:32–87. doi:10.1016/j.ppnp.2017.06.002

37. Nguyen NB, Waldecker SJ, Nunes FM, Charity RJ, Dickhoff WH. Transfer reactions and the dispersive optical model. *Phys Rev C* (2011) 84:044611. doi:10.1103/PhysRevC.84.044611

38. Ross A, Titus LJ, Nunes FM, Mahzoon MH, Dickhoff WH, Charity RJ. Effects of nonlocal potentials on transfer reactions. *Phys Rev C* (2015) 92:044607. doi:10.1103/PhysRevC.92.044607

39. Potel G, Perdikakis G, Carlson BV, Atkinson M, Capel P, Dickhoff WH, et al. Toward a complete theory for predicting inclusive deuteron breakup away from stability. *Eur Phys J A* (2017) 53:178. doi:10.1140/epja/i2017-12371-9

40. Mahzoon MH, Atkinson MC, Charity RJ, Dickhoff WH. Neutron skin thickness of Ca48 from a nonlocal dispersive optical-model analysis. *Phys Rev Lett* (2017) 119:222503. doi:10.1103/PhysRevLett.119.222503

41. Descouvemont P, Baye D. The r -matrix theory. *Rep Prog Phys* (2010) 73:036301. doi:10.1088/0034-4885/73/3/036301

42. Atkinson MC. Developing nucleon self-energies to generate the ingredients for the description of nuclear reactions. Springer (2020).

43. Atkinson MC, Dickhoff WH, Piarulli M, Rios A, Wiringa RB. Reexamining the relation between the binding energy of finite nuclei and the equation of state of infinite nuclear matter. *Phys Rev C* (2020) 102:044333. doi:10.1103/PhysRevC.102.044333

44. Atkinson MC, Dickhoff WH, Piarulli M, Rios A, Wiringa RB. Reply to "comment on 'reexamining the relation between the binding energy of finite nuclei and the equation of state of infinite nuclear matter' ". *Phys Rev C* (2021) 104:059802. doi:10.1103/PhysRevC.104.059802

45. Bell JS, Squires EJ. A formal optical model. *Phys Rev Lett* (1959) 3:96–7. doi:10.1103/PhysRevLett.3.96

46. Perey F, Buck B. A non-local potential model for the scattering of neutrons by nuclei. *Nucl Phys* (1962) 32:353–80. doi:10.1016/0029-5582(62)90345-0

47. Charity RJ, Sobotka LG, Dickhoff WH. Asymmetry dependence of proton correlations. *Phys Rev Lett* (2006) 97:162503. doi:10.1103/PhysRevLett.97.162503

48. Charity RJ, Mueller JM, Sobotka LG, Dickhoff WH. Dispersive-optical-model analysis of the asymmetry dependence of correlations in ca isotopes. *Phys Rev C* (2007) 76:044314. doi:10.1103/PhysRevC.76.044314

49. Mueller JM, Charity RJ, Shane R, Sobotka LG, Waldecker SJ, Dickhoff WH, et al. Asymmetry dependence of nucleon correlations in spherical nuclei extracted from a dispersive-optical-model analysis. *Phys Rev C* (2011) 83:064605. doi:10.1103/PhysRevC.83.064605

50. Dickhoff WH, Van Neck D, Waldecker SJ, Charity RJ, Sobotka LG. Nonlocal extension of the dispersive optical model to describe data below the fermi energy. *Phys Rev C* (2010) 82:054306. doi:10.1103/PhysRevC.82.054306

51. Waldecker SJ, Barbieri C, Dickhoff WH. Microscopic self-energy calculations and dispersive optical-model potentials. *Phys Rev C* (2011) 84:034616. doi:10.1103/PhysRevC.84.034616

52. Dussan H, Waldecker SJ, Dickhoff WH, Müther H, Polls A. Microscopic self-energy of ^{40}ca from the charge-dependent bonn potential. *Phys Rev C* (2011) 84:044319. doi:10.1103/PhysRevC.84.044319

53. Brida I, Pieper SC, Wiringa RB. Quantum Monte Carlo calculations of spectroscopic overlaps in$A\leqslant 7$nuclei. *Phys Rev C* (2011) 84:024319. doi:10.1103/physrevc.84.024319

54. Atkinson MC, Mahzoon MH, Keim MA, Bordelon BA, Pruitt CD, Charity RJ, et al. Dispersive optical model analysis of ^{208} generating a neutron-skin prediction beyond the mean field. *Phys Rev C* 101 (2020) 044303. doi:10.1103/PhysRevC.101.044303

55. Lane AM. Isobaric spin dependence of the optical potential and quasi-elastic (p, n) reactions. *OSTI.GOV* (1962) 35:676–85. doi:10.1016/0029-5582(62)90153-0

56. Fiedeldey H. The equivalent local potential and the perey effect. *Nucl Phys* (1966) 77:149–56. doi:10.1016/0029-5582(66)90682-1

57. Press WH, Teukolsky SA, Vetterling WT, Flannery BP. *Numerical recipes in fortran 90*. Cambridge University Press (1996).

58. Pruitt CD, Charity RJ, Sobotka LG, Atkinson MC, Dickhoff WH. Systematic matter and binding-energy distributions from a dispersive optical model analysis. *Phys Rev Lett* (2020) 125:102501. doi:10.1103/PhysRevLett.125.102501

59. Pruitt CD, Charity RJ, Sobotka LG, Elson JM, Hoff DEM, Brown KW, et al. Isotopically resolved neutron total cross sections at intermediate energies. *Phys Rev C* (2020) 102:034601. doi:10.1103/PhysRevC.102.034601

60. Brand M, Allaart K, Dickhoff WH. *Nucl Phys* (1990) A509:1.

61. Schwandt P, Meyer HO, Jacobs WW, Bacher AD, Vigdor SE, Kaitchuck MD, et al. Analyzing power of proton-nucleus elastic scattering between 80 and 180 mev. *Phys Rev C* (1982) 26:55–64. doi:10.1103/PhysRevC.26.55

62. Direct Interactions FG, Reaction N. New York: Gordon & Breach (1963).

63. Forest D, Jr. Off-shell electron-nucleon cross sections: the impulse approximation. *Nucl Phys A* (1983) 392:232–48. doi:10.1016/0375-9474(83)90124-0

64. Auce A, Ingemarsson A, Johansson R, Lantz M, Tibell G, Carlson RF, et al. Reaction cross sections for protons on 12, and 208 at energies between 80 and 180 mev. *Phys Rev C* (2005) 71:064606. doi:10.1103/PhysRevC.71.064606

65. Dussan H, Mahzoon MH, Charity RJ, Dickhoff WH, Polls A. Elastic nucleon-nucleus scattering as a direct probe of correlations beyond the independent-particle model. *Phys Rev C* (2014) 90:061603. doi:10.1103/PhysRevC.90.061603

66. de Vries H, de Jager CW, de Vries C. Nuclear charge-density-distribution parameters from elastic electron scattering. *Nucl Data Tables* (1987) 36:495–536. doi:10.1016/0092-640x(87)90013-1

67. Sick I, Bellicard JB, Cavedon JM, Frois B, Huet M, Leconte P, et al. Charge density of 40Ca. *Phys Lett B* (1979) 88:245–8. doi:10.1016/0370-2693(79)90458-1

68. Dickhoff WH, Barbieri C. Self-consistent green's function method for nuclei and nuclear matter. *Prog Part Nucl Phys* (2004) 52:377–496. doi:10.1016/j.ppnp.2004.02.038

69. Giusti C, Meucci A, Pacati FD, Co' G, De Donno V. Quasifree reactions on nuclei with neutron excess. *Phys Rev C* (2011) 84:024615. doi:10.1103/PhysRevC.84.024615

70. Kramer G, Blok H, Lapikás L. *Nucl Phys A* (2001) 679:267–86. doi:10.1016/S0375-9474(00)00379-1

71. Varner R, Thompson W, McAbee T, Ludwig E, Clegg T. A global nucleon optical model potential. *Phys Rep* (1991) 201:57–119. doi:10.1016/0370-1573(91)90039-O

72. Anderson BD, Bevington PR, Cverna FH, McNaughton MW, Willard HB, Barrett RJ, et al. Proton total reaction cross section measurements for 40,44,48 at 700 mev. *Phys Rev C* (1979) 19:905–12. doi:10.1103/PhysRevC.19.905

73. Hen O, Miller GA, Piasetzky E, Weinstein LB. Nucleon-nucleon correlations, short-lived excitations, and the quarks within. *Rev Mod Phys* (2017) 89:045002. doi:10.1103/RevModPhys.89.045002

74. Duer M, Hen O, Piasetzky E, Hakobyan H, Weinstein LB, Braverman M, et al. Probing high-momentum protons and neutrons in neutron-rich nuclei. *Nature* (2018) 560:617–21. doi:10.1038/s41586-018-0400-z

75. Rios A, Polls A, Dickhoff WH. Depletion of the nuclear fermi sea. *Phys Rev C* (2009) 79:064308. doi:10.1103/PhysRevC.79.064308

76. Rios A, Polls A, Dickhoff WH. Density and isospin-asymmetry dependence of high-momentum components. *Phys Rev C* (2014) 89:044303. doi:10.1103/PhysRevC.89.044303

77. Lichtenstadt J, Heisenberg J, Papanicolas CN, Sargent CP, Courtemanche AN, McCarthy JS. High-spin states of in 208 studied by. *Phys Rev C* (1979) 20:497–503. doi:10.1103/PhysRevC.20.497

78. Pandharipande VR, Papanicolas CN, Wambach J. Occupation probabilities of shell-model orbits in the lead region. *Phys Rev Lett* (1984) 53:1133–6. doi:10.1103/PhysRevLett.53.1133

79. Quint ENM, van den Brand JFJ, den Herder JWA, Jans E, Keizer PHM, Lapikás L, et al. Relative spectroscopic strength in 206 and 208 studied with the knockout reaction. *Phys Rev Lett* (1986) 57:186–9. doi:10.1103/PhysRevLett.57.186

80. Quint ENM, Barnett BM, van den Berg AM, van den Brand JFJ, Clement H, Ent R, et al. Evidence for partial occupancy of the 3 proton orbit in ^{208}. *Phys Rev Lett* (1987) 58:1088–91. doi:10.1103/PhysRevLett.58.1088

81. van Batenburg MF. *Thesis* (university of utrecht) (2001).

82. Noro T, Sakaguchi S, Wakasa T, Dozono M, Fujioka H, Fujita K, et al. Experimental study of (*p*, 2*p*) reactions at 197 MeV on 12C, 16O, 40,48Ca, and 90Zr nuclei leading to low-lying states of residual nuclei. *Prog Theor Exp Phys* (2023) 2023. doi:10.1093/ptep/ptad116

83. Darden SE. 39. University of Wisconsin Press, Madison (1971).

84. Koning A, Delaroche J. Local and global nucleon optical models from 1 kev to 200 mev. *Nucl Phys A* (2003) 713:231–310. doi:10.1016/S0375-9474(02)01321-0

85. Hama S, Clark BC, Cooper ED, Sherif HS, Mercer RL. Global Dirac optical potentials for elastic proton scattering from heavy nuclei. *Phys Rev C* (1990) 41:2737–55. doi:10.1103/PhysRevC.41.2737

86. Cooper ED, Hama S, Clark BC, Mercer RL. Global Dirac phenomenology for proton-nucleus elastic scattering. *Phys Rev C* (1993) 47:297–311. doi:10.1103/PhysRevC.47.297

87. Cooper ED, Hama S, Clark BC. Global Dirac optical potential from helium to lead. *Phys Rev C* (2009) 80:034605. doi:10.1103/PhysRevC.80.034605

88. Franey MA, Love WG. Nucleon-nucleon matrix interaction for scattering at intermediate energies. *Phys Rev C* (1985) 31:488–98. doi:10.1103/PhysRevC.31.488

89. Amos K, Dortmans PJ, von Geramb HV, Karataglidis S, Raynal J. Nucleon-nucleus scattering: a microscopic nonrelativistic approach. *Adv Nucl Phys* (2000) 25:276–536. doi:10.1007/0-306-47101-9_3

90. Radici M, Dickhoff W, Roth Stoddard E. Consistency of spectroscopic factors from reactions at different momentum transfers. *Phys Rev C* (2002) 66:014613. doi:10.1103/PhysRevC.66.014613

91. Carlson RF, Cox AJ, Nimmo JR, Davison NE, Elbakr SA, Horton JL, et al. Proton total reaction cross sections for the doubly magic nuclei 16, 40, and 208 in the energy range 20-50 mev. *Phys Rev C* (1975) 12:1167–75. doi:10.1103/PhysRevC.12.1167

92. Turner J, Ridley B, Cavanagh P, Gard G, Hardacre A. Optical model studies of proton scattering at 30 mev: (ii). proton total reaction cross sections at 28.5 1.5 mev. *Nucl Phys* (1964) 58:509–14. doi:10.1016/0029-5582(64)90562-0

93. Morris JM. *Thesis* Washington university in St. *Louis* (2011). doi:10.7936/K7959FN2

frontiers | Frontiers in Physics

TYPE Perspective
PUBLISHED 29 January 2025
DOI 10.3389/fphy.2024.1507544

OPEN ACCESS

EDITED BY
Alan Wuosmaa,
University of Connecticut, United States

REVIEWED BY
Alessandra Guglielmetti,
University of Milan, Italy

*CORRESPONDENCE
K. A. Chipps,
✉ chippska@ornl.gov

RECEIVED 21 November 2024
ACCEPTED 23 December 2024
PUBLISHED 29 January 2025

CITATION
Chipps KA (2025) Gas jet targets for direct reaction studies.
Front. Phys. 12:1507544.
doi: 10.3389/fphy.2024.1507544

Gas jet targets for direct reaction studies

K. A. Chipps*

Physics Division, Oak Ridge National Laboratory, Oak Ridge, TN, United States

The study of direct reactions is of broad interest in nuclear physics, providing constraint to models of nuclear structure evolution and data to better understand the creation of the elements. In many cases, however, the data of interest are hindered by backgrounds and poor resolution from contaminants in either the beam, the target, or both. The use of a gas jet can overcome some of these issues through clever engineering, providing a reaction target that is chemically pure and thin enough to significantly reduce the impact on experimental resolution. This Perspective will discuss the effort to design, construct, and operate gas jet targets for direct reaction studies in the rare isotope era.

KEYWORDS

nuclear reactions, direct reactions, gas targets, gas jets, nuclear structure

1 Introduction

Direct reactions have long been a tool in nuclear physics to probe the evolution of nuclear structure and the role nuclei play in astrophysical events. With the development of rare isotope beams, however, new opportunities brought with them new challenges.

For one, beams of more and more exotic nuclei are less intense, due to the difficulty in producing them (increasing energy and decreasing production cross sections). To achieve the same results, then, either the time for a measurement or the target density must be increased, or indeed both. To ensure that the statistics that are collected do not suffer from backgrounds induced by unwanted target components (such as backing foils or spectator atoms in a chemical compound), pure targets are desired.

In addition to reduced intensities compared to stable beams, rare isotope beams are also more prone to be delivered on-target as "cocktail" beams, with multiple beam constituents alongside the nuclei of interest. This is due to production mechanisms like fragmentation and in-flight reactions. Because reactions are possible on any of the nuclei present in the beam, the purity of the targets is again a significant concern.

Lastly, as rare beams often result in decreased statistics, improvements in detectors are also needed–and need to be accommodated. Next-generation gamma arrays like GRETA [1], high-segmentation, high-coverage charged particle arrays like ORRUBA [2], and electromagnetic devices to separate reactions from unreacted beam like SECAR [3] or EMMA [4], all have strict mechanical and electronic requirements for interfacing with them. A new target technology loses value if it cannot accommodate the new detector technology needed to make use of it.

Gas jet targets take advantage of increased engineering–in the form of more complicated pumping schemes and fluid dynamics borrowed from aerospace–to achieve a dense, pure, and highly localized target of gas, as can be seen in Figure 1.

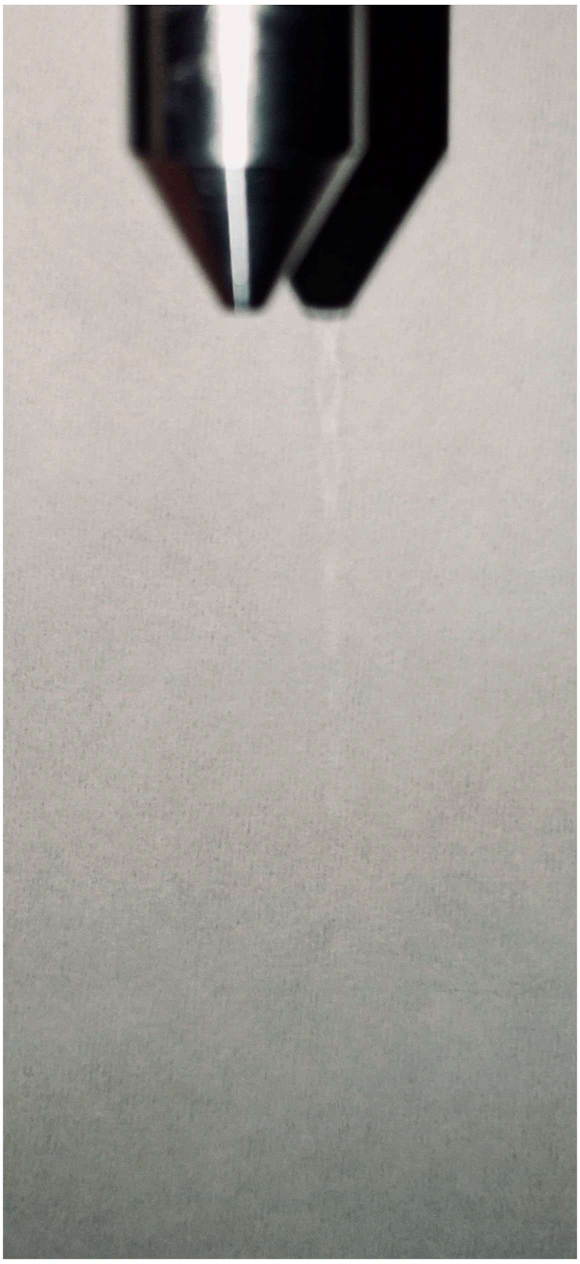

FIGURE 1
Photograph of a gas jet expanding into atmosphere.

Some of the earliest gas jets for nuclear reaction studies were built and operated in Germany in the 1970s through the early 2000s [5–17]. Others (e.g., Refs. 18–22) were built in the United States and abroad for various applications. Of these, the Jet Experiments in Nuclear Structure and Astrophysics (JENSA) gas jet target [23–25] is the most dense gas jet target for direct reaction studies in the world.

2 The JENSA gas jet target

To expand the use of gas jets to rare isotope facilities, such as the Argonne Tandem-Linac Accelerator System (ATLAS) facility or the Facility for Rare Isotope Beams (FRIB) in the United States, changes to the basic design of the target were needed. Beam intensities are, by their exotic nature, lower than for stable beams, necessitating an increase in the target density. Correspondingly, lower intensities require more detector coverage to maximize statistics, and the design of the target chamber has to accommodate this. Additional detectors to measure the heavy outgoing recoil or any gamma rays de-exciting the populated levels may also be desired. The Jet Experiments in Nuclear Structure and Astrophysics (JENSA) gas jet target system was designed and built to meet these new requirements.

2.1 ^{15}N(α,α)^{15}N

While JENSA was designed explicitly for performing reaction studies in inverse kinematics with rare isotope beams, early science measurements focused on demonstrations of the system performance and comparison to existing reaction data. One such measurement was a study of ^{15}N elastic scattering on a ^{4}He jet target. This measurement was undertaken to constrain R-matrix analysis of the ^{15}N + α entrance channel, relevant to the astrophysically-important ^{15}N(α,p) and ^{15}N(α,γ) reactions. The JENSA data, taken in inverse kinematics with a pure beam of ^{15}N produced "batch-mode" from the Holifield Radioactive Ion Beam Facility (HRIBF) and a pure target of research-grade ^{4}He–a difficult task as both beam and target species are naturally gaseous–were compared with normal kinematics data taken at the University of Notre Dame FN tandem using an alpha beam and melamine target enriched in ^{15}N. This comparison was done for 15 energies spanning roughly 3.9–4.8 MeV in the center of mass, with the elastically-scattered particles detected in the SIlicon Detector ARray (SIDAR).

Not only were the yields consistent between the two techniques, but the use of the JENSA gas jet target allowed for extension of the scattering data down to much lower center-of-mass angles: as the target exhibits cylindrical symmetry, detectors can be placed all the way to 90° in the laboratory frame without the target or target frame material impeding the reaction products.

2.2 ^{20}Ne(p,d)^{19}Ne

A distinct benefit to the use of gas jets for direct reaction studies is the ability to enable reactions between two gaseous elements to be studied in high precision. A proton beam of 30 MeV, produced by the HRIBF, impinged on the JENSA target operating with natural neon. Deuterons from the (p,d) reaction, populating states in ^{19}Ne of astrophysical interest, were selected in the SIDAR detector array using standard energy loss techniques. An example spectrum is shown in Figure 2. In Figure 6 of Ref. 26, a similar spectrum is compared against the results of a test with a neon-implanted carbon foil. The reduction in background and improvement in the resolution due to JENSA is clear.

In the case of ^{18}F(p,α)^{15}O reaction, which is known to destroy ^{18}F in novae, the spin and parity of a resonance at 6,288 keV in the compound nucleus ^{19}Ne was the largest unknown. By using the ^{20}Ne(p,d)^{19}Ne reaction to populate this level, with a pure neon gas target from JENSA, this uncertainty was removed. This resulted

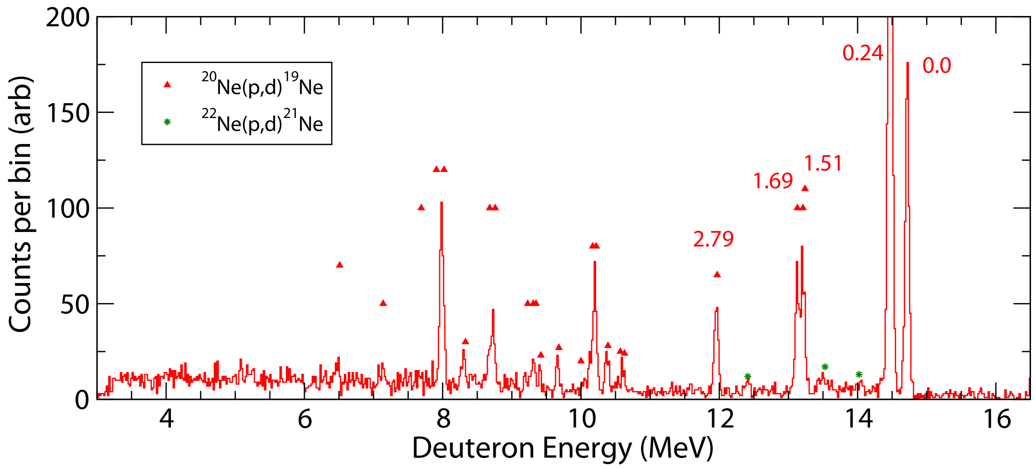

FIGURE 2
Example spectrum, taken for one angle, from the ^{20}Ne(p,d)^{19}Ne reaction measurement using JENSA. The first few states in ^{19}Ne are labeled. Peaks due to reactions on the naturally-occurring ^{22}Ne in the neon gas target (~9%) are labeled with green stars. Adapted from Ref. 27.

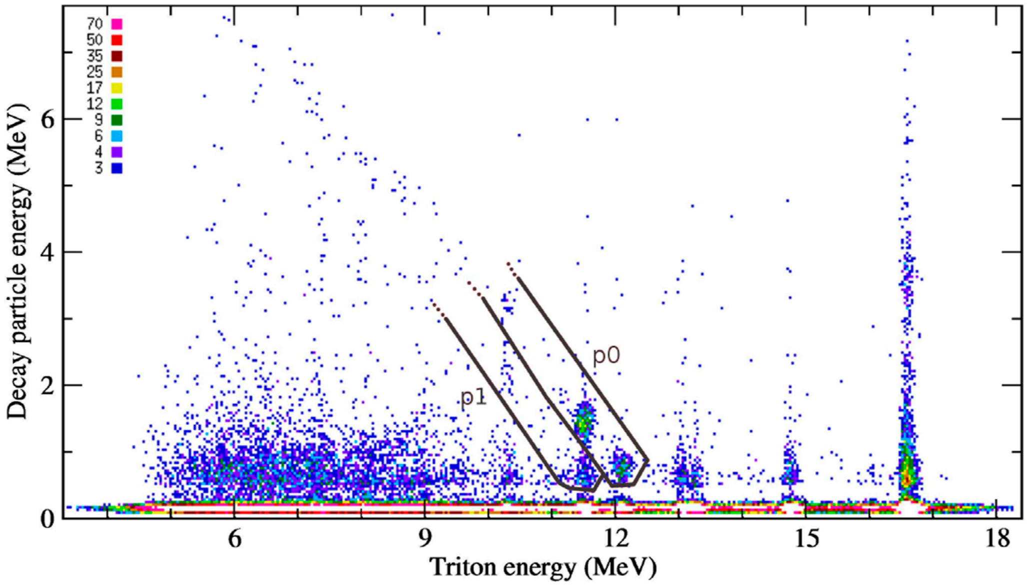

FIGURE 3
Preliminary matrix of the energy of any particle in coincidence with a reaction triton from JENSA (vertical axis) *versus* the triton energy (horizontal axis). Two bands, associated with the p0 and p1 decay channels from ^{18}Ne, are indicated with the black bands. Protons originating from the ~4,500 keV and 5,150 keV levels in ^{18}Ne form clearly visible groups in the spectrum.

in a factor of 2.8 reduction in the uncertainty of detection of astronomical ^{18}F due to the underlying nuclear reaction rate. These results, along with additional data from this measurement, were published by Bardayan et al. [27–29].

2.3 ^{14}N(p,t)^{12}N

As with gas jets in previous decades, the relatively thin jet (with respect to energy loss) allows for precision particle spectroscopy from direct reaction studies. JENSA was used with a natural nitrogen jet to study the ^{14}N(p,t)^{12}N reaction, looking for potential new levels in ^{12}N. Because the energy straggling of the incoming beam as well as the outgoing tritons through the jet was small, the resolution of the measurement was dominated by the resolution of the detectors (SIDAR in "lampshade" mode), and the width of broad, unbound levels in ^{12}N was immediately apparent in the spectra.

Two potentially new levels were observed in this direct reaction measurement with JENSA, including a strongly-populated level at ~4.5 MeV excitation energy with a width of approximately 500 keV. The results illuminated the ongoing need for spectroscopic

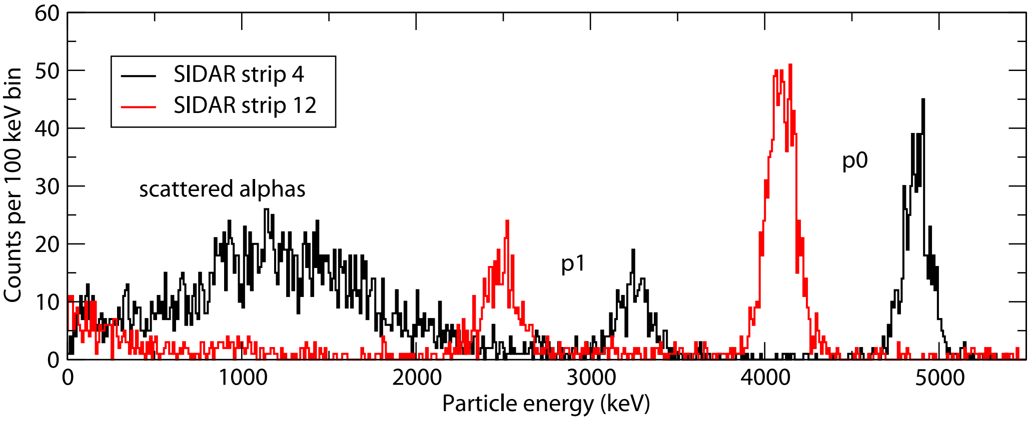

FIGURE 4
JENSA $^{14}N(\alpha,p)$ spectra from two angles in SIDAR. The p0 and p1 channels are visible, as are the elastically-scattered alphas.

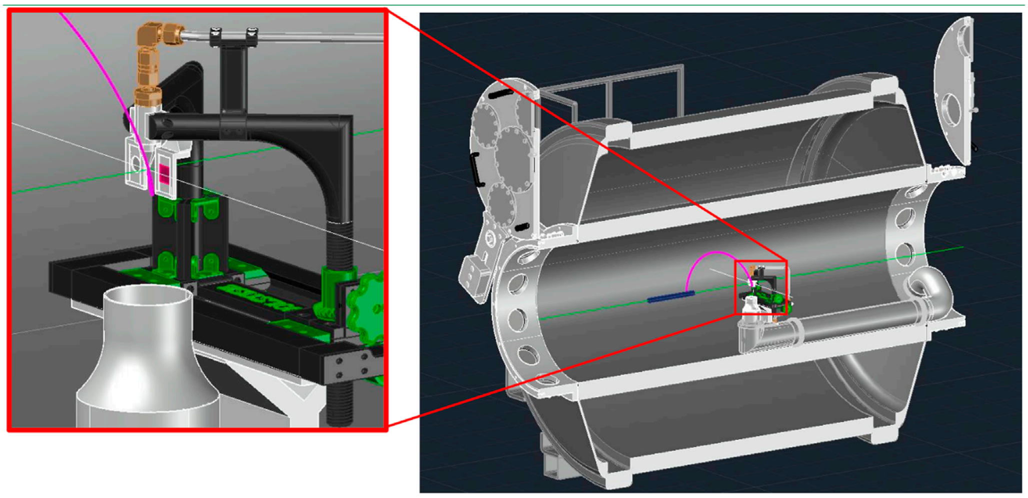

FIGURE 5
Computer aided design drawing of the SOLSTISE gas jet target setup inside of the SOLARIS solenoidal spectrometer magnet bore. CAD courtesy of M. Hall.

information of light-mass, weakly-bound nuclei. These results were published by Chipps et al. [30].

In addition to the direct spectroscopy capability, decay particles–such as protons or alphas emitted by the product of the reaction–are able to escape the thin jet target and potentially be detected. In the case of ^{12}N, protons corresponding to the p0 (to the ground state of ^{11}C), p1 (^{11}C $E_x = 2$ MeV), and p2 (^{11}C $E_x = 4.3$ MeV) decays, were observed in coincidence with the tritons of the reaction. Branching ratios for the decay channels as a function of energy can be extracted. This analysis was first done with JENSA data by Chipps et al. [31].

2.4 $^{20}Ne(p,t)^{18}Ne$

Taking advantage of the unique combination of a gas jet target with a facility able to deliver high-energy proton beams, the $^{20}Ne(p,t)^{18}Ne$ reaction was studied, again at HRIBF. Due to the very high Q-value barrier for this reaction (~20 MeV), a 37 MeV proton beam was utilized. At these energies and angles, the reaction proceeded partially through direct reactions, and partially through a multi-step process. Tritons from the (p,t) reaction were detected in the SIDAR array using standard energy loss techniques.

The spin and parity of the level at 6,150 keV, which appeared as a shoulder on top of the 6,297 + 6,353 doublet, has been contested, as has the width of this level: depending on the spin assignment, variations of up to a factor of 2.4 in the $^{14}O(\alpha,p)$ reaction rate are possible. The JENSA data favor a reassignment of the levels in this triplet versus the adopted ordering in the literature. This work was the thesis project of UTK PhD student Thompson [32].

As before, the thin jet target allowed for decay particles to escape and be detected in coincidence with reaction tritons. This is shown in Figure 3. A determination of the branching ratio from the 6,150 keV level to the ground state of ^{17}F will help to confirm whether the state contributes strongly to the $^{14}O(\alpha,p)$ reaction rate in explosive proton-rich nucleosynthesis.

FIGURE 6
Size comparison between the SOLSTISE (center) and JENSA gas jet nozzles. Despite the difference in external size, the internal nozzle design is the same.

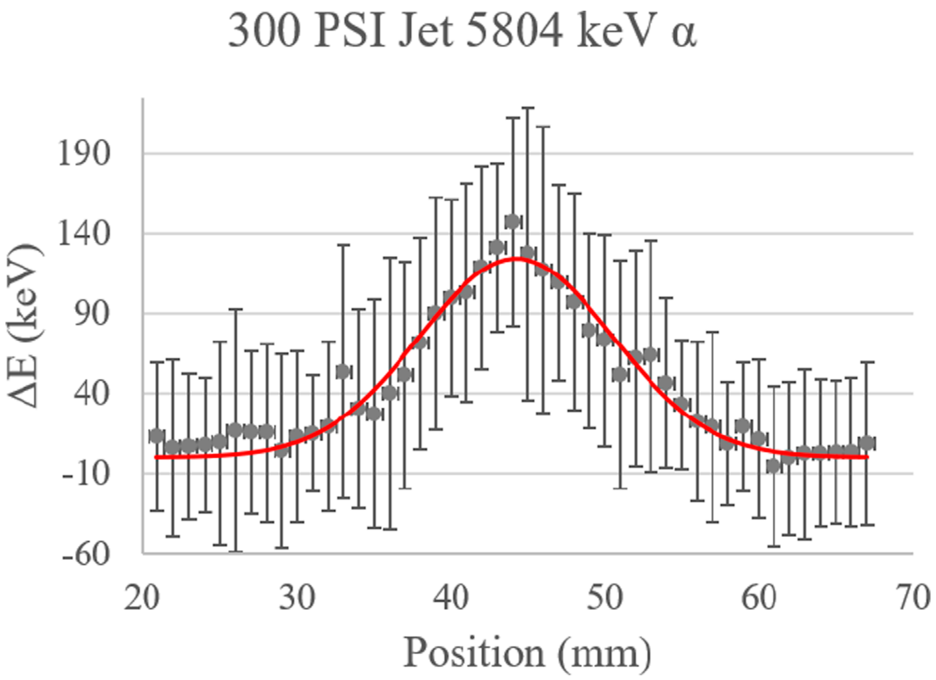

FIGURE 7
Energy losses for a known alpha source passing through a jet from SOLSTISE produced with 300 psi of nitrogen gas. For nitrogen, an energy loss of ~160 keV corresponds to an areal density of 10^{19} atoms/cm^2.

2.5 JENSA at ReA3: (*α*,p) studies

(*α*,p) reactions of relevance to astrophysical environments such as novae and x-ray bursts, while known to proceed through levels in the compound nucleus and hence falling outside of the scope of this review, nevertheless demonstrate the opportunities for studying direct reactions with rare isotope beams and gas jets.

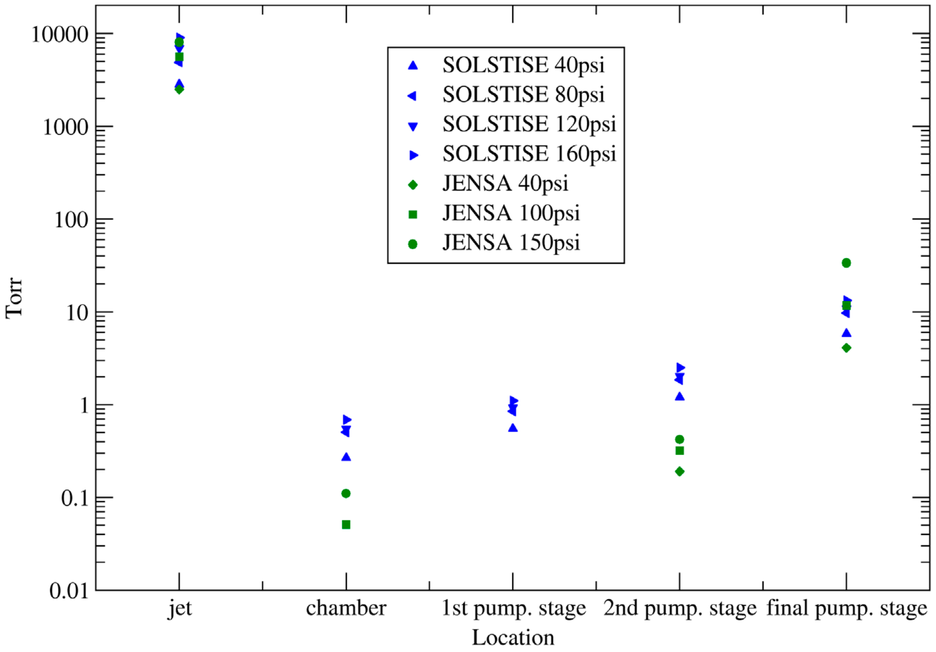

FIGURE 8
System pressures for SOLSTISE and JENSA compared at various stages, for nitrogen. For equivalent jet densities, the pressures inside the SOLSTISE system are comparable to JENSA.

During its tenure in the reaccelerated (ReA3) hall at the new Facility for Rare Isotope Beams (FRIB), JENSA has been used to study several (α,p) reactions, including ^{14}N, ^{34}Ar [33], ^{56}Ni, and ^{26}Al (α,p).

The ^{14}N(α,p)^{17}O reaction was first observed by accident: Ernest Rutherford, measuring the scattering of alpha particles from other light particles, was surprised to discover that protons were being produced when alpha particles hit air molecules in his test chamber. Almost 100 years later, the measurement was repeated with JENSA. The protons from the reaction are clearly visible (Figure 4).

A spectroscopic measurement of the ^{34}Ar(α,p)^{37}K reaction cross section was undertaken and published by Browne et al. [33]. The ^{56}Ni(α,p)^{59}Cu and ^{26}Al(α,p)^{29}Si reactions are under analysis. The latter measurement constitutes the first use of the JENSA gas jet target to study a reaction cross section into the Gamow window.

3 Combining technologies: the SOLSTISE gas jet

Gas jet targets offer several significant advantages to traditional targets, such as improved resolution, improved purity, and the ability to measure reactions near 90°, for a tradeoff in the scale of engineering required. One way to push the boundaries of particle spectroscopy even farther are to combine this target technology with other advances in beam production and particle detection: this is the goal of the SOLenoid and Supersonic Target In Structure Experiments (SOLSTISE) project. SOLSTISE is a gas jet target designed for operation inside of a solenoidal spectrometer such as HELIOS [34] or SOLARIS [35]. Figure 5 shows a CAD drawing of the SOLSTISE setup inside of the SOLARIS spectrometer at FRIB.

Due to the constraints of operating inside of a solenoidal magnetic field, the design of SOLSTISE is such that the amount of material–in particular, components made from materials which may impact the magnetic field lines–is minimized. In Figure 6, the impact of this design criterion on the size of the jet nozzle is apparent. In fact, the SOLSTISE project has taken significant advantage of additive manufacturing, producing many internal components such as receiver cones, frames, supports, and even jet nozzles using precision 3D printing techniques. Despite these design changes, the SOLSTISE system has been demonstrated to produce an equivalent jet to JENSA for nitrogen (see Figure 7). Additional changes to the pumping scheme between the two systems have resulted in improvements to the SOLSTISE pumping stage pressures, despite a lower overall pumping capacity. A comparison can be seen in Figure 8.

The SOLSTISE system has been designed to be compatible with both the HELIOS and SOLARIS spectrometers. Plans for first experimental measurements at ATLAS are underway.

4 Conclusion

Ongoing advances in rare isotope beam production, detector technology, analysis techniques, and reaction theory have given us unprecedented access to the nature of exotic nuclei. Gas jets can provide a pure, dense, and localized target to further improve the state of the art of direct reaction measurements.

Data availability statement

The data analyzed in this study is subject to the following licenses/restrictions: Data available upon request. Requests to access these datasets should be directed to chippska@ornl.gov.

Author contributions

KC: Conceptualization, Formal Analysis, Funding acquisition, Investigation, Methodology, Project administration, Supervision, Writing–original draft, Writing–review and editing.

Funding

The author(s) declare that financial support was received for the research, authorship, and/or publication of this article. This material is based upon work supported by the U.S. DOE, Office of Science, Office of Nuclear Physics under contract DE-AC05-00OR22725 (ORNL).

Acknowledgments

The author would like to thank the members of the JENSA Collaboration, M. Hall, B. P. Kay, H. Stemp, and M. Cantrell.

Conflict of interest

The author declares that the research was conducted in the absence of any commercial or financial relationships that could be construed as a potential conflict of interest.

Generative AI statement

The authors declare that no Generative AI was used in the creation of this manuscript.

Publisher's note

References

1. GRETA. *GRETA/GRETINA* (2024). Available from: https://greta.lbl.gov/ (Accessed October 23, 2024)

2. ORRUBA. *ORRUBA* (2024). Available from: https://orruba.org/ (Accessed October 23, 2024).

3. Berg GPA, Couder M, Moran MT, Smith K, Wiescher M, Schatz H, et al. Design of SECAR a recoil mass separator for astrophysical capture reactions with radioactive beams. *Nucl Instr Methods Phys Res A* (2018) 877:87–103. doi:10.1016/j.nima.2017.08.048

4. Davids B, Davids CN. Emma: a recoil mass spectrometer for isac-ii at triumf. *Nucl Instr Methods Phys Res Section A: Acc Spectrometers, Detectors Associated Equipment* (2005) 544:565–76. doi:10.1016/j.nima.2005.01.297

5. Ulbricht J, Clausnitzer G, Graw G. High density windowless gas target. *Nucl Inst Meth* (1972) 102:93–9. doi:10.1016/0029-554x(72)90526-5

6. Tietsch W, Bethge K, Feist H, Schopper E. *GSI report* (1975). p. 3–75.

7. Schuster W. *Teacher certification thesis* (1977).

8. Bittner G, Kretschmer W, Schuster W. A windowless high-density gas target for nuclear scattering experiments. *Nucl Instr Meth* (1979) 167:1–8. doi:10.1016/0029-554x(79)90465-8

9. Tietsch W, Bethge K. High density windowless gas jet target. *Nucl Instr Methods* (1979) 158:41–50. doi:10.1016/S0029-554X(79)90340-9

10. Becker H, Buchmann L, Görres J, Kettner K, Kräwinkel H, Rolfs C A supersonic jet gas target for \gamma-ray spectroscopy measurements. *Nucl Instr Methods Phys Res* (1982) 198:277–92. doi:10.1016/0167-5087(82)90265-4

11. Gaul G. *Habilitation thesis* (1985).

12. Gorres J, Becker H, Krauss A, Redder A, Rolfs C, Trautvetter H. The influence of intense ion beams on the density of supersonic jet gas targets. *Nucl Instr Methods Phys Res Section A: Acc Spectrometers, Detectors Associated Equipment* (1985) 241:334–8. doi:10.1016/0168-9002(85)90586-8

13. Pfannekuche H-W. *Diplom thesis* (1986).

14. Knee H. *Diplom thesis* (1987).

15. Griegel T, Drotleff HW, Hammer JW, Knee H, Petkau K. Physical properties of a heavy-ion-beam-excited supersonic jet gas target. *J Appl Phys* (1991) 69:19–22. doi:10.1063/1.347743

16. Dombrowski H. *Doctoral thesis* (1995).

17. Hammer JW, Biermayer W, Grieger T, Knee H, Petkau K. Rhinoceros, the versatile stuttgart gas target facility (part i). *unpublished* (2000).

18. Shapira D, Ford JLC, Novotny R, Shivakumar B, Parks RL, Thornton ST, et al. The HHIRF supersonic gas jet target facility. *Nucl Instr Meth A* (1985) 228:259.

19. Kontos A, Schurman D, Akers C, Couder M, Gorres J, Robertson D, et al. *Nucl Instr Methods A* (2011) 664:272. doi:10.1016/j.nima.2011.10.039

20. Schmid K, Veisz L. Supersonic gas jets for laser-plasma experiments. *Rev Sci Instrum* (2012) 83:053304. doi:10.1063/1.4719915

21. Rapagnani D, Buompane R, DiLeva A, Gialanella L, Busso M, DeCesare M A supersonic jet target for the cross section measurement of the ^{12}C(a,g)^{16}O reaction with the recoil mass separator ERNA. *Nucl Instr Methods Phys Res Section B: Beam Interactions Mater Atoms* (2017) 407:217–21. doi:10.1016/j.nimb.2017.07.003

22. Schlimme BS, Aulenbacher S, Brand P, Littich M, Wang Y, Achenbach P, et al. Operation and characterization of a windowless gas jet target in high-intensity electron beams. *Nucl Instrum Methods Phys Res A* (2021) 1013:165668. doi:10.1016/j.nima.2021.165668

23. Chipps KA, Greife U, Bardayan DW, Blackmon JC, Kontos A, Linhardt LE, et al. The jet experiments in nuclear structure and astrophysics (JENSA) gas jet target. *Nucl Instrum Methods Phys Res* (2014) A763:553. doi:10.1016/j.nima.2014.06.042

24. Chipps KA. Reaction measurements with the jet experiments in nuclear structure and astrophysics (JENSA) gas jet target. *Nucl Instrum Methods Phys Res* (2017) B407:297–303. doi:10.1016/j.nimb.2017.07.023

25. Schmidt K, Chipps KA, Ahn S, Bardayan DW, Browne J, Greife U, et al. Status of the JENSA gas-jet target for experiments with rare isotope beams. *Nucl Instr Methods Phys Res A* (2018) 911:1–9. doi:10.1016/j.nima.2018.09.052

26. Pain SD. Advances in instrumentation for nuclear astrophysics. *AIP Adv* (2014) 4:041015. doi:10.1063/1.4874116

27. Bardayan DW, Chipps KA, Ahn S, Blackmon JC, deBoer RJ, Greife U, et al. The first science result with the jensa gas-jet target: confirmation and study of a strong subthreshold ^{18}F(p,α)^{15}O resonance. *Phys Lett B* (2015) 751:311.

28. Bardayan DW, Chipps KA, Ahn S, Blackmon JC, deBoer RJ, Greife U, et al. Spectroscopic study of ^{20}ne+p reactions using the JENSA gas-jet target to constrain the astrophysical ^{18}f(p,α)^{15}o rate. *Phys Rev C* (2017) 96:055806. doi:10.1103/PhysRevC.96.055806

29. Bardayan DW, Chipps KA, Ahn S, Blackmon JC, Greife U, Jones KL, et al. Particle decay of astrophysically-important ^{19}Ne levels. Journal of physics conference series (IOP). *J Phys Conf Ser* (2019) 1308:012004. doi:10.1088/1742-6596/1308/1/012004

30. Chipps KA, Pain SD, Greife U, Kozub RL, Nesaraja CD, Smith MS, et al. Levels in ^{12}n via the ^{14}n(p,t) reaction using the JENSA gas-jet target. *Phys Rev C* (2015) 92:034325. doi:10.1103/PhysRevC.92.034325

31. Chipps KA, Pain SD, Greife U, Kozub RL, Nesaraja CD, Smith MS, et al. Particle decay of proton-unbound levels in ^{12}N. *Phys Rev C* (2017) 95:044319. doi:10.1103/PhysRevC.95.044319

32. Thompson PJ. *A study of spin-parity assignments in ^{18}Ne using the ^{20}Ne(p, t)^{18}Ne reaction*. Knoxville, Tennessee: University of Tennessee (2018). Ph.D. thesis.

33. Browne J, Chipps KA, Schmidt K, Schatz H, Ahn S, Pain SD, et al. First direct measurement constraining the ^{34}Ar (α p) ^{37}K reaction cross section for mixed hydrogen and helium burning in accreting neutron stars. *Phys Rev Lett* (2023) 130:212701. doi:10.1103/PhysRevLett.130.212701

34. Back BB, Baker SI, Brown BA, Deibel CM, Freeman SJ, DiGiovine BJ, et al. First experiment with HELIOS: the structure of ^{13}B. *Phys Rev Lett* (2010) 104:132501. doi:10.1103/PhysRevLett.104.132501

35. Chen J, Kay B, Hoffman C, Tang T, Tolstukhin I, Bazin D, et al. Evolution of the nuclear spin-orbit splitting explored via the ^{32}Si(d,p)^{33}Si reaction using SOLARIS. *Phys Lett B* (2024) 853:138678. doi:10.1016/j.physletb.2024.138678

Frontiers in Physics

TYPE Brief Research Report
PUBLISHED 18 February 2025
DOI 10.3389/fphy.2025.1510848

*CORRESPONDENCE
Jie Chen,
✉ chenjie@sustech.edu.cn

RECEIVED 14 October 2024
ACCEPTED 22 January 2025
PUBLISHED 18 February 2025

CITATION
Chen J (2025) Systematic trends in the spin-orbit splitting toward weak-binding.
Front. Phys. 13:1510848.
doi: 10.3389/fphy.2025.1510848

Systematic trends in the spin-orbit splitting toward weak-binding

Jie Chen*

Department of Physics, Southern University of Science and Technology, Shenzhen, Guangdong, China

Spin–orbital (SO) splitting in atomic nuclei results from the coupling between a nucleon's spin and its orbital angular momentum, fundamentally influencing nuclear structure, especially near the magic numbers. This paper reviews the impact of various effects on SO-splitting, including tensor and weak-binding effects in neutron-rich and weakly bound nuclei, focusing on both theoretical interpretations and recent experimental results. The study summarizes new experimental results on SO-splitting in isotopes such as ^{34}Si, ^{32}Si, and ^{132}Sn, showing a consistent smooth reduction in SO energy for weakly bound orbits, attributed to extended radial wave functions rather than a reduced SO potential strength. These findings reinforce the need for further experimental research with advanced radioactive ion beam facilities to understand the intricate behaviors of SO interactions in exotic nuclei.

KEYWORDS

spin–orbital splitting, transfer reactions, shell model, density functional theory, weak binding effect

1 Introduction

The study of atomic nuclei remains an important topic for understanding it as a complex system governed by the strong nuclear force. One of the key concepts in nuclear structure is the nuclear shell model [1, 2], which granted enormous success in understanding the nuclear structure near stability. In the nuclear shell model, the nucleons group in quantized energy levels or "shells" within the nucleus, which is analogous to electrons in an atom where electrons fill up discrete energy levels. The concept of "magic numbers" was introduced to denote specific numbers of nucleons that result in particularly stable atomic nuclei. Unstable nuclei generally possess lower binding energies, rendering them more susceptible to various quantum effects not observed in stable nuclei. With advancements in radioactive beam facilities worldwide, numerous new phenomena have been discovered, including halo nuclei [3], cluster structures [4], and the migration of magic numbers [5].

Spin–orbital (SO) splitting refers to the energy difference between nuclear states that arises due to the coupling of a nucleon's spin with its orbital angular momentum. It was first proposed to interpret the fine structure in atomic spectra, and the concept was later adapted to nuclear physics by Goeppert-Mayer and Haxel et al. [1, 2] to explain similar splittings observed in nuclear energy levels. This phenomenon is a direct consequence of the SO interaction, which was manually added to the shell model to explain the "magic numbers." Magic numbers 2, 8, and 20 are formed by the harmonic oscillator levels, while all the magic numbers above 20 are dominantly driven by the SO splittings. For example, the lowering of the $j = \ell + 1/2$ orbitals with large ℓ ($f_{7/2}$, $g_{9/2}$, and $h_{11/2}$) caused by strong SO splittings results in the shell closure at 28, 50, 82, etc. Any changes in SO potential may impact the shell gaps, binding energies, and lifetime of the nuclei, which possibly influence the neutron capture rate determining the heavy element synthesis [6]. In heavy elements, different theoretical descriptions of the SO potential can also affect predictions of the dripline and the location of the island of stability. Some theoretical predictions suggest that the SO interaction contributes to the stability of superheavy elements by creating energy gaps at higher nucleon numbers, leading to islands of stability in the superheavy region.

Although there is not yet a quantitative understanding of the microscopic origins of the SO term in the nuclear Hamiltonian, it appears to be influenced by the meson-theoretical three-body force [7], the tensor force [8], and the two-body SO term from the meson exchange. Fujita and Miyazawa first proposed that the three-body nucleon force with an intermediate Δ excitation results in an SO-splitting [7]. Second, Terasawa showed that the tensor-force also contributes to the SO-splitting [9]. Later, in the proposed relativistic mean field (RMF) theory [10], nucleons are treated as relativistic particles that interact through the exchange of mesons, and the SO interaction term arises due to the coupling between the nucleon's spin and its motion in the central potential field created by the mesons. When the non-relativistic expansion is performed, the SO coupling term appears as

$$V_{\text{so}} = \frac{1}{2M^2R}\frac{dV_{\text{eff}}}{dR}(\boldsymbol{\ell}\cdot\boldsymbol{s}), \tag{1}$$

where M is the mass of the nucleon (proton or neutron), V_{eff} is an effective potential that includes contributions from the scalar and vector meson fields, $\boldsymbol{\ell}$ is the orbital angular momentum, $\boldsymbol{s}$ is the intrinsic spin of the nucleon, and R is the radial distance from the center of the nucleus. The derivative of the effective potential indicates how steeply this potential changes with distance. The resulting SO-splitting scales approximately with node number and angular momentum of the orbitals as $24.5/n(\ell+1/2)A^{-0.597}$ [11], where A refers to the mass number and n refers to the quantum number of the harmonic oscillator. However, it has been observed in many cases that the SO-splitting may deviate from this trend due to different effects, which will be discussed below.

From Equation 1, we can see that the SO interaction can be influenced by the mass of the nuclei and depends on the orbital angular momentum of the nucleon. Higher orbital angular momentum states experience a more substantial SO-splitting. Therefore, the SO splittings generate all the magic numbers above 20 for orbitals with higher ℓ values, as stated above. The orientation of the orbital angular momentum and the intrinsic spin lead to splittings of different states with $j = \ell \pm s$. The dependence on the $1/R$ term in the formula indicates that this interaction has a significant impact at smaller radii. Given its proportionality to the derivative of the potential with respect to distance, it is natural to expect the SO interaction to be a surface term. This is because the density in the central region of nuclei is remarkably consistent across most stable nuclei, despite the wide variety in nuclear sizes. However, there are some theoretical predictions that suggest depletion in central density in some exotic nuclei, which leads to a sudden change in the SO potential of these nuclei.

This article aims to provide a succinct summary of the recent research on SO-splitting in nuclei, with a focus on the weak-binding effect on it. We will examine the current experimental status of SO-splitting with a focus on the Si isotopes and discuss possible underlying mechanisms. By delving into these specific studies, we will analyze the evolution of SO-splitting in these nuclei and its implications.

2 SO interaction evolution as a function of proton and neutron numbers

There are many factors that contribute to the SO interactions, including, but not limited to the tensor force, the three-body force. Moreover, as experimental studies extend to nuclei away from stability, the finite binding energy may also impact the SO splittings. Reference [12] provides a comprehensive historical overview on the impact of the three-body force on the SO-splitting, so we will focus on the other two aspects.

2.1 Effect of tensor force on SO splittings

The tensor force is a crucial component of the nuclear interaction that plays a significant role in determining the energy levels of nuclei, especially for nucleons in high-angular-momentum states and in nuclei far from the stability (23). In the nuclei far from stability or with high isospin asymmetry, the neutrons and protons can occupy different orbitals. Since the tensor component of the nuclear force arises primarily from the exchange of pions (π-mesons) between nucleons, the exchange process contributes dominantly to the monopole part of the tensor force, which is much stronger for the proton–neutron ($T = 0$) interaction, and is approximately twice as strong as the ($T = 1$) interaction. The tensor force causes the effective interactions between the proton orbital with $j_> = \ell + 1/2$ (or $j_< = \ell - 1/2$) and neutron orbitals $j'_<$ (or $j'_>$) to be more attractive, whereas $j_>$ and $j'_>$ (or $j'_<$ and $j'_<$) repel each other. This effect accumulates as the proton–neutron asymmetry increases, and the shell evolution occurs consequently.

It is, therefore, natural to expect that the neutron SO splittings evolve with the change in the proton number. As the proton fills the $j_>$ orbitals, the SO-splitting decreases, and *vice versa*, which is supported by experimental data. For example, in the Ca isotopes, it was shown that the proton $0d_{3/2}$ is attracted (lowered in energy), while $0d_{5/2}$ is repelled (raised in energy) due to the neutron filling of the $0f_{7/2}$ orbit [13]. Similarly, in the Sb isotopes, as more neutrons occupy $0h_{11/2}$, the protons $0h_{11/2}$ and $0g_{7/2}$ move apart [14]. This trend is also consistent with a decrease in the nuclear SO interaction.

2.2 SO splittings in weakly bound nuclei

Since the SO interaction is majorly a surface term, it could be modified in neutron-rich nuclei away from stability, where neutrons may have a diffuse surface density distribution due to weak binding. Hamamoto et al. [15] predicted the SO splittings of weakly bound orbits in light, neutron-rich nuclei to decrease due to the extended radial wavefunctions of neutron orbits, with no reduction in the SO potential strength.

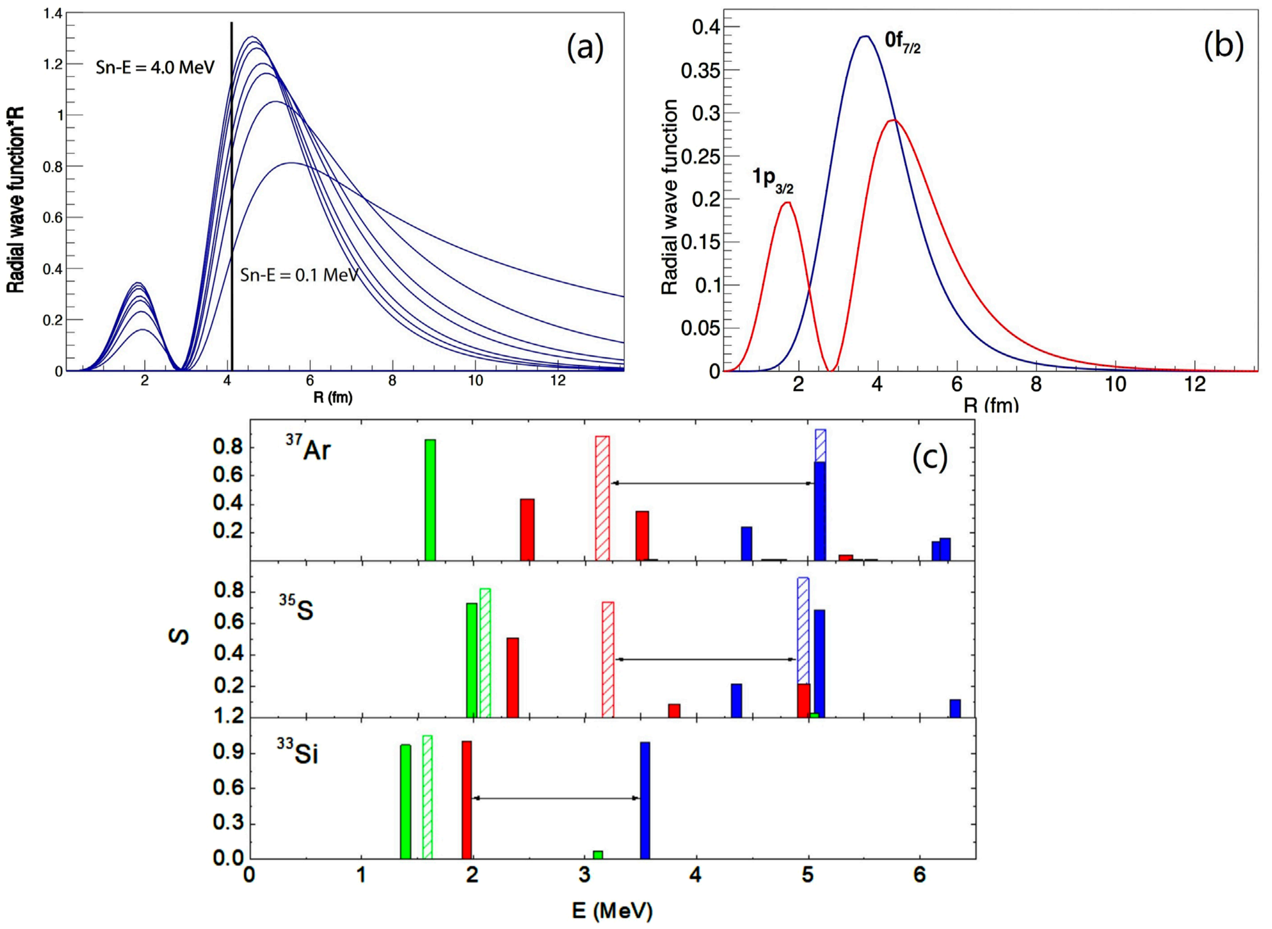

FIGURE 1
(A) Term $R\Psi(R)$ plotted as a function of the radius R under different binding energies $S_n - E$. **(B)** Radial neutron wave functions of the $1p_{3/2}$ (red solid line) and $0f_{7/2}$ orbital (blue solid line). The vertical solid black line shows the estimated matter radius of the nucleus ^{34}Si $R_0 = 4.05$ fm. **(C)** Excitation energies and corresponding spectroscopic factors of the low-lying states in ^{37}Ar, ^{35}S, and ^{33}Si measured in the (d,p) reaction, with transitions to the $0f_{7/2}$ (green), $1p_{3/2}$ (red), and $1p_{1/2}$ (blue) orbitals. The weighted average of the corresponding orbitals is labeled with the slashed bars, if different from the dominant states.

By approximating SO potential to a δ function at the nuclear surface, a simple evaluation of the SO-splitting was established in Reference [16],

$$\Delta_{SO} \propto V_{so}(\boldsymbol{\ell}\cdot\boldsymbol{s})\, r_0^2 R\Psi^2(R), \tag{2}$$

where V_{so} is the SO potential strength, $\Psi(R)$ is the radial wavefunction, r_0 is the scaling parameter for the radius of nuclei (usually taken as 1.2 fm), and R is the radial distance from the center of nuclei. Figure 1A plots the radial $1p_{3/2}$ wavefunctions multiplied by the radius under different binding energies, showing that the SO-splitting decreases as the corresponding orbitals become less bound.

3 SO interaction evolution near the proposed "bubble" nucleus

3.1 SO splittings in N = 21 isotones

Due to the saturation and short-range nature of the nuclear force, it is natural to expect that the density in the center of nuclei is constant. However, there have been many theoretical studies supporting the existence of central depletion in ^{34}Si [17, 18]. ^{34}Si is a candidate for a so-called "bubble" nuclei, providing a valuable test case for the SO potential in the center of nuclei. The prediction of central depletion in ^{34}Si arises from its doubly magic characteristic ($N = 20$ and $Z = 14$), which results in an extremely low proton occupancy number in the $1s_{1/2}$ orbital. This occupancy was determined to be between 0.17 and 0.24 in the proton knockout reaction [19]. As a large fraction of the radial part of the $1s_{1/2}$ orbital peaks in the center of the nucleus, the lack of $1s_{1/2}$ naturally induces a central density depletion. Despite no direct proof of such central depletion, experimental developments in electron scattering measurements, ideally suited for such studies, of radioactive isotopes are being made [20].

Since the SO-splitting is proportional to the derivative of the density distribution (see Equation 1), it is expected to change due to the presence of density depletion. The one-neutron adding reaction is useful for determining the angular momentum transfer ℓ and spectroscopic factors through comparison to the reaction models, and the population strength indicates the single-particle strength in each state. Therefore, the SO splittings can be mapped out with the addition and removal of single-particle strengths and the corresponding binding energies [21],

$$E_j = \sum G_j^+ E_j^+ + \sum G_j^- E_j^-, \tag{3}$$

with $G_j^+ + G_j^- = 1.0$. For the case in which the single-particle removal strengths were not measured, the energy centroid can be used to determine the single-particle energies

$$E_j = \sum G_j^+ E_j^+, \tag{4}$$

with $G_j^+ = 1$.

A significant reduction in SO-splitting is predicted for ^{34}Si compared to other $N = 20$ isotones due to central density depletion. This prediction seems to be supported by the nearly 50% reduction in the SO-splitting in ^{34}Si compared to ^{36}S, as determined using the dominant single-particle component [19, 22] (see Figure 2A). However, this assertion was questioned because only dominant single-particle strength was considered, instead of including the fragmented components of the $\ell = 1$ single-particle strength as in Equation 3, which may result in overestimation of SO splittings. After taking them into account, a smooth reduction from ^{41}Ca via ^{39}Ar and ^{37}S to ^{35}Si was shown (see Figure 2A), which was explained by the finite binding energies of the neutron states [23]. So far, the interpretation remains highly debated. There is an ongoing investigation into whether the observed changes in the $1p$ SO-splitting are driven by the weak-binding effect or by the weakening of the two-body SO potential in this region [6, 24]. This motivated the recent measurement of the $N = 19$ isotones.

3.2 SO splittings in N = 19 isotones

In order to enhance our understanding of the microscopic origins of the SO interaction, studying the SO interaction near the S and Si isotopes is crucial. The evolution from Si to S is particularly important since only the $1s_{1/2}$ proton orbital is filled between these two nuclei. Consequently, the resulting proton–neutron interaction involves no tensor component because it vanishes for $\ell = 0$; only the SO part of the nuclear force plays a role.

For ^{32}S to ^{30}Si ($N = 16$), the proton $1s_{1/2}$ occupancy changes from 1.35 to 0.65 (not 2.0 to 0.0) based on the proton knockout reaction data [25], making ^{30}Si not an ideal candidate to study the proton central depletion. However, for ^{32}Si, the neighboring even–even isotope of ^{34}Si, both density functional theory and shell model calculation predict a very small proton $1s_{1/2}$ occupancy (~0.3) compared to ^{34}S, where $1s_{1/2}$ is almost fully occupied. Furthermore, density functional theory calculations of ^{32}Si predict a depletion similar to that of ^{34}Si in the proton density distribution, as well as a sudden reduction in SO-splitting in ^{32}Si compared to ^{34}S (see Figures 2C, D). It provides another testing ground for investigating if there is a sudden reduction in SO-splitting due to proton depletion. It should also be noted that one major difference in ^{32}Si is that its neutrons are more deeply bound than ^{34}Si, so it should be less influenced by the weak binding effect.

The single-particle energies of shell-model orbitals in $N = 19$ isotones (^{33}Si, ^{35}S, and ^{37}Ar) can be mapped out with the addition and removal of single-particle strengths using Equations 3, 4. The neutron addition data of the $N = 19$ isotone ^{37}Ar and ^{35}S can be found in Refs. [26–29]. With these data, the weighted average values of the $0f_{7/2}$ and $1p_{1/2,3/2}$ orbitals were obtained and are plotted in Figure 1C. It was found that the location of the weighted average is clearly different from the dominant strength, showing that considering the fragmented strength is important. The single-particle removal strength of these orbitals was also considered where one-neutron removal data exist for ^{37}Ar and ^{35}S. Only the $1p_{3/2}$ and $0f_{7/2}$ single-particle energies of ^{37}Ar have been shifted downward by approximately 100 and 250 keV, respectively. The pf-shell orbitals of ^{35}S have been shifted less than 50 keV. However, no such previous addition or removal data exist for ^{33}Si.

In order to quantitatively determine the SO-splitting, a measurement of ^{32}Si$(d,p)^{33}$Si cross-sections was carried out at the ReA6 beamline in FRIB using the newly constructed solenoid spectrometer SOLARIS in the silicon array mode [30]. The solenoid spectrometer is capable of measuring the transfer reactions, in particular the one-neutron adding (d,p) reactions with high resolution. The experimental spectroscopic factors and the single-particle energies of the $1p_{3/2,1/2}$ and $0f_{7/2}$ orbitals are plotted in Figure 1C and compared with its S and Ar $N = 19$ isotones.

In the relativistic mean field (RMF) calculation with the DD-ME2 interaction [31], ^{32}Si was predicted to exhibit a depletion in central density, similar to ^{34}Si, due to low $1s_{1/2}$ proton occupancy. This calculation predicts a sudden reduction of the neutron $1p$-shell SO-splitting in^{33}Si compared to ^{35}S, similar to the $N = 21$ isotones. However, as observed from the present measurement, the SO-splitting in ^{33}Si is similar to that of ^{35}S, in contradiction to the RMF calculation (see Figure 2B). The mismatch of this calculation might be attributed to the fact that the proton–neutron quadrupole correlations are not taken into account in the RMF calculation. Therefore, this study does not support the existence of a sudden reduction in SO-splitting associated with a proton bubble.

3.3 Systematic description of the SO splittings with the weak binding effect

To explore this weak binding effect on SO splittings, the calculation was carried out with a Woods–Saxon (WS) potential. Figure 4 of Reference [30] shows the binding energy of $1p_{1/2}$ and $1p_{3/2}$ orbitals from existing experimental data, together with the WS calculation, using the radius and diffuseness parameters $r_0 = 1.2$ fm, $a_0 = 0.7$ fm, $r_{so} = 1.3$ fm, $a_{so} = 0.65$ fm, and SO strength $V_{so} = 6$ MeV. The depth of the potential was chosen to reproduce the binding energies of these two orbitals with a χ^2 minimization method. The SO strength is not varied in the calculation.

It can be seen immediately that the SO-splitting and single-particle energies of the $1p$ orbitals have been reproduced by the calculation without changing the SO potential strength. The good agreement with the calculation with WS formalism indicates that the evolution of the p-shell single-particle energies was described by the behavior of the wavefunctions resulted from the geometric effect (a large radius or diffuseness) of the low-ℓ orbitals as they become less bound. This was achieved without inducing a weakening of the SO potential strength or other additional effects.

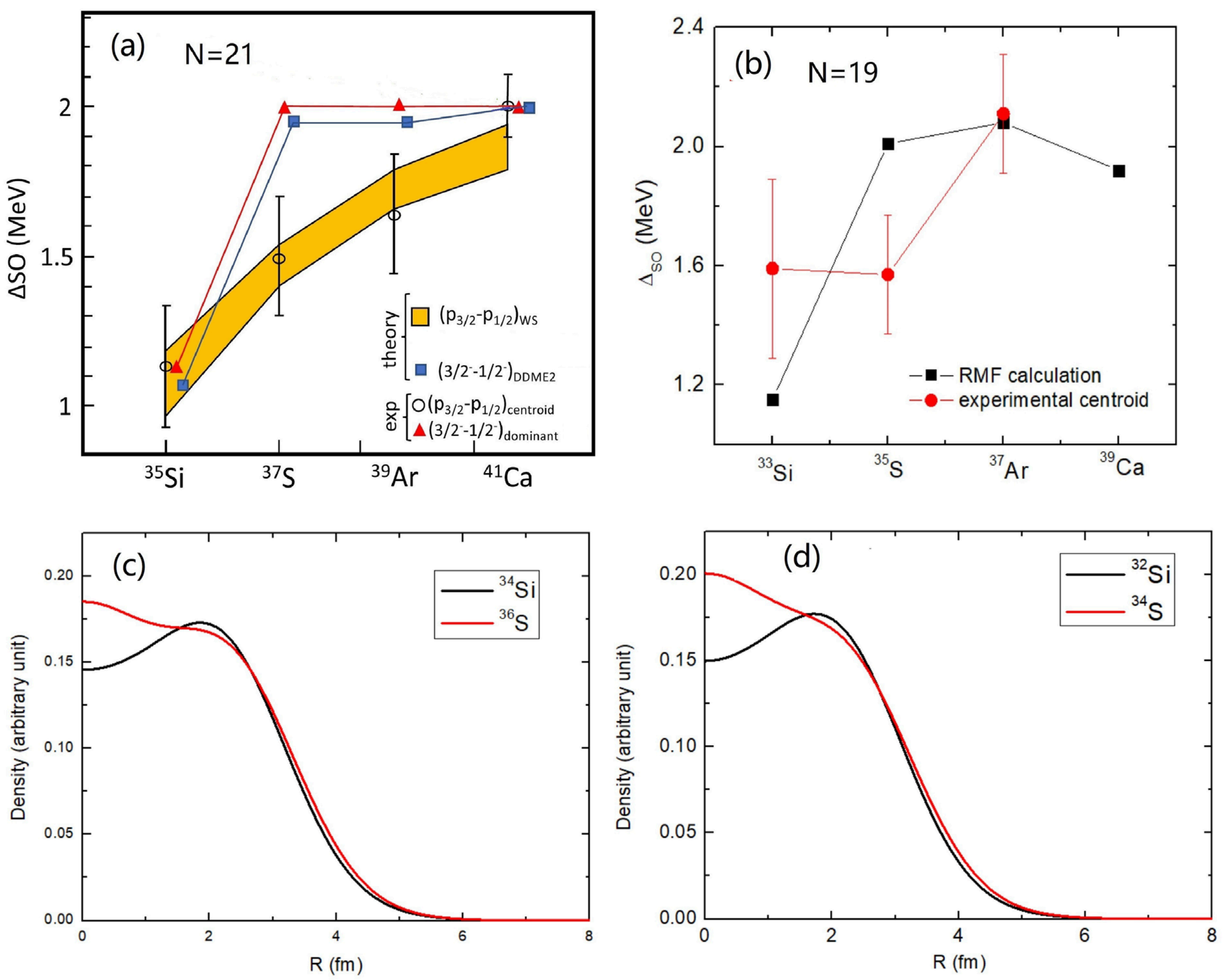

FIGURE 2
(A) Evolution of the $1p_{3/2} - 1p_{1/2}$ or 3/2⁻-1/2⁻ SO-splitting, for the $N = 21$ isotones. Black open circles (with estimated error bars) correspond to the centroid of the single-particle strength derived in [23], in which Woods–Saxon calculations were made (orange band). Red filled triangles are obtained using the energy difference between the 3/2⁻ and 1/2⁻ states having the dominating spectroscopic factor value, when populated by the (*d*,*p*) reaction. Blue squares correspond to covariant energy density functional calculations with the DDME2 parametrization of the 3/2⁻ and 1/2⁻ states shifted upward by 340 keV. Some symbols have been slightly shifted to the left or right to be better distinguished. This figure is adopted from Reference [24]. **(B)** Evolution of the $1p_{3/2} - 1p_{1/2}$ or 3/2⁻1/2⁻ SO-splitting, for the $N = 19$ isotones. Red squares (with estimated error bars) correspond to the centroid of the single-particle strength derived in [30]. Black squares correspond to covariant energy density functional calculations, shifted downward by 450 keV. This figure is adopted from Reference [30]. Proton density of ^{34}Si and ^{36}S calculated with the DD−ME2 interaction using the covariant energy density functional method. **(D)** Same as **(C)**, but for ^{32}Si and ^{34}S. This figure is adopted from Reference.

From Equation 2, it is seen that the SO-splitting depends on the term $R\Psi(R)$ if the strength of the SO potential V_{so} remains unchanged. In Figure 1A, this term is plotted as a function of R. The radius of the nucleus R_0 was taken as $1.25\ \text{fm} \times A^{1/3} = 4.05$ fm. It is clearly seen that the term $R\Psi(R)$ reduces as the binding energies approach to 0, diminishing to more than 60% of its original value. This indicates that the reduction observed in the 1*p*-orbital SO-splitting can be fully accounted for by the evolution of the wavefunctions toward weak binding.

^{32}Si should have a similar $1s_{1/2}$ occupancy as ^{34}Si, according to the latest safe Coulomb excitation measurement [32], as also supported by the theories. It is noted that there is yet no experimental measurement informing on the proton occupancy. Related measurements to determine its proton occupancy in the $1s_{1/2}$ orbital are being planned with the Active-Target Time Projection Chamber (AT-TPC) [33] coupled with the HELIOS solenoid. Using the proton addition or removal reaction, the proton occupancy of ^{32}Si in the $s_{1/2}$ orbital will be determined.

3.4 SO splittings of orbitals with $\ell = 1$ and $\ell = 3$

The discussion above mostly focuses on the SO-splitting of the 1*p*-shell orbitals. One may wonder if the weak binding or central depletion effect may be revealed in the SO-splitting of the 0*f* orbitals. The radial wavefunction of the 0*f* orbital is compared with that of the 1*p* orbital in Figure 1B. In addition, Equation 1 shows that the changes in the wavefunction at the smaller radius would have a larger impact on the SO potential. Therefore, some may expect that there would be a sudden reduction in the SO-splitting in case of a central depletion. However, the $0f$ orbital wavefunction seems to have very little sensitivity to the change in the potentials in the very center of nuclei ($R < 2$ fm), where the depletion was presented. Consequently, the central depletion should have very little impact on the SO-splitting of the $0f$ orbitals.

On the other hand, the weak binding effect may still impact the SO-splitting of the $0f$ orbitals, although much less than the $1p$ orbital. According to a calculation with the WS potential, the change in the SO-splitting from binding energy is approximately 50% less compared to that of $1p$ orbitals. However, this effect will still be clearly seen based on the usual uncertainties of approximately 100–200 keV for determining the single-particle energies from the transfer reactions. Future experiments to measure the $0f$ orbital SO splittings in Si and S under weak binding would be important to further study whether the weak binding effect or the central density depletion plays a major role.

4 SO interactions in heavy nuclei

In heavy nuclei, the SO interaction is even stronger due to the higher angular momentum and larger node number. For examples, in the nucleus of ^{132}Sn, the SO splittings of the $1f$, $2p$, and $1d$ orbits were investigated, which shows a reduction in the SO-splitting of weakly bound $1p$ orbits compared to well-bound $1d$ orbits [34]. Similarly to the $N = 19$ and $N = 21$ cases discussed before, the reduction can be explained by the extended radial wavefunctions of the weakly bound orbits rather than a weakened SO interaction strength. The work also highlights the importance of understanding the SO interaction for calculations related to neutron-capture cross-sections in the r-process. Although the weak binding effect was shown to be dominant in this case, the effect of tensor force on the single-particle energies of the odd-mass Sb isotopes can also convincingly describe the data [8, 14]. More experimental studies are still needed in the future for a systematic study to understand the microscopic origins of the SO-splitting in heavy nuclei, which will be important for the predictions for the stability of superheavy elements. For example, the SO splittings near the $2s_{1/2}$ orbital would be interesting since there is no tensor component evolved.

5 Summary

SO-splitting plays a critical role in the nuclear shell model and the stability of nuclei, particularly those with magic numbers. An overview of the recent research on SO-splittings in atomic nuclei was presented. The microscopic origins of the SO term in the nuclear Hamiltonian and the possible contribution of the tensor forces and the weak-binding effect were examined. The concept of central density depletion in "bubble" nuclei like ^{34}Si and its impact on SO-splitting is investigated, using experimental data and theoretical calculations, which shows a smooth reduction in SO-splitting and the need for considering the fragmented single-particle strengths. Overall, the importance of the weak binding effect is highlighted in explaining the existing experimental data. The present review also emphasizes the need for advanced experimental studies to further unravel the driven mechanism of the SO interactions for the understanding of nuclear structure, the synthesis of heavy elements, and the prediction of stability in superheavy regions.

Data availability statement

The datasets presented in this study can be found in online repositories. The names of the repository/repositories and accession number(s) can be found in the article/supplementary material.

Author contributions

JC: writing–original draft and writing–review and editing.

Funding

The author(s) declare that financial support was received for the research, authorship, and/or publication of this article. This work was supported by the National Natural Science Foundation of China (Grant Numbers 12475120 and 12435010).

Acknowledgments

The author would like to express deepest gratitude to all those who provided the assistance to complete this project. The author is particularly grateful for the assistance given by the author's colleagues Calem R. Hoffman and Ben P. Kay at Argonne National Laboratory, who offered invaluable suggestions for the research.

Conflict of interest

The author declares that the research was conducted in the absence of any commercial or financial relationships that could be construed as a potential conflict of interest.

The handling editor SF declared a past co-authorship with the author.

Generative AI statement

The author(s) declare that no Generative AI was used in the creation of this manuscript.

Publisher's note

References

1. Mayer MG. On closed shells in nuclei. II. *Phys Rev* (1949) 75:1969–70. doi:10.1103/PhysRev.75.1969

2. Haxel O, Jensen JHD, Suess HE. On the "magic numbers" in nuclear structure. *Phys Rev* (1949) 75:1766. doi:10.1103/PhysRev.75.1766.2

3. Tanihata I, Savajols H, Kanungo R. Recent experimental progress in nuclear halo structure studies. *Prog Part Nucl Phys* (2013) 68:215–313. doi:10.1016/j.ppnp.2012.07.001

4. Freer M, Horiuchi H, Kanada-En'yo Y, Lee D, Meißner UG. Microscopic clustering in light nuclei. *Rev Mod Phys* (2018) 90:035004. doi:10.1103/RevModPhys.90.035004

5. Sorlin O, Porquet MG. Nuclear magic numbers: new features far from stability. *Prog Part Nucl Phys* (2008) 61:602–73. doi:10.1016/j.ppnp.2008.05.001

6. Otsuka T, Gade A, Sorlin O, Suzuki T, Utsuno Y. Evolution of shell structure in exotic nuclei. *Rev Mod Phys* (2020) 92:015002. doi:10.1103/RevModPhys.92.015002

7. Ji F, Miyazawa H. Spin-orbit coupling in heavy nuclei. *Prog Theor Phys* (1957) 17:366–72. doi:10.1143/PTP.17.366

8. Otsuka T, Suzuki T, Fujimoto R, Grawe H, Akaishi Y. Evolution of nuclear shells due to the tensor force. *Phys Rev Lett* (2005) 95:232502. doi:10.1103/PhysRevLett.95.232502

9. Terasawa T. Spin-orbit splitting and tensor force. i. *Prog Theor Phys* (1960) 23:87–105. doi:10.1143/ptp.23.8723.87

10. Meng J, Ring P, Zhao P. Relativistic mean-field theory. In *Relativistic Density Functional for Nuclear Structure*. World Scientific Publishing Co. Pvt. Ltd. (2016). 21–81.

11. Mairle G. Scaling of measured nuclear spin-orbit splittings. *Phys Lett B* (1993) 304:39–44. doi:10.1016/0370-2693(93)91396-5

12. Uesaka T. Spins in exotic nuclei: ri beam experiments with polarized targets. *Eur Phys J Plus* (2016) 131:403. doi:10.1140/epjp/i2016-16403-1

13. Cottle PD, Kemper KW. Persistence of the N = 28 shell closure in neutron-rich nuclei. *Phys Rev C* (1998) 58:3761–2. doi:10.1103/PhysRevC.58.3761

14. Schiffer JP, Freeman SJ, Caggiano JA, Deibel C, Heinz A, Jiang CL, et al. Is the nuclear spin-orbit interaction changing with neutron excess? *Phys Rev Lett* (2004) 92:162501. doi:10.1103/PhysRevLett.92.162501

15. Hamamoto I, Lukyanov S, Zhang X. Kinetic energy and spin-orbit splitting in nuclei near neutron drip line. *Nucl Phys A* (2001) 683:255–65. doi:10.1016/S0375-9474(00)00443-7

16. Bohr A, Mottelson BR. *Nulear struture*. Singapore: World Sientific (1998). 218.

17. Karakatsanis K, Lalazissis GA, Ring P, Litvinova E. Spin-orbit splittings of neutron states in n = 20 isotones from covariant density functionals and their extensions. *Phys Rev C* (2017) 95:034318. doi:10.1103/PhysRevC.95.034318

18. Grasso M, Anguiano M. Neutron 2p and 1f spin-orbit splittings in 40Ca, 36S, and 34Si n = 20 isotones: tensor-induced and pure spin-orbit effects. *Phys Rev C* (2015) 92:054316. doi:10.1103/PhysRevC.92.054316

19. Mutschler A, Lemasson A, Sorlin O, Bazin D, Borcea C, Borcea R, et al. A proton density bubble in the doubly magic ^{34}Si nucleus. *Nat Phys* (2017) 13:152–6. doi:10.1038/nphys3916

20. Tsukada K, Abe Y, Enokizono A, Goke T, Hara M, Honda Y, et al. First observation of electron scattering from online-produced radioactive target. *Phys Rev Lett* (2023) 131:092502. doi:10.1103/PhysRevLett.131.092502

21. Baranger M. A definition of the single-nucleon potential. *Nucl Phys A* (1970) 149:225–40. doi:10.1016/0375-9474(70)90692-5

22. Burgunder G, Sorlin O, Nowacki F, Giron S, Hammache F, Moukaddam M, et al. Experimental study of the two-body spin-orbit force in nuclei. *Phys Rev Lett* (2014) 112:042502. doi:10.1103/PhysRevLett.112.042502

23. Kay BP, Hoffman CR, Macchiavelli AO. Effect of weak binding on the apparent spin-orbit splitting in nuclei. *Phys Rev Lett* (2017) 119:182502. doi:10.1103/PhysRevLett.119.182502

24. Sorlin O, de Oliveira Santos F, Ebran J. Reduced spin-orbit splitting in ^{35}Si: weak binding or density-depletion effect? *Phys Lett B* (2020) 809:135740. doi:10.1016/j.physletb.2020.135740

25. Mackh H, Mairle G, Wagner GJ. Proton shell structure of mass 28–32 nuclei *Z Physik* (1974) 269:353–364. doi:10.1007/BF01668607

26. Piskoř S, Franc P, Křemének J, Schäferlingová W. Spectroscopic information on ^{35}S and ^{37}S from the (d, p) reaction. *Nucl Phys A* (1984) 414:219–39. doi:10.1016/0375-9474(84)90641-9

27. Mermaz MC, Whitten CA, Champlin JW, Howard AJ, Bromley DA. Study of the (d, p) reaction on ^{28}Si, ^{32}S, and ^{36}Ar at E_d = 18.00 mev. *Phys Rev C* (1971) 4:1778–800. doi:10.1103/PhysRevC.4.1778

28. Van Der Baan J, Leighton H. Investigation of the ^{34}S(d, p)^{35}S reaction at ed = 10 mev. *Nucl Phys A* (1971) 170:607–15. doi:10.1016/0375-9474(71)90240-5

29. Sen S, Hollas CL, Riley PJ. Reaction ^{36}Ar(d, p)^{37}Ar. *Phys Rev C* (1971) 3:2314–22. doi:10.1103/PhysRevC.3.2314

30. Chen J, Kay B, Hoffman C, Tang T, Tolstukhin I, Bazin D, et al. Evolution of the nuclear spin-orbit splitting explored via the ^{32}Si(d, p)^{33}Si reaction using solaris. *Phys Lett B* 853 (2024) 138678. doi:10.1016/j.physletb.2024.138678

31. Lalazissis GA, Nikšić T, Vretenar D, Ring P. New relativistic mean-field interaction with density-dependent meson-nucleon couplings. *Phys Rev C* (2005) 71:024312. doi:10.1103/PhysRevC.71.024312

32. Heery J, Henderson J, Hoffman CR, Hill AM, Beck T, Cousins C, et al. Suppressed electric quadrupole collectivity in ^{32}Si. *Phys Rev C* (2024) 109:014327. doi:10.1103/PhysRevC.109.014327

33. Bradt J, Bazin D, Abu-Nimeh F, Ahn T, Ayyad Y, Beceiro-Novo S, et al. Commissioning of the active-target time projection chamber. *Nucl Instr Methods Phys Res Section A: Acc Spectrometers, Detectors Associated Equipment* (2017) 875:65–79. doi:10.1016/j.nima.2017.09.013

34. Orlandi R, Pain S, Ahn S, Jungclaus A, Schmitt K, Bardayan D, et al. Neutron-hole states in ^{131}Sn and spin-orbit splitting in neutron-rich nuclei. *Phys Lett B* (2018) 785:615–20. doi:10.1016/j.physletb.2018.08.005

frontiers | Frontiers in Physics

TYPE Original Research
PUBLISHED 19 March 2025
DOI 10.3389/fphy.2025.1530428

OPEN ACCESS

EDITED BY
Sean Freeman,
European Organization for Nuclear Research (CERN), Switzerland

REVIEWED BY
Grigory Nigmatkulov,
University of Illinois Chicago, United States
Daniel Bazin,
Michigan State University, United States

*CORRESPONDENCE
Augusto O. Macchiavelli,
✉ macchiavelao@ornl.gov

RECEIVED 18 November 2024
ACCEPTED 20 January 2025
PUBLISHED 19 March 2025

CITATION
Macchiavelli AO, Paschalis S and Petri M (2025) Some aspects of the quenching of single-particle strength in atomic nuclei. *Front. Phys.* 13:1530428.
doi: 10.3389/fphy.2025.1530428

Some aspects of the quenching of single-particle strength in atomic nuclei

Augusto O. Macchiavelli[1]*, Stefanos Paschalis[2] and Marina Petri[2]

[1]Physics Division, Oak Ridge National Laboratory, Oak Ridge, TN, United States, [2]School of Physics, Engineering and Technology, University of York, York, United Kingdom

In this article, we discuss some aspects of the quenching of the single-particle strength with emphasis on the isospin dependence of long- and short-range correlations. A phenomenological analysis that connects recent Jefferson Laboratory studies with data on spectroscopic factors, is contrasted with the results of the Dispersive Optical Model approach. We consider some consequences of the model on the nature of the dressed nucleons in the nuclear medium, their effective masses, as well as other aspects of nuclear structure such as charge radii, effective charges, and spin-spin correlations. Qualitative estimates indicate that short-range correlations must play a significant role on those aspects. Despite the fact that our conclusions are perhaps speculative at this stage, we trust that the results will stimulate further experimental and theoretical work, specifically on exotic nuclei far from stability.

KEYWORDS

single-particle strength, long- and short-range correlations, nuclear reactions, isospin dependence, effective mass, neutron matter, charge radii and effective charges, spin-spin correlations

1 Introduction

The year 2024 marks the 75^{th} anniversary of the publication of the seminal papers by Maria Goeppert-Mayer and Hans Jensen on the nuclear shell model [1, 2]; their work together with the collective model [3] established the pillars of our understanding of nuclear structure. Despite the fact that atomic nuclei consist of strongly interacting nucleons forming a dense quantum system, the notion of independent particle motion in a mean-field has been highly successful and has provided the framework to explain many nuclear properties, notably the so-called magic numbers. However, as Goeppert-Mayer remarked in her Nobel Lecture [4] *"The assumption of the occurrence of clear individual orbits of neutrons and protons in the nucleus is open to grave doubts"*, and went on to say *"It still remains surprising that the model works so well"*[1].

An appealing argument has been given by Mottelson [6] based on the quantality parameter:

$$\Lambda = \frac{\hbar^2/Ma^2}{V_0},$$

---

[1] The validity of the shell model is discussed in detail in Ref. [5].

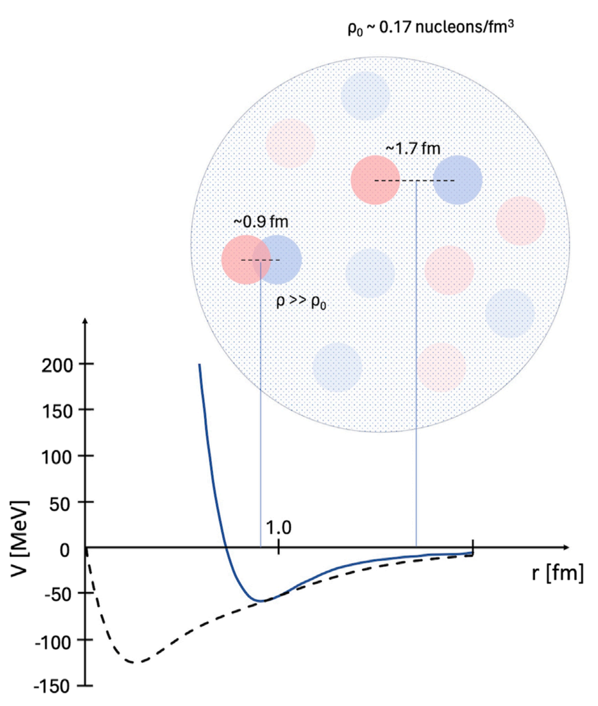

FIGURE 1
Central (solid line) and tensor (dashed line) AV18 potentials for the $S = 1, T = 0$ channel [8] and a schematic representation of a nucleus showing the average nucleon-nucleon separation and that in a short-range correlated pair.

with *a* the inter-constituents distance, which measures the ratio of the zero point motion kinetic energy to the strength of the interaction (V_0). With the typical values shown in Figure 1, the quantality parameter for nuclei is of order $\Lambda \approx 0.4$, similar to those in ^{3}He and ^{4}He which are liquids at zero temperature (for comparison, values for solids are $\Lambda < 0.07$). Thus, nuclei should behave like a quantum Fermi liquid [7], with *quasi-particles* taking the role of the particles in the Independent Particle Model (IPM).

Considering the nucleus in the simplest approximation of a non-interacting Fermi gas, the occupation probability distribution of orbitals n_j with momentum p is a step function, i.e., $n_j = 1$ for $p \leq p_F$ and $n_j = 0$ for $p > p_F$, with p_F the Fermi momentum. In a Fermi liquid, where correlations between nucleons are considered, the mean-field approximation gets modified, diluting the pure independent-particle picture due to excitations across p_F, as illustrated in Figure 2. To some extent, the effects of the correlations could be embedded in the concept of a *quasi-particle (qp)*, with energy:

$$e(qp) \approx \frac{(p^2 - p_F^2)}{2m} + V(p) \approx v_F(p - p_F)$$

from which it follows that the *qp* acquires an effective mass:

$$m^* = \frac{p_F}{v_F} = \frac{m}{1 + m\partial^2 V/\partial p^2}$$

Due to the Pauli principle the phase-space for scattering, which goes as $(p - p_F)^2$, is drastically reduced giving the quasi-particle a lifetime much longer than the characteristic orbit transit time $\Delta t \sim 1/\omega_0$, with ω_0 a typical harmonic oscillator frequency. Thus, the conclusion that emerges is that the independent particles of the shell or collective models should be interpreted as *"dressed"* nucleons.

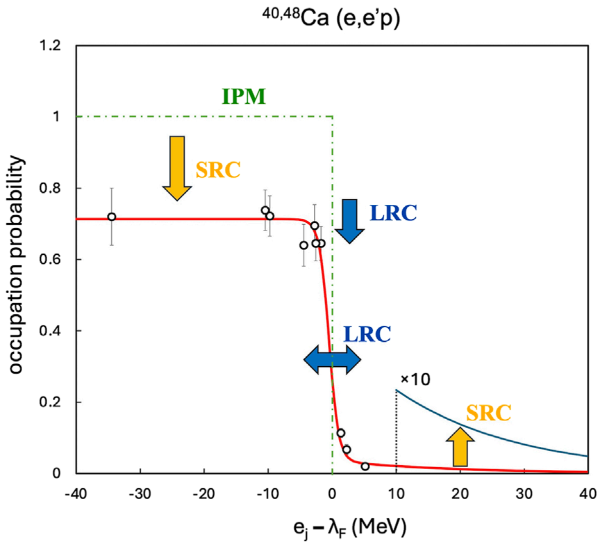

FIGURE 2
Occupation probabilities in ^{40,48}Ca as determined by $(e,e'p)$ reactions data. Deviations from the IPM (dashed green) due to LRC (blue) and SRC (yellow) are indicated by the arrows (see text).

Crucial evidence for the departure from the IPM comes from high-energy electron scattering showing that the nuclear ground-state wavefunction must have a marked admixture of high-momentum components. The high-momentum tail, typically parameterized as $exp(-p^2/p_0^2)$ with $\frac{p_0^2}{2m} \approx 19$ MeV [9, 10], can be understood as the result of nucleon-nucleon (*NN*) short-range correlations (SRC) introduced by the strong nuclear force, and corresponds to single-particle excitations, $\Delta E \sim \Delta p^2/2m \gtrsim 60$ MeV. In reference to the geometrical picture depicted in Figure 1, a nucleon finds itself within a relative distance of 1 fm about 20% $\left(\approx (1/1.7)^3\right)$ of the time. Furthermore, the strong attraction due to the tensor force in the spin - triplet $^3S_1$ channel [11] suggests that at short distances, nucleon pairs are correlated in the same way as they are in the deuteron or in free scattering processes [10].

In the following, we discuss the implications of the concepts above to some aspects of the structure of atomic nuclei with an emphasis on the evolution with isospin (neutron-proton asymmetry).

2 Quenching of spectroscopic factors

Direct reactions continue to play a major role in our understanding of the nuclear elementary modes of excitation, particularly in the characterization of the single-particle degrees of freedom and their correlations. A reaction is called direct if it proceeds directly from the initial to the final state without the formation of an intermediate compound state and, to a good approximation, the cross section can be factorized into a nuclear-structure term and a reaction term corresponding to that of a single-particle state. Thus, these reactions have been used to test models of nuclear structure by comparing spectroscopic overlaps between initial and final nuclear states. The spectroscopic overlaps are represented by spectroscopic factors, derived from the experimentally measured cross section divided by the calculated one for a single-particle state with the same energy and quantum numbers (effectively reduced cross sections).

In more detail we have for the case of a particle-adding reaction:

$$d\sigma^{(+)}\left(j, I_i \to I_f\right) = \frac{1}{2j+1}\frac{2I_f+1}{2I_i+1}\mathscr{S}_{if}^{(+)} d\sigma_{sp}^{(+)}(j)$$

where

$$\mathscr{S}_{if}^{(+)} = \frac{1}{2I_f+1}\langle I_f \| a^{\dagger}(j) \| I_i\rangle^2$$

is the spectroscopic factor giving the structure information and $d\sigma_{sp}^{(+)}(j)$ a single-particle reaction cross section, with similar expressions for particle-removing reactions. Depending on the type of reaction being studied, the single-particle cross section can be calculated in different approximations, for example: distorted-wave Born approximation (DWBA), distorted-wave impulse approximation (DWIA), Eikonal approximation, *etc.* (see Refs. [12–17] and references therein).

Using the commutation rules and tensor properties of the creation and annihilation operators $a^{\dagger}(jm)$ and $a(jm)$ one can obtain the Macfarlane-French sum rules [18]:

$$\sum_{I_f}\frac{2I_f+1}{2I_i+1}\mathscr{S}_{if}^{(+)} = 2j+1-n(j) = \text{Number of vacancies}$$

$$\sum_{I_f}\mathscr{S}_{if}^{(-)} = n(j) = \text{Number of particles}$$

An important consequence of the equations above is that in cases where both addition and removal reactions could me measured, such as (d,p) and (p,d), there is a total sum rule that measures the orbit degeneracy, independent of the details of how the particles and vacancies are distributed:

$$\sum_{I_f}\frac{2I_f+1}{2I_i+1}\mathscr{S}_{if}^{(+)} + \sum_{I_f}\mathscr{S}_{if}^{-} = 2j+1 \tag{1}$$

In addition to the high-momentum tails observed in high-energy electron scattering, the depletion of the single-proton strength as observed in $(e,e'p)$ reactions in the quasi-free scattering regime [19, 20] is perhaps one of the best indicators for the departure from a mean-field approximation to the structure of nuclei. Experimental data for 16 stable targets point to a quenching of proton spectroscopic factors of 0.55 (0.07 rms) with respect to the IPM expectations[2] expressed as:

$$R = \frac{\mathscr{S}_{if}^{(-)}}{n(j)} \approx 0.6 \tag{2}$$

Recently, there has been some debate regarding the meaning of spectroscopic factors, as these are not true observables [23, 24]. To address this question, Schiffer and collaborators [25] studied neutron-adding, neutron-removal, and proton-adding transfer reactions on the stable even Ni isotopes, with particular attention to the cross-section determinations. Spectroscopic factors derived from a consistent analysis of the data, in terms of the DWBA, were used to extract valence-orbit occupancies (vacancies) following from the sum rules discussed above. The deduced occupancies are consistent at the level of 5% indicating that, in the absence of a full *ab initio* calculation of structure and reaction cross sections, spectroscopic factors provide an empirically meaningful quantity to compare with theory. The use of shape deformation parameters, ϵ_{λ}, in the interpretation of collective nuclei comes to mind as a similar case.

Following on that work, the Argonne group carried out an extensive survey and self-consistent analysis of single-nucleon transfer reactions [26]. Summed spectroscopic strengths (Equation 1) were used to determine the factor (Equation 2) by which the observed cross sections, corrected for the reaction mechanism, differ from expectations. Across the 124 cases they analyzed, including various proton- and neutron-transfer reactions and with angular momentum transfer $\ell = 0$–7, spectroscopic factors are quenched with respect to the values expected from mean-field theory by a constant factor of 0.55, with an rms spread of 0.10, and consistent with that determined in $(e,e'p)$. The factor appears to be independent of whether the reaction is nucleon adding or removing, whether a neutron or proton is transferred, the mass of the nucleus, the reaction type, and angular-momentum transfer. This provides compelling evidence for a uniform quenching of single-particle motion in the nuclear medium.

The topic continues to be of much interest in the field [17] and open questions remain in regard to the evolution of *NN* correlations in nuclei with large neutron-proton asymmetry which are becoming accessible by radioactive beam studies of transfer, knockout, and quasi-free scattering (QFS) reactions. In these exotic systems, the effects of weak binding and coupling to the continuum might also play an important role.

An intriguing (rather controversial) result receiving attention is the (apparent) quenching observed in one-proton (and one-neutron) removal reactions carried out at intermediate energies around 100 MeV/nucleon. The study of Refs. [27, 28] showed an unexpected dependence of the quenching, as a function of the difference (ΔS) in proton and neutron separation energies, $S_p - S_n$ ($S_n - S_p$), of the initial system, at odds with the results obtained in transfer and QFS $(p,2p)$ reactions [17]. Whether the origin of this dependence is due to the effect of correlations or deficiencies in the reaction model is still a matter of debate.

2.1 Long-range and short-range correlations

The in-medium effects are captured by the concept of a *quasi-particle*. At any given moment, only 60% – 70% of the states below the Fermi momentum are occupied, with 30% – 40% of the nucleons participating in more complex configurations [19, 20, 26, 29–34].

---

[2] At this point it is important to note that the quenching extracted from $(e,e'p)$ measurements may depend on the momentum transfer, Q^2 [21, 22]. Although the Q^2 dependence of the quenching needs to be better understood, here we analyze the (well established) low-Q^2 data, where the scale resolution should be sensitive to probe the quenching due to both SRC and LRC [21].

The *NN* correlations that modify the mean-field approximation picture are often distinguished into long-range correlations (LRC) and short-range correlations (SRC), referring to their spatial separation and the part of the *NN* potential they are most sensitive to [30, 35, 36]. Therefore, both LRC and SRC deplete the occupancy of single-particle states, with LRC primarily mixing states near the nuclear Fermi momentum and SRC populating states well above it. It is important to note that within the context of this work, LRC are defined as (surface) pairing (PC) and particle-vibration coupling (PVC). While generally in low-energy nuclear structure one refers to pairing correlations as the short-range part of the force, as compared to the quadrupole force which is of longer range, here pairing is not considered part of the SRC associated with high-momentum components.

In Figure 2, we summarize the situation with the cases of ^{40,48}Ca that have been extensively studied. On one hand the sharp cutoff at the Fermi surface, expected for a non-interacting system, is seen to be broaden by the effect of the LRC admixing n-particle–n-hole configurations, typically of order ± the pairing gap, Δ, around λ_F. On the other hand, SRCs (tensor force) are thought to induce the high-momentum tail via the formation of correlated high-momentum isospin $T = 0$, spin $S = 1$ neutron-proton (*np*) pairs, a *quasi-deuteron*. In fact, results from Jefferson Lab (JLab) presented in Ref. [37] indicate that ≈90% of the nucleons with high-momentum are correlated in those *np* configurations.

2.2 Isospin dependence

The isospin dependence of LRC and SRC, and their competition in very asymmetric nuclei is a question that requires further studies. By explicitly incorporating the observed [38] increase of the high-momentum component of the protons in neutron-rich nuclei, we recently proposed a phenomenological approach to examine the role of both SRC and LRC in the quenching of the single-particle strength (SP) in atomic nuclei, specifically their evolution in asymmetric nuclei and neutron matter [39]. In our approach, we start by proposing that the wave-function of the *quasi-particle*, representing a *dressed* nucleon in the nuclear medium can be written in the linear form:

$$|qp\rangle = K_{SP}|SP\rangle + K_{LRC}|LRC\rangle + K_{SRC}|SRC\rangle. \tag{3}$$

This conjecture and the lack of interference terms stem from the underlying assumption that the SP, LRC, and SRC states are all orthogonal to each other. This is supported by the fact that SRC induce mixing to states of very high momentum and energy in the nuclear spectral function and there should be a small overlap with the SP and LRC components [29, 40, 41]. In near doubly magic nuclei, for which both pairing and deformation manifest themselves as vibrations, the individual terms in Equation 3 can be justified in first order perturbation as one-particle–one-hole (1p1h) (PVC) and two-particle–two-hole (2p2h) (PC) excitations. From the general arguments given in Ref. [39], we adopted the following expressions for the isospin dependence of PVC and PC:

$$K^2_{\mathrm{PVC}} = \alpha\left(1 + \frac{33}{51}\frac{N-Z}{A}\right)^2,$$

$$K^2_{PC} = \beta\left(1 - 6.07\left(\frac{N-Z}{A}\right)^2\right)^2.$$

The findings in Ref. [38] from JLab exclusive $(e, e'p)$ measurements of the correlated proton and neutron momenta, readily suggest the phenomenological expressions,

$$K^2_{SRC,minority} = \gamma\left(1 + SL^{minority}_{\mathrm{SRC}}|N-Z|/A\right), \tag{4}$$

$$K^2_{SRC,majority} = \gamma\left(1 - SL^{majority}_{\mathrm{SRC}}|N-Z|/A\right), \tag{5}$$

with the slope parameters $SL^{minority}_{\mathrm{SRC}} = 2.8 \pm 0.7$ and $SL^{majority}_{\mathrm{SRC}} = 0.3 \pm 0.2$ giving the isospin-dependence of the SRC contribution. Majority and minority define the protons, neutrons in asymmetric systems; protons are the majority at $(N-Z)/A < 0$ and neutrons are the majority at $(N-Z)/A > 0$. The results of our fit of the experimental data on doubly magic nuclei give: $\alpha = 10\% \pm 2\%$, $\beta = 3\%$[3], and $\gamma = 22\% \pm 8\%$. The different contributions are shown in Figure 3. The quenched single-particle strength, R (Equation 2), is expressed in terms of the independent components as

$$R = 1 - \left(K^2_{SRC} + K^2_{\mathrm{PVC}} + K^2_{PC}\right). \tag{6}$$

We end this section by comparing our predictions with the results of Refs. [27, 28]. For this purpose, we use the equations given in Ref. [42] to convert A, Z and N into $S_p - S_n$. The two trends are shown as shaded areas in Figure 4. As seen, our results give a less pronounced dependence on ΔS (in excellent agreement with, e.g., [43–46]); although not conclusive, it may point to a deficiency in the nucleon knockout reaction model rather than structure effects.

2.3 Comparison with the dispersive optical model

Dickhoff and collaborators have led extensive studies on the application of the dispersive-optical-model (DOM) to describe simultaneously a wealth of structure and reaction experimental data (see Ref. [47] for a review). Of particular relevance here is their study of the neutron-proton asymmetry dependence of correlations in nuclei [48]. In that work, elastic-scattering measurements, total and reaction cross-section measurements, $(e, e'p)$ data, and single-particle energies for magic and doubly-magic nuclei were analyzed within the DOM framework to generate optical-model potentials that can be related to spectroscopic factors and occupation probabilities. Their results show that,

---

[3] The value of $\beta = 3\%$ has been estimated based on lowest order pairing vibrations that introduce 2p2h admixtures in the unperturbed (0p0h) ground-state configurations and has not been fitted to experimental data, hence there is no uncertainty associated with it.

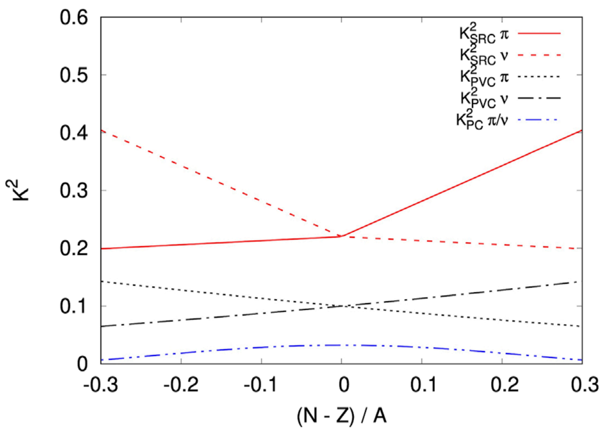

FIGURE 3
Square amplitude (K^2) for each correlation term (SRC, PVC, PC) as a function of neutron–proton asymmetry, derived from [38, 39].

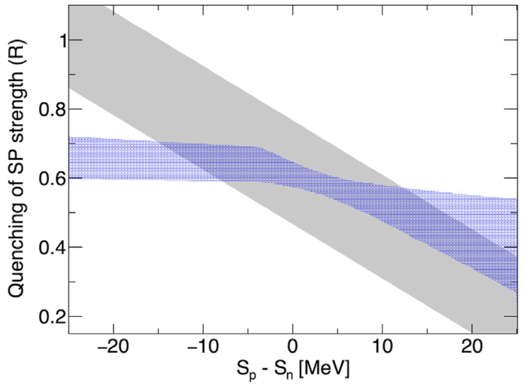

FIGURE 4
Quenching of proton single-particle strength (R) measured in nucleon-removal reactions (gray-shaded area) [27, 28] as a function of the difference in separation energies. Our predictions are shown with the blue-shaded (patterned) area (within 2σ).

for stable nuclei with $N \geq Z$, the imaginary surface potential for protons exhibits a strong dependence on the neutron-proton asymmetry, leading to a modest dependence of the spectroscopic factors on asymmetry. The appealing aspect of the DOM approach is that both LRC and SRC are described by surface and volume imaginary potentials, respectively. It is of interest to compare the predicted DOM results for the $g_{9/2}$ proton spectroscopic factors in stable Sn isotopes with our calculations. This is done in Figure 5, showing remarkable agreement between the two predictions, which adds additional support to our phenomenological model. Furthermore, in the DOM analysis of all considered nuclei, the neutron imaginary potential displays very little dependence on the neutron-proton asymmetry, also in line with our findings for $N \geq Z$ nuclei (Figure 3).

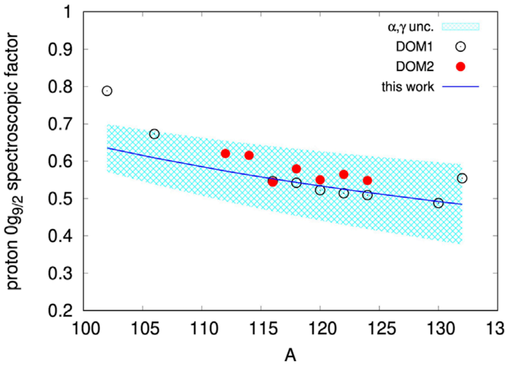

FIGURE 5
Comparison of dispersive-optical-model calculations [48] of the proton $0g_{9/2}$ spectroscopic factors (relative to IPM values) for Sn isotopes–obtained with fits where the depth of the Hartree-Fock potential was adjusted to reproduce the Fermi energy (DOM2) and where the depth was adjusted to reduce the correct $0g_{9/2}$ level energy (DOM1) – to our predictions. The shaded area reflects the uncertainty in our predictions originating from the uncertainties in the SRC ($\delta\gamma = 8\%$) and PVC ($\delta\alpha = 2\%$) contributions. Pairing correlations have been fixed at $\beta = 3\%$.

3 The nature of the dressed nucleons

As discussed earlier, the arguments put forward by Brueckner [10] suggest that in the presence of SRC components in the *NN* interaction, a "bare" nucleon becomes "dressed" in a virtual *quasi-deuteron* cloud about 20% of the time, as measured by the coefficient γ of Equations 4, 5. The implications of SRC and the *quasi-deuteron* concept have been discussed and elaborated in many works, e.g. [49–54], which we are not in a position to discuss here. Rather, we focus on the qualitative (phenomenological) approach to discuss the potential impact of the *qp* nature, induced by SRC, in low-energy observables for which, *a priori*, the properties of the finite system are quite essential.

In terms of the underlying independent single-particle shell structure, we could qualitatively interpret the effect as follows: a high-momentum proton (neutron) scatters from a neutron (proton) in a j–orbit forming a *quasi-deuteron* in a higher j' level while leaving behind a hole (j^{-1}) below the Fermi level. In more detail,

$$|\tilde{j_\pi}\rangle \approx \mathcal{A}_j|j_\pi\rangle + n_{j_\nu}\sum_{j'}^{n_{j'}} b_{jj'}|j_\nu^{-1}\rangle \otimes |j'_\pi j'_\nu\rangle^{1^+}.$$

If we further assume that $b_{jj'} = b_j$, then we can rewrite the equation above as:

$$|\tilde{j_\pi}\rangle \approx \mathcal{A}_j|j_\pi\rangle + \mathcal{B}_j|j_\nu^{-1}\rangle \otimes \left(\frac{\sum_{j'}^{n_{j'}}|j'_\pi j'_\nu\rangle^{1^+}}{n_{j'}}\right). \qquad (7)$$

with $\mathcal{B}_j = b_j n_{j_\nu} n_{j'}$, and where the last term in parenthesis can be interpreted as an effective *qd*. The high-momentum components of the nucleon wavefunction requiring single-particle excitations of the order of $\gtrsim 60$MeV will correspond to a *quasi-deuteron* generated from harmonic oscillator j' orbitals associated with changes in the principal oscillator quantum number, $\Delta N \sim \Delta E/\hbar\omega_0$. In reference to Figure 1, a typical shell model mixing matrix element in the triplet-even channel, using harmonic oscillator wavefunctions, can be estimated [55]:

$$\langle V_{\;^3S_1} \rangle \approx 10\,\mathrm{MeV}/A^{2/3},$$

giving a mixing amplitude in Equation 7 of

$$b_j \sim \langle V_{\;^3S_1} \rangle / (2\Delta E) = \frac{10/A^{2/3}}{120}.$$

Assuming a single-j valence shell, we approximate $n_{j_v} \sim 2j+1 \approx 2A^{1/3}$. The number of orbits $n_{j'}$ available to scatter the qd is of order:

$$n_{j'} \approx N_{valence} + \Delta N \approx A^{1/3} + \frac{\Delta E}{\hbar\omega_0} \approx A^{1/3}(1 + 60/41) \approx 2.5A^{1/3},$$

leading finally to $\mathcal{B}_j \approx 0.42$, in line with the SRC strength amplitude empirically determined from Equations 4, 5, i.e., $\sqrt{\gamma} = 0.47$ [39].

4 Effective mass

The concept of nucleon effective mass, m^*, was originally developed by Brueckner [9] to describe the motion of nucleons in a momentum-dependent potential with the motion of a quasi-nucleon of mass m^* in a momentum-independent potential. The momentum dependence of the neutron and proton mean field is reflected in the nucleon effective masses, with varying theoretical predictions depending on the approach and interaction used, see, e.g., [56]. What is particularly important is the so-called effective mass splitting, i.e., $m_n^* - m_p^*$, in asymmetric nuclear matter. This impacts the equilibrium neutron/proton ratio in primordial nucleosynthesis, properties of neutron stars and mirror nuclei, and the location of the neutron and proton drip-lines, to name a few[4]. Although the nature of the splitting has been largely resolved in neutron-rich asymmetric nuclear matter, with the neutron effective mass being larger than that of the proton, the magnitude of the splitting remains an open question. The latter is determined by the momentum dependence of the isovector part of the single-nucleon potential, while the effective mass of symmetric nuclear matter also plays a role. Thus, probing the nucleon effective mass from a different perspective can give us insights into the momentum dependence of the nuclear mean field and can address the question of the proton-neutron effective mass splitting.

Bertsch and Kuo [29] have connected the effective mass to the depletion of the single-particle strength. By evaluating the contributions to the single-particle energy in second-order perturbation theory, they obtained the relation:

$$\frac{m}{m^*} - 1 \approx 2\frac{\Sigma V^2}{E_x^2},$$

approximately equal to the depletion of the single-particle strength of the state. By relating to Equations 2, 6, we can rewrite the expression above in terms of R:

$$\frac{m^*}{m} \approx \frac{1}{2-R},$$

from which we predict the neutron and proton effective masses as a function of $(N-Z)/A$, shown in Figure 6.

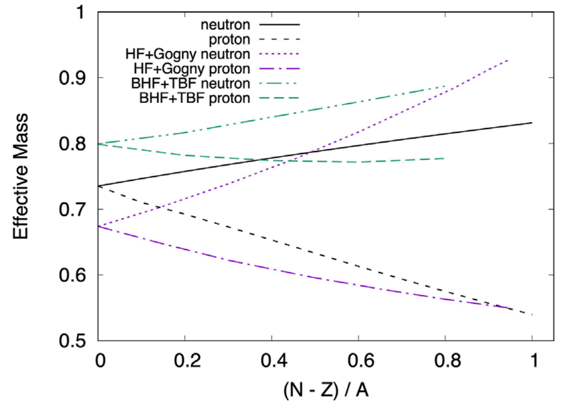

FIGURE 6
Effective mass for protons and neutrons following Ref. [29] and the quenching factor calculated in Ref. [39] (assuming 22% SRC component), and how this compares with calculations using the Hartree-Fock approach and a modified Gogny effective interaction (HF + Gogny) from [59], and calculations using the Brueckner-Hartree-Fock approach with Argonne V18 two-body interaction and a microscopic three-body force (BHF + TBF) from [60].

Our results are compared with the values obtained in Ref. [58] from a single-nucleon potential derived within the Hartree-Fock approach using a modified Gogny effective interaction (MDI) [59]. We also compare with the nuclear matter predictions on the effective mass (at nuclear saturation density) in a Brueckner-Hartree-Fock (BHF) nuclear many-body approach [60]. In this model, which gives satisfactory nuclear matter bulk properties, the nucleon force includes a two-body component from the Argonne V18 potential and a three-body term constructed from the meson-exchange-current approach. As seen, both predictions give different nucleon effective masses, reflecting their dependence on the interaction used. It is interesting to note that in order to reproduce the nuclear matter predictions, we would need a SRC component of 11% in the reduction of the single-particle strength, in contrast to the established value of ≈20%.

As discussed in [39] we can also speculate about the nature of a *quasi-proton* (nuclear polaron [61]) in neutron matter (nM). For infinite matter at saturation density we can neglect surface and pairing coupling terms, both expected to be small, and take the limit of $A \to \infty$ and $(N-Z)/A \to 1$. We predict a proton quenching factor of $R_{nM}^p = 1 - \gamma(1 - SL_{SRC}^p) \sim 0.16$ and an effective mass, $m_p^*(nM) \approx 0.54$, in good agreement with the nuclear matter calculations of Refs. [57, 58].

In the following, we turn our attention to finite nuclei and the implications of the phenomenological model to aspects of nuclear structure such as charge radii, effective charges, and spin-spin correlations.

5 Charge radii

The nuclear charge radius is a measure of the distribution of protons in the nucleus and it constitutes one of the fundamental

---

[4] For an overview on effective masses we point to the review of Bao-An Li and collaborators [57] and references therein.

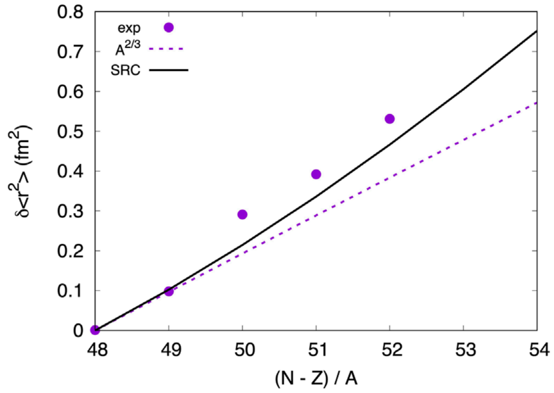

FIGURE 7
Change in the nuclear mean-square charge radii, $\delta\langle r^2\rangle$, of neutron-rich Ca isotopes with respect to ^{48}Ca [62] and how this compares with the expected increase following the size of the nucleus ($A^{2/3}$). This discrepancy could be qualitatively compensated with the inclusion of SRCs as explained in the text.

nuclear properties that, together with masses, can challenge nuclear models. A laser spectroscopy measurement [62] reported anomalously large charge radii in ^{50,52}Ca relative to ^{48}Ca, beyond what state-of-the-art *ab initio* calculations could reproduce. This result could indicate the occurrence of proton excitations (core-breaking) across the $Z = 20$ gap in the neutron-rich Ca isotopes, challenging the doubly-magic nature of ^{52}Ca with implications beyond the scope of this article. A recent study employing quasi-free one-neutron knockout from ^{52}Ca [63] showed that the rms radius of the neutron $p_{3/2}$ orbital is significantly larger than that of the $f_{7/2}$ orbital, suggesting that the large charge radii in the Ca isotopes could be attributed to the extended spatial distribution of p neutron orbitals. Another interpretation, however, was discussed by Miller and collaborators [64], who suggested that the increase in the charge radii could be attributed to SRC with the deficiency of *ab initio* calculations reproducing this anomaly coming from the use of soft potentials that do not capture the effects of SRC in charge radii; indeed, in neutron-rich nuclei we anticipate protons spending more time in the high-momentum part of the nucleon momentum density distribution, impacting the distribution of charges and hence the charge radii.

A simple estimate of the effect due to SRC follows from the consideration that protons in the *quasi-deuteron* configuration are associated with orbits with higher principal oscillator numbers that induce a change in the proton radius

$$\delta\langle r^2\rangle \approx \gamma r_0^2 \Delta N\left(1 + SL^{p}_{SRC}|N-Z|/A\right),$$

where $\Delta N \sim \Delta E/\hbar\omega_0$ and with an isospin dependence that resembles the experimental trend, as shown in Figure 7. Indeed, SRCs can induce an increase in the nuclear mean-square charge radius, $\delta\langle r^2\rangle$, beyond what is expected following the size of the nucleus ($A^{2/3}$). This result demonstrates the impact that SRCs can have on properties like charge radii and highlights the importance of including them in the theoretical description of atomic nuclei.

6 Effective charges

It is interesting to comment that the same mechanism will contribute to the nucleons' effective charges. In the shell model, core polarization effects result in $e^{\pi}_{eff} \sim 1 + \delta e$ and $e^{\nu}_{eff} \sim \delta e$, with a typical value of $\delta e \sim 0.5$ [65]. Specific values for different mass regions are usually fitted to reproduce quadrupole electromagnetic properties. A contribution from SRC can be estimated along the same line as above:

$$\delta e_{SRC} \approx \gamma \frac{\Delta N}{A^{2/3}}\left(1 + SL^{p}_{SRC}|N-Z|/A\right),$$

giving a value of the order of 0.1 near ^{40}Ca. This contribution should be present even in the absence of any core-polarization effect.

7 Ground-state spin-spin correlations

This section explores the possible effect of SRCs to the ground-state spin-spin correlations in order to provide a plausible explanation for the reported discrepancy between experimental and shel-model results.

Within the context of understanding the role played by isoscalar pairing in the ground states of $N \approx Z$ nuclei [66], the Osaka group has led a series of studies [67, 68] to probe neutron–proton spin–spin correlations in the ground states of $N = Z$ nuclei in the *sd* shell. The relevant observable is the scalar product between the total spins of the neutrons and protons, $\langle \vec{S}_{\mathrm{n}} \cdot \vec{S}_{\mathrm{p}}\rangle$, which can be measured by spin $M1$ excitations produced by inelastic hadronic scattering at medium energies.

The $M1$ operator consists of spin and orbital angular-momentum terms which can be of isoscalar (IS: $\Delta T = 0$) and isovector (IV: $\Delta T = 1$) nature. The IS and IV spin-$M1$ reduced nuclear matrix elements (ME) for transitions from the ground state $|gs\rangle$ of an even-even nucleus to an excited state $|f\rangle$ are defined by

$$M_f(\vec{\sigma}) = \langle f\| \sum_{k=1}^{A} \vec{\sigma}_k \|gs\rangle \text{ and } M_f(\vec{\sigma}\tau_z) = \langle f\| \sum_{k=1}^{A} \vec{\sigma}_k \tau_{z,k} \|gs\rangle.$$

These can be determined by measuring the (p, p') differential cross-section at 0°, which is proportional to the squared matrix elements above. The conversion from cross sections to absolute ME is done through a unit cross section and a kinematic factor, similar to the case of Gamow-Teller (GT) transitions [69]. Once the ME are determined,

$$\langle \vec{S}_n \cdot \vec{S}_p\rangle \approx \Delta_{spin}(E_x) = \frac{1}{16}\sum_{E_f<E_x}\left(|M_f(\vec{\sigma})|^2 - |M_f(\vec{\sigma}\tau_z)|^2\right),$$

where the sums are typically up to $E_x \approx 16$ MeV. Since the values in the two-particle system are distinctively different:

$$\langle \vec{s}_{\mathrm{n}} \cdot \vec{s}_{\mathrm{p}}\rangle = \begin{cases} +1/4, & \text{for IS np pair (deuteron)} \\ -3/4, & \text{for IV np pair} \end{cases}$$

$\langle \vec{S}_{\mathrm{n}} \cdot \vec{S}_{\mathrm{p}}\rangle$ will also depend strongly on the type of pairs being scattered across the Fermi surface.

In the experiments carried out at the RCNP facility in Osaka, high energy-resolution proton inelastic scattering at $E_{\mathrm{p}} =$ 295 MeV was studied in ^{24}Mg, ^{28}Si, ^{32}S and ^{36}Ar [67]. The

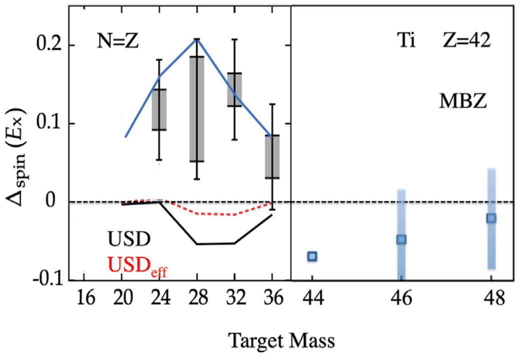

FIGURE 8
Left panel: Spin-spin correlations for $N = Z$ nuclei and shell model results with the USD (black line) and a modified USD$_{eff}$ (red dashed line) interactions. The blue line gives an upper limit estimate of the correction due to SRC, given in Equation 8. Right panel: Predicted shell-model results with the MBZ interaction for ^{46,48}Ti with an estimate of the experimental uncertainty anticipated for the iThemba measurement. Figure adapted from [67].

results in Figure 8, show positive values of $\langle \vec{S}_n \cdot \vec{S}_p \rangle$ for the *sd* shell suggesting a predominance of *quasi-deuterons*, at variance with USD shell-model calculations that are unable to reproduce the experimental results.

In Ref. [70] a formalism was developed to calculate the matrix elements of the $\vec{S}_n \cdot \vec{S}_p$ operator in a variety of coupling schemes and apply it to the solution of a schematic model consisting of nucleons in a single-l shell. The study showed that for all possible parameter values in the model Hamiltonian the expectation value $\langle \vec{S}_n \cdot \vec{S}_p \rangle$ is found to be ≤ 0 in the ground state of all even–even $N = Z$ nuclei, and the spin–orbit term in the nuclear mean field leads to more negative values.

What could be the reason for the positive values? Is it possible that we are observing the effects of the deuteron cloud dressing the nucleons related to the SRC quenching of spectroscopic factors? In fact, we can estimate a correction to the USD results based on the value of γ discussed earlier. Taking either ^{16}O or ^{40}Ca as the closest spin saturated cores for the *sd*-shell, the number of valence *quasi-deuterons* present in the paired ground states could contribute up to a positive value of $\approx \frac{1}{4}$ to the USD values,

$$\delta\Delta_{spin}(E_x) \lesssim \gamma(1-\gamma)\frac{1}{4}N_{sd}^{qd}, \tag{8}$$

bringing the estimates closer to the experimental measurements as shown in Figure 8. It seems clear that further theoretical and experimental work is required to fully answer remaining questions as to the microscopic origin of the spin–spin correlations. In particular, a compelling experimental direction to follow would be to study their isospin dependence. An approved experiment at iThemba [71] will extend the studies of Ref. [67] measuring the spin-spin correlations in the ground states of ^{46,48}Ti (see right panel in Figure 8), for which the shell model using the MBZ interaction [72] predicts negative values. For $N > Z$ targets, a combination of (p,p') and (d,d') scattering is required to disentangle the IS and IV components of the $M1$ operator.

8 Conclusion

The quenching of single-particle strength in atomic nuclei continues to be an active area of research in nuclear physics. Modern advances in direct reactions, particularly suited to probe nucleon occupancies, are providing new insights for a quantitative understanding of this phenomenon, intimately related to the fundamental nature of nucleons in the nuclear medium. In an attempt to connect recent studies on SRC from Jefferson Laboratory with data on spectroscopic factors, we have proposed a phenomenological model discussed in Sec. 2 that includes the combined effects of SRC and LRC (PVC and PC). Our results are in agreement with those of the DOM.

We have explored potential implications of our phenomenological analysis on some other aspects of nuclear structure, with special emphasis on the evolution with isospin. In particular, we discussed the subjects of effective masses, charge radii and effective charges, and spin-spin correlations. We showed that our estimates for the asymmetry dependence of effective masses due to SRC are consistent with microscopic calculations. More qualitative estimates of charge radii and effective charges, and spin-spin correlations reveal observable effects due to SRC on these properties.

While perhaps rather speculative at this stage, our conclusions suggest the significant role that SRC play in the nature of dressed nucleons in the nuclear medium, and we trust that our results will stimulate additional work. On the experimental side, existing accelerator facilities and new detector systems with increased sensitivity and resolving power are positioning us to access exotic beams to study exclusive direct reactions, in reverse kinematics, to explore the isospin degree of freedom and shed further light on the topic. On the theory side, new *ab initio* developments and the large increase in computer power becoming available are shaping a path to a predictive model of nuclei and their reactions. Achieving that ultimate goal will require a strong synergy between experiment and theory to design the best possible experiments that will inform of important improvements in the model. In turn, new theoretical insights will lead to new experimental programs that will be, again, contrasted with theory. One cannot but look forward to these exciting developments.

Data availability statement

The data analyzed in this study is subject to the following licenses/restrictions: None. Requests to access these datasets should be directed to Augusto O. Macchiavelli macchiavelao@ornl.gov.

Author contributions

AOM: Writing–original draft, Writing–review and editing. SP: Writing–original draft, Writing–review and editing. MP: Writing–original draft, Writing–review and editing.

Funding

The author(s) declare that financial support was received for the research, authorship, and/or publication of this article. This work was supported by the Royal Society, the United Kingdom STFC under Grant numbers ST/P003885/1, ST/M006433/1, ST/V001035/1, ST/L005727/1, the Laboratory Directed Research and Development (LDRD) Program of Oak Ridge National Laboratory, and the U.S. Department of Energy, Office of Science, Office of Nuclear Physics under Contract No. DE-AC05-00OR22725.

Acknowledgments

AOM would like to thank the Royal Society for financial support and the Department of Physics at the University of York for their kind hospitality during the course of this work and the many *"cortados"* that were crucial for the completion of the manuscript.

Conflict of interest

The authors declare that the research was conducted in the absence of any commercial or financial relationships that could be construed as a potential conflict of interest.

Generative AI statement

The author(s) declare that no Generative AI was used in the creation of this manuscript.

Publisher's note

References

1. Mayer MG. On closed shells in nuclei. ii. *Phys Rev* (1949) 75:1969–70. doi:10.1103/PhysRev.75.1969

2. Haxel O, Jensen JHD, Suess HE. On the "magic numbers" in nuclear structure. *Phys Rev* (1949) 75:1766. doi:10.1103/PhysRev.75.1766.2

3. Bohr A, Mottelson BR. Nuclear structure, volumes I and II. World Scientific (2008).

4. Mayer MG. The shell model. *Nobel Lecture* (1963) 32–90. doi:10.1016/b978-0-08-009840-1.50007-4

5. Gomes L, Walecka J, Weisskopf V. Properties of nuclear matter. *Ann Phys* (1958) 3:241–74. doi:10.1016/0003-4916(58)90019-8

6. Mottelson B. Why are nuclei described by independent particle motion. *Nucl Phys A* (1999) 649:45. doi:10.1016/s0375-9474(99)00037-8

7. De Witt Huberts P. Are nuclei strongly correlated fermi liquids? empirical evidence from (e,ep) spectral functions. *Prog Part Nucl Phys* (1990) 24:205–18. doi:10.1016/0146-6410(90)90017-X

8. Wiringa RB, Arriaga A, Pandharipande VR. Quadratic momentum dependence in the nucleon-nucleon interaction. *Phys Rev C* (2003) 68:054006. doi:10.1103/PhysRevC.68.054006

9. Brueckner K. Two-body forces and nuclear saturation. iii. details of the structure of the nucleus. *Phys Rev* (1955) 97:1353–66. doi:10.1103/PhysRev.97.1353

10. Brueckner KA. Particle theories. *Proc Rutherford Jubilee Int Conf Manchester* (1961).

11. Schiavilla R, Wiringa RB, Pieper SC, Carlson J. Tensor forces and the ground-state structure of nuclei. *Phys Rev Lett* (2007) 98:132501. doi:10.1103/physrevlett.98.132501

12. Akhiezer A, Sitenko A. *SOVIET PHYSICS JETP* (1957) 5:652.

13. Glauber R, et al. Lectures in theoretical physics. New York, NY: Interscience Publishers, Inc, (1959) 1. 315 p.

14. Bertulani CA. Relativistic continuum-continuum coupling in the dissociation of halo nuclei. *Phys Rev Lett* (2005) 94:072701. doi:10.1103/PhysRevLett.94.072701

15. Gade A, Adrich P, Bazin D, Bowen MD, Brown BA, Campbell CM, et al. Reduction of spectroscopic strength: weakly-bound and strongly-bound single-particle states studied using one-nucleon knockout reactions. *Phys Rev C* (2008) 77:044306. doi:10.1103/PhysRevC.77.044306

16. Ogata K, Bertulani CA. Dynamical relativistic effects in breakup processes of halo nuclei. *Prog Theor Phys* (2010) 123:701–18. doi:10.1143/PTP.123.701

17. Aumann T, Barbieri C, Bazin D, Bertulani C, Bonaccorso A, Dickhoff W, et al. Quenching of single-particle strength from direct reactions with stable and rare-isotope beams. *Prog Part Nucl Phys* (2021) 118:103847. doi:10.1016/j.ppnp.2021.103847

18. Macfarlane MH, French JB. Stripping reactions and the structure of light and intermediate nuclei. *Rev Mod Phys* (1960) 32:567–691. doi:10.1103/RevModPhys.32.567

19. Lapikas L. Quasi-elastic electron scattering off nuclei. *Nucl Phys A* (1993) 553:297–308. doi:10.1016/0375-9474(93)90630-G

20. Kramer G, Blok H, Lapikas L. A consistent analysis of (e,e'p) and (d,3he) experiments. *Nucl Phys A* (2001) 679:267–86. doi:10.1016/S0375-9474(00)00379-1

21. Lapikás L, van der Steenhoven G, Frankfurt L, Strikman M, Zhalov M. Transparency of ^{12}C for protons. *Phys Rev C* (2000) 61:064325. doi:10.1103/PhysRevC.61.064325

22. Frankfurt L, Strikman M, Zhalov M. Single-particle strength restoration and nuclear transparency in high-Q2 exclusive (e,e′p) reactions. *Phys Lett B* (2001) 503:73–80. doi:10.1016/S0370-2693(01)00173-3

23. Furnstahl R, Hammer HW. Are occupation numbers observable? *Phys Lett B* (2002) 531:203–8. doi:10.1016/S0370-2693(01)01504-0

24. Furnstahl RJ, Schwenk A. How should one formulate, extract and interpret 'non-observables' for nuclei? *J Phys G: Nucl Part Phys* (2010) 37:064005. doi:10.1088/0954-3899/37/6/064005

25. Schiffer JP, Hoffman CR, Kay BP, Clark JA, Deibel CM, Freeman SJ, et al. Test of sum rules in nucleon transfer reactions. *Phys Rev Lett* (2012) 108:022501. doi:10.1103/PhysRevLett.108.022501

26. Kay BP, Schiffer JP, Freeman SJ. Quenching of cross sections in nucleon transfer reactions. *Phys Rev Lett* (2013) 111:042502. doi:10.1103/PhysRevLett.111.042502

27. Tostevin JA, Gade A. Systematics of intermediate-energy single-nucleon removal cross sections. *Phys Rev C* (2014) 90:057602. doi:10.1103/PhysRevC.90.057602

28. Tostevin JA, Gade A. Updated systematics of intermediate-energy single-nucleon removal cross sections. *Phys Rev C* (2021) 103:054610. doi:10.1103/PhysRevC.103.054610

29. Bertsch G, Kuo T. Effective mass in nuclei. *Nucl Phys A* (1968) 112:204–8. doi:10.1016/0375-9474(68)90230-3

30. Dickhoff W, Barbieri C. Self-consistent green's function method for nuclei and nuclear matter. *Prog Part Nucl Phys* (2004) 52:377–496. doi:10.1016/j.ppnp.2004.02.038

31. Brueckner KA, Eden RJ, Francis NC. High-energy reactions and the evidence for correlations in the nuclear ground-state wave function. *Phys Rev* (1955) 98:1445–55. doi:10.1103/PhysRev.98.1445

32. Flavigny F, Gillibert A, Nalpas L, Obertelli A, Keeley N, Barbieri C, et al. Limited asymmetry dependence of correlations from single nucleon transfer. *Phys Rev Lett* (2013) 110:122503. doi:10.1103/PhysRevLett.110.122503

33. Devins D, Friesel D, Jones W, Attard A, Svalbe I, Officer V, et al. The 12c(p,2p)11b reaction at 100 mev. *Aust J Phys* (1979) 32:323–34. doi:10.1071/ph790323

34. Atkinson MC, Blok HP, Lapikás L, Charity RJ, Dickhoff WH. Validity of the distorted-wave impulse-approximation description of ^{40}Ca(e, e'p)^{39}Kdata using only ingredients from a nonlocal dispersive optical model. *Phys Rev C* (2018) 98. doi:10.1103/PhysRevC.98.044627

35. Hen O, Miller GA, Piasetzky E, Weinstein LB. Nucleon-nucleon correlations, short-lived excitations, and the quarks within. *Rev Mod Phys* (2017) 89:045002. doi:10.1103/revmodphys.89.045002

36. Frankfurt LL, Strikman MI. High-energy phenomena, short range nuclear structure and QCD. *Phys Rept* (1981) 76:215–347. doi:10.1016/0370-1573(81) 90129-0

37. Subedi R, Shneor R, Monaghan P, Anderson BD, Aniol K, Annand J, et al. Probing cold dense nuclear matter. *Science* (2008) 320:1476–8. doi:10.1126/science.1156675

38. The CLAS collaboration. Probing high-momentum protons and neutrons inneutron-rich nuclei. *Nature*(2018) 560:617–21. doi:10.1038/s41586-018-0400-z-1154-1155

39. Paschalis S, Petri M, Macchiavelli A, Hen O, Piasetzky E. Nucleon-nucleon correlations and the single-particle strength in atomic nuclei. *Phys Lett B* (2020) 800:135110. doi:10.1016/j.physletb.2019.135110

40. Ciofi degli Atti C. In-medium short-range dynamics of nucleons: recent theoretical and experimental advances. *Phys Rept* (2015) 590:1–85. doi:10.1016/j.physrep.2015.06.002

41. Weiss R, Korover I, Piasetzky E, Hen O, Barnea N. Energy and momentum dependence of nuclear short-range correlations - spectral function, exclusive scattering experiments and the contact formalism. *Phys Lett B* (2019) 791:242–8. doi:10.1016/j.physletb.2019.02.019

42. Vogt K, Hartmann T, Zilges A. Simple parametrization of single- and two-nucleon separation energies in terms of the neutron to proton ratio n/z. *Phys Lett B* (2001) 517:255–60. doi:10.1016/S0370-2693(01)01014-0

43. Pohl T, Sun YL, Obertelli A, Lee J, Gómez-Ramos M, Ogata K, et al. Multiple mechanisms in proton-induced nucleon removal at ~ 100 MeV/Nucleon. *Phys Rev Lett* (2023) 130:172501. doi:10.1103/PhysRevLett.130.172501

44. Atar L, Paschalis S, Barbieri C, Bertulani CA, Díaz Fernández P, Holl M, et al. Quasifree (*p, 2p*) reactions on oxygen isotopes: observation of isospin independence of the reduced single-particle strength. *Phys Rev Lett* (2018) 120:052501. doi:10.1103/PhysRevLett.120.052501

45. Kay BP, Tang TL, Tolstukhin IA, Roderick GB, Mitchell AJ, Ayyad Y, et al. Quenching of single-particle strength in a = 15 nuclei. *Phys Rev Lett* (2022) 129:152501. doi:10.1103/PhysRevLett.129.152501

46. Manfredi J, Lee J, Rogers AM, Tsang MB, Lynch WG, Anderson C, et al. Quenching of single-particle strengths in direct reactions. *Phys Rev C* (2021) 104:024608. doi:10.1103/PhysRevC.104.024608

47. Dickhoff WH, Charity RJ, Mahzoon MH. Novel applications of the dispersive optical model. *J Phys G: Nucl Part Phys* (2017) 44:033001. doi:10.1088/1361-6471/44/3/033001

48. Mueller JM, Charity RJ, Shane R, Sobotka LG, Waldecker SJ, Dickhoff WH, et al. Asymmetry dependence of nucleon correlations in spherical nuclei extracted from a dispersive-optical-model analysis. *Phys Rev C* (2011) 83:064605. doi:10.1103/PhysRevC.83.064605

49. Levinger J. Modified quasi-deutron model. *Phys Lett B* (1979) 82:181–2. doi:10.1016/0370-2693(79)90730-5

50. Levinger J. Fifty years of the quasi-deuteron model. *Nucl Phys A* (2002) 699:255–60. doi:10.1016/S0375-9474(01)01501-9

51. Neff T, Feldmeier H. Tensor correlations in the unitary correlation operator method. *Nucl Phys A* (2003) 713:311–71. doi:10.1016/S0375-9474(02) 01307-6

52. Neff T, Feldmeier H, Horiuchi W. Short-range correlations in nuclei with similarity renormalization group transformations. *Phys Rev C* (2015) 92:024003. doi:10.1103/PhysRevC.92.024003

53. Tropiano AJ, Bogner SK, Furnstahl RJ, Hisham MA. Quasi-deuteron model at low renormalization group resolution. *Phys Rev C* (2022) 106:024324. doi:10.1103/PhysRevC.106.024324

54. Burrello S, Typel S. Embedding short-range correlations in relativistic density functionals through quasi-deuterons. *The Eur Phys J A* (2022) 58:120. doi:10.1140/epja/s10050-022-00765-z

55. Etchegoyen A, Etchegoyen M, Vergini E. Evaluation of Hamiltonian two-body matrix elements. *Computer Phys Commun* (1989) 55:227–31. doi:10.1016/0010-4655(89)90079-9

56. Xu J, Chen LW, Li BA, Ma HR. Effects of isospin and momentum dependent interactions on thermal properties of asymmetric nuclear matter. *Phys Rev C* (2008) 77:014302. doi:10.1103/PhysRevC.77.014302

57. Li BA, Cai BJ, Chen LW, Xu J. Nucleon effective masses in neutron-rich matter. *Prog Part Nucl Phys* (2018) 99:29–119. doi:10.1016/j.ppnp.2018.01.001

58. Li BA, Chen LW. Nucleon-nucleon cross sections in neutron-rich matter and isospin transport in heavy-ion reactions at intermediate energies. *Phys Rev C* (2005) 72:064611. doi:10.1103/PhysRevC.72.064611

59. Das CB, Das Gupta S, Gale C, Li BA. Momentum dependence of symmetry potential in asymmetric nuclear matter for transport model calculations. *Phys Rev C* (2003) 67:034611. doi:10.1103/PhysRevC.67.034611

60. Li A, Hu JN, Shang XL, Zuo W. Nonrelativistic nucleon effective masses in nuclear matter: Brueckner-Hartree-Fock model versus relativistic Hartree-Fock model. *Phys Rev C* (2016) 93:015803. doi:10.1103/PhysRevC.93.015803

61. Kutschera M, Wójcik W. Proton impurity in the neutron matter: a nuclear polaron problem. *Phys Rev C* (1993) 47:1077–85. doi:10.1103/PhysRevC.47.1077

62. Garcia Ruiz RF, Bissell ML, Blaum K, Ekström A, Frömmgen N, Hagen G, et al. Unexpectedly large charge radii of neutron-rich calcium isotopes. *Nat Phys* (2016) 12:594–8. doi:10.1038/nphys3645

63. Enciu M, Liu HN, Obertelli A, Doornenbal P, Nowacki F, Ogata K, et al. Extended $p_{3/2}$ neutron orbital and the $n = 32$ shell closure in ^{52}Ca. *Phys Rev Lett* (2022) 129 262501. doi:10.1103/PhysRevLett.129.262501

64. Miller G, Beck A, Beck SMT, Weinstein L, Piasetzky E, Hen O. Can long-range nuclear properties be influenced by short range interactions? a chiral dynamics estimate. *Phys Lett B* (2019) 793:360–4. doi:10.1016/j.physletb.2019.05.010

65. Bohr A, Mottelson BR. Nuclear structure, volume II. World Scientific (2008).

66. Frauendorf S, Macchiavelli A. Overview of neutron–proton pairing. *Prog Part Nucl Phys* (2014) 78:24–90. doi:10.1016/j.ppnp.2014.07.001

67. Matsubara H, Tamii A, Nakada H, Adachi T, Carter J, Dozono M, et al. Nonquenched isoscalar spin-*m1* excitations in *sd*-shell nuclei. *Phys Rev Lett* (2015) 115 102501. doi:10.1103/PhysRevLett.115.102501

68. Matsubara H. Isoscalar and isovector spin-M1 transitions from the even-even, N = Z nuclei across the sd-shell region. *Ph.D Thesis, Department Physics, Osaka Univesity* (2010).

69. Sasano M, Sakai H, Yako K, Wakasa T, Asaji S, Fujita K, et al. Gamow-teller unit cross sections of the (p, n) reaction at 198 and 297 mev on medium-heavy nuclei. *Phys Rev* (2009) 79:024602. doi:10.1103/PhysRevC.79.024602

70. Van Isacker P, Macchiavelli AO. Neutron–proton spin–spin correlations in the ground states of N=Z nuclei. *Eur Phys J A* (2021) 57:178. doi:10.1140/epja/s10050-021-00489-6

71. Macchiavelli AO, Crawford HL, Campbell CM, Clark RM, Cromaz M, Fallon P. Ground state neutron-proton spin-spin correlations studied by (p,p') and (d,d') scattering. *iThemba Proposal PR353* (2019).

72. McCullen JD, Bayman BF, Zamick L. Spectroscopy in the nuclear $1f_{7/2}$ shell. *Phys Rev* (1964) 134 B515–B538. doi:10.1103/PhysRev.134.B515

frontiers | Frontiers in Physics

TYPE Original Research
PUBLISHED 24 March 2025
DOI 10.3389/fphy.2025.1539148

Direct reactions with the AT-TPC

Yassid Ayyad[1]*, Daniel Bazin[2,3], Francesca Bonaiti[3,4], Jie Chen[5], Xiaobin Li[5], Adam Anthony[6], Melina Avila[7], Saul Beceiro-Novo[8], Khushi Bhatt[7], Cristina Cabo[1], Tatsuya Furuno[9], Valdir Guimarães[10], Alex Hall-Smith[7], Curtis Hunt[3], Heshani Jayatissa[7], Takahiro Kawabata[9], Harriet Kumi[8], Jose Manuel López-González[1], Juan Lois-Fuentes[3], Augusto Macchiavelli[4], Gordon McCann[3], Claus Müller-Gatermann[7], Alicia Muñoz-Ramos[1], Wolfgang Mittig[2,3], Bruno Olaizola[11], Zarif Rahman[3], Daniel Regueira[1], Javier Rufino[12], Soki Sakajo[9], Clementine Santamaria[3], Michael Z. Serikow[2,3], Tianxudong Tang[2,3], Ivan Tolstukhin[7], Nathan Turi[2,3], Nathan Watwood[7] and Juan Zamora[3]

[1]Instituto Galego de Física de Altas Enerxías, Universidade de Santiago de Compostela, Santiago de Compostela, Spain, [2]Department of Physics and Astronomy, Michigan State University, East Lansing, MI, United States, [3]Facility for Rare Isotope Beams, Michigan State University, East Lansing, MI, United States, [4]Physics Division, Oak Ridge National Laboratory, Oak Ridge, TN, United States, [5]College of Science, Southern University of Science and Technology, Shenzhen, Guangdong, China, [6]Department of Physics and Astronomy, High Point University, High Point, NC, United States, [7]Physics Division, Argonne National Laboratory, Lemont, IL, United States, [8]Universidade da Coruña, Campus Industrial, Departamento de Física y Ciencias de la Tierra, Centro de Investigacion en Tecnologías Navales e Industriales, Ferrol, Spain, [9]Department of Physics, Osaka University, Toyonaka, Osaka, Japan, [10]Instituto de Física, Universidade de São Paulo, Sao Paulo, Brazil, [11]Instituto de Estructura de la Materia, Consejo Superior de Investigaciones Científicas, Madrid, Spain, [12]Department of Physics, University of Notre Dame, Notre Dame, IN, United States

Introduction: Direct reactions are crucial tools for accessing properties of the atomic nucleus. Fundamental and exotic phenomena such as collective modes, pairing, weakbinding effects and evolution of single-particles energies can be investigated in peripheral collisions between a heavy nucleus and a light target. The necessity of using inverse kinematics to reveal how these structural properties change with isospin imbalance renders direct reactions a challenging technique when using the missing mass method.

Methods: In this scenario, Active Target Time Projection Chambers (AT-TPC) have demonstrated an outstanding performance in enabling these types of reactions even under conditions of very low beam intensities. The AT-TPC of the Facility for Rare Isotope Beams (FRIB) is a next generation multipurpose Active Target. When operated inside a solenoidal magnet, direct reactions benefit from the measurement of the magnetic rigidity that enables particle identification and the determination of the excitation energy with high resolution without the need of auxiliary detectors. Additionally, the AT-TPC can be coupled to a magnetic spectrometer improving even further its spectroscopic investigation capability.

Results: In this contribution, we discuss inelastic scattering and transfer reaction data obtained via the AT-TPC and compare them to theory. In particular, we present the results for the ^{14}C(p,p′) and ^{12}Be (p,d)^{11}Be reactions.

EDITED BY
Alan Wuosmaa,
University of Connecticut, United States

REVIEWED BY
Grigory Nigmatkulov,
University of Illinois Chicago, United States
Julian Kahlbow,
Berkeley Lab (DOE), United States

*CORRESPONDENCE
Yassid Ayyad,
✉ yassid.ayyad@usc.es

RECEIVED 03 December 2024
ACCEPTED 28 February 2025
PUBLISHED 24 March 2025

CITATION
Ayyad Y, Bazin D, Bonaiti F, Chen J, Li X, Anthony A, Avila M, Beceiro-Novo S, Bhatt K, Cabo C, Furuno T, Guimarães V, Hall-Smith A, Hunt C, Jayatissa H, Kawabata T, Kumi H, López-González JM, Lois-Fuentes J, Macchiavelli A, McCann G, Müller-Gatermann C, Muñoz-Ramos A, Mittig W, Olaizola B, Rahman Z, Regueira D, Rufino J, Sakajo S, Santamaria C, Serikow MZ, Tang T, Tolstukhin I, Turi N, Watwood N and Zamora J (2025) Direct reactions with the AT-TPC.
Front. Phys. 13:1539148.
doi: 10.3389/fphy.2025.1539148

Discussion: For ^{14}C, we compare the experimental excitation energy of the first 1^- excited state with coupled-cluster calculationsbased on nuclear interactions from chiral effective field theory and with available shell-model predictions. For ^{12}Be, we determine the theoretical spectroscopic factors of the ^{12}Be (p,d)^{11}Be transfer reaction in the shell modeland compare them to the experimental excitation spectrum from a qualitative standpoint.

KEYWORDS

direct reactions, transfer, inelastic scattering, active target, time projection chamber, solenoidal spectrometer

1 Introduction

Direct reactions, such as scattering, nucleon transfer and removal, are among the most powerful tools for extracting spectroscopic information about nuclear structure through charged-particle spectroscopy [1]. These reactions are very selective and can provide insights into both single-particle and collective nuclear excitations. A wide range of phenomena can be uncovered, including migration of nuclear magic numbers, modifications in single-particle structures, pairing modes and strengths, and the emergence of collective features in complex nuclei [2]. Direct reactions also play a key role in modeling nuclear processes relevant to explosive nucleosynthesis [3] and testing fundamental symmetries [4]. At large isospin imbalance, such phenomena may evolve along isotopic and isotonic chains revealing properties usually not found near the valley of stability. In this context, the nucleon-nucleon interaction and the interplay between collectivity and single-particle structure are essential to the nuclear shell model, a cornerstone of nuclear structure theory. In light of this, the conventional magic numbers may vanish. At the limits of stability where these phenomena predominantly occur, weak-bindings effects become more significant and are manifested through specific near-threshold resonances that highlight the role of the coupling to the continuum, formation of halos (skins) and weakening of the spin-orbit splittings.

The choice of an specific reaction is crucial when probing both single-particle and collective phenomena. Single-nucleon transfer reactions have been used preferentially to access experimental information on the location and occupation of nuclear levels because of its selectivity. Moreover, the cross section yields direct information on the overlap between the initial- and final-state wave functions as well as on the angular momentum and spin-parity of the states of interest. The process is described by a simple picture of a transferred particle/hole orbiting around the core. The normalization factor between the experimental cross section and the calculated single-particle cross section, known as spectroscopic factor, reveals the single-particle strengths of the populated levels, indicating the configuration mixing in the wave function. Both neutron and proton transfer reactions have been extensively used to study the evolution of single-particles energies and to reveal effective interactions between nucleons [5]. On the other hand, two-particle transfer reactions, particularly those involving neutrons, have been one of the essential tools for investigating the ubiquitous pairing in its many forms, naturally leading to the exploration of particle-particle correlations and its role on halo and Borromean systems. Accessing nuclear spectroscopic information can also be achieved using elastic and inelastic scattering with light targets/projectiles such as proton, deuteron or α particles, although with much reduced selectivity. In addition to fundamental spectroscopy studies, inelastic scattering has been extensively employed to probe many forms of nuclear collectivity, for example, to extract the contribution of protons and neutrons to electric and magnetic transitions by considering their deformation lengths through the cross sections [6–8], to infer about cluster structures characterized by large monopole transitions [9, 10] and pygmy and giant resonances and electromagnetic responses of different natures [11–13]. Traditionally, Coulomb excitation (Coulex) has been the preferred reaction mechanism as electromagnetic probe. However, as mentioned before, hadronic probes provide insight into the contribution of the neutron motion to the collective matrix elements as well as the isoscalar and isovector components of the nucleus electromagnetic response. The Coulex and nuclear contributions to the reaction mechanism are highly dependent on the energy of the beam and the angle of measurement. Hadronic probes such as proton inelastic scattering are dominated by excitation through virtual photon exchange at zero degrees which opens a doorway to perform Coulex experiments under more favorable conditions [14, 15].

In the emerging era of next-generation radioactive ion-beam facilities, direct reactions will play a crucial role in the study of the nuclear structure at the edge of stability. Most experimental efforts are focused on advancing radioactive beam production and detection systems in tandem. Due to the limited production of the most exotic isotopes, experimental apparatuses that provide high detection efficiency are required to explore the limits of the landscape. Active Target Time Projection Chambers are particularly suited for direct reactions, in particular for low-intensity beams and for the multiple detection of low-energy particles [16–18]. Coupling Active Targets to a solenoid magnet enhances its sensitivity dramatically and its resolution thanks to the measurement of the particle magnetic rigidity [19]. These devices are known as solenoidal spectrometers, with the Helical Orbit Spectrometer (HELIOS) being the first and a pioneer in this field [20], followed by Solaris Sol [21] and the Isolde Solenoidal Spectrometer (ISS) [22]. In this work we discuss the performance of the Active Target Time Projection Chamber (AT-TPC) of the Facility for Rare Isotope Beams (FRIB) for experiments with radioactive beams. We will

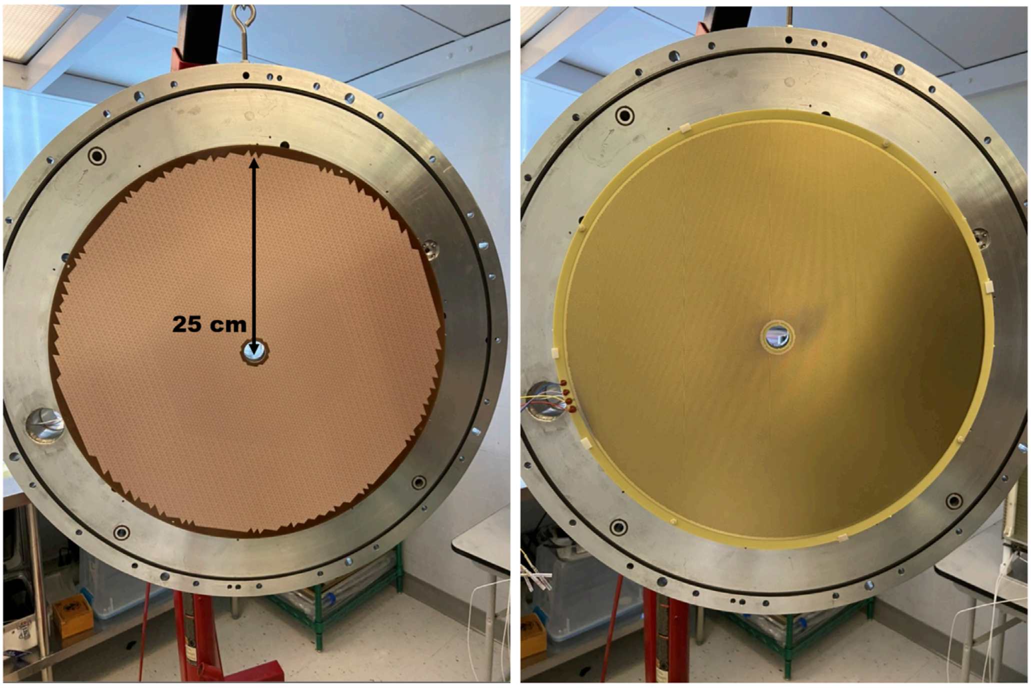

FIGURE 1
Left panel: Micromegas pad plane. Right panel: M-THGEM installed on top of the micromegas.

present results from two experiments performed with the AT-TPC coupled to the HELIOS magnet using low-intensity ^{14}C and ^{12}Be radioactive beams on a proton target. First, we focus on ^{14}C proton inelastic scattering data, allowing for the extraction of low-energy excited states. In particular, the obtained value for the excitation energy of the first 1^{-} state is compared to the results of *ab initio* calculations [23, 24] from coupled-cluster theory [25] based on chiral effective field theory interactions [26–28]. Second, we consider the ^{12}Be (p,d)^{11}Be transfer reaction and provide predictions for the corresponding spectroscopic factors employing the shell model.

2 Materials and methods

The experiments were performed at Argonne National Laboratory using the combination of AT-TPC and the HELIOS magnet. The AT-TPC is a cylindrical Active Target of 1 m length and 25 cm of radius. The sensor consists of a dual micropattern gas detector (MPGD) featuring a 10,240 channel micromegas [29] pad plane and a multilayer thick gas electron multiplier M-THGEM [30] (See Figure 1). The use of the M-THGEM provides the sufficient gain to operate the detector with pure elemental gases such as hydrogen, deuterium or helium. The pad plane is read out by the General Electronics for TPCs, a dedicated data acquisition system capable of recording the drift time of ionization electrons with frequencies from 1 to 100 MHz [31]. The dynamic range can be adjusted from 120 fC to 10 pC, well suited for active target experiments where the injected beam may produce a much larger ionization than the scattered particle.

The HELIOS magnet is a decommissioned Magnetic Resonance Imaging (MRI) magnet that features constant radial and axial fields within the volume of the detector up to 2.85 T and a 0.9 m bore [20]. The magnet was adapted to deploy the AT-TPC and to couple it to the Argonne In-Flight Radioactive Ion Separator (RAISOR) beamline, as shown in Figure 2. The downstream end of the AT-TPC was coupled to a pair of silicon detectors and a LYSO crystal scintillator to detect the beam particle in coincidence with the scattered target and to evaluate the isomer content in the ^{12}Be beam. A small ion chamber (2.54 cm diameter and 5 cm of length) was installed upstream of the AT-TPC to identify the incoming particles and also to serve as time reference for the data acquisition. The ion chamber windows were made of 12 μm of Poly [p-phenylene terephthalamide) (PPTA) and was filled with 50 torr of tetrafluoromethane CF_4].

The analysis of the AT-TPC data is a complex procedure involving the reconstruction of three-dimensional point clouds that capture the interaction of reaction products with the target gas as recorded by the pad plane. The convergence of the data analysis is tested using two distinct analysis frameworks, ATTPCROOTv2 and SPYRAL, which employ different tracking algorithms based on a linear quadratic estimator (Kalman filter) [19, 32] and a interpolator-based non-linear least squares fitter [33], respectively. The results presented in this paper are derived from the SPYRAL framework, with validation performed using both approaches. SPYRAL superior excitation energy resolution and improved efficiency for detecting short particle tracks. A more detailed description of the AT-TPC working principle and its associated data analysis can be found in Refs Bradt et al. [34]; Bazin et al. [18]; Ayyad et al. [17,19] and in the documentation of the data analysis frameworks [35].

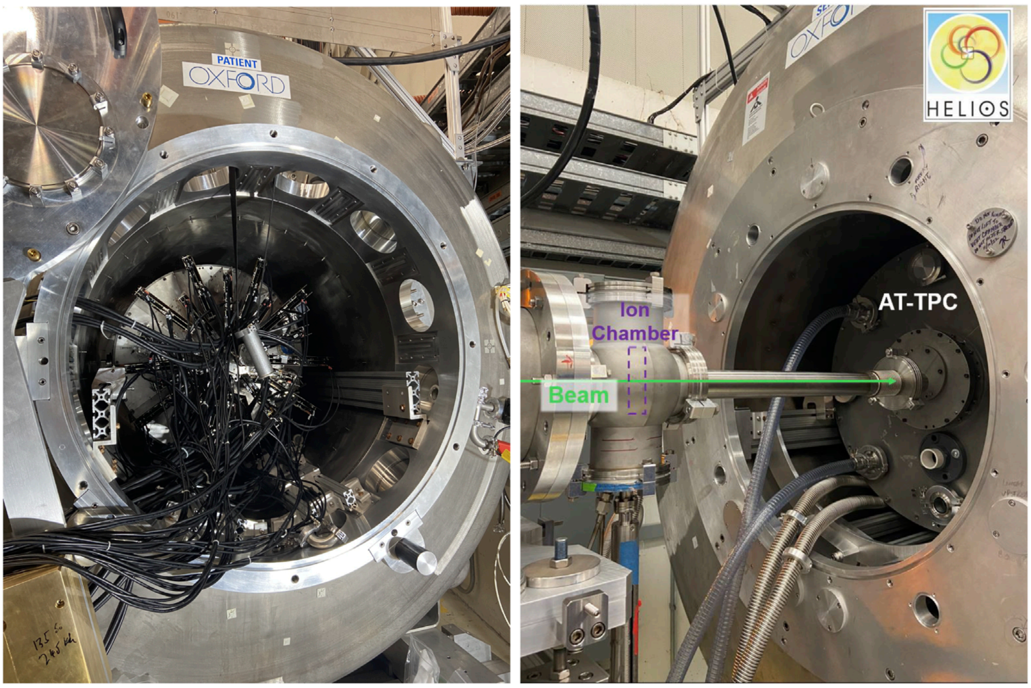

FIGURE 2
Left panel: Downstream end of the AT-TPC and the GET electronics installed. Right panel: Upstream end of the AT-TPC coupled to RAISOR through an ion chamber.

3 Results

3.1 Proton inelastic scattering of ^{14}C

The low-energy spectrum of ^{14}C was determined by proton inelastic scattering using a^{14}C beam of about 12.4A MeV and an intensity of about 2,000 pps for about 25 h of beam time. The AT-TPC was filled with 300 torr of pure hydrogen gas H_2 under static pressure. The beam energy after the AT-TPC window (also 12 μm of PPTA) was about 12.4A MeV. The magnetic field was set to 2.85 T. The trajectory of the reaction products was determined on a event-by-event basis, enabling the inference of the angle and the magnetic rigidity through the track point cloud. The magnetic rigidity and the energy loss are used to identify the reaction products, as shown in the left panel of Figure 3. The most intense band on this plot corresponds to scattered protons.

The excitation energy spectrum of ^{14}C has been obtained after selecting the protons in the identification matrix and correcting for the energy loss of the beam in the detector. The characteristic kinematic lines of ^{14}C excited states are shown in the right panel of Figure 3. The dashed lines refer to the calculated kinematics at the center of the detector for the ground state and the first excited state. The magnetic rigidity vastly increases the dynamic range of the detector as can be seen in the proton energy range covered in this reaction. It is important to highlight that at high proton energies there is a systematic deviation of the data with respect to the calculated kinematics. This discrepancy is likely caused by the electric field edge effects at the outer radius of the detector volume, which impact the reconstruction of high-rigidity particles.

The excitation energy spectrum of ^{14}C is shown in the upper left panel of Figure 4. Besides the ground state, we are able to resolve the first excited state (6.091 MeV, 1^-_1) and the 2^+_2 at 8.317 MeV. The group of states at around 7 MeV has been identified as 6.728 MeV 3^-_1, 7.012 2^+_1 and 7.341 MeV 2^-_1, in agreement with Ref. Lozowski [36]. The values of the energy levels were extracted from the Nuclear Structure and Decay Data (NuDat) database [37]. The experimental resolution in this case, determined from a gaussian fit to the ground state peak, is 150 keV (standard deviation), with an accuracy of 30 keV [19]. The apparent peak at about 9 MeV is attributed to an excited state in ^{14}N above the proton emission threshold, which is populated through the (p,n) charge-exchange reaction. Such events are identified by momentum conservation since the efficiency for the detection of neutrons in the AT-TPC is very low, although not negligible working as a proton target. The angular distribution associated to the 1^-_1 state, shown in the upper right panel of Figure 4, was directly deduced from 20° to 100° in CM. In this angular domain, the peak is well isolated from the neighboring states. The angular distribution was corrected for acceptance and reconstruction efficiency effects. This correction utilized a comprehensive simulation that accounted for both the geometry and response of the AT-TPC. The simulated angular distribution, shown in the lower panel of Figure 4, was obtained generating events by sampling from a flat distribution between 0° and 180° in center of mass (CM). The gradual loss of efficiency between 0° and 40° can be attributed to the limited acceptance imposed by the pad plane's hole for particles emitted at forward angles. At angles above 110°, the energy loss of the protons becomes insufficient to ensure 100% of trigger efficiency. It is evident from

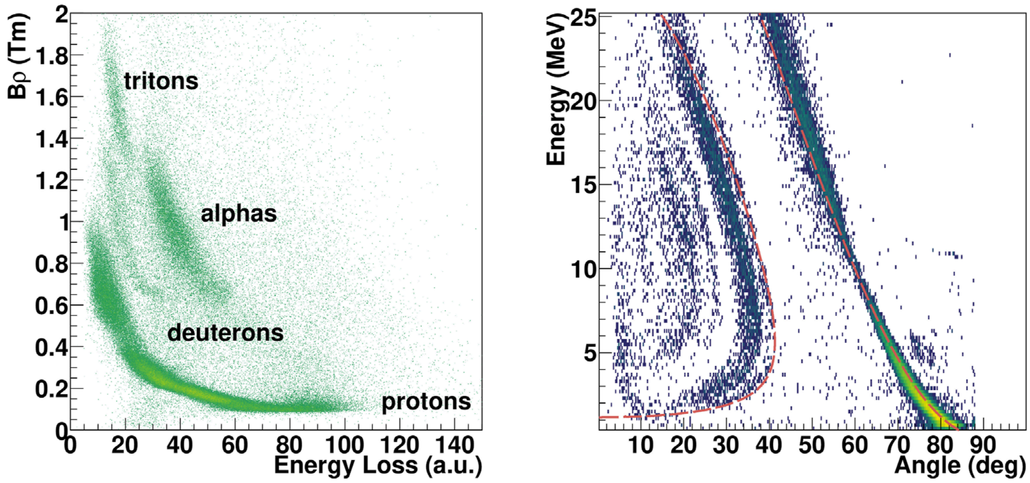

FIGURE 3
Left panel: Energy loss as a function of the magnetic rigidity of the reaction products. Right panel: Kinematics of the ^{14}C + p reaction.

the region of the distribution where the efficiency exceeds one that a fraction of misreconstructed events is not rejected but instead assigned incorrect angles or energies.

3.2 Neutron pick up on ^{12}Be

Among the intricate structures of neutron-rich beryllium isotopes, ^{12}Be stands as a candidate to observe a halo-like structure built on an excited state of a nucleus [38]. Its structure can be understood as the coupling between a valence neutron and a ^{11}Be core. Therefore, one could expect the possibility of observing an excited state on ^{12}Be with a strong overlap to the ^{11}Be ground state, a paradigmatic neutron halo nucleus. The bound structure of ^{12}Be favors this hypothesis because the 1_1^- state is located around 400 keV below the neutron emission threshold ($S_n = 3.170$ MeV), a common feature of weakly-bound systems with a large spatial distribution. We designed an experiment to investigate an enhanced transition $l = 1$ from the 0_2^+ isomeric state in ^{12}Be as a possible signature of a halo structure in an excited state via inelastic scattering as primary probe. To validate the detection method, the setup was commissioned to detect the scattered proton in coincidence with the beam-like ^{12}Be isomer. Concurrently, we measured cross sections for the ^{12}Be (p,d) transfer reaction, which provides valuable information on the ^{12}Be-^{10}Be⊗n overlap. In this work, we present results on the latter reaction.

The experiment was conducted using a low-intensity ^{12}Be beam of about 150 pps at 12*A* MeV. The AT-TPC was filled with 600 torr of pure hydrogen gas. The data analysis was performed in the same fashion as discussed for the proton inelastic scattering on ^{14}C.

The kinematics for the ^{12}Be (p,d)^{11}Be reaction and the ^{11}Be excitation energy spectrum are shown in the left and right panels or Figure 5, respectively. Within our experimental resolution of 200 keV (standard deviation) and an accuracy of about 20 keV, we observe the population of several states of ^{11}Be with established J^{π}: ground state, 0.320 MeV ($1/2_1^-$), 1.78 MeV ($5/2_1^+$), 2.65 MeV ($3/2_1^-$) and a doublet consisting of the 3.89 ($3/2^-$ or $5/2^-$) and 3.96 MeV ($3/2_3^-$). Although the ground and first excited states are unresolved, we can infer quantitative information on the population strength by considering the corresponding angular distributions. Extracting spectroscopic information with such a low-intensity beam clearly demonstrates the outstanding capabilities of Active Targets for experiments with radioactive beams. A detailed analysis of the angular distributions will be addressed in a separate publication to allow for a more thorough exploration.

4 Comparison with theory

4.1 Low-energy spectrum of ^{14}C

The low-energy spectrum obtained for ^{14}C via proton inelastic scattering can be compared to *ab initio* calculations employing nuclear interactions from chiral effective field theory. To solve the quantum many-body problem, we employ the coupled-cluster (CC) approach, where one starts from a mean-field solution $|\Phi_0\rangle$ and parametrizes the nuclear ground state wavefunction as (Equation 1)

$$|\Psi_0\rangle = e^T|\Phi_0\rangle \tag{1}$$

Here, T is the so-called cluster operator, which can be expanded as a sum of n-particle-n-hole excitations: $T = T_1 + T_2 + T_3 + \ldots$. In this framework, excited states can be accessed employing the equation-of-motion coupled-cluster (EOM-CC) method [39]. In EOM-CC, the target state $|\Psi_f\rangle$ is computed via the ansatz (Equation 2)

$$|\Psi_f\rangle = Re^T|\Phi_0\rangle \tag{2}$$

where also the EOM excitation operator R can be written in terms of a particle-hole expansion. In CC theory, both the cluster operator T and the EOM operator R are truncated due to computational limitations. Coupled-cluster singles and doubles (CCSD), where T and R are truncated at the 2p-2h level, is

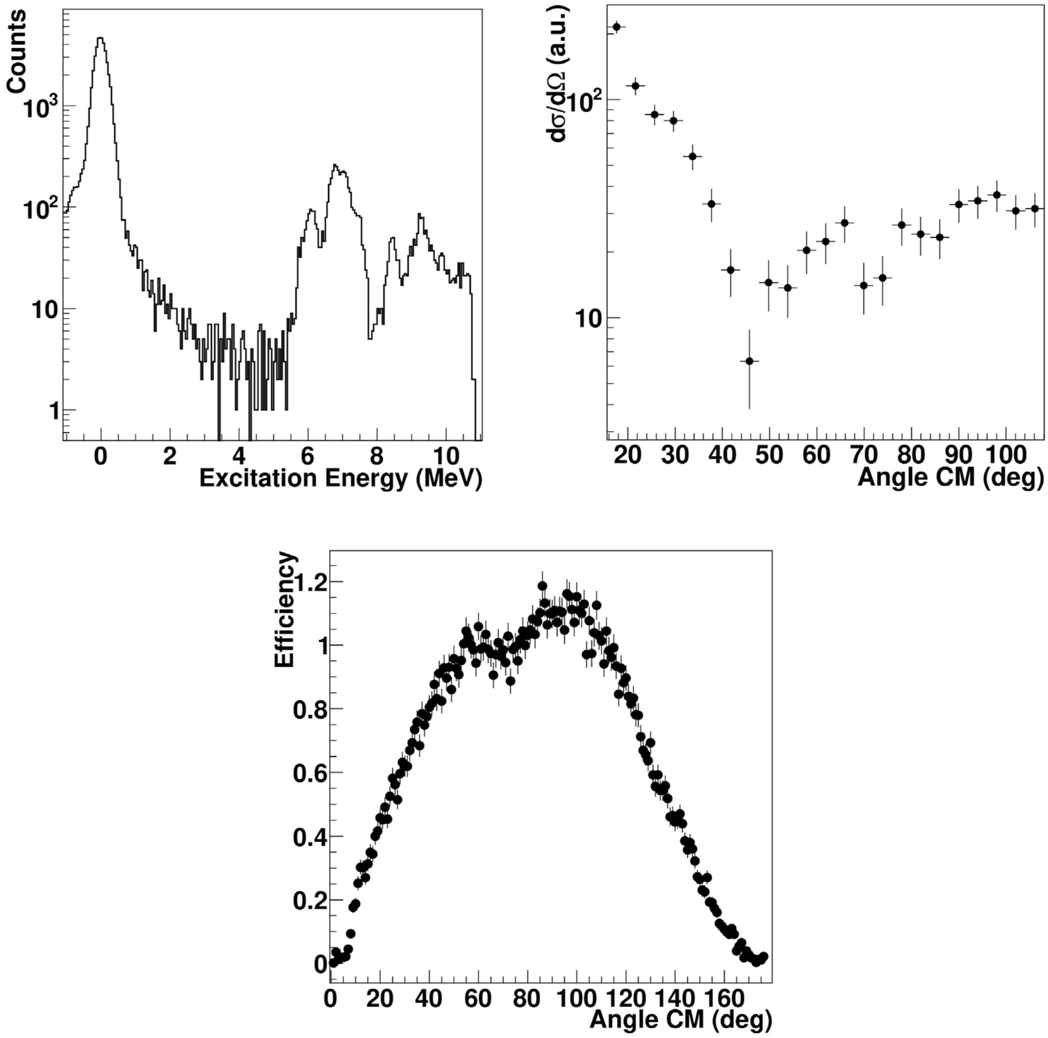

FIGURE 4
Upper left panel: Excitation energy spectrum obtained for the ^{14}C + p reaction. Upper right panel: Angular distribution of the 6.091 MeV state 1_1^- of ^{14}C including statistical error bars. Lower panel: Detection efficiency determined through simulations that accounted for both the detector acceptance and the track reconstruction process.

the most frequently used approximation. Adding linear 3p-3h excitations in the so-called CCSDT-1 approximation [40] leads to increased precision.

As an example, we focus here on the first 1^- state in the spectrum of ^{14}C and compare it to the experimental spectrum obtained with the AT-TPC. To this aim, we employ the chiral ΔNNLO$_{\text{GO}}$(394) and ΔNNLO$_{\text{GO}}$(450) interactions [41]. These nuclear force models, given at next-to-next-to-next-to-leading order in the chiral expansion, contain the Δ isobar as an explicit degree of freedom and they have been successfully employed in several applications [42, 43]. We performed CC calculations starting from a Hartree-Fock Slater determinant including up to 15 major harmonic oscillator shells, and we studied convergence by varying the harmonic oscillator frequency $\hbar\Omega$ between 12 and 16 MeV.

Our results for the excitation energy of the first 1^- state are shown in Table 1. Theoretical uncertainties account for the residual dependence on the model space parameters, and for the truncation of the coupled-cluster expansion according to the strategy employed in Simonis et al. [44]; Acharya et al. [45]. We observe that our predictions lie higher than the experimental determination at around 6.1 MeV. However, it is worth pointing out that the addition of linear 3p-3h excitation reduces the excitation energy of an amount varying between 15% and 18% on the basis of the interaction, moving theory in the direction of the experimental result. A complete analysis of model uncertainties, including the effect of the chiral EFT truncation and of different optimization protocols for the low-energy constants, is left for future work.

The experimental results on the first excited state of ^{14}C can also be compared to available shell-model calculations. In Ref. Yuan et al. [46], the first 1^- excited state of ^{14}C is calculated with three different shell-model interactions (YSOX [46], SFO [47], WBP [48]) optimized for the *psd*-shell region. The latter predict excitation

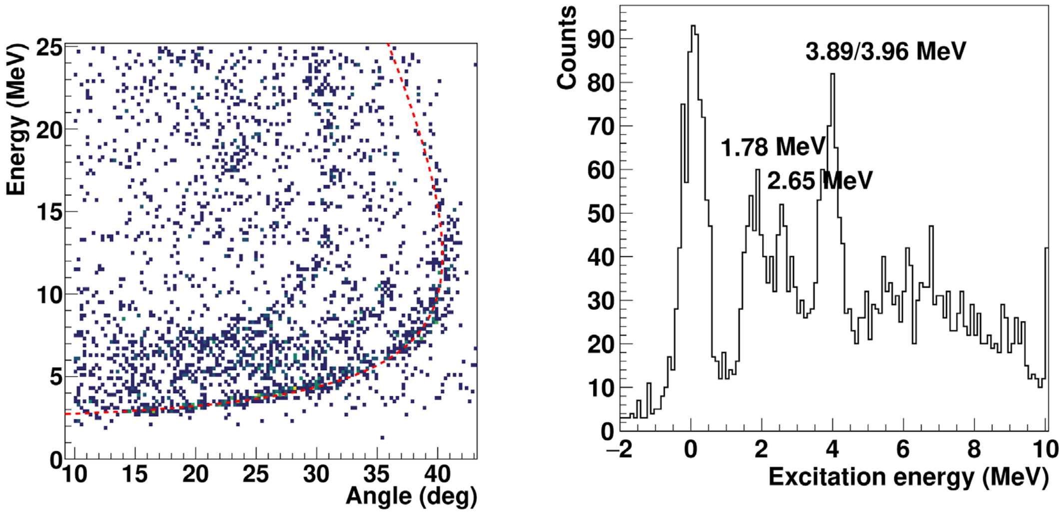

FIGURE 5
Left panel: Kinematics of the ^{12}Be (p,d) reaction. Right panel: ^{11}Be excitation energy spectrum obtained via ^{12}Be (p,d).

TABLE 1 Excitation energies of the first 1^- excited state of ^{14}C in the CCSDT-1 approximation.

Interaction	Excitation energy [MeV]
$\Delta\text{NNLO}_{\text{GO}}(394)$	7.7 (0.7)
$\Delta\text{NNLO}_{\text{GO}}(450)$	7.9 (0.9)

energies ranging from 5.5 to 6 MeV, in close proximity to the experimental data.

Future experimental campaigns will exploit the AT-TPC to study electromagnetic responses up to the giant dipole resonance region. Electromagnetic strength data could be compared to calculations combining CC theory with the Lorentz Integral Transform technique [49] in the so-called LIT-CC method [50, 51]. This approach allows for an *ab initio* desciption of electromagnetic reaction observables in nuclei at and in the vicinity of closed-shells [44, 52, 53]. It is based on the calculation of an integral transform with Lorentzian kernel of the response. Considering small values of the Lorentzian width, we can construct a discretized strength function, where continuum excited states of the nucleus are represented by bound pseudo-states. As an example, let us focus on the E1 strength function of ^{14}C, shown in Figure 6. At low energy, below 8 MeV, we distinguish the first 1^- excited state under analysis in this work. Its transition strength amounts to around 5% of the one observed for states at excitation energies above 15 MeV.

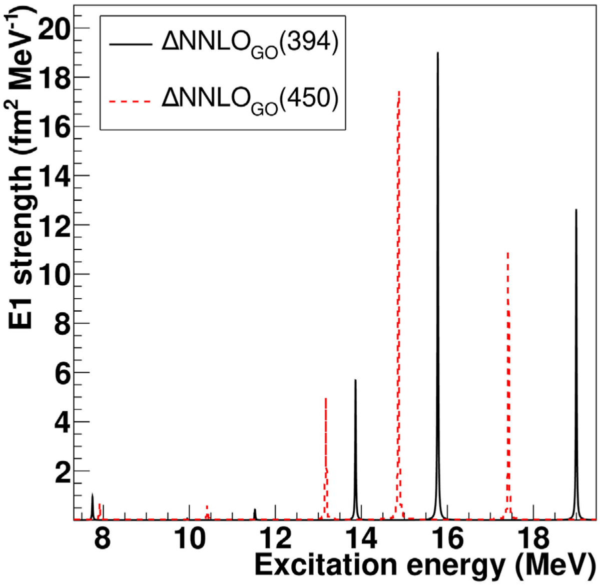

FIGURE 6
Discretized dipole response functions for the two different chiral forces in the CCSDT-1 approximation. The curves have been obtained using a model space size of 15 major oscillator shells and a harmonic oscillator frequency of 12 MeV.

4.2 Shell model calculations for ^{11}Be

We have studied the structure of ^{11}Be from a qualitative point of view from the spectrum obtained in the transfer measurement. We have applied shell model calculations, with the YSOX interaction [46] to calculate the spectroscopic factors of the $^{12}\text{Be}(p,d)^{11}\text{Be}$ reaction. This interaction works in a full $p-sd$ model space, including $(0-3)\hbar\Omega$ excitations, and it can give good description of the energy, quadrupole and spin properties of the psd-shell nuclei. The calculated spectroscopic factors are compared to the experimental results shown in Figure 7. The spectroscopic factors represent the neutron occupancy of the $0p_{1/2}$, $0p_{3/2}$, $1s_{1/2}$ and $0d_{5/2}$ orbitals. It can be seen that the ground state and the first two excited states are populated, showing that the shell model

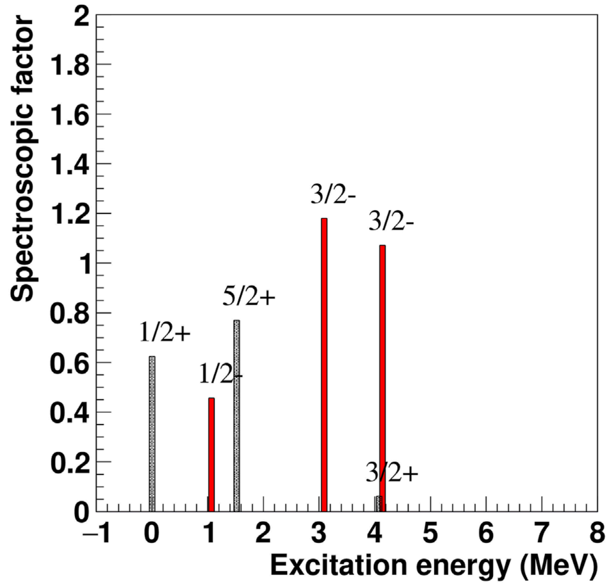

FIGURE 7
Theoretical spectroscopic factors for the ^{12}Be(p,d)^{11}Be reaction obtained from shell model calculations. Black and red bars refer to positive and negative parity states, respectively.

is predicting a very strong configuration mixing in the ground state of ^{12}Be due to the breakdown of $N = 8$ magic number. This is in agreement with the experimental spectrum, except that the ground and the first excited states are not well isolated. However, it is expected that their individual contributions can be determined by the angular distribution, owing to their very different shapes. The higher $3/2^-$ excited states are populated due to the removal strength from the $0p_{3/2}$ orbital. Significantly, the energy of the $1/2^-$ state deviates from the experimental results because the effective energy of the interaction is not optimized for nuclei far from the stability, and the continuum coupling effect was not accounted for. The experimental results presented in this work show strong agreement with previous findings from knock-out [54] and transfer [55] experiments, although a comprehensive discussion will be provided in a forthcoming publication.

5 Conclusion

In this work, we have showcased the use of solenoidal spectrometers in active target mode for direct reactions through the measurement of proton inelastic scattering on ^{14}C and the neutron transfer reaction ^{12}Be(p,d)^{11}Be in inverse kinematics, both using the AT-TPC. This detection scheme enables the measurement of these reactions with beam intensities as low as 100 pps and with adequate resolution. The combination of target thickness and magnetic rigidity results in a broad dynamic range covered by the detector. These capabilities are reflected in the data we have obtained in these measurements. The low-lying E1 strength of ^{14}C was employed to benchmark *ab initio* calculations including interactions from chiral effective field theory. The comparison between theory and experiment, although limited in excitation energy range, paves the way to investigate the E1 strength up to high-excitation energies. The measurement of the full electromagnetic response at very forward angles can be realized using the AT-TPC coupled to a magnetic spectrometer (see Refs. [19, 56]). Such an experimental program has been already initiated at FRIB with the measurement of the E1 response of ^{11}Li via proton inelastic scattering at forward angles. We have also performed shell model calculations, using the YSOX interaction, to clarify the structure of ^{11}Be obtaining a good agreement with the experimental results, from a qualitative standpoint. Obtaining relevant spectroscopic information in such conditions opens a wide range of opportunities for conducting transfer reaction experiments with the most exotic species currently producible.

Data availability statement

The raw data supporting the conclusions of this article will be made available by the authors, without undue reservation.

Author contributions

YA: Conceptualization, Data curation, Formal Analysis, Funding acquisition, Investigation, Methodology, Project administration, Resources, Software, Supervision, Validation, Visualization, Writing–original draft, Writing–review and editing. DB: onceptualization, Data curation, Formal Analysis, Funding acquisition, Investigation, Methodology, Project administration, Resources, Software, Supervision, Validation, Visualization, riting–original draft, Writing–review and editing. FB: Formal Analysis, Investigation, Methodology, Software, Validation, Writing–original draft, Writing–review and editing. JC: Conceptualization, Data curation, Formal Analysis, Investigation, Methodology, Resources, Supervision, Validation, Visualization, Writing–original draft, Writing–review and editing. XL: Formal Analysis, Investigation, Methodology, Writing–review and editing. AA: Methodology, Software, Validation, Writing–review and editing. MA: Writing–review and editing. SB-N: Writing–review and editing. KB: Writing–review and editing. CC: Writing–review and editing. TF: Writing–review and editing. VG: Writing–review and editing. AH-S: Writing–review and editing. CH: Writing–review and editing. HJ: Writing–review and editing. TK: Writing–review and editing. HK: Writing–review and editing. JL-G: Writing–review and editing, Formal Analysis. JL-F: Writing–review and editing. AM: Writing–review and editing. GM: Formal Analysis, Software, Writing–review and editing, Data curation, Investigation, Methodology, Visualization. CM-G: Writing–review and editing. AM-R: Writing–review and editing, Formal Analysis, Software. WM: Writing–review and editing. BO: Writing–review and editing. ZR: Writing–review and editing. DR: Writing–review and editing. JR: Writing–review and editing. SS: Writing–review and editing. CS: Writing–review and editing. MS: Writing–review and editing, Formal Analysis, Software. TT: Writing–review and editing. IT: Writing–review and editing. NT: Software, Writing–review and editing. NW: Writing–review and editing. JZ: Software, Writing–review and editing.

Funding

The author(s) declare that financial support was received for the research, authorship, and/or publication of this article. This work has received financial support from the Xunta de Galicia (CIGUS Network of Research Centres) and the European Union; from the U.S. Department of Energy, Office of Science, Office of Nuclear Physics, under Contract Number DE-AC02-06CH11357 (Argonne), DE-SC0020451 (FRIB). SOLARIS is funded by the DOE Office of Science under the FRIB Cooperative Agreement DE-SC0000661. Y.A. is supported by grant RYC2019-028438-I and PID2021-125995NA-I00 funded by MCIN/AEI/10.13039/501100011033 and by the Regional Government of Galicia under the program "Proyectos de excelencia" Grant No. ED431F 2022/13. SB is supported by Grant RYC2020-030669 and PID2022-142557NA-I00 funded by MCIN/AEI/10.13039/501100011033. FB's work is supported by the U.S. Department of Energy, Office of Science, Office of Nuclear Physics, under the FRIB Theory Alliance award DE-SC0013617, and Office of Advanced Scientific Computing Research and Office of Nuclear Physics, Scientific Discovery through Advanced Computing (SciDAC) program (SciDAC-5 NUCLEI). This research used resources of the Oak Ridge Leadership Computing Facility located at Oak Ridge National Laboratory, which is supported by the Office of Science of the Department of Energy under contract No. DE-AC05-00OR22725. Computer time was provided by the Innovative and Novel Computational Impact on Theory and Experiment (INCITE) program.

Acknowledgments

FB would like to thank Gaute Hagen for access to the spherical coupled-cluster code and Thomas Papenbrock for helpful discussions.

Conflict of interest

The authors declare that the research was conducted in the absence of any commercial or financial relationships that could be construed as a potential conflict of interest.

The author(s) declared that they were an editorial board member of Frontiers, at the time of submission. This had no impact on the peer review process and the final decision.

Generative AI statement

The author(s) declare that no Generative AI was used in the creation of this manuscript.

Publisher's note

References

1. Hansen P, Tostevin J. Direct reactions with exotic nuclei. *Annu Rev Nucl Part Sci* (2003) 53:219–61. doi:10.1146/annurev.nucl.53.041002.110406

2. Wimmer K. Nucleon transfer reactions with radioactive beams. *J Phys G: Nucl Part Phys* (2018) 45:033002. doi:10.1088/1361-6471/aaa2bf

3. Bardayan DW. Transfer reactions in nuclear astrophysics. *J Phys G: Nucl Part Phys* (2016) 43:043001. doi:10.1088/0954-3899/43/4/043001

4. Leach KG, Garrett PE, Ball GC, Bender PC, Bildstein V, Brown BA, et al. Searching for 0^+ states in ^{50}Cr: implications for the superallowed β decay of ^{50}Mn. *Phys Rev C* (2016) 94:011304. doi:10.1103/PhysRevC.94.011304

5. Schiffer JP, True WW. The effective interaction between nucleons deduced from nuclear spectra. *Rev Mod Phys* (1976) 48:191–217. doi:10.1103/RevModPhys.48.191

6. Chen J, Kay BP, Tang TL, Tolstukhin IA, Hoffman CR, Li H, et al. Probing the quadrupole transition strength of ^{15}C via deuteron inelastic scattering. *Phys Rev C* (2022) 106:064312. doi:10.1103/PhysRevC.106.064312

7. Jiang Y, Lou JL, Ye YL, Liu Y, Tan ZW, Liu W, et al. Quadrupole deformation of ^{16}C studied by proton and deuteron inelastic scattering. *Phys Rev C* (2020) 101:024601. doi:10.1103/PhysRevC.101.024601

8. Corsi A, Boissinot S, Obertelli A, Doornenbal P, Dupuis M, Lechaftois F, et al. Neutron-driven collectivity in light tin isotopes: proton inelastic scattering from 104sn. *Phys Lett B* (2015) 743:451–5. doi:10.1016/j.physletb.2015.03.018

9. Yang ZH, Ye YL, Li ZH, Lou JL, Wang JS, Jiang DX, et al. Observation of enhanced monopole strength and clustering in ^{12}Be. *Phys Rev Lett* (2014) 112:162501. doi:10.1103/PhysRevLett.112.162501

10. Kawabata T, Akimune H, Fujita H, Fujita Y, Fujiwara M, Hara K, et al. 2α +t cluster structure in 11b. *Phys Lett B* (2007) 646:6–11. doi:10.1016/j.physletb.2006.11.079

11. Harakeh MN, van der Borg K, Ishimatsu T, Morsch HP, van der Woude A, Bertrand FE (1977). Direct evidence for a new giant resonance at $80A^{-\frac{1}{13}}$ mev in the lead region. *Phys Rev Lett* 38, 676–9. doi:10.1103/PhysRevLett.38.676

12. Morsch HP, Rogge M, Turek P, Mayer-Böricke C. New giant resonances in 172-mev α scattering from ^{208}Pb. *Phys Rev Lett* (1980) 45:337–40. doi:10.1103/PhysRevLett.45.337

13. Kanungo R, Sanetullaev A, Tanaka J, Ishimoto S, Hagen G, Myo T, et al. Evidence of soft dipole resonance in ^{11}Li with isoscalar character. *Phys Rev Lett* (2015) 114:192502. doi:10.1103/PhysRevLett.114.192502

14. Tamii A, Poltoratska I, von Neumann-Cosel P, Fujita Y, Adachi T, Bertulani CA, et al. Complete electric dipole response and the neutron skin in ^{208}Pb. *Phys Rev Lett* (2011) 107:062502. doi:10.1103/PhysRevLett.107.062502

15. Tamii A, Kobayashi N. Studies on electromagnetic dipole responses of atomic nuclei at rcnp. *AAPPS Bull* (2024) 34:7. doi:10.1007/s43673-023-00108-0

16. Beceiro-Novo S, Ahn T, Bazin D, Mittig W. Active targets for the study of nuclei far from stability. *Prog Part Nucl Phys* (2015) 84:124–65. doi:10.1016/j.ppnp.2015.06.003

17. Ayyad Y, Bazin D, Beceiro-Novo S, Cortesi M, Mittig W. Physics and technology of time projection chambers as active targets. *The Eur Phys J A* (2018) 54:181. doi:10.1140/epja/i2018-12557-7

18. Bazin D, Ahn T, Ayyad Y, Beceiro-Novo S, Macchiavelli A, Mittig W, et al. Low energy nuclear physics with active targets and time projection chambers. *Prog Part Nucl Phys* (2020) 114:103790. doi:10.1016/j.ppnp.2020.103790

19. Ayyad Y, Anthony AK, Bazin D, Chen J, McCann GW, Mittig W, et al. Kinematics reconstruction in solenoidal spectrometers operated in active target mode. *The Eur Phys J A* (2023) 59:294. doi:10.1140/epja/s10050-023-01205-2

20. Lighthall J, Back B, Baker S, Freeman S, Lee H, Kay B, et al. Commissioning of the helios spectrometer. *Nucl Instr Methods Phys Res Section A: Acc Spectrometers, Detectors Associated Equipment* (2010) 622:97–106. doi:10.1016/j.nima.2010.06.220

21. SOLARIS SOL. A solenoidal spectrometer apparatus for reaction studies white paper. *Tech Rep* (2018).

22. Tang TL, Kay BP, Hoffman CR, Schiffer JP, Sharp DK, Gaffney LP, et al. First exploration of neutron shell structure below lead and beyond n = 126. *Phys Rev Lett* (2020) 124:062502. doi:10.1103/PhysRevLett.124.062502

23. Ekström A, Forssén C, Hagen G, Jansen GR, Jiang W, Papenbrock T. What is *ab initio* in nuclear theory? *Front Phys* (2023) 11. doi:10.3389/fphy.2023.1129094

24. Hergert H. A guided tour of *ab initio* nuclear many-body theory. *Front Phys* (2020) 8. doi:10.3389/fphy.2020.00379

25. Hagen G, Papenbrock T, Hjorth-Jensen M, Dean DJ. Coupled-cluster computations of atomic nuclei. *Rep Prog Phys* (2014) 77:096302. doi:10.1088/0034-4885/77/9/096302

26. Epelbaum E, Hammer H-W, Meißner U-G. Modern theory of nuclear forces. *Rev Mod Phys* (2009) 81:1773–825. doi:10.1103/RevModPhys.81.1773

27. Machleidt R, Entem D. Chiral effective field theory and nuclear forces. *Phys Rep* (2011) 503:1–75. doi:10.1016/j.physrep.2011.02.001

28. Hammer H-W, König S, van Kolck U. Nuclear effective field theory: status and perspectives. *Rev Mod Phys* (2020) 92:025004. doi:10.1103/RevModPhys.92.025004

29. Giomataris Y, Rebourgeard P, Robert J, Charpak G. Micromegas: a high-granularity position-sensitive gaseous detector for high particle-flux environments. *Nucl Instr Methods Phys Res Section A: Acc Spectrometers, Detectors Associated Equipment* (1996) 376:29–35. doi:10.1016/0168-9002(96)00175-1

30. Cortesi M, Rost S, Mittig W, Ayyad-Limonge Y, Bazin D, Yurkon J, et al. Multi-layer thick gas electron multiplier (M-THGEM): a new MPGD structure for high-gain operation at low-pressure. *Rev Scientific Instr* (2017) 88:013303. doi:10.1063/1.4974333

31. Pollacco E, Grinyer G, Abu-Nimeh F, Ahn T, Anvar S, Arokiaraj A, et al. Get: a generic electronics system for tpcs and nuclear physics instrumentation. *Nucl Instr Methods Phys Res Section A: Acc Spectrometers, Detectors Associated Equipment* (2018) 887:81–93. doi:10.1016/j.nima.2018.01.020

32. Anthony A, Ayyad Y. ACeulemans, freund17, lisacarpenter, cnhunt, Héctor AT-TPC collaboration. At-tpc document Alvarez Pol, Juan Zamora, Nabin Rijal, Alicia Muñoz Ramos, bolaizol, AriAtari, Ruchi-GADGETII, Simon, Wieskejo, & diazcort. (2023). ATTPCROOT (v0.4.0-beta). Zenodo. doi:10.5281/zenodo.10027879

33. [Dataset] McCann G. Attpc/spyral: v0.16.0rc0. *Turinath* (2024). doi:10.5281/zenodo.14165743

34. Bradt J, Bazin D, Abu-Nimeh F, Ahn T, Ayyad Y, Beceiro Novo S, et al. Commissioning of the active-target time projection chamber. *Nucl Instr Methods Phys Res Section A: Acc Spectrometers, Detectors Associated Equipment* (2017) 875:65–79. doi:10.1016/j.nima.2017.09.013

35. AT-TPC collaboration. At-tpc documentation (2024). Available online at: https://attpc.github.io/. Accessed January 15, 2025

36. Lozowski W. Three diverse target preparations: 14c (12 mg/cm2), 71ga24mg (12 mg/cm271ga, 3 mg/cm224mg), and 66,67zn (1.8–14.9 mg/cm2). *Nucl Instr Methods Phys Res Section A: Acc Spectrometers, Detectors Associated Equipment* (1989) 282:54–61. doi:10.1016/0168-9002(89)90108-3

37. National Nuclear Data Center, Brookhaven National Laboratory. (2008, March 18). NuDat (Nuclear Structure and Decay Data). Available online at: https://www.nndc.bnl.gov/nudat3/. Accessed March 11, 2025

38. Potel G, Idini A, Barranco F, Vigezzi E, Broglia RA. Nuclear field theory predictions for 11li and 12be: shedding light on the origin of pairing in nuclei. *Phys At Nuclei* (2014) 77:941–68. doi:10.1134/S106377881407014X

39. Stanton JF, Bartlett RJ. The equation of motion coupled-cluster method. a systematic biorthogonal approach to molecular excitation energies, transition probabilities, and excited state properties. *The J Chem Phys* (1993) 98:7029–39. doi:10.1063/1.464746

40. Watts JD, Gauss J, Bartlett RJ. Coupled-cluster methods with noniterative triple excitations for restricted open-shell Hartree–Fock and other general single determinant reference functions. energies and analytical gradients. *The J Chem Phys* (1993) 98:8718–33. doi:10.1063/1.464480

41. Jiang WG, Ekström A, Forssén C, Hagen G, Jansen GR, Papenbrock T. Accurate bulk properties of nuclei from a = 2 to ∞ from potentials with Δ isobars. *Phys Rev C* (2020) 102:054301. doi:10.1103/PhysRevC.102.054301

42. Hu B, Jiang W, Miyagi T, Sun Z, Ekström A, Forssén C, et al. *Ab initio* predictions link the neutron skin of 208pb to nuclear forces. *Nat Phys* (2022) 18:1196–200. doi:10.1038/s41567-022-01715-8

43. Sun ZH, Ekström A, Forssén C, Hagen G, Jansen GR, Papenbrock T (2025). Multiscale Physics of Atomic Nuclei from First Principles. *Phys. Rev. X*. 15(1) 011028. doi:10.1103/PhysRevX.15.011028

44. Simonis J, Bacca S, Hagen G. First principles electromagnetic responses in medium-mass nuclei - recent progress from coupled-cluster theory. *Eur Phys J* (2019) A 55:241. doi:10.1140/epja/i2019-12825-0

45. Acharya B, Bacca S, Bonaiti F, Li Muli SS, Sobczyk JE. Uncertainty quantification in electromagnetic observables of nuclei. *Front Phys* (2023) 10:1066035. doi:10.3389/fphy.2022.1066035

46. Yuan C, Suzuki T, Otsuka T, Xu F, Tsunoda N. Shell-model study of boron, carbon, nitrogen, and oxygen isotopes with a monopole-based universal interaction. *Phys Rev C* (2012) 85:064324. doi:10.1103/PhysRevC.85.064324

47. Suzuki T, Fujimoto R, Otsuka T. Gamow-teller transitions and magnetic properties of nuclei and shell evolution. *Phys Rev C* (2003) 67:044302. doi:10.1103/PhysRevC.67.044302

48. Warburton EK, Brown BA. Effective interactions for the 0p1s0d nuclear shell-model space. *Phys Rev C* (1992) 46:923–44. doi:10.1103/PhysRevC.46.923

49. Efros VD, Leidemann W, Orlandini G, Barnea N. The lorentz integral transform (lit) method and its applications to perturbation-induced reactions. *J Phys G: Nucl Part Phys* (2007) 34:R459–528. doi:10.1088/0954-3899/34/12/R02

50. Bacca S, Barnea N, Hagen G, Orlandini G, Papenbrock T. First principles description of the giant dipole resonance in ^{16}**O**. *Phys Rev Lett* (2013) 111:122502. doi:10.1103/PhysRevLett.111.122502

51. Bacca S, Barnea N, Hagen G, Miorelli M, Orlandini G, Papenbrock T. Giant and pigmy dipole resonances in ^{4}He, ^{16,22}O, and ^{40}Ca from chiral nucleon-nucleon interactions. *Phys Rev C* (2014) 90:064619. doi:10.1103/PhysRevC.90.064619

52. Bonaiti F, Bacca S, Hagen G, Jansen GR. Electromagnetic observables of open-shell nuclei from coupled-cluster theory. *Phys Rev C* (2024) 110:044306. doi:10.1103/PhysRevC.110.044306

53. Marino F., Bonaiti F., Bacca S., Hagen G., Jansen G., Tichai A. (2024). *Recent advances in coupled cluster computations of open-shell atomic nuclei*. Available online at: https://arxiv.org/abs/2410.19511

54. Navin A, Anthony DW, Aumann T, Baumann T, Bazin D, Blumenfeld Y, et al. Direct evidence for the breakdown of the N = 8 shell closure in^{12}*be*. *Phys Rev Lett* (2000) 85:266–9. doi:10.1103/PhysRevLett.85.266

55. Pain SD, Catford WN, Orr NA, Angélique JC, Ashwood NI, Bouchat V, et al. Structure of ^{12}Be: intruder d-wave strength at n = 8. *Phys Rev Lett* (2006) 96:032502. doi:10.1103/PhysRevLett.96.032502

56. Giraud S, Zamora JC, Zegers RGT, Bazin D, Ayyad Y, Bacca S, et al. β^{+} gamow-teller strengths from unstable ^{14}O via the (d,^{2}He) reaction in inverse kinematics. *Phys Rev Lett* (2023) 130:232301. doi:10.1103/PhysRevLett.130.232301

Frontiers in Physics

TYPE Original Research
PUBLISHED 05 June 2025
DOI 10.3389/fphy.2025.1525170

OPEN ACCESS

EDITED BY
Benjamin Kay,
Argonne National Laboratory (DOE),
United States

REVIEWED BY
Stefano Burrello,
Laboratori Nazionali del Sud (INFN), Italy
Malte Albrecht,
Jefferson Lab (DOE), United States

*CORRESPONDENCE
C. Hebborn,
hebborn@ijclab.in2p3.fr

RECEIVED 08 November 2024
ACCEPTED 07 May 2025
PUBLISHED 05 June 2025

CITATION
Hebborn C and Nunes FM (2025) Systematic study of the propagation of uncertainties to transfer observables.
Front. Phys. 13:1525170.
doi: 10.3389/fphy.2025.1525170

Systematic study of the propagation of uncertainties to transfer observables

C. Hebborn[1,2,3]* and F. M. Nunes[2,3]

[1]Université Paris-Saclay, CNRS/IN2P3, IJCLab, Orsay, France, [2]Facility for Rare Isotope Beams, Michigan State University, East Lansing, MI, United States, [3]Department of Physics and Astronomy, Michigan State University, East Lansing, MI, United States

A systematic study of parametric uncertainties in transfer reactions is performed using the recently developed uncertainty quantified global optical potential (KDUQ). We consider reactions on the doubly-magic spherical nucleus ^{48}Ca and explore the dependence of the predicted (d,p) angular distribution uncertainties at different beam energies and for different properties of the final single-particle state populated by the reaction. Our results show that correlations between the uncertainties associated with the bound state potential and with the optical potentials may be important for correctly determining the uncertainty in the transfer cross sections (in our case, these do not add in quadrature). In general, we find small uncertainties in the predicted transfer observables: half-width of the 68% credible interval is roughly $5-10\%$, which is comparable to the experimental error on the transfer data. Finally, our results show that the relative magnitude of the parametric uncertainty in transfer observables increases with the beam energy and does not depend strongly on the properties of the final state.

KEYWORDS

nuclear reactions, optical model, single-nucleon transfer reactions, uncertainty quantification, single-particle properties

1 Introduction

Transfer reactions are widely used in nuclear experimental studies, either for extracting astrophysical information that cannot be obtained directly or for studying properties of the nucleus of interest (e.g., Refs. [1–11]). However, reaction theory is essential to interpret transfer reactions measurements [12, 13]. The properties we wish to extract from transfer reactions, such as spectroscopic factors (SF), asymptotic normalization coefficients (ANC) or neutron capture rates, depend strongly on the normalization of the transfer cross section while the model used to describe the reaction carries uncertainties that affect the normalization [12]. Thus, for a reliable interpretation of transfer measurements, it is crucial that we understand the uncertainties associated with the theory.

In this work we focus on (d,p) reactions. The preferred model for interpreting single-nucleon (d,p) transfer reactions is the adiabatic wave approximation (ADWA) [14, 15]. This model has the advantage that it includes deuteron breakup non-perturbatively, without increasing the computational cost as compared to the Distorted Wave Born Approximation (DWBA). It has also been shown to fare well compared to the state-of-the-art models in the field [16, 17]. In ADWA, the input interactions are nucleon optical potentials, in addition to potentials that bind the deuteron and the final state. From all the studies performed so far, optical potentials are the dominant source of uncertainty in ADWA predictions for transfer (d,p) cross sections. It is important not only to quantify those uncertainties but also understand how they may change with beam energy and specific properties of the final state being produced.

In the last few years, many studies have been performed to quantify the uncertainty in (d,p) reactions using Bayesian statistics [18–21]. These studies use optical potentials fitted for one projectile-target combination, at a specific beam energy, constrained with a single or a couple data sets. Typically, proton or neutron elastic scattering data at the relevant beam energies are used in a Bayesian calibration to obtain parameter posterior distributions for the optical potentials. The uncertainties in the (d,p) cross sections for the reaction are then obtained by sampling these posterior distributions, which are then propagated using the ADWA framework. Uncertainties obtained in [18–21] are large, in part due to the choice of the likelihood function [22]. By propagating uncertainties from each optical potential independently, no correlations between the neutron and proton optical potentials in the entrance channel are included, nor between those and the proton optical potential in the exit channel. Recent work on charge-exchange reactions has shown that the inclusion of such correlations can make a significant difference in the uncertainty estimate [23, 24].

Moreover, Ref. [21] studies the uncertainties coming from the single-particle potential that binds the neutron in the final state in (d,p) reactions, in addition to the uncertainties in the optical potential. By constraining the geometry of the binding potential with the asymptotic normalization coefficient, one can greatly reduce the uncertainties (see Figure 2 of Ref; [21]). If the ANC squared is poorly known the uncertainties in the (d,p) cross section are very large. If the ANC squared is known to say 10% then the uncertainties in the cross section are greatly reduced.

The recent development of an uncertainty-quantified global optical model (KDUQ) [25], based on the original work [26], provides another avenue to study the uncertainties in reactions. Propagating the parametric uncertainties from KDUQ to reaction observables has been done for specific cases (e.g., for knockout and transfer [27, 28] and charge-exchange [24]). In general, the uncertainties due to optical potentials in reaction observables can be influenced by many different details of the reaction process [29, 30]. Due to strong non-linearities in the reaction model, it is important to study these uncertainties more systematically to understand the impact of correlations in optical potential parameters and whether there are general features that emerge. KDUQ provides a unified effective framework to perform this study.

This work is a systematic study of the uncertainties associated with the optical potentials in transfer (d,p) observables. We use ^{48}Ca$(d,p)^{49}$Ca to set up the problem and consider a range of beam energies as well as a variety of final bound states with different properties. In Section 2, we briefly describe the reaction and statistical models used. In Section 3.1, we compare the predictions obtained with KDUQ to existing elastic scattering and transfer data, to establish our framework for a realistic case. In the rest of Section 3, we vary beam energies and final bound state properties (separation energy, angular momentum, nodes, etc.) and analyze the dependencies of the resulting uncertainties. Section 4 presents the conclusions of this work.

2 A brief summary of the theory used

2.1 Reaction theory

The finite-range ADWA [14] starts out by considering a full three-body picture for the transfer reaction $A(d,p)B$. As detailed in Ref. [14], it uses Weinberg states to then simplify the T-matrix to

$$T^{ADWA} = \langle \phi_{nA}\chi^{(-)}_{pB}|V_{np}|\phi_{np}\chi^{ad}_{d}\rangle. \tag{1}$$

In Equation 1, ϕ_{np} and ϕ_{nA} correspond to the deuteron bound state and single-particle state of the final nucleus B, V_{np} is the neutron-proton interaction and χ_{pB} is the outgoing distorted wave of the proton relative to the final nucleus B, obtained with the optical potential U_{pB} at the energy of the outgoing proton. The adiabatic distorted wave χ^{ad}_{d} is generated from the effective adiabatic potential:

$$U^{\text{eff}}_{Ap} = -\langle \phi_o|V_{np}\left(U_{nA}+U_{pA}\right)|\phi_o\rangle,$$

where U_{nA} and U_{pA} are the nucleon optical potentials between neutron/proton and the target evaluated at half the deuteron incoming energy. The wave function ϕ_o is the first Weinberg basis state, which is directly proportional to the deuteron bound state [14]. The T-matrix of Equation 1 assumes that the remnant term $(U_{nA}-U_{pB})$ is negligible. In ADWA calculations, the sources of parametric uncertainties are therefore the optical potentials used to generate the scattering states and the single-particle potentials used to model bound states.

More details about the ADWA and how to obtain numerical solutions for bound and scattering states can be found in Ref. [31]. In this work, we use the code NLAT [15] to perform all ADWA transfer calculations and the code FRESCO [32] to perform the elastic scattering calculations.

2.2 Statistical model

As mentioned in Section 1, we use the global optical potentials KDUQ [25] for all nucleon-nucleus interactions needed in the reaction model of Section 2.1, which is valid for $24 \le A \le 209$ and 1 keV $\le E \le 200$ MeV. In this work, we chose the democratic version of KDUQ which weighs every data point equally[1]. By performing a Bayesian calibration using a large set of reaction data (including nucleon elastic scattering angular distributions and analyzing powers, neutron total cross sections and proton reaction cross sections, all on stable nuclei), the authors of KDUQ obtained parameter posterior distributions and correlations for the 46 parameters of their global optical model. In this work, we use the 416 samples of their posterior distributions, published in Ref. [25], to compute the uncertainties in the transfer cross sections. We quantify the uncertainty in the transfer angular distribution in terms of the relative half-width of the 1σ credible interval at the peak of the angular distributions (corresponding to a scattering angle θ_{max}):

---

[1] We also consider the federal version of KDUQ [25], in which each data type is given equal weight on the overall likelihood. Using the federal KDUQ, we obtained transfer angular distributions exhibiting similar uncertainties as the ones obtained with the democratic KDUQ

$$\varepsilon_{68\%} = \frac{\sigma^{68\%}_{max}(\theta_{max}) - \sigma^{68\%}_{avg}(\theta_{max})}{\sigma^{68\%}_{avg}(\theta_{max})} \tag{2}$$

$$\text{with} \quad \sigma^{68\%}_{avg}(\theta_{max}) = \frac{\sigma^{68\%}_{max}(\theta_{max}) + \sigma^{68\%}_{min}(\theta_{max})}{2}$$

The test case we focus on is based on the ^{48}Ca(d,p)^{49}Ca (g.s) reaction. Our choice is mainly motivated by the availability of elastic and transfer data. Moreover, since no ^{48}Ca data were included in the KDUQ corpus, the analysis performed in this work share similar challenges as the ones on transfer data populating exotic nuclei. All optical potentials are taken *consistently* from KDUQ and evaluated at the relevant energies, i.e., all three nucleon-nucleus optical potentials are derived from the same KDUQ sample. This consistent treatment hence includes correlations between the various optical potential parameters. For describing the final state of the neutron, we take a standard radius and diffuseness $r_R = 1.25$ fm and $a_R = 0.65$ fm (STD) or we take the geometry of the real part of the KDUQ interaction (KDUQ-real). In both cases, we adjust the depth to reproduce the neutron separation energy and the parameters in the spin orbit term for the final bound-state potential are fixed: the depth is $V_{so} = 6$ MeV, the radius is $r_{so} = 1.25$ fm and the diffuseness is $a_{so} = 0.65$ fm. In the physical ^{49}Ca ground state, the neutron is in a $1p3/2$ orbital, bound by $S_n = 5.146$ MeV. We also consider in Section 3.3 other configurations for the final state being populated in the (d,p) reaction.

It must be underlined that KDUQ posterior distributions contain no constraints from bound state data. Our assumption is to consider that the geometry of the mean field generated by the target nucleus does not change considerably from bound to scattering states. This is consistent with the KDUQ assumption, since it uses an energy-independent parametrization for the radius and diffuseness of the real term, and these parameters are well constrained by the Bayesian calibration. When using 416 samples for the real radius and diffuseness of KDUQ and refitting the real depth to reproduce the correct neutron separation energy (KDUQ-real). The resulting ANC-squared $\mathcal{C}^2$ distribution (not shown) is slightly multimodal and is well constrained: its half-width is about 5%. Interestingly, the value predicted by KDUQ-real $\mathcal{C}^2 = 28.6 \pm 1.3$ fm^{-1} is consistent with the value $\mathcal{C}^2 = 32.1 \pm 3.2$ fm^{-1} [33] determined from the analysis of various ^{48}Ca(d,p)^{49}Ca (g.s.) datasets at various energies, i.e., 2 MeV, 13 MeV, 19 MeV, 30 MeV and 56 MeV [34–36]. This surprising agreement seems fortuitous, as ANCs for states of ^{87}Kr, ^{8}B and ^{10}B predicted by KDUQ do not match the values extracted from transfer and breakup data [37–39]. The KDUQ-real posteriors obtained in this way will also be used to quantify uncertainties from the neutron singe-particle interaction in ϕ_{nA}.

3 Results

3.1 The physical ^{48}Ca (*d,p*)^{49}Ca (g.s) reaction

Optical potentials are determined primarily from observables that are sensitive to the on-shell T-matrix. Transfer observables are also sensitive to properties of the T-matrix off-shell. It is thus not guaranteed, even if the optical potentials reproduce the corresponding elastic channels, that they describe the transfer data. Using the reaction ^{48}Ca(d,p)^{49}Ca (g.s) at 19 MeV, for which there is data [35].[2] We compare predictions using KDUQ with the corresponding data to assess the quality of the uncertainty quantification. We select nucleon elastic scattering data that is close to the energies relevant to the transfer reaction of interest ($E_n = 9.5$ MeV and $E_p = 9.5$ MeV in the entrance channel and $E_p = 21.9$ MeV in the exit channel) and compare the credible intervals generated from the KDUQ parameter posteriors with the actual data (with the quoted experimental error bars) [40–42]. The corresponding angular distributions are shown in Figure 1: (a) neutron elastic scattering for $E_{lab} = 12$ MeV, (b) proton elastic scattering for $E_{lab} = 14$ MeV, (c) proton elastic scattering for $E_{lab} = 25$ MeV. Note that the KDUQ global optical potential was not fitted on these data sets. The dark (light) shade corresponds to the 68% (95%) credible intervals[3].

The empirical coverage provides a sanity check for uncertainty quantification. Our empirical coverages for a x% model uncertainty are calculated as the number of data points, including a x% experimental error, that fall into the theoretical x% credible interval divided by the total number of data points in an angular distribution. These are shown in Figures 1D–F for the corresponding three elastic scattering examples. In an ideal situation, the predicted empirical coverage should line up with the black diagonal line[4]. In our calculations for proton elastic scattering, empirical coverages calculated at the high-confidence level are only slightly underestimated. However, for neutron scattering, there is a severe mismatch. This suggests that, in this case, the error on the data [40] and/or on the KDUQ parameters are seriously under-reported. To include unaccounted-for uncertainties, we have inflated the width of the posterior distributions of the depths, radii and diffuseness of the neutron-target potential, so that we can reproduce the correct empirical coverage specifically for 1σ. We do this by approximating the parameter distributions of the neutron-target potential U_{nA} to a multivariate Gaussian. We then rescale the covariance matrix by a factor: it turns out that we need to rescale these by 38, effectively rescaling uncertainties by a factor of $\sqrt{38} \sim 6$. Note that such approach, although simplistic, allows to keep the correlations between the optical potentials parameters informed by the large KDUQ corpus. We refer to this as KDUQ-n. Replacing KDUQ by KDUQ-n for U_{nA} results in the green bands in Figure 1A and the green dots in Figure 1D. As can be seen, the empirical coverage obtained for the 68% is now exactly 68%.

We now use these parameter posterior distributions and propagate the uncertainties to the ^{48}Ca(d,p)^{49}Ca (g.s.) reaction at beam energy $E_{lab} = 19$ MeV. In Figure 2, we show the predicted credible intervals for the corresponding transfer angular distributions: we compare the results obtained with the original KDUQ (blue bands) and those obtained when the neutron

---

[2] The uncertainties of this data set are not clearly reported. We consider a 10% relative error per data point, which is a typical error for transfer data on stable nuclei

[3] The x% credible intervals are computed as the smallest interval that include x% of the cross section predicted by the 416 samples of KDUQ

[4] All results in blue in Figure 1 correspond to the uncertainties from KDUQ when the data protocol is democratic [25].

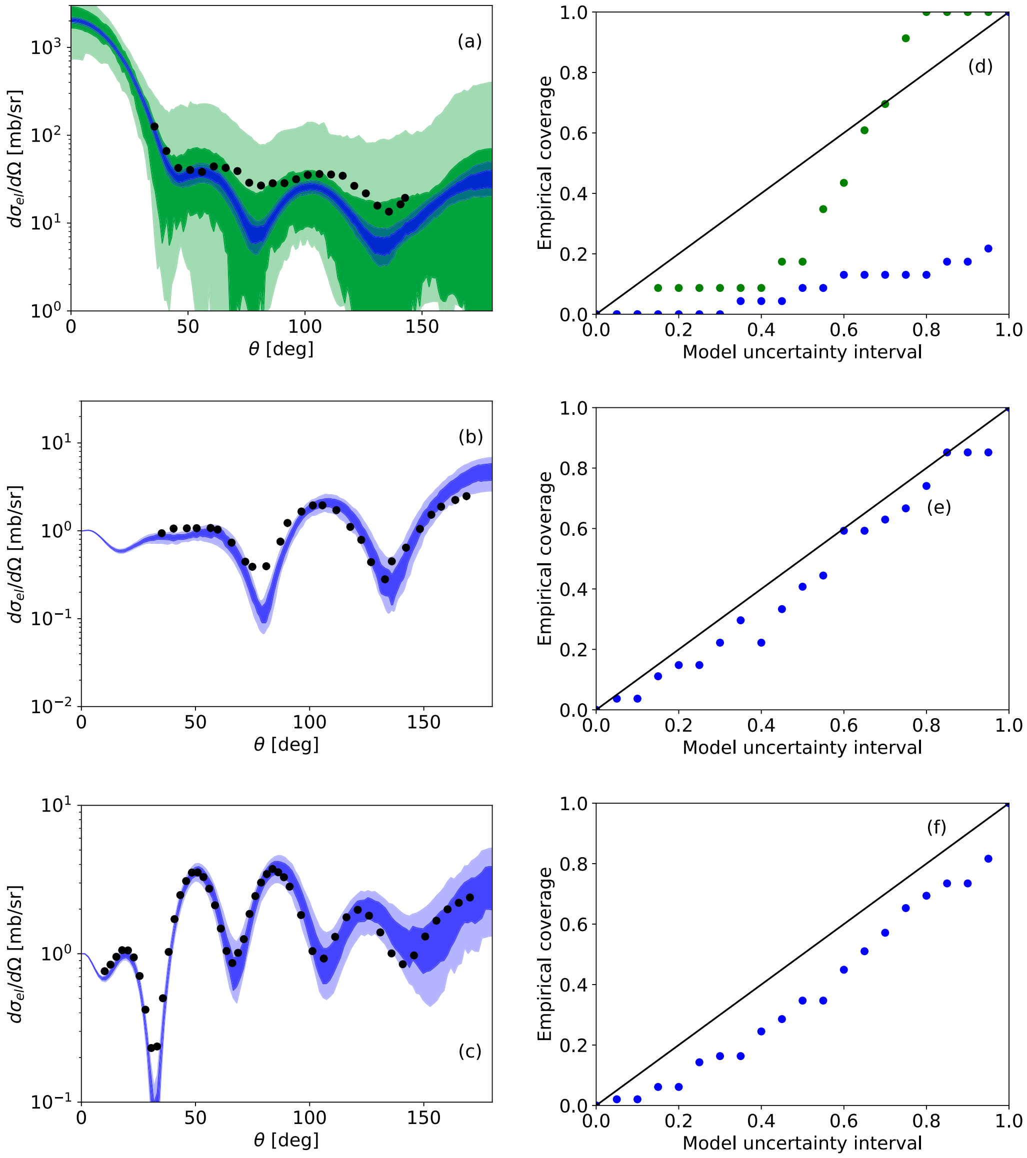

FIGURE 1
Angular distributions for the elastic scattering of **(A)** n+^{48}Ca at 12 MeV, **(B)** p+^{48}Ca at 14 MeV and **(C)** p+^{48}Ca at 25 MeV. The dark and light shaded blue bands correspond respectively to the 68% and 95% credible intervals obtained with optical potentials derived from the KDUQ posterior distribution. The green bands are obtained with rescaled KDUQ posterior distributions (referred as KDUQ-n) in the text. These predictions are compared with data from Refs. [40–42]. **(D–F)** Corresponding empirical coverage for elastic-scattering data.

interaction is replaced by KDUQ-n (green bands). In these calculations, we fix the neutron bound state using the STD geometry (discussed in Section 2.2). Figure 2 already includes the scaling by the SF, taking into account both the optical potential parameter uncertainties propagated in the ADWA model and the experimental error on the transfer data. This is done by adding in quadrature the errors ε_{opt} associated with the optical potential and $\bar{\varepsilon}_{SF}$ resulting from the fitting procedure to the transfer data. The uncertainty ε_{opt} is the standard deviation of the 416 SFs minimizing the χ^2 obtained from the transfer data and the theoretical predictions, e.g., obtained with each KDUQ sample. The variance $\bar{\varepsilon}^2_{SF}$ is calculated by averaging the variances on the SFs associated with each of the 416 fits. Further tests have shown that the total uncertainty on the SF is completely dominated by ε_{opt} for transfer data errors $\lesssim 10\%$, i.e., the total errors on the SFs are the same regardless of we include $\bar{\varepsilon}_{SF}$ or not.

The theoretical predictions for $\frac{d\sigma}{d\Omega}$ agree well with the data. At the 1σ level, the relative half-width $\varepsilon_{68\%}$ Equation 2 is 5% (16%) when using KDUQ (KDUQ-n). These uncertainties can be compared with the 20% full-width uncertainty shown in green in Figure 3 of [21] for the same reaction, at slightly higher beam energy. Note that the work in [21] uses local potentials with mock data (with 10% error) and systematically renormalizes the likelihood, effectively increasing the error on both proton and neutron optical potentials. These results demonstrate the benefit of a global parametrization: although there are no ^{48}Ca elastic angular distributions in the data corpus used to calibrate the KDUQ parameters, the uncertainties on

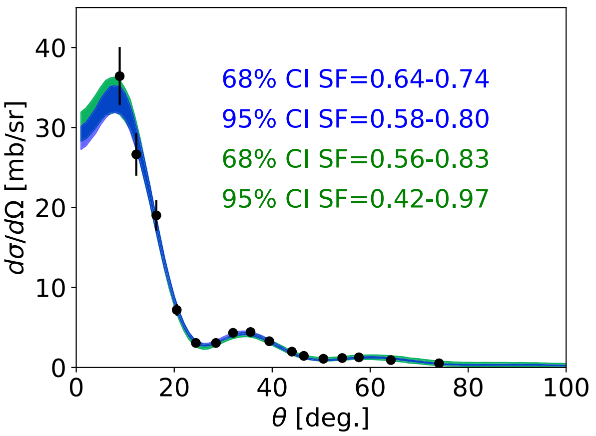

FIGURE 2
Angular distribution for ^{48}Ca(d,p)^{49}Ca (g.s.) at 19 MeV scaled to reproduce the first four forward data point, with the corresponding scaling factors (SFs) and their uncertainties. The shaded blue band corresponds to the 68% credible intervals respectively obtained with optical potentials derived from the same sample of the KDUQ posterior distribution. The green band is obtained using the KDUQ-n posterior distribution for U_{nA} and KDUQ posterior distribution for U_{pA} and U_{pB}. These predictions are compared with data from Ref. [35].

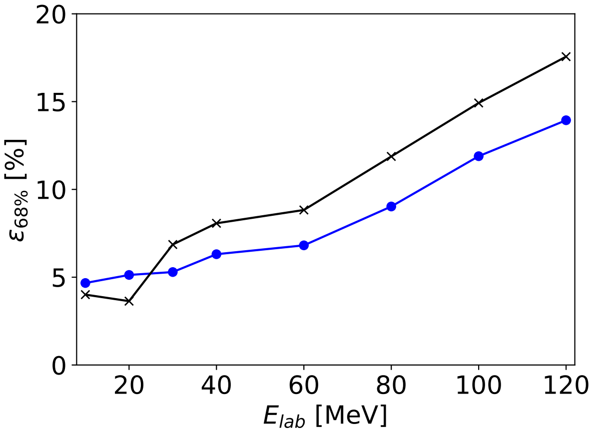

FIGURE 3
Relative half-width $\varepsilon_{68\%}$ Equation 2 for ^{48}Ca(d,p)^{49}Ca (g.s.), as a function of the beam energy. In blue are the results obtained with nucleon-nucleus interactions needed for the ADWA calculations derived consistently from the same KDUQ sample. The black line corresponds to the situation where all three interactions are derived from different KDUQ samples.

TABLE 1 Relative half-width $\varepsilon_{68\%}$ Equation 2 for ^{48}Ca(d,p)^{49}Ca (g.s.) at 19 MeV and, in parentheses, the corresponding relative half-width of the 1σ credible interval of the extracted SFs using the data from Ref. [35]. We consider the KDUQ original samples and the rescaled KDUQ posterior KDUQ-n (discussed in the text). Results are obtained when propagating only the uncertainties due to the optical potentials (first two lines), only the uncertainties due to the single-particle potential (third line) and both uncertainties (last line).

Uncertainties	Final bound state	KDUQ original	KDUQ-n
only scatt. States	STD	5% (SF 6%)	13% (SF 16%)
	KDUQ-real	5% (SF 5%)	13% (SF 16%)
only bound state	KDUQ-real	4% (SF 4%)	22% (SF 23%)
both scatt. States and bound state	KDUQ-real	5% (SF 5%)	24% (SF 20%)

the transfer predictions are reliable (of the Ca isotopes, the KDUQ data corpus includes only ^{40}Ca elastic angular distributions).

To complement our analysis, we also study the uncertainties associated with the single-particle potential used to generate the final bound state. We quantify its uncertainties using the geometry of the real part of the KDUQ interaction (KDUQ-real), as discussed in Section 2.2. We consider various cases in Table 1 for which we compute the relative half-widths of the transfer angular distribution $\varepsilon_{68\%}$ and of the extracted SF, which also account for the errors on the experimental transfer data. Specifically, we investigate if the geometry of the single-particle potentials, used to generate the final state, has an impact on the relative uncertainties due to the optical potentials in transfer observables. First, we include only uncertainties in the optical potential, for two choices of single-particle potentials. In the first two lines of Table 1, we compare the results obtained when using the STD single-particle potential ($r_R = 1.25$ fm and $a_R = 0.65$ fm) and the mean values of the real radius and diffuseness of KDUQ-real ($r_R = 1.17$ fm and $a_R = 0.689$ fm). One can see that the relative uncertainties stay rather constant, showing that the magnitude of relative uncertainties due to the optical potentials do not depend strongly on the geometry of the single-particle potential in the final state.

Then, we evaluate the uncertainties due to the choice of single-particle potentials, using the geometry of the real volume term of 416 KDUQ and KDUQ-n samples. In the KDUQ case, the uncertainty half-widths $\varepsilon_{68\%}$ are below 4% for both the peak of the distribution and the extracted SF, indicating that the KDUQ posterior distributions for r_R and a_R are quite constrained. The magnitude of the uncertainties on the peak of the transfer cross sections are similar to those on the ANC squared (see Section 2.2), suggesting that this reaction is quite peripheral. As expected, the uncertainties when using the KDUQ-n samples are larger. Interestingly, they are scaled by roughly the same factor $\sqrt{38} \sim 6$, as the one used to scale the KDUQ uncertainties (compare left and right column of the third line). This suggests that the uncertainties in the single-particle radius and diffuseness seem to propagate linearly to transfer observables. Finally, we include both the uncertainties due to the single-particle potential and the optical potentials (last line). Contrary to what was found in [21], in both cases KDUQ original and KDUQ-n, the total uncertainties cannot be deduced simply by summing in quadrature the two source uncertainties, hinting at the presence of strong correlations. These correlations are due to the interplay between the extension of the single-particle wavefunction, and the range of the real part of the neutron-target optical potential. Although in [21] the ANC-squared is explicitly used as a constrain, the single-particle potential parameter sampling is independent of the sampling of the optical potential parameters, whereas in this work, KDUQ-real used for the single-particle potential is perfectly correlated to KDUQ (or KDUQ-n) used for the optical potentials.

Having established a realistic foundation for the uncertainty estimates of the angular distributions of the ^{48}Ca$(d,p)^{49}$Ca (g.s.) reaction at $E_{lab} = 19$ MeV, for which we can compare to experimental data, we now explore how these uncertainties change with beam energy and how they evolve with various properties of the final bound state. In this exploration, no uncertainty quantification is included for the bound state interactions - the mean field that binds the neutron in the final state is kept fixed. We vary either the kinematics or the structure of the final state, and take the optical potential parameters from the same original KDUQ posterior distributions. This is done in order to show how the same parameter posteriors for optical potentials propagate through the model differently, depending on the details of the reaction. Obviously, because we are not including the additional error in KDUQ-n, nor the uncertainty in the bound state interaction, the overall magnitude of the uncertainty estimates shown in Sections 3.2 and 3.3 are underestimated. It is their variation with beam energy or single-particle properties that matters.

3.2 Uncertainties in transfer reactions with beam energy

We first analyze the dependence of the uncertainties on the beam energy. For this study, we keep the final bound state fixed using the STD single-particle geometry as described in Section 3.1, and take all optical potential posteriors from the original KDUQ parametrization. The relative half-width $\varepsilon_{68\%}$ Equation 2, evaluated at the peak of the transfer angular distribution for ^{48}Ca$(d,p)^{49}$Ca (g.s.), are shown in Figure 3. There is no convolution with the experimental error on the transfer data in this plot; only the theoretical uncertainties are considered.

We first consider ADWA calculations using all three optical potentials derived consistently from the same KDUQ sample (blue line). We find that the relative half-width $\varepsilon_{68\%}$ Equation 2 increases with the beam energy[5]. This can be explained by the fact that at higher beam energy, transfer observables become more sensitive to the short-range part of scattering wave functions, which are typically less constrained by observables used to calibrate optical potentials. This explanation was verified by comparing the relative uncertainties obtained when computing the short-range contribution to the radial integral of the T-matrix Equation 1, i.e., considering only d-^{48}Ca distances smaller than $R < r_R * 48^{1/3}$, to the uncertainties associated with the long-range contribution to the T-matrix.

To investigate the importance of correlations in the uncertainties of the optical potentials, we consider ADWA calculations using optical potentials derived from different KDUQ samples (black line). For almost all beam energies, the relative uncertainties are slightly larger than in the previous results, where all potentials were derived consistently from the same KDUQ sample. At the highest beam energies studied, the shift in $\varepsilon_{68\%}$ is about 25%.

3.3 Dependence on the properties of the final bound state

Next, we consider the effects of different properties of the final bound state, namely, the dependence of the uncertainty with the r.m.s Radius squared $\langle r^2 \rangle$, the angular momentum l, the number of nodes n_r and the separation energy S_n.

We first consider the effect of the single-particle potential radius r_R used to generate the final bound state wave function on the reaction ^{48}Ca$(d,p)^{49}$Ca (g.s) at 23 MeV. We take the original n-^{48}Ca bound wave function, in a $1p3/2$ orbital, and vary the mean field radius parameter in STD in the range $r_R = 1.0 - 1.4$ fm, along with the depth to reproduce the same separation energy. The results are shown in Figure 4: the transfer angular distributions for a range of single-particle potential radii are shown (on the left, panels a–e) and the relative half-width $\varepsilon_{68\%}$ Equation 2 as a function of the r.m.s Single-particle radius squared (on the right, panel f). The same message is relayed when plotting the uncertainty estimates as a function of the ANC squared.

We find that the diffraction pattern of the transfer angular distributions do not change significantly with radius. Expectedly, the magnitude of the transfer cross section increases with the single-particle potential radius r_R. Since these reactions are primarily peripheral, they scale with the ANC squared, which in turn is directly related to the r.m.s radius squared. However, the percent uncertainty remains roughly constant and small, similar to what was observed in Table 1. Further tests have shown that the same conclusions, i.e., independence of the shape, larger magnitude, small and constant uncertainties for the transfer cross sections, can be drawn when increasing the diffuseness a_R.

Next, we consider the dependence on the separation energy of the final state, of the uncertainty for the transfer cross section due to the optical potentials. We fix the STD geometry for the neutron single-particle potential to the original values (= 1.25 fm and $a_R = 0.65$ fm) and adjust the depth of this interaction to reproduce the neutron separation energies $S_n = 1.146$-15.146 MeV in the $1p3/2$ wave. We repeat the procedure considering a bound state in a $0p3/2$ orbital. The corresponding wave functions are shown in Figures 5A,B. The lower the separation energy, the more extended is the single-particle wave function. The resulting (d,p) angular distributions in Figure 6, panels (a-h) (resp. (i-n)) are obtained with a final bound state in the $1p3/2$ (resp. $0p3/2$) wave. In both cases, the peak of the angular distribution shifts to large angles for larger separation energy, as this directly increases the Q-value for the reaction and the momentum matching. The magnitude of the cross section is also affected: the cross sections are larger for bound states with smaller separation energies. This is due to the spatial extension of the final bound-state wave function.

The resulting relative half-width $\varepsilon_{68\%}$ Equation 2 are summarized in Figure 7. Here we include not only the uncertainties due to the optical potentials for transfer observables populating a bound state in the $1p3/2$ orbital (blue) and in the $0p3/2$ orbital (red), but also in the $1s1/2$ orbital (magenta). The uncertainties remain small (below 10%), regardless of separation energy, the number of nodes n_r and the angular momentum l of the neutron orbital in the final state.

---

[5] We do not compute transfer cross sections beyond $E_b = 120$ MeV as the cross sections then become forbiddingly small to measure

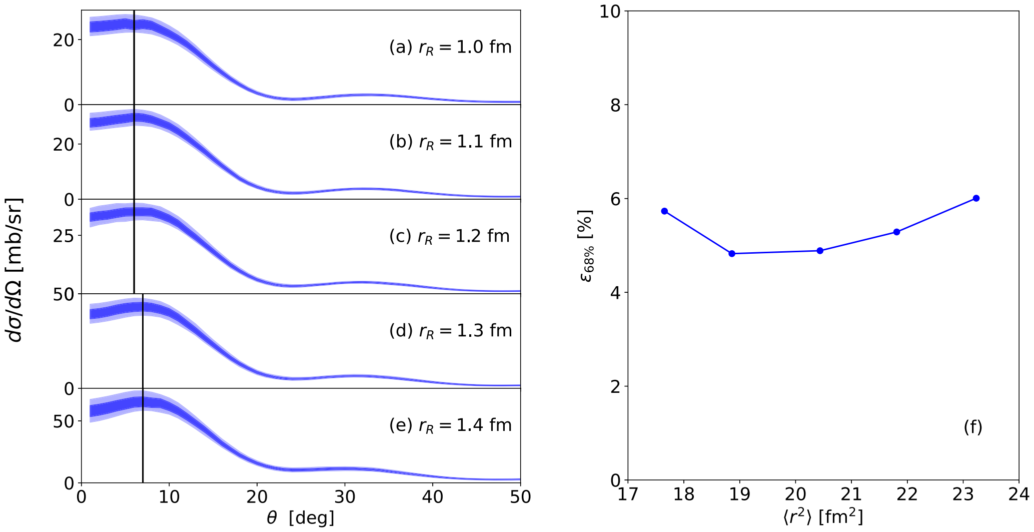

FIGURE 4
(a–e) Transfer angular distributions for ^{48}Ca(d,p)^{49}Ca (g.s.) at 23 MeV for a range of single-particle radii and **(f)** the relative half-width $\varepsilon_{68\%}$ Equation 2 as a function of the squared of the single-particle r.m.s radius $\langle r^2\rangle$. The vertical black lines in panels **(a–e)** represent the position of the peaks of the transfer distribution θ_{max}.

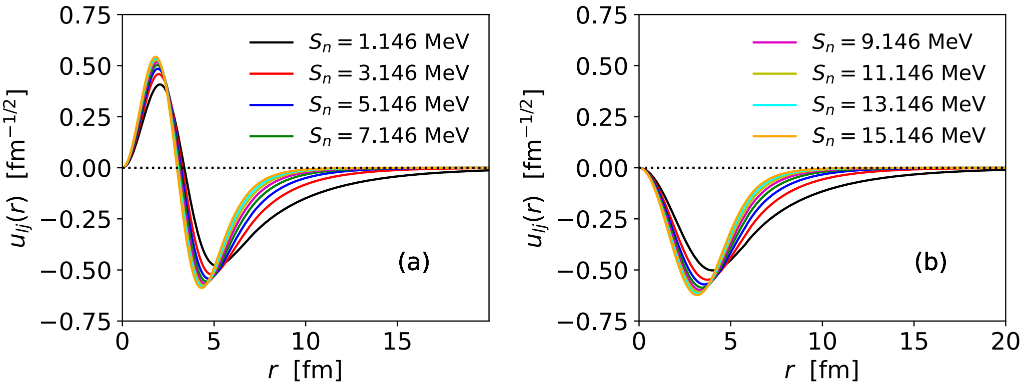

FIGURE 5
^{48}Ca s. p. Wave function for a n in a **(a)** $1p3/2$ and **(b)** $0p3/2$ states reproducing various separation energies S_n = 1.146-15.146 MeV.

4 Conclusion

In this work, we perform a systematic study of parametric uncertainties in (d,p) reactions, and their sensitivity to the kinematics of the reaction, as well as to the properties of the final bound state. The results were obtained using the posterior distribution of the global optical potential KDUQ, enabling us to study the impact of optical potential correlations on transfer observables.

By first analyzing a realistic case, we show that for proton scattering off the doubly-magic spherical nucleus ^{48}Ca, the elastic-scattering cross sections predicted with the KDUQ global optical potential reproduce well the available scattering data. The empirical coverage lies close to the ideal case, i. e., the diagonal, demonstrating the reliability of the uncertainty estimates of the KDUQ optical potential. However, KDUQ does not reproduce well the neutron scattering data on ^{48}Ca, suggesting that either the error on the data are seriously under-reported or the uncertainties of KDUQ are unrealistically small. To account for this, we rescale the KDUQ posterior to obtain an ideal empirical coverage at the 1σ level. By propagating the posterior distributions in a ADWA model, we find that the relative half-width of the 1σ credible interval at the peak of the transfer angular distributions is about 5% when using the KDUQ parameters, and 25% when using the rescaled KDUQ-n parameters. Moreover, we note that the uncertainties due to the single-particle binding potentials are below 5% when using KDUQ and 25% for the rescaled KDUQ-n. Interestingly, our results also show that, in transfer observables, the two uncertainties (from the single-particle binding potential and from the optical potentials) do not add in quadrature. This suggests the impact of correlations between the single-particle binding potential and the optical potential parameters is significant.

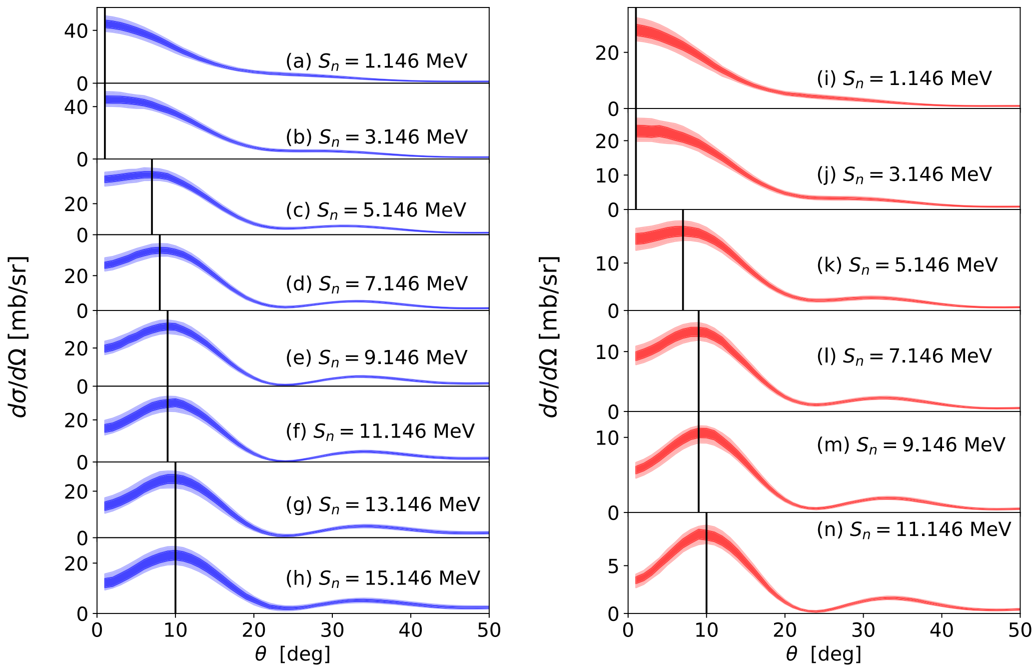

FIGURE 6
Transfer angular distributions for ^{48}Ca(d,p)^{49}Ca (g.s.) at 23 MeV, for different wave function shown in Figure 5. Panels **(a–h)** (resp. **(i–n)**) are obtained with ^{48}Ca s. p. Wave function for a n in a $1p3/2$ (resp. $0p3/2$). The vertical black lines in panels **(a–h)** represent the position of the peaks of the transfer distribution θ_{max}.

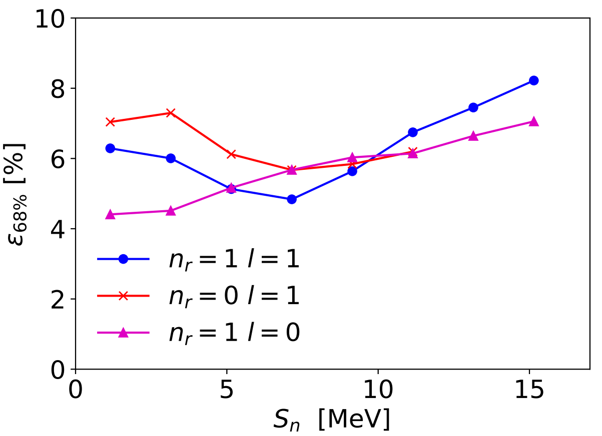

FIGURE 7
Relative half-widths $\varepsilon_{68\%}$ Equation 2 for various cases: the blue dots correspond to transfer cross sections populating a $1p3/2$ state, the red crosses to the population of a $0p3/2$ state and the magenta triangles to the population of a $1s1/2$ state. The corresponding single-particle wave functions and transfer observables are plotted in Figures 5, 6.

Then fixing the geometry of the single-particle potentials and considering the same KDUQ posterior distribution, we investigate how the uncertainties in transfer observables are influenced by the beam energy of the reaction and the properties of the final bound state. Since the same KDUQ posterior parameters are taken in all cases, the different uncertainties do not come from the evolution of KDUQ uncertainties across nuclei or with the beam energy, but are a direct consequence on how uncertainties propagate through the model differently, depending on the details of the reaction.

We show that at higher beam energy, the uncertainties in transfer observables increase. This is a direct consequence of the radial range probed by transfer reactions at various beam energies: transfer reactions at higher beam energies are more sensitive to the short-range part of the T-matrix, which is not well constrained for optical potentials fitted on elastic observables. We find that the correlations in the optical potentials used to generate the scattering states can change the uncertainty estimate by $20-25\%$.

We also investigate how uncertainties due to optical potentials depend on the properties of the final bound state: we vary the geometry of the single-particle potential, the binding energy, the orbital angular momentum and the number of nodes. As expected, the magnitude and the shape of the transfer cross sections change, as they are influenced by the spatial extension of the bound-state wave function, its orbital angular momentum and the Q-value of the reaction. Nevertheless, the relative half-widths $\varepsilon_{68\%}$ Equation 2 remain below 10% for all the cases covered in this study. When using KDUQ, the magnitude of the optical model uncertainties on transfer observables is not strongly dependent on the properties of the bound state.

Although our results are quite general, there were important simplifying assumptions that should be kept in mind. First, our analysis does not account for uncertainties associated with the ADWA approximation to the three-body dynamics. In particular, the neglect of the remnant term is likely to become inaccurate for reactions on light nuclei or populating halo final states. Second, we use the same KDUQ posterior distributions for all cases. This assumption likely leads to an underestimation of parametric uncertainties for transfer reactions at higher beam energies, since KDUQ's relative uncertainties are larger at higher energy (as illustrated in the volume integral in Figure 13 of Ref; [25]). Finally, the KDUQ posterior distribution we chose is likely unrealistic for nuclei with low separation energies, since these isotopes are far from the valley of stability. No data on unstable nuclei or deformed nuclei were included in the calibration of KDUQ and, therefore, one expects the uncertainties to grow substantially as we move to more exotic territory.

This systematic study enables us to draw three important take-away points. First, for well constrained potentials, such as KDUQ, small uncertainties in transfer observables can be expected, typically around 5%–10%. Second, there are significant correlations between the single-particle potential and optical potential parameters that impact the estimated uncertainties on the transfer. This argues for a framework where bound state data and scattering data can both be used to constrain the same interaction consistently, something that is obtained by imposing the dispersive relation [43]. We should expect that, because in the dispersive optical model bound state data is used to the potential, it may lead to a better constrained off-shell part of the T-matrix, hence reducing the uncertainties on reaction observables that do not solely depend on the on-shell properties (such as elastic scattering). Third, our results show that the relative uncertainty estimates of transfer angular distributions are not sensitive to detailed properties of the neutron orbital in the final state populated by the transfer reaction.

Data availability statement

The raw data supporting the conclusions of this article will be made available by the authors, without undue reservation.

Author contributions

CH: Conceptualization, Data curation, Formal analysis, Investigation, Software, Visualization, Writing – original draft, Writing – review and editing. FN: Conceptualization, Formal analysis, Investigation, Writing – original draft, Writing – review and editing.

Funding

The author(s) declare that financial support was received for the research and/or publication of this article. The work of FN was in part supported by the U.S. Department of Energy grant DE-SC0021422 and National Science Foundation CSSI program under award No. OAC-2004601 (BAND Collaboration).

Acknowledgments

CH and FN. thank Kyle Beyer, Manuel Catacora-Rios, Garrett King and other members of the few-body reaction group at MSU for their careful reading of the manuscripts and their comments. CH thanks Cole Pruitt and Gregory Potel for interesting discussions regarding the results of this work. We gratefully acknowledge computational support from iCER at Michigan State University.

Conflict of interest

The authors declare that the research was conducted in the absence of any commercial or financial relationships that could be construed as a potential conflict of interest.

The handling editor BK declared a past co-authorship with the author CH.

Generative AI statement

The author(s) declare that no Gen AI was used in the creation of this manuscript.

Publisher's note

References

1. Kay BP, Schiffer JP, Freeman SJ. Quenching of cross sections in nucleon transfer reactions. *Phys Rev Lett* (2013) 111:042502. doi:10.1103/physrevlett.111.042502

2. Avila ML, Rogachev GV, Koshchiy E, Baby LT, Belarge J, Kemper KW, et al. Constraining the 6.05 MeV 0^+ and 6.13 MeV 3^- cascade transitions in the $^{12}C(\alpha,\gamma)^{16}O$ reaction using the asymptotic normalization coefficients. *Phys Rev Lett* (2015) 114:071101. doi:10.1103/physrevlett.114.071101

3. Walter D, Pain SD, Cizewski JA, Nunes FM, Ahn S, Baugher T, et al. Constraining spectroscopic factors near the *r*-process path using combined measurements: $^{86}Kr(d,p)^{87}Kr$. *Phys Rev C* (2019) 99:054625. doi:10.1103/physrevc.99.054625

4. Salathe M, Crawford HL, Macchiavelli AO, Kay BP, Hoffman CR, Ayangeakaa AD, et al. Search for the $1/2^+$ intruder state in ^{35}P. *Phys Rev C* (2020) 102:064317. doi:10.1103/physrevc.102.064317

5. Lalanne L, Sorlin O, Assié M, Hammache F, de Séréville N, Koyama S, et al. Evaluation of the $^{35}K(p,\gamma)^{36}Ca$ reaction rate using the $^{37}Ca(p,d)^{36}Ca$ transfer reaction. *Phys Rev C* (2021) 103:055809. doi:10.1103/PhysRevC.103.055809

6. Hammache F, de Sereville N. Transfer reactions as a tool in nuclear astrophysics. *Front Phys* (2021) 8:2020. doi:10.3389/fphy.2020.602920

7. Kay BP, Tang TL, Tolstukhin IA, Roderick GB, Mitchell AJ, Ayyad Y, et al. Quenching of single-particle strength in A = 15 nuclei. *Phys Rev Lett* (2022) 129:152501. doi:10.1103/physrevlett.129.152501

8. Lalanne L, Sorlin O, Poves A, Assié M, Hammache F, Koyama S, et al. Structure of ^{36}Ca under the coulomb magnifying glass. *Phys Rev Lett* (2022) 129:122501. doi:10.1103/physrevlett.129.122501

9. Jones KL, Bey A, Burcher S, Allmond JM, Galindo-Uribarri A, Radford DC, et al. Neutron transfer reactions on the ground state and isomeric state of a ^{130}Sn beam. *Phys Rev C* (2022) 105:024602. doi:10.1103/physrevc.105.024602

10. Bennett SA, Garrett K, Sharp DK, Freeman SJ, Smith AG, Wright TJ, et al. Direct determination of fission-barrier heights using light-ion transfer in inverse kinematics. *Phys Rev Lett* (2023) 130:202501. doi:10.1103/physrevlett.130.202501

11. Hebborn C, Avila ML, Kravvaris K, Potel G, Quaglioni S. Impact of the ^{6}Li asymptotic normalization constant onto α-induced reactions of astrophysical interest. *Phys Rev C* (2024) 109:L061601. doi:10.1103/physrevc.109.l061601

12. Nunes F, Potel G, Poxon-Pearson T, Cizewski J. Nuclear reactions in astrophysics: a review of useful probes for extracting reaction rates. *Annu Rev Nucl Part Sci* (2020) 70:147–70. doi:10.1146/annurev-nucl-020620-063734

13. Timofeyuk NK, Johnson RC. Theory of deuteron stripping and pick-up reactions for nuclear structure studies. *Prog Part Nucl Phys* (2020) 111:103738. doi:10.1016/j.ppnp.2019.103738

14. Johnson RC, Tandy PC. An approximate three-body theory of deuteron stripping. *Nucl Phys A* (1974) 235:56–74. doi:10.1016/0375-9474(74)90178-x

15. Titus LJ, Ross A, Nunes FM. Transfer reaction code with nonlocal interactions. *Comput Phys Commun* (2016) 207:499–517. doi:10.1016/j.cpc.2016.06.022

16. Nunes FM, Deltuva A. Adiabatic approximation versus exact faddeev method for (*d, p*) and (*p, d*) reactions. *Phys Rev C* (2011) 84:034607. doi:10.1103/physrevc.84.034607

17. Upadhyay NJ, Deltuva A, Nunes FM. Testing the continuum-discretized coupled channels method for deuteron-induced reactions. *Phys Rev C* (2012) 85:054621. doi:10.1103/physrevc.85.054621

18. Lovell AE, Nunes FM. Constraining transfer cross sections using bayes' theorem. *Phys Rev C* (2018) 97:064612. doi:10.1103/physrevc.97.064612

19. King GB, Lovell AE, Nunes FM. Uncertainty quantification due to optical potentials in models for (*d, p*) reactions. *Phys Rev C* (2018) 98:044623. doi:10.1103/physrevc.98.044623

20. Lovell AE, Nunes FM, Catacora-Rios M, King GB. Recent advances in the quantification of uncertainties in reaction theory. *J Phys G: Nucl Part Phys* (2020) 48:014001. doi:10.1088/1361-6471/abba72

21. Catacora-Rios M, Lovell AE, Nunes FM. Complete quantification of parametric uncertainties in (*d, p*) transfer reactions. *Phys Rev C* (2023) 108:024601. doi:10.1103/physrevc.108.024601

22. Pruitt CD, Lovell AE, Hebborn C, Nunes FM. The role of the likelihood for elastic scattering uncertainty quantification. *Phys Rev C* (2024) 110:064606. doi:10.1103/PhysRevC.110.064606

23. Whitehead TR, Poxon-Pearson T, Nunes FM, Potel G. Prediction for (*p, n*) charge-exchange reactions with uncertainty quantification. *Phys Rev C* (2022) 105:054611. doi:10.1103/physrevc.105.054611

24. Smith AJ, Hebborn C, Nunes FM, Zegers RGT. Uncertainty quantification in (*p, n*) reactions. *Phys Rev C* (2024) 110:034602. doi:10.1103/physrevc.110.034602

25. Pruitt CD, Escher JE, Rahman R. Uncertainty-quantified phenomenological optical potentials for single-nucleon scattering. *Phys Rev C* (2023) 107:014602. doi:10.1103/physrevc.107.014602

26. Koning A, Delaroche J. Local and global nucleon optical models from 1 keV to 200 MeV. *Nucl Phys A* (2003) 713:231–310. doi:10.1016/s0375-9474(02)01321-0

27. Hebborn C, Nunes FM, Lovell AE. New perspectives on spectroscopic factor quenching from reactions. *Phys Rev Lett* (2023) 131:212503. doi:10.1103/physrevlett.131.212503

28. Hebborn C, Nunes FM, Lovell AE. Erratum: new perspectives on spectroscopic factor quenching from reactions. *Phys Rev Lett* (2024) 132:139901. doi:10.1103/physrevlett.132.139901

29. Hebborn C, Whitehead TR, Lovell AE, Nunes FM. Quantifying uncertainties due to optical potentials in one-neutron knockout reactions. *Phys Rev C* (2023) 108:014601. doi:10.1103/PhysRevC.108.014601

30. Hebborn C, Nunes FM, Potel G, Dickhoff WH, Holt JW, Atkinson MC, et al. Optical potentials for the rare-isotope beam era. *J Phys G: Nucl Part Phys* (2023) 50:060501. doi:10.1088/1361-6471/acc348

31. Thompson IJ, Nunes FM. *Nuclear reactions for astrophysics*. Cambridge University Press (2009).

32 . Thompson IJ. Coupled reaction channels calculations in nuclear physics. *Comp Phys Rep* (1988) 7:167–212. doi:10.1016/0167-7977(88)90005-6

33. Mukhamedzhanov AM, Nunes FM, Mohr P. Benchmark on neutron capture extracted from (*d, p*) reactions. *Phys Rev C* (2008) 77:051601. doi:10.1103/PhysRevC.77.051601

34. Rapaport J, Sperduto A, Salomaa M. Analysis of the 48Ca(d,p)49Ca reaction for incident energies below and above the coulomb barrier. *Nucl Phys A* (1972) 197:337–51. doi:10.1016/0375-9474(72)91015-9

35. Metz WD, Callender WD, Bockelman CK. Forbidden transitions in the ^{48}Ca(*d,p*)^{49}Ca reaction. *Phys Rev C* (1975) 12:827–44. doi:10.1103/PhysRevC.12.827

36. Uozumi Y, Iwamoto O, Widodo S, Nohtomi A, Sakae T, Matoba M, et al. Single-particle strengths measured with 48Ca(d,p)49Ca reaction at 56 mev. *Nucl Phys A* (1994) 576:123–37. doi:10.1016/0375-9474(94)90740-4

37. Walter D, Pain SD, Cizewski JA, Nunes FM, Ahn S, Baugher T, et al. Constraining spectroscopic factors near the *r*-process path using combined measurements: ^{86}Kr (*d,p*)^{87}Kr. *Phys Rev C* (2019) 99:054625. doi:10.1103/PhysRevC.99.054625

38. Sürer O, Nunes FM, Plumlee M, Wild SM. Uncertainty quantification in breakup reactions. *Phys Rev C* (2022) 106:024607. doi:10.1103/PhysRevC.106.024607

39. Fernandes JC, Crespo R, Nunes FM. How unique is the asymptotic normalization coefficient method? *Phys Rev C* (2000) 61:064616. doi:10.1103/PhysRevC.61.064616

40. Mueller JM, Charity RJ, Shane R, Sobotka LG, Waldecker SJ, Dickhoff WH, et al. Asymmetry dependence of nucleon correlations in spherical nuclei extracted from a dispersive-optical-model analysis. *Phys Rev C* (2011) 83:064605. doi:10.1103/physrevc.83.064605

41. Lombardi JC, Boyd RN, Arking R, Robbins AB. Nuclear sizes in ^{40,44,48}Ca. *Nucl Phys A* (1972) 188:103–14. doi:10.1016/0375-9474(72)90186-8

42. McCamis RH, Nasr TN, Birchall J, Davison NE, van Oers WTH, Verheijen PJT, et al. Elastic scattering of protons from ^{40,42,44,48}Ca from 20 to 50 MeV and nuclear matter radii. *Phys Rev C* (1986) 33:1624–33. doi:10.1103/physrevc.33.1624

43. Dickhoff W, Charity R. Recent developments for the optical model of nuclei. *Prog Part Nucl Phys* (2019) 105:252–99. doi:10.1016/j.ppnp.2018.11.002

frontiers | Frontiers in Physics

TYPE Review
PUBLISHED 26 June 2025
DOI 10.3389/fphy.2025.1537948

OPEN ACCESS

EDITED BY
Alan Wuosmaa,
University of Connecticut, United States

REVIEWED BY
Mengoni Daniele,
National Institute of Nuclear Physics of Padova, Italy
Chong Qi,
Royal Institute of Technology, Sweden

*CORRESPONDENCE
S.D. Pain,
✉ painsd@ornl.gov

RECEIVED 02 December 2024
ACCEPTED 30 April 2025
PUBLISHED 26 June 2025

CITATION
Pain SD (2025) Direct reactions for astrophysical p-capture rates with ORRUBA and GODDESS.
Front. Phys. 13:1537948.
doi: 10.3389/fphy.2025.1537948

Direct reactions for astrophysical p-capture rates with ORRUBA and GODDESS

S. D. Pain*

Physics Division, Oak Ridge National Laboratory, Oak Ridge, TN, United States

Understanding the nucleosynthesis and energy generation in quiescent and explosive stellar burning requires a detailed understanding of reaction rates on many unstable nuclides. Such reaction rates are often governed by the properties of low-lying, isolated proton resonances. Though direct measurements of resonance strengths are ultimately desired, and are a focus of rare isotope beam facilities worldwide, such tour-de-force experiments must be guided by indirect techniques, in order to know resonance energies, J^{π} assignments, and estimated widths, to inform targeted measurements. Furthermore, some important low-lying resonances may be too weak for direct measurements with radioactive beams, and indirect techniques provide the only practical constraints. Additionally, there has been growing interest in the astrophysical role of isomeric states, which can influence the reaction flow in nucleosynthetic reaction networks, and hence impact the quantitative interpretation of astronomical observables, such as γ-ray signatures, and elemental and isotopic ratios. Properties of single-proton resonances can be obtained by exploiting the selectivity of direct reactions, such as single-nucleon transfer and charge-exchange reactions. Constraining proton-capture rates via direct reactions has been a focus of the astrophysics program at ORNL for over two decades, spurring the development of the ORRUBA and GODDESS detector systems. Herein, a review of recent developments in instrumentation and radioactive beam delivery (including isomeric beam experiments) is presented, along with some specific examples of astrophysically interesting *sd*-shell nuclides, which have been a target of recent ORRUBA and GODDESS experiments.

KEYWORDS

direct reactions, isomers, nucleosynthesis, novae, x-ray bursts

1 Introduction

Astrophysical radiative proton-capture reaction rates are often governed by the properties of low-lying discrete proton resonances. In order to constrain the astrophysical reaction rate, the location and strengths of these resonances must be known. However, as the reaction network typically involves short-lived nuclides, complete measurements of proton excitation functions over the astrophysically-important energy range on many important nuclides are not within reach. Consequently, only the most important resonances must be targeted for direct measurement of their strengths. To this end, recoil separators optimized for measuring radiative-capture reactions from isolated resonances in inverse kinematics have been developed across the globe, including the DRAGON recoil separator at TRIUMF, the Daresbury Recoil Separator at the (now closed) Holifield Radioactive Ion

Beam Facility (HRIBF), the St George separator at the Nuclear Science Laboratory at Notre Dame, and most recently the SECAR recoil separator at the nascent Facility for Rare Isotope Beams (FRIB).

Though ultimately such direct measurements of resonance strengths are desired, indirect techniques are needed to initially locate and constrain the resonances, so that the most important resonances can be identified. Furthermore, in some cases, important low-energy resonances are too weak for direct radiative-capture reaction measurements with radioactive beams in the foreseeable future; in these cases, indirect techniques are the only way of ascertaining these resonance strengths. Various direct reactions, such as single-particle transfer and charge-exchange reactions, have long been employed for this purpose. The reaction can be chosen to selectively populate certain states (such as states of strong single-particle character, or those of low spin). Such reactions can provide resonance energies, determine the proton orbital angular momenta (ℓ_p) and J^π assignments (determining barrier penetrabilities) and in some cases spectroscopic factors (informing the single-particle width of the resonance) that are critical to determining the resonance strengths and hence the astrophysical reaction rate.

In recent years, as focus shifted toward reactions of radioactive nuclides, which dominate the reaction network in explosive nucleosynthesis, instrumentation and techniques for performing direct reactions in inverse kinematics with radioactive beams have been advanced. There have been a number of excellent reviews of recent progress [1–4]. Herein, some specific developments are reviewed in the context of the silicon detector array ORRUBA (Section 3.1), encompassing the GODDESS coupling to the large germanium detector arrays Gammasphere and GRETINA (Section 3.2), and utilization of new opportunities in rare isotope beam delivery enabling reaction measurements on beams in isomeric states (Section 5).

The manuscript is organized as follows. In Section 2, the formalism of radiative-capture reactions though isolated resonances is outlined. In Section 3, the ORRUBA/GODDESS instrumentation for the measurement of direct reactions is discussed. Following this, Section 4 details some methods by which direct reactions can be used to constrain resonance strengths. Section 5 outlines recent efforts and opportunities aimed at constraining reactions on nuclei in isomeric states. Finally, in Section 6, a number of astrophysically-motivated cases are discussed, pertaining to proton-induced nucleosynthesis in massive stars, novae and x-ray bursts. These cases all involve odd-odd $N = Z$ *sd*-shell nuclides, which have been a focus of the ORRUBA and GODDESS physics program over the past two decades.

2 Radiative-capture reactions through isolated resonances

Though direct measurements of radiative-capture reactions on radioactive nuclides are ultimately desired, the limited intensities and high cost associated with radioactive beams makes the measurement of complete excitation functions across the Gamow window unfeasible. However, at the low temperatures associated with quiescent stellar burning, and the hot CNO cycle and breakout into the rp process in novae, radiative-capture rates are often dominated by capture through isolated low-lying discrete resonances. In an astrophysical environment of temperature T, the reaction rate per-particle-pair for radiative capture through an isolated resonance is given by

$$< \sigma v > = \left(\frac{2\pi}{\mu kT}\right)^{2/3} \exp\left(\frac{-E_r}{kT}\right)\omega\gamma, \tag{1}$$

where μ is the reduced mass for the entrance channel. This reaction rate is proportional exponentially to the resonance energy E_r, and linearly to the resonance strength ($\omega\gamma$), where

$$\omega\gamma = \frac{2J_f + 1}{(2J_t + 1)(2J_p + 1)} \frac{\Gamma_p \Gamma_\gamma}{\Gamma}. \tag{2}$$

Here, Γ represents the total width of the resonance for all open channels ($\Gamma = \Gamma_p + \Gamma_\gamma + \cdots$), and J_p, J_t and J_f are respectively the spins of the proton, “target” nucleus, and the resonance through which the reaction proceeds.

Rather than measure the complete excitation function over the Gamow window, it is therefore possible to target only the most important resonances, and sum their contributions as a function of temperature, to obtain the total reaction rate. Though this substantially reduces amount of experimental data needed, to just measurements of the strength of a handful of important resonances, it introduces a problem that the resonances (and hence the bombarding energies at which to measure) are not known *a priori*. It is therefore critical that the energies and approximate strengths of resonances in the vicinity of the Gamow window must first be identified, such that direct measurements can subsequently target only those resonances anticipated to contribute appreciably to the astrophysical reaction rate.

It can be seen from Equation 2 that determining the energies of resonances in the proximity of the Gamow window is the most crucial component, as this highlights which states may contribute, and constrains their contribution due to the exponential dependence on resonance energy. Having determined resonance energies, further constraints on $\omega\gamma$ can stem from determining the spins of the states, or constraining the widths from scattering or branching ratio measurements. For low-energy resonances, where the barrier penetrability dominates, constraints on energies and spins can be substantially constraining on $\omega\gamma$.

Though there are numerous ways in which resonances can be identified and their strengths constrained, direct reactions, such as transfer and charge-exchange reactions, provide a number of benefits [1, 3], including being able to constrain energies, spins, and ultimately strengths of multiple resonances in a single measurement. Level energies can be determined, either through two-body reaction kinematics or, often more precisely, via the detection of de-excitation γ rays. J^π assignments can be made by measurement of the angular distributions of reaction ejectiles, which are characteristic of the angular momentum of the transferred particle. Furthermore, if a reaction can be selected which populates the states of interest via transfer of the same particle as is captured in the astrophysical reaction, cross sections from the transfer reaction can be used to constrain the resonant-capture cross section. This is usually undertaken by gaining insight into the overlap of the many-body wavefunction of the state with a pure single-particle state: i.e., the extraction of single-particle spectroscopic factors. This is discussed further in Section 4.3.

3 Direct reaction instrumentation

Using direct reactions with radioactive beams to constrain astrophysical reaction rates has been a major focus of the astrophysics program at Oak Ridge National Laboratory over the last two decades. Stemming from the astrophysics program at the HRIBF, charged-particle detectors for radioactive-beam experiments have been developed in collaborations based at ORNL, including silicon detector arrays optimized for inverse-kinematics experiments (the SIDAR array of YY1 detectors [5], based on the LEDA design [6], followed by the development of ORRUBA [7, 8]), and fast ionization chambers for the detection and identification of beam-like recoils [9]. Since the closure of the HRIBF over a decade ago, these detectors have been deployed at various facilities across the US, coupled to the large semiconductor γ-ray arrays (Gammasphere and GRETINA) and large recoil separators (S800, FMA, and, in future, SECAR) and the JENSA gas-jet target. Below, some basic details of these detectors are discussed.

3.1 ORRUBA

ORRUBA [7] is a high-solid-angle silicon detector array designed for the measurement of charged-particle reactions with radioactive beams. The position sensitivity of the array, which amounts to approximately 1° resolution in polar angle, was designed around the requirements of inverse-kinematics experiments with radioactive beams at Coulomb-barrier energies (~5 MeV/u). The design was initially optimized for measuring (d,p) reactions on heavy fission fragment beams, which were a focus of the research program at the HRIBF at ORNL. The original array comprised two 12-fold rings of custom-designed resistive-strip X3 detectors from Micron Semiconductor, covering angles from ~ 45° to 135°. In the downstream ring, detector telescopes were deployed (using 65-μm-thick BB10 detectors) backed by 1000-μm-thick X3 detectors) for particle identification. For the upstream barrel, which typically only detects particles lighter than the target (i.e., protons), a single layer of 1000-μm-thick X3 detectors were deployed. Angles further upstream were subtended, when needed, by the SIDAR array of YY1 detectors, typically in a lampshade configuration.

In more recent years, the X3 detectors have been replaced with sX3 detectors (Figure 1), which include 4-fold non-resistive segmentation on the Ohmic contact, for improved energy resolution. Concurrently, the YY1 lampshade was replaced by an annular QQQ5 detector endcap to the sX3 barrel [8, 10], resulting in a more compact array, with near seamless polar angular coverage, enabling the array to be mounted inside major γ-ray detector arrays (see Section 3.2). The design of the QQQ5 detectors involves radial segmentation which is graded in pitch, placing increasingly finer segmentation away from the beam axis, to match the steepness of the kinematic shifts from either pickup or stripping reactions in inverse kinematics, in order to optimize resolution and channel count.

ORRUBA operates as a standalone detector using a fast ionization chamber as a recoil detector (Section 3.3), coupled to recoil separators such as the S800 at FRIB, and operates as the main particle detector for the JENSA gas-jet target [11, 12].

3.2 GODDESS

For many direct-reaction measurements, the detection of γ rays in coincidence with charged particles is either necessary (Coulomb-excitation measurements, for instance) or highly advantageous. For measurements such as particle transfer reactions, γ rays aid significantly in separating closely-spaced states populated in the reaction. In addition to the improved energy resolution of γ-ray detection, in many cases neighboring levels decay to different states, leading to better separation in γ-ray energy than the difference in excitation energy. Furthermore, γ rays carry additional information on the states populated (their decay paths, angular distributions, lifetimes, etc.) and can provide information on states not populated directly in the transfer reaction, but fed by decay.

Motivated by these advantages, there has been much investment across the globe in couplings of high-resolution and high-efficiency charged-particle and γ-ray detectors, with a focus on measuring direct reactions on radioactive beams in inverse kinematics. These include TIARA [13] coupled to EXOGAM (GANIL), the SHARC array [14] coupled to the TIGRESS (TRIUMF), TREX [15] and more recently HI-TREX [16] coupled to Miniball (ISOLDE), MUGAST coupled to AGATA [17] (GANIL), and the GODDESS coupling [18] of ORRUBA [7] to Gammasphere [19] and GRETINA [20–24].

GODDESS [18] (Pain et al., forthcoming) is a coupling of an upgraded version of ORRUBA to the large semiconductor γ-ray detector arrays in the US: Gammasphere and GRETINA (and, in the near future, GRETA [25]). GODDESS has been in routine operation with GRETINA since 2019 (see Figure 2), following its original deployment with Gammasphere in 2015. To date, GODDESS campaigns have been performed at ATLAS (2015, 2019, 2021, 2025), and FRIB (2024). In its default configuration, GODDESS provides near-seamless charged-particle coverage from ~15° to ~165°, with ~1° of polar angular resolution and ~80% azimuthal coverage throughout this range, with particle identification in the forward hemisphere. GODDESS can be operated with a compact ionization chamber (Section 3.3) that mounts at zero degrees, or coupled to recoil separators such as the FMA and the S800.

In preparation for the deployment of GRETA at FRIB, at the time of writing GODDESS is being upgraded. A slightly smaller configuration, with new endcap detectors and a new vacuum chamber, will allow compatibility with the nearly full implementation of GRETA. This will provide a quasi-4π particle-γ spectrometer with semiconductor resolution for FRIB.

3.3 MAGIC

For inverse-kinematics experiments with radioactive beams, detection and identification of the beam-like recoil is often desirable. Firstly, RIBs are often delivered with contaminants, so event-by-event identification of the recoil is needed to associate reaction ejectiles with the beam constituent of interest. Secondly, reactions are often performed on targets with undesired elements (such as the carbon component of polyethylene and deuterated polyethylene targets). Reactions on these nuclides, such as fusion-evaporation reactions, result in substantially different recoils (both nuclide and energy), which can be readily separated by measurement of the beam-like recoil downstream of the target.

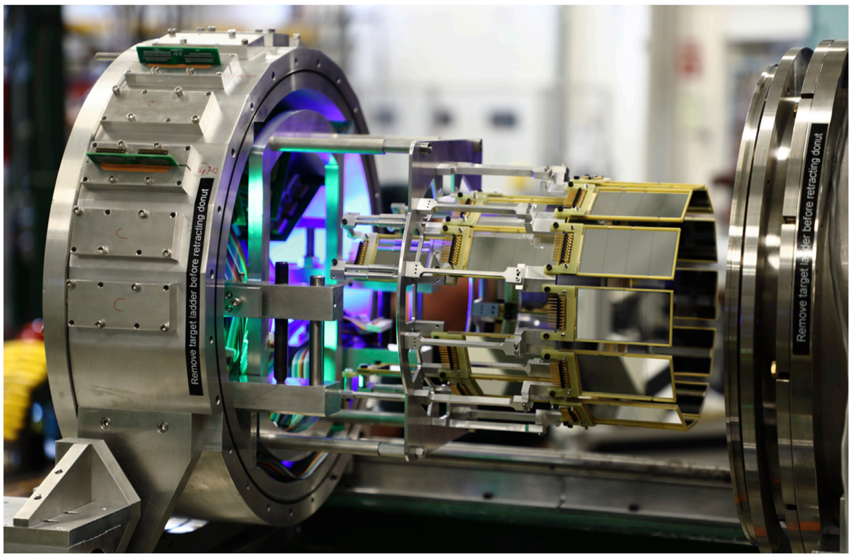

FIGURE 1
Photograph of ORRUBA, showing two complete rings of sX3 Si detectors, deployed at ReA (beam direction right-to-left). The Si signals are taken out of vacuum immediately to air-cooled preamplifier boxes (removed in photo), mounted from the preamplifier ring in the downstream direction.

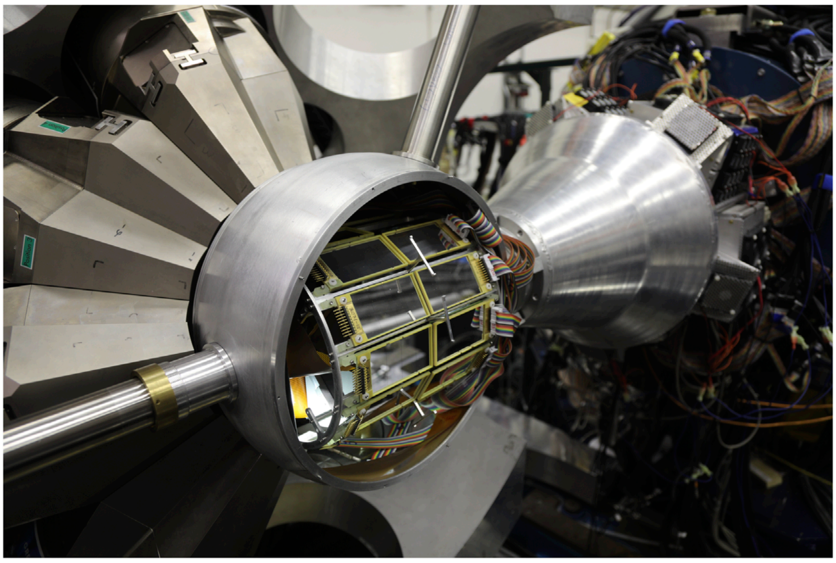

FIGURE 2
Photograph of GODDESS, deployed with GRETINA at ATLAS at Argonne National Laboratory (beam direction left-to-right). The 720-channels of Si signals are taken out of vacuum immediately to air-cooled preamplifier boxes, in the downstream direction. The beam-right hemisphere of GRETINA is retracted for access.

Though recoil separators provide numerous benefits for recoil detection, they are not always available, or necessary. Furthermore, their use is complicated in many cases by the energy, angle and charge-state distributions of beam-like recoils after the reaction target. Alternatively, for beam intensities below ~10^6 ions/second, a zero-degree detector that sees the entire beam flux can often be used. Ionization chambers can be very effective as such detectors. They can be segmented along the stopping axis, and easily tuned in pressure to match the required stopping power to the energy and charge of the incoming ion, to optimize particle identification via ΔE-E. They are radiation hard, and can deliver good (typically a few percent) resolution at reasonable count rates ($< 10^{4-6}$, depending on design).

Conventional transverse-field gridded ionization chambers have been used as zero-degree detectors (e.g., [26]), but they are rate limited to ~10^4 ions/second, due to the long drift times. More recently, a number of axial-field ionization chambers have been developed with increased count-rate capability. The

TEGIC detector [27], was designed for high-energy ions (~100 MeV/u), using a series of aluminized Mylar foils, stacked along the beam axis, to form parallel transmission electrodes, alternately biased to form a series of anodes and cathodes. In this manner, the electron and ion drift distance can be substantially reduced (typically to 1–2 cm) compared to a more conventional transverse-field gridded ionization chamber (where drifts are typically 5–10 cm). The TEGIC electrodes are tilted from the beam axis at 30°, to help reduce recombination. The reduced drift distance results in substantially increased counting rate capacity, enabling this detector to operate at up to 10^6 ions/second.

Because the foils provide too much dead material for this design to be used for low-energy ions (such as in the 5–10 MeV/u direct-reaction experiments discussed herein), an axial-field ionization chamber was built in support of the ORRUBA program. This detector was based upon the concept of the TEGIC detector, but replaced the foils with a series of high-transmission wire grids (using ~18 μm diameter wires, spaced by 2 mm, giving $> 99\%$ transmission per grid) [9], so that the ions do not traverse dead material between electrodes (instead, a few percent of the ions stop prematurely, by hitting a wire as they traverse the detector). In this detector, groups of anodes were electrically connected together and read out via charge-sensitive preamplifiers to provide ΔE and residual energy signals, while the cathodes were grounded. This provided particle identification at rates up to 10^6 ions/second [9].

Subsequently, a number of other axial-field ionization chamber detectors have been built upon the wire-grid design, incorporating various improvements. A more compact tilted-grid ionization chamber was built, to operate in the much more confined space of GODDESS [18]. An ionization chamber for ANASEN [28] simplified the design by removing the tilt from the grids, and along with it broadening due to tilted windows and asymmetric dead gas lengths, with minimal impact on resolution or count rate capacity [29]. This larger detector also introduced individual wire readout on the entrance anodes, with the rotation of the grids oriented for XY measurement of position of the ion as it enters the detector, with 3 mm resolution. The TRIFIC detector [30] was developed at TRIUMF, using the tilted-grid approach, but biasing the anodes and cathodes symmetrically (rather than grounding the cathodes) for reduced fringe-field effects and enabling operation at higher electric fields.

The most recent detector in this series, MAGIC (Multi Axial-field Gridded Ionization Chamber), is purposefully built for GODDESS (Pain et al., forthcoming). In order to operate in the small space available, while maintaining maximum acceptance and easy reconfiguration, the perpendicular grids are self-supporting and stacked using electric headers (see Figure 3), which provide both mechanical support, and electrical connections from each of the grids to the back flange, where signals are brought out of vacuum. This design makes the detector easily adjustable and serviceable. In this detector, the front two anodes use individual wire readout, for XY position measurement, with 2 mm resolution. The remaining anode signals are brought out of vacuum individually, and can easily be recombined (via a custom preamplifier motherboard) to optimize the anode groupings for particle identification. Furthermore, this is the first detector that provides readout of the cathode signal in addition to the anodes, which facilitates gain matching and improved sensitivity (Pain et al., forthcoming).

4 Using transfer reactions to constrain resonance strengths

This section highlights some manners in which direct reactions can be utilized to constrain resonance strengths, illustrated by some specific examples from ORRUBA/GODDESS experiments.

4.1 Constraining resonance strengths by determination of resonance energies

To constrain the reaction rate from a single isolated low-lying resonance, three things are needed: the resonance energy E_r, the J^π of the resonance, and its resonance strength $\omega\gamma$. Determination of the energy of the resonance is most critical; for a given resonance strength, it impacts the reaction rate exponentially (Equation 1). It also impacts the resonance strength itself (along with the J^π of the resonance, which constrains the orbital angular momentum of the captured particle) by impacting barrier penetrabilities; at low energies, the barrier penetrabilities, and hence resonance strength, also exhibit an exponential dependence on resonance energy.

The combination of high resolution charged-particle and γ-ray detection can enable the use of transfer reactions as a mechanism to populate states of astrophysical interest, using high-resolution γ-ray spectroscopy to obtain precise energies of the states populated. In such measurements, the detection, identification and energy measurement of the outgoing ejectile can give unambiguous determination of the nucleus populated, and the approximate formation energy. By detecting angle of the outgoing proton not only helps with the kinematic reconstruction of the two-body reaction, but also enables determination of the momentum vector of the recoiling nucleus, which can be used for a more-precise Doppler correction to the γ rays, and can provide angular distributions that can be used for J^π assignments.

In this approach, it is not important whether the reaction proceeds via the component of the wavefunction important for the capture reaction; that is, the resonance strength is not constrained from the cross sections, only by the energy and J^π assignments derived from the analysis. This can often reduce uncertainties on resonance strength from experiments with relatively simple analyses, without the concerns pertaining to efficiencies, acceptances, deadtime and normalization that must be addressed in order to extract reaction cross sections for spectroscopic factors (as discussed in Section 4.2). To this end, a series of (^{3}He,t) experiments have been performed with GODDESS; examples of such experiments are given in Sections 6.1 and 6.6.

4.2 Constraining resonance strengths by measuring spectroscopic factors

For low-lying resonances, Γ_p is a particularly important parameter for determining $\omega\gamma$. Indeed, in very low-lying resonances (below ~500 keV), Γ_p is generally much smaller than Γ_γ. In this case, the resonance strength can be approximated as:

$$\omega\gamma = \frac{2J_f + 1}{\left(2J_t + 1\right)\left(2J_p + 1\right)}\Gamma_p,$$

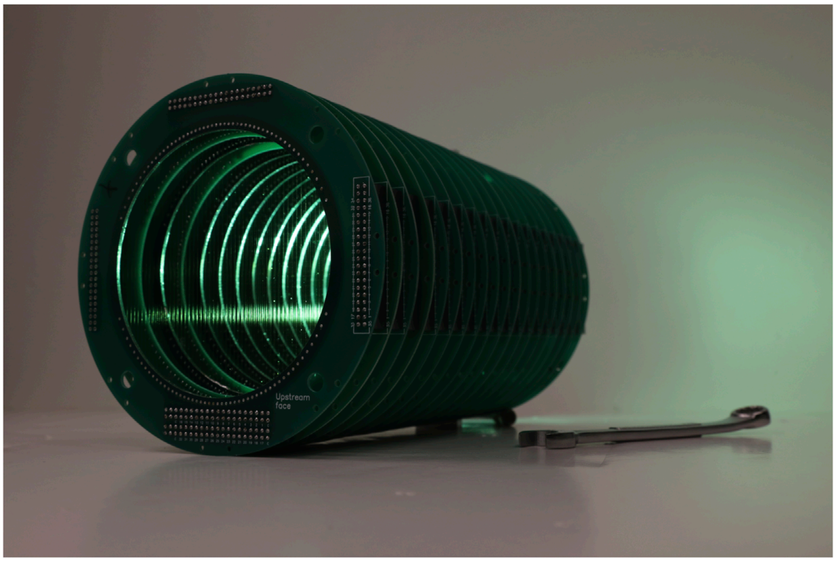

FIGURE 3
Photograph of the self-supporting grids of the MAGIC detector (see text). The wires (2 mm pitch) of the first two anodes are read out individually, for XY position measurement of incident ions.

where Γ_p depends critically on E_r and J^π of the resonance.

In the absence of further information, the maximum strength of a pure single-particle resonance at E_r and with J^π can be calculated. At such low energies, the value of this width, Γ_{sp}, is dominated by the penetrability of the Coulomb and angular-momentum barriers, so is strongly dependent on E_r and J^π (or, more strictly, the orbital angular momentum of the proton, ℓ_p). The single-proton width can be determined by calculating single-particle wavefunctions corresponding to the elastic scattering of a proton by a realistic diffuse potential, such as a Woods-Saxon well [31], at the resonance energy of interest [32, 33]. Tuned by adjusting the potential depth, the width of the pure single-proton resonance is determined by the energy dependence of the phase shift δ, and can be calculated by codes such as DWUCK and WSPOT [34, 35].

The proton width of a given resonance is further dependent on the overlap between the many-body nuclear wavefunction of the resonance and the pure single-proton wavefunction - i.e., the proton spectroscopic factor, C^2S:

$$\Gamma_p = C^2 S\, \Gamma_{sp}. \tag{3}$$

The many-body wavefunction is, *a priori*, unknown for a given resonance. However, it can be constrained by a nuclear structure model, such as shell-model calculations, or ideally by experimental data, such as from a transfer reaction [3].

The proportionality between cross sections (i.e., spectroscopic factors) from proton-transfer reactions and radiative proton direct-capture [36] and resonant capture reactions [33, 37, 38] is documented. It is important to note that in the extraction of resonance strengths from transfer reactions, the same potential should be used for the calculation of the transfer-reaction cross sections as for the calculation of the single-particle proton widths, as was suggested by the late John Schiffer [32]. Particularly, a strong dependency between the geometry of the single-particle binding potential and reaction cross sections is well known; providing a consistent potential is employed between the two reactions, much of the uncertainty associated with this potential choice cancels [32, 39–41].

The use of transfer reactions to obtain resonance strengths has a number of advantages. Firstly, it can be used to study multiple resonances in a single measurement. Secondly, because the transfer reactions are measured at energies above the Coulomb barrier (typically, several MeV/u upward), the cross sections are not hindered by barrier penetrability. This allows transfer reactions to be used to study very low-lying resonances that are out of reach for direct measurements in the foreseeable future.

4.3 Benchmarking resonance strengths from (d,p) against direct (p,γ) measurements

Though proton-transfer reactions, such as (^{3}He,d) and (d,n), are the reactions of choice for extracting proton spectroscopic factors, the application of these reactions to experiments in inverse kinematics with radioactive beams remains a challenge. Both (^{3}He,d) and (d,n) reactions are experimentally complicated, by target requirements and the complexities of spectroscopic neutron detection, respectively. Recently, the technique of measuring angle-integrated cross sections by γ-ray tagging the final state, such as a number of recent measurements using GRETINA and the S800 [42, 43], has been employed. Though this approach can be effective, it relies on knowledge of proton-γ branching ratios, corrections for feeding, and on the spins of the final states being known in order to infer ℓ_p. Furthermore, for transfer onto states with non-zero spins, even knowledge of J^π assignments of final states is insufficient for a conclusive interpretation, as the total angle-integrated cross section for a given final J^π can be composed of a sum of multiple proton orbital angular momentum couplings. Without a method to deconvolve these components, it is impossible to assign more than limits on spectroscopic factors for the individual orbital angular components, which inherently have vastly different contributions to the astrophysical reaction rate, due to barrier penetrabilities. Combining these experiments with neutron detection helps address this issue, at the cost of efficiency and the complexity of neutron detection.

However, the isospin independence of the nuclear force can be exploited to constrain proton spectroscopic factors from their neutron counterparts, by using the mirrored reaction (for example, the (d,p) reaction) to extract neutron spectroscopic factors for the equivalent state in the mirror system. There are several experimental advantages to using this technique of measuring (d,p) on proton-rich nuclei, including simple targets, high particle-detection efficiency that is well understood, a compact setup that can be fielded with large germanium detector arrays, and positive Q values which reduce kinematic compression in inverse-kinematic stripping reactions. This approach has been benchmarked for a number of astrophysically-interesting cases in the *sd* shell, finding general systematic agreement between proton and neutron spectroscopic factors (extracted from (^{3}He,d) and (d,p) reactions, respectively), and associated direct measurements of proton resonance strengths, to within about 30% [37]. The (d,p) reaction has recently exploited using isobaric analog states in neighboring isobars, at the NSCL using the ^{26}Si(d,pγ)^{27}Si to constrain the ^{26m}Al(p,γ)^{27}Si reaction [44], and at TRIUMF using the ^{23}Ne(d,pγ)^{24}Ne reaction to constrain the ^{23}Al(p,γ)^{24}Ne reaction [45].

Furthermore, a number of astrophysically-interesting nuclides for proton capture lie on or close to the $N = Z$ line (See Section 6). The technique described above is further simplified in the case of the $N = Z$ nuclides, as the ‘target’ nucleus is self-conjugate, and hence identical for the two mirror systems. ^{26}Al represents an important testing ground for this approach, as it is a radioactive $N = Z$ nuclide with strong astrophysical interest [46], yet the ground state (^{26g}Al) has a long enough lifetime that it can be fabricated into target. Consequently, numerous resonances in the ^{26g}Al(p,γ) reaction have been well studied in both normal [47] and inverse [48] kinematics, as well as with indirect techniques such as ^{26g}Al (^{3}He,d) [47, 49] using an ^{26g}Al target, and inverse kinematics (d,p) measurements using beams of ^{26}Al [50–52]. The lowest resonance for which there have been direct measurements of the resonance strength via ^{26g}Al(p,γ) is the 189-keV resonance. This has been measured [47] using an ^{26g}Al target to be 0.055 (9) meV [47] and, via inverse kinematics using a 10^{9} ions/s radioactive beam at TRIUMF using the DRAGON recoil separator to be 0.035 (7) meV [48]. An indirect measurement of the ^{26g}Al(^{3}He,d)^{27}Si reaction using an ^{26g}Al target and a Q3D spectrograph yielded a resonance strength of 0.064 for an $\ell_p = 1$ transfer, with unreported uncertainty (statistical errors on the differential cross section amount to ~20%)[1]. This experiment was unable to probe lower-energy resonances due to the strong backgrounds from the ^{27}Al component of the target.

More recently (d,p) experiments using radioactive ^{26}Al beams have been used to determine the strengths of resonances out of current reach of direct (p,γ) measurements [50, 51], which are unconstrained by target impurities that limited the ^{26g}Al(^{3}He,d)^{27}Si experiment. These experiments are described in Section 6.3. Concurrently, as a benchmarking of the (d,p) technique, spectroscopic factors for the mirrors to high-lying resonances were extracted, and resonance strengths determined and compared to direct measurements using (p,γ) reactions [50].

When constraining resonance strengths via mirror symmetry, it is important to note that the mirror states in the two systems lie at different energies with respect to the separation energy. For example, the low-lying resonances in the ^{26}Al + p system lie hundreds of keV above S_p in ^{27}Si, whereas the mirror states in the ^{26}Al + n system lie 2–3 MeV below S_n in ^{27}Al. Though the wavefunctions of the mirror states are of a highly similar structure, there are differences due to the effects of different couplings to the continuum. In some studies (e.g., [51]), the spectroscopic factors are assumed to be equal in the two systems to about 30%, which is often a reasonable approximation, compared to other uncertainties in the experiments, and certainly to the potential orders of magnitude uncertainty in resonance strengths prior to experimental constraint. However, a rigorous approach is to explicitly account for the systematic difference in spectroscopic factors in the two systems due to coupling to the continuum. In [50], spectroscopic factors were calculated for bound ^{27}Al states and unbound ^{27}Si in the Shell Model Embedded in the Continuum (SMEC) formalism [53, 54], using the USDb interaction [55]. The ratio of spectroscopic factors between the two mirror systems was then used to scale the experimentally-determined spectroscopic factors between ^{27}Al and ^{27}Si. This scaling, which is dependent on the energies of the states with respect to their separation energies, and the orbital angular momentum, is typically of the order 10–40%.

5 Opportunities with isomeric beams

There is a growing understanding of the importance that isomers play in astrophysical reaction networks (astromers) [46, 56–62], impacting reaction flow and effective lifetimes, in scenarios ranging from massive stars, to novae, supernovae, and r-process nucleosynthesis [44, 46, 63, 64]. For example, many odd-odd $N = Z$ nuclides in the *sd* and *fp* shells are of substantial astrophysical interest (see Section 6), affecting reaction flow, and impacting astronomical observables such as isotopic ratios and prompt γ-ray signatures [46]). Many also have low-lying spin isomers which must be incorporated into the reaction network (see Table 1; Figure 4).

The lack of information on reaction cross sections on isomers in radioactive nuclides presents a particular challenge. Beam production techniques typically populate both the ground state (GS) and isomeric state (IS) of such nuclides. However, in general, the ratio is difficult to predict or control without undesired impacts on other beam properties.

---

[1] Note that in this experiment, the statistics in differential cross sections (see Figure 6 of [49]) were insufficient to constrain ℓ_p, and for many years this state was assigned positive parity. Recent (d,p) data (see below) indicate an $\ell_p = 1$ transfer to the mirror of this state.

TABLE 1 Properties of the ground and isomeric states in odd-odd nuclides in the *sd* shell and lower *fp* shell. In most cases, either the ground state or isomer has a lifetime of comparable duration to the possible range of holdup times (10s of ms to seconds) in the ReA system, potentially enabling the employment of the hold-up technique (see text) to manipulate the GS:IS content of the beam.

Nuclide	J^π (GS)	J^π (IS)	$t_{1/2}$ (GS)	$t_{1/2}$ (IS)
^{22}Na	3^+	1^+	2.6 years	240 ns
^{24}Al	4^+	1^+	2 s	130 ms
^{26}Al	5^+	0^+	0.7 My	6.3 s
^{30}P	1^+	0^+	2.5 min	96 fs
^{34}Cl	0^+	3^+	1.5 s	32 min
^{38}K	3^+	0^+	6.7 min	0.9 s
^{42}Sc	0^+	7^+	0.7 s	1 min

5.1 Production and control of mixed GS:IS beams at FRIB

Recent developments at the ReA facility at FRIB are enabling the delivery of beams containing isomeric states in which the GS:IS composition can be controlled without impact on the other properties of the reaccelerated beam [65, 66]. This is achieved by completely stopping the fragmentation beam, and reaccelerating it to energies appropriate for either direct measurements at astrophysical energies, or to Coulomb-barrier energies that are appropriate for indirect techniques for constraining astrophysical reaction rates, such as direct reactions. The GS:IS ratio of the reaccelerated beam can be controlled by two mechanisms. Firstly, the tuning of the fragment separator can be employed to change the GS:IS content of the fragmentation beam before stopping and reacceleration. Secondly, if the lifetimes of the two states are conducive, the adjustable hold-up times in the reacceleration system can be used to further modify the GS:IS composition of the reaccelerated beam. Crucially, because of the stopping and reacceleration, the final beam properties (energy, emittance, etc.) are largely isolated from these adjustments to the GS:IS ratio. These two mechanisms are discussed in Section 5.1.1 and Section 5.1.2.

5.1.1 Selection by fragment momentum

In general, projectile fragmentation populates nuclei in an ensemble of excited states, which subsequently γ decay in-flight; in nuclides with isomers, this can result in feeding of the isomer as well as the ground state. If that isomer has a comparable lifetime to the flight-time of the beam, a beam can be delivered with a mixed GS:IS composition. Due to the differences in spin between the GS and IS, some control over GS:IS ratio can be achieved by selectively tuning the fragment separator to transmit a subset of the fragmentation momentum distribution. In two studies, performed at the NSCL prior to FRIB operations, the production of mixed GS:IS beams of ^{38}K [65] and ^{34}Cl [66] were investigated. In both cases, the beams were produced via the 1p-1n removal channel of the fragmentation of a primary beam (^{40}Ca and ^{36}Ar, respectively), incident at similar energies (140 and 150 MeV/u) on a beryllium production target. It is noteworthy that both nuclides have the same GS and IS spins (though reversed ordering), and comparable lifetimes (see Table 1). In both studies, the GS and IS were populated in the fragmentation reaction with approximately equal proportions. Tuning the fragment separator to transmit the low-momentum tail of the fragmentation distribution (which stems from smaller-impact-parameter fragmentation events with on-average larger momentum transfer) was found to enhance the fractional population of the higher-spin state (the 3^+ GS in ^{38}K, and the 3^+ IS in ^{34}Cl) [65, 66], albeit at the cost of total production yields.

5.1.2 Selection by lifetime

In addition to the spin selectivity obtainable by the tuning of the fragment separator, the content of the reaccelerated beam is subject to the holdup times inherent to the ReA system. If one or both of the lifetimes of GS or IS is comparable to the range of available hold-up times, the content of the reaccelerated beam can be manipulated by adjusting the hold-up time. The reacceleration process involves stopping the fragmentation beam in a gas stopper, preparing the ions in a cooler-buncher trap, and charge-breeding the ions in an electron-beam ion trap (EBIT), before reacceleration in the ReA linac. In this process, the ions spend an equal amount of time in the cooler-buncher and EBIT; this time is adjustable, in the range of 10s of ms to seconds. By setting this holdup time based on the lifetime of the ground and/or isomeric states involved, the composition of the beam can be adjusted by controlling how much of each species is allowed to β decay before reacceleration. The advantages of this approach are several-fold:

- Beams at ReA can be delivered at energies spanning direct astrophysics measurements (100s of keV/u to a few MeV/u) to transfer-reactions (5–15 MeV/u).
- The high-quality reaccelerated beam emittance ($<0.5\%$ energy spread, ~2-mm beam spot size) is critical to recoil-separator acceptance for radiative-capture measurements, and to resolution in kinematic reconstruction in direct reactions, such as transfer reactions or inelastic scattering.
- Data can be acquired with two different GS:IS beam compositions without affecting other properties of the reaccelerated beam. This enables a straightforward deconvolution of the GS and IS yields, without having to account for additional changes to the experimental response.

5.1.3 Production of pure isomeric beams

In addition, it is possible to produce certain beams almost entirely in one either of isomeric state or ground state, by taking advantage of the selectivity of β decay, which often very preferentially populates just one of the of two states in a nuclide, and the lifetimes of the nuclides involved. For example, the β decay of ^{26}Si results almost entirely in population of the isomeric state of ^{26}Al($>99.9\%$). So, rather than tuning the fragment separator for ^{26}Al in the method described above, which would produce a beam of ^{26}Al in both the ground and isomeric states, the fragment separator can instead be tuned for the β-decay parent, ^{26}Si. The ^{26}Si can then be held up in the ReA system for long enough that a substantial fraction β decays to ^{26}Al, exclusively in the IS, which can then be

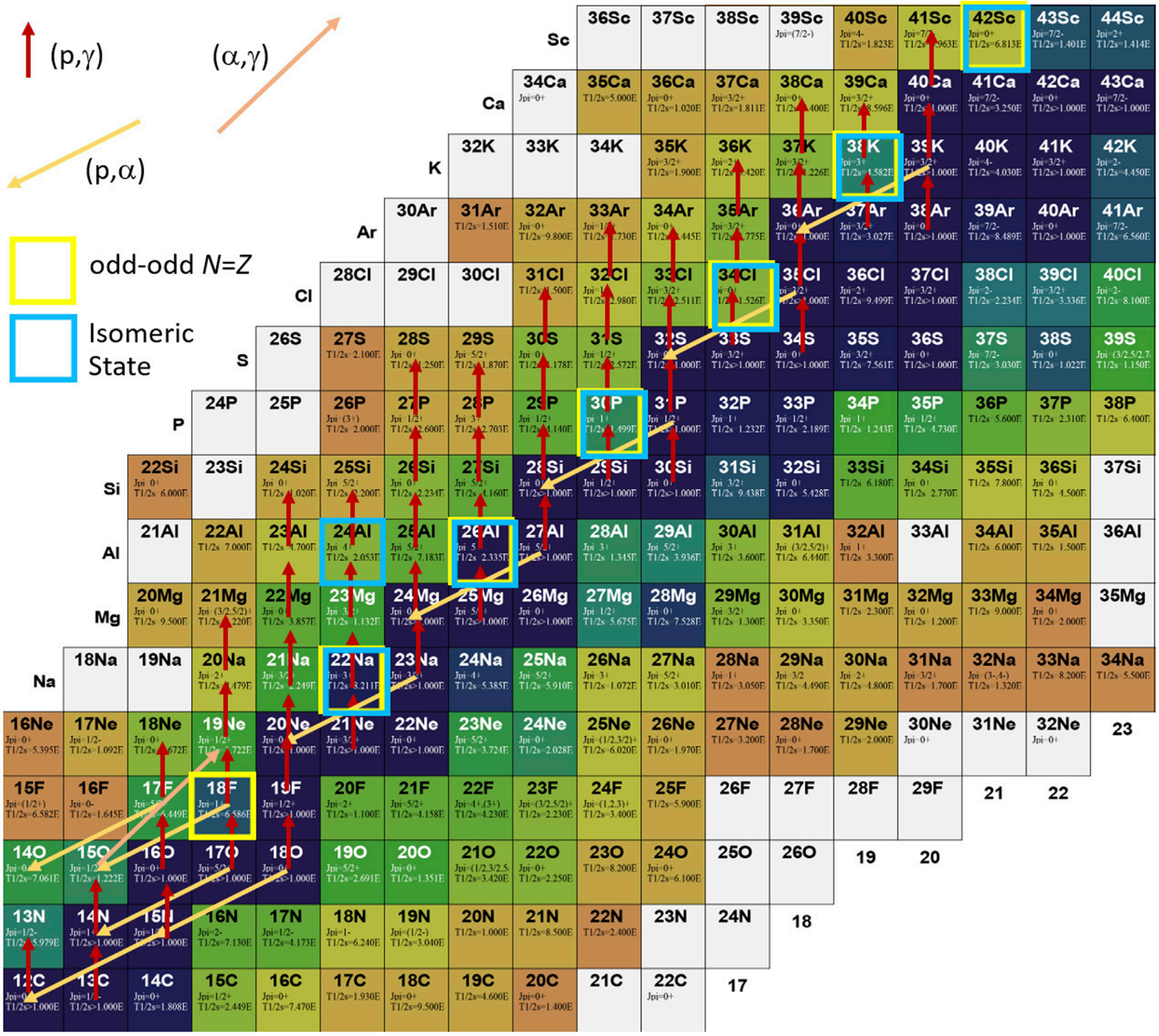

FIGURE 4
Simplified reaction network for nova nucleosynthesis, omitting β decays and photodissociation reactions for clarity. The odd-odd $N = Z$ nuclides, which are all of particular astrophysical interest (see text), are highlighted, along with nuclides with isomeric states (see Table 1) on which capture cross sections are needed.

reaccelerated. The resultant beam is then a mix of ^{26}Si and ^{26}Al, with the ^{26}Al component exclusively in the IS. Though the beam is not isobarically pure, the contaminant is a different element, rather than a different state in the same nuclide, which is much easier to handle in experiments due the Z difference, either by identification of recoils in a zero degree detector (such as an ionization chamber, discussed in Section 3.3) or a recoil separator. The first experiment using this approach has been approved for beam time at FRIB [67]. This experiment will measure the ^{26m}Al(α,p) reaction using the JENSA gas-jet target and ORRUBA, and is currently awaiting scheduling.

6 The odd-odd N = Z *sd*-shell nuclides

This section highlights the usage of the techniques and instrumentation described above to determine astrophysical reaction rates due to isolated proton resonances, on nuclides in ground and isomeric states. These examples are located within a region of the nuclear chart (the odd-odd $N = Z$ nuclides in the *sd* shell) which has been a focus of the ORRUBA/GODDESS program, highlighting some experiments which have been performed, and some which are planned for the near future.

Figure 4 shows a simplified reaction network for nova nucleosynthesis, including the hot CNO cycle and breakout reactions into the rp process. The odd-odd $N = Z$ nuclides are highlighted, as these are of elevated astrophysical interest. The ^{18}F(p,γ)^{18}Ne reaction competes with the ^{18}F(p,α) reaction, governing breakout from the hot CNO cycle and the synthesis of heavier elements. The radioisotope ^{22}Na is anticipated to be produced in sufficient quantities that the 1.275-MeV γ-ray from its decay may be a prompt observable from nova explosions, yet its abundance is subject to uncertainties on the astrophysical rate of the ^{22}Na(p,γ)^{22}Na destruction reaction. ^{26}Al is the most-studied radionuclide, with the 1.8 MeV γ-ray line associated with its β decay being the subject of years of data collected with the HEAO [68, 69], the COMPTEL and INTEGRAL satellite γ-ray telescopes [70–73], and is used to map regions of star formation and to trace stellar ejecta in the interstellar medium [74]. However, the destruction reaction ^{26}Al(p,γ)^{27}Si impacts the quantitative interpretation of this signal. The rate of the ^{30}P(p,γ)^{31}S reaction is crucial for classical nova nucleosynthesis, bottle-necking the reaction flow into the A = 30–40 mass range. The ^{34}S/^{32}S isotopic ratio in pre-solar grains, which is believed to be a strong indicator of nova origin, is impacted by the ^{34}Cl(p,γ)^{35}Ar reaction rate, which governs the reaction flow due to the unbound nature of ^{34}K. The ^{38}K(p,γ)^{39}Ca reaction likewise bottlenecks the reaction flow to higher masses due to the unbound nature of ^{39}Sc.

The situation is further complicated because many of these $N = Z$ nuclides have low-lying isomers with sufficiently long lifetimes that they can contribute to the reaction network. At low temperatures, the ground and isomeric states can be independently populated and destroyed by capture reactions and β decay, so are typically treated as independent species in reaction networks. However, at elevated temperatures they can be connected, via thermal excitations to higher levels. In the limit of high-enough temperature, the two states are in thermal equilibrium, and can be treated as a single effective species. At intermediate temperatures, there is a transition between these two scenarios, resulting in strongly temperature-dependent effective properties [57, 75]. For the reaction network, proton-capture cross sections are required on both ground state and isomer. With new techniques of isomeric beam production (such as those outlined in Section 5), indirect techniques are being used to unambiguously study resonances that are sensitive to the overlap in the many-body wavefunction to single-particle resonances on both ground states and isomers. Examples of such experiments are described in Sections 6.3, 6.5, and 6.6.

6.1 The ^{18}F(p,γ)^{19}Ne reaction

Understanding the reaction flow breaking out of the hot CNO cycle, and the abundance of ^{18}F produced in novae (a major source of 511-keV radiation, and hence a potential prompt γ-ray observable), is influenced by the strengths of resonances in ^{19}Ne, which impact the ^{18}F(p,α)^{15}O and ^{18}F(p,γ)^{19}Ne reactions. An experiment was performed to measure the ^{18}F(d,p)^{19}F reaction to determine spectroscopic factors in the mirror system, to constrain the proton widths in ^{19}Ne [76]. An isotopically-pure ^{18}F beam was from the HRIBF was impinged at 6 MeV/u upon a 160 μg/cm^2 deuterated polyethylene target. In this pioneering experiment using a (d,p) reaction in inverse-kinematics with a radioactive beam, and an application of the mirror-symmetry approach, proton ejectiles were detected at backward angles in the SIDAR array. In coincidence, the very forward-focused ^{19}Ne recoils were detected in coincidence at the focal plane of the Daresbury Recoil Separator, while the ^{15}N recoils from the α emission channel were detected in an annular silicon detector at forward angles. Angular distributions for the protons were measured, and spectroscopic factors extracted from a DWBA analysis, from which proton widths were determined using mirror symmetry. These were used to calculate the astrophysical rate of the ^{18}F(p,α)^{15}O reaction, which was found to be reduced by approaching an order of magnitude over the temperature range of classical novae [76, 77]. However, systematic uncertainties remained pertaining to the precise mirror assignments between ^{19}Ne and ^{19}F.

More recently, uncertainties in this reaction rate stemming from uncertainties in the energies of low-lying resonances ^{19}Ne have been addressed, using the ^{19}F(^{3}He,$t\gamma$)^{19}Ne reaction, measured using GODDESS at ATLAS [10, 78]. The experiment used a 30-MeV ^{3}He beam incident on a ~1 mg/cm^2 CaF$_2$ target, and outgoing tritons were detected and identified in the ORRUBA silicon detectors. De-excitation γ rays were measured in coincidence in the Gammasphere array of Compton-suppressed HPGe detectors. Over forty decays from 21 energy levels were identified. In particular, the positions of two 3/2$^+$ states near the proton threshold were determined, and the location of an 11/2$^+$ state, previously thought to be unbound, was found to be sub-threshold. This reduced the upper limit to the ^{18}F(p,α)^{15}O reaction rate by a factor of 1.5–17 across the nova temperature range, reducing the nova detection probability uncertainty by a factor of two [10, 78].

6.2 The ^{22}Na(p,γ)^{23}Na reaction

The radioisotope ^{22}Na is one of the most promising targets of discrete γ-ray astronomy, producing a 1.275 MeV γ-ray line with a lifetime ($t_{1/2}$ = 2.6 years) that is sufficiently short to maintain spatial correlation with localized sources, yet long enough to last beyond the opaque conditions at the peak of a nova explosion. ^{22}Na is predicted to be produced in sufficient quantity in novae to be detectable, and therefore ^{22}Na is a leading candidate for a prompt γ-ray signature for nova nucleosynthesis in our galaxy. Current and previous instruments may be close in sensitivity to detecting the ^{22}Na line [79–82], and planning has begun for future missions with greater sensitivity [83]. Understanding the quantity of ^{22}Na produced in a typical nova explosion is crucial to informing such missions, by predicting the number of novae that are within detectable distance, and enabling a quantitative interpretation of this potential signature, should it be detected. This requires reliable models of nova nucleosynthesis, including reaction rates which affect the ^{22}Na abundance ejected.

The ^{22}Na(p,γ)^{23}Mg reaction is one of the main destruction mechanisms affecting ^{22}Na yields in nova models. Despite decades of direct and indirect study of the proton resonances important for ^{22}Na(p,γ), there is no consensus on the resonance strengths for this important reaction. The resonance believed to be most important at nova temperatures is the 205 keV (7/2)$^+$ resonance. There have been two absolute determinations of the strength of this resonance through direct measurements of the (p,γ) reaction [84–86], performed in 1990 and 2010.[2] These experiments differ in resonance strength by about a factor of about 2.5, resulting in a discrepancy in ^{22}Na yields from novae, and hence the possibility of prompt γ detection, of a factor of 1.4–2.0. It should be noted that all of these challenging direct (p,γ) measurements utilized ^{22}Na-implanted targets. Such measurements are subject to possible systematic uncertainties associated with beam/target overlap due to non-uniformities of implanted ^{22}Na ions (in both depth and transverse profiles) and the beam profile, and uncertainties in the stopping power of the target. This is further complicated by target degradation from irradiation with intense proton beams (typically tens of μA), and backgrounds from the mCi-activity of the targets.

Because of this, and its astrophysical importance, the 205-keV $(7/2)^+$ resonance has also been the subject of a number of indirect studies, based on measurements of branching ratios of this state, fed by β decay. However, rather than resolving the situation, these indirect studies yield resonance strengths with even greater disagreement, spanning over an order of magnitude, and typically with lower strengths than the direct measurements. A recent result yields the lowest number yet [88]. This stems from an experiment using the new gas-filled detector GADGET [89], which is designed to substantially suppress β backgrounds compared to silicon-based setups, to aid in measuring low-energy β-delayed protons. This experiment yielded a substantially smaller proton branching ratio for the 205-keV resonance, despite being in agreement with previous results for the 275-keV and 583-keV resonances [90]. Nominally, the result from the GADGET measurement suggests a resonance strength that is a factor of 7 and 22 below the two direct measurements.

However, in all the β-delayed proton experiments, the branching ratios obtained must be combined with the absolute lifetime of the state in order to determine a resonance strength, and it has been suggested that the lifetime of the state be revisited [91]. The universally-adopted value for the lifetime of the 205-keV $(7/2)^+$ resonance is 10 (3) fs, stemming from a fusion-evaporation measurement using Gammasphere [92, 93], in which the lifetime was determined from the fractional Doppler-shift technique. A more recent measurement at TRIUMF has placed a 3σ upper limit on the lifetime of 12 fs [94] using the Doppler-shift Attenuation Method. However, shell-model calculations suggest a shorter lifetime (0.6–1.7 fs) [91, 95], which would systematically raise all the resonance strengths from indirect measurements by about an order of magnitude.

A detailed systematic study of the spectroscopic strengths of single-proton states in ^{23}Mg would considerably enlighten the situation, as the large variations in resonance strengths correspond to equally large variations in proton spectroscopic factors for these states, as in Equation 3. Though some proton spectroscopic factors have been determined using the ^{22}Na(^{3}He,d)^{23}Mg reaction [96] in an experiment using an implanted ^{22}Na target and a Q3D spectrometer, only upper limits were obtained for most of the resonances in the astrophysically interesting region. Despite the excellent resolution afforded by the spectrometer, the experiment was hampered by strong background lines and less distinct angular distribution shapes from (^{3}He,d), and the need for substantial shielding to cope with the activity of the ^{22}Na target.

To address this, the GODDESS collaboration undertook a measurement of the ^{22}Na(d,p)^{23}Na reaction in inverse kinematics, to determine single-particle spectroscopic factors of the neutron mirror states, and thereby inform the resonance strengths in ^{23}Mg independently of the systematics of the previous measurements. Spectroscopic strengths in $N = Z$ mirror systems are typically preserved to ~20%–30% level, a considerably smaller uncertainty than the discrepancies in the resonance strengths, and the differences in mirror systems can further be addressed by SMEC calculations [50] (see Section 4.3). The measurement utilized a 10-MeV/A^{22}Na beam produced by the ^{21}Ne(d,p)^{22}Na reaction at 10 MeV/A using the RAISOR facility at ATLAS at Argonne National Laboratory. The beamline was tuned for ^{22}Na($q = 11+$), providing suppression of Ne (fully stripped Ne ions have $q = 10+$), with further suppression of scattered beam by the RF sweeper. This energy is well-suited to the population of the astrophysically-important low-angular-momentum states, and produces distinctive angular distributions. Such measurements in inverse kinematics involve substantially smaller quantities of ^{22}Na, thereby avoiding the radiological complications of experiments with ^{22}Na targets. As with a many *sd*-shell $N = Z$ nuclei, ^{22}Na has a 1^+ isomer a few hundred keV above the ground state. Though the ^{21}Ne(d,n)^{22}Na reaction populates both the ground state and isomer, the ^{22}Na isomer γ decays with a 243 ns half life to the ^{22}Na ground state. The flight path between the production target and the experimental target is ~150 feet - which is equivalent to ~5 half lives. Therefore, 97% of the isomeric component of the beam decayed to the ground state by the time the ions reached the experimental target.

The GODDESS position-sensitive fast ionization chamber provided real-time beam diagnostics, including beam composition, rates by particle type, and mm-precision spatial feedback, to aid in tuning of the beamline and optimization of the RF sweeper phase. Protons emitted in the ^{22}Na(d,pγ)^{23}Na reaction were detected in the ORRUBA silicon detectors, and de-excitation γ rays in GRETINA. The data from this experiment are currently under analysis.

6.3 The ^{26}Al(p,γ)^{27}Si reaction

The 1.8 MeV γ-ray line from the decay of ^{26}Al is a major target of γ-ray astronomy. Its distribution in galactic coordinates has been extensively mapped, and its Doppler shift studied, indicating that it is co-rotating with, and hence pervasive across, the galaxy. Though it is likely that multiple sites contribute to the 1.8-MeV signature, clues to possible sources can be garnered from its correlation with other signatures that have also been directionally-mapped [97]. Notably, the 1.8-MeV γ ray shows strong correlation with 53 GHz free-free microwave emission, which is an indicator of ionized dust clouds, and hence regions of massive star formation [98]. It is likely that massive stars contribute substantially to the ^{26}Al signature,

---

[2] A third study of direct ^{22}Na(p,γ)^{23}Mg measurement [87], performed at Bochum, extended measurements to lower energy resonances, but measured relative yields only, using the 274-keV and 583-keV resonances to normalize the their data to the Münster experiment [84], so provide no independent constraint on the absolute value of the strength of the 205-keV resonance

and the rate ^{26g}Al(p,γ)^{27}Si reaction at stellar temperatures impacts the net production of ^{26}Al. Although many direct measurements constraining ^{26g}Al (p,γ) resonance strengths have been performed, at such low temperatures ($<$ 0.1 GK) the main resonances within the Gamow window for massive stars are out of reach. As discussed in Section 4.3, the lowest energy for which a direct (p,γ) measurement has been possible is the 189-keV resonance, studied in both normal [47] and inverse kinematics [48].

A 9/2$^+$ resonance at 127 keV is likely to dominate in massive stars, which can be populated via $\ell_p = 0$ proton capture on the 5$^+$ ^{26g}Al. However, due to the lower energy, this resonance is several orders of magnitude weaker than the 189-keV resonance, and hence out of reach for direct measurements. An indirect measurement of the ^{26g}Al(^{3}He,d)^{27}Si reaction [49] using an ^{26g}Al target and a Q3D spectrograph was unable to provide more than an upper limit on this resonance, due to the strong backgrounds from reactions on the ^{27}Al component of the target. More recently, (d,p) experiments using radioactive ^{26}Al beams have been used to determine the strengths of resonances out of current reach of direct (p,γ) measurements [50, 51], which are unconstrained by target impurities that limited the ^{26g}Al(^{3}He,d)^{27}Si experiment. These experiments, performed at the HRIBF with ORRUBA [50] and at TRIUMF [51], are in remarkable agreement, constraining the strength of the 127-keV resonance ($\omega\gamma$ = $2.6^{+0.7}_{-0.9}$ $\times 10^{-5}$ meV [50] and 2.5 (5) $\times 10^{-5}$ meV [51]). The resonance strength was found to be 4 times higher than the previously adopted upper limit, and to dominate the reaction rate at temperatures between 0.04 GK and 0.1 GK [50]. The experiments also placed upper limits on the strength of the even lower-lying 68 keV resonance ($\omega\gamma$ $\leq$ 3.0×10^{-12} meV [50] and 8 $\times$ 10^{-13} meV [51]).

6.4 The ^{30}P(p,γ)^{31}S reaction

^{30}P is of particular interest for understanding classical nova nucleosynthesis on ONe white dwarfs [99], due in part to the long lifetime of ^{30}P (~2.5 min) with respect to the timescale of a nova outburst. The ^{30}P(p,γ)^{31}S reaction is a potential bottleneck, affecting the reaction flow into the A = 30–40 mass range during the nova [100]. As a consequence, the rate affects the abundances of isotopes of phosphorus, sulphur and silicon - critical elements for observational constraints on novae. The ^{30}P(p,γ)^{31}S reaction rate directly affects the isotopic ratio of ^{30}Si/^{28}Si, which is an important nova identifier in the analysis of pre-solar grains [101]. Furthermore, the O/S, S/Al, O/P and P/Al elemental ratios have recently been shown to be particularly sensitive probes of nova peak temperatures, with final abundance ratios varying by 2–3 orders of magnitude due to peak temperature changes between ~230 and ~310 MK. In this detailed study, in which these ratios were found to be one-to-two orders of magnitude more sensitive than ratios solely of elements lighter than phosphorus [102], the impact of various reaction rates on the ratios was examined. The uncertainty in the ^{30}P(p,γ)^{31}S rate was highlighted as the major nuclear physics uncertainty in interpreting these ratios, currently hampering the use of these ratios to constrain the energetics of novae.

The rate of this reaction depends critically on the spectroscopic strengths of levels between 6 and 7 MeV excitation in ^{31}S. The ^{30}P(d,pγ)^{31}P reaction was measured with GODDESS in inverse kinematics, using mirror symmetry to inform state in ^{31}S. An 8 MeV/u beam of ^{30}P (~80% pure) was produced via the ^{29}Si(d,p)^{30}P reaction, using the RAISOR facility at ATLAS, and delivered to the GODDESS particle-γ spectrometer.

The protons emitted from the ^{30}P (d,p)^{31}S reaction on a ~600 μg/cm^2 C_2D_4 target were measured in the ORRUBA detectors. The GODDESS position-sensitive ionization chamber was used to identify P recoils, and aid in the kinematic reconstruction using the recoil position to help account for the large in-flight beam spot. Using coincident γ rays to aid in resolution, angular distributions were measured and spectroscopic factors determined. As in the case of ^{26}Al, states of a particular J$^\pi$ can be populated via multiple ℓ_n transfers, due to the 1$^+$ ground-state spin. A manuscript on these results is currently in preparation (Ghimire et al., forthcoming).

6.5 The ^{34}Cl(p,γ)^{35}Ar reaction

The elemental and isotopic composition of dust grains formed during the cooling of nova outflows can provide a signature of the nova origin of these grains, and furthermore provide metrics against which nova models can be tested. Such pre-solar grains can be found in primitive meteorites within the solar system [103]. However, the majority of grains originate from supernovae and massive stars and, although a number of isotopic ratios (including C, N and Si isotopes) are indicators of nova origins, none provide an unambiguous nova signature. A promising candidate for pre-solar grain classification is the ^{34}S/^{32}S ratio, which recent studies have suggested is constrained to a narrow range in nova grains [101], limit its usefulness. The ^{34}Cl(p,γ) reaction impacts the nucleosynthetic flow in the sulfur region; if the rate proceeds fast enough with respect to ^{34}Cl β decay, the reaction flow bypasses ^{34}S. However, the ^{34}Cl(p,γ) reaction rate is subject to substantial uncertainties. In nova sensitivity studies [100], a statistical Hauser-Feshbach calculation is adopted for the ^{34}Cl(p,γ) reaction rate, and assigned factor of 100 uncertainty due to the lack of experimental constraint, resulting in $\times 5$ variations of final ^{34}S abundance. However, in addition to the 0$^+$ ^{34}Cl ground state ($t_{1/2}$ = 1.53 s), the uncertainties are compounded by a low-lying long-lived 3$^+$ isomer at 146 keV ($t_{1/2}$ = 32 min), which can both be produced directly via the nucleosynthesis network, and by thermal population at nova temperatures [57, 75]. Notably, the reaction network in [100] did not treat the isomer explicitly. It is necessary to assess the reaction rate on both ^{34g}Cl and ^{34m}Cl, and include both explicitly in network calculations.

A recent spectrograph measurement [104] located levels in ^{35}Ar but was unable to constrain the J^π or widths relevant to the ^{34}Cl(p,γ)^{35}Ar reaction rate. A theoretical study of rp-process nuclei with low-lying isomers [105] used shell-model calculations of spectroscopic factors and γ widths to estimate stellar enhancement factors for radiative capture rates on the isomeric states due to thermal population. For ^{34}Cl(p,γ), an enhancement factor of 10^3 was found, peaked at 0.2 GK. As calculations were performed using the USD interaction [106], only positive-parity states were included. However, in other mid *sd*-shell nuclei, substantial spectroscopic strength is expected for $\ell_p = 1$ resonances, as the lowest states from the *fp*-shell are typically located close to the proton separation energy in these nuclei [50, 52, 107–109]. A more recent (2020) study [107] in $(0 + 1\ \hbar\omega)$ space using the *sdpf-mu* interaction [110] predicted negative parity states in the astrophysically interesting energy range. However, with no experimental constraint on these levels, 200-keV uncertainties were assumed on excitation energies, and factor 2 uncertainties on spectroscopic factors (partial widths), leading to large uncertainties in the reaction rate. As the authors note: 'In a study by Fry et al., 17 ^{35}Ar levels have been detected in the energy region Ex = 5.9–6.7 MeV and their excitation energies have been determined, but not spins, parities, widths, or branching ratios. Because of the paucity of such information, it is not yet possible to derive meaningful experimental ^{34g,m}Cl(p,γ)^{35}Ar reaction rates' [107].

A systematic experimental determination of the distribution of single-proton spectroscopic strengths as a function of excitation energy in ^{35}Ar, for both ^{34g}Cl and ^{34m}Cl, would considerably enlighten the situation. A^{34g,m}Cl(d,p)^{35}Cl experiment has been approved by the FRIB PAC [111], using the techniques outlined in Sections 5 and 6.6, and is awaiting scheduling at the time of writing.

6.6 The ^{38}K(p,γ)^{39}Ca reaction

The ^{38}K(p,γ)^{39}Ca reaction is an important bottleneck to the end-point of the rp-process chain. The reaction rate has been estimated to be uncertain by a factor of 10^4 [100], leading to large uncertainties in abundances from novae [100, 112]. Further, in Type I x-ray bursts on neutron stars, the rp process branches and proceeds either via ^{36}K (β^+, $t_{1/2}$ = 0.342 s)^{36}Ar(p,γ)^{37}K(p,γ)^{38}Ca or ^{36}K(p,γ)^{37}Ca(β^+, $t_{1/2}$ = 0.175 s)^{37}K(p,γ)^{38}Ca. Since ^{39}Sc is almost proton unbound, the rp flow must wait for ^{38}Ca(β^+, $t_{1/2}$ = 0.440 s)^{38}K(p,γ)^{39}Ca [113, 114]. The ^{38}K(p,γ)^{39}Ca reaction is thus an important path to the formation of heavier elements. However, there is limited experimental constraint; the current rate widely used for nucleosynthesis calculations (JINA REACLIB v2.0) is a theoretical rate based on a Hauser-Feshbach statistical model calculation [115]. Furthermore, the relatively short-lived ($t_{1/2}$ = 924.3 ms) ^{38}K isomer is important, as it is the endpoint of 76.5% of the ^{38}Ca decays [116] and the rise times of x-ray bursts typically fall in the range of 1–10 s. As such, capture on both ground (^{38g}K, $J^\pi = 3^+$) and isomeric (^{38m}K, $J^\pi = 0^+$) states plays an important role in the astrophysical network, and needs experimental constraint.

Though a direct measurement of the ^{38g}K(p,γ)^{39}Ca reaction has been reported in recent papers [112, 117], many significant questions remain open. This experiment targeted three known $5/2^+$ states (at 386±10 keV, 515±10 keV, and 689±10 keV) in ^{39}Ca, assumed to be populated by $\ell = 0$ protons coupled to the 3^+ ^{38}K ground state. Only upper limits were set for the lower two resonances. A strength for the 689-keV resonance was extracted, but its energy was found to lie 10 keV lower than the adopted energy, at 679 keV. This reaction rate has been addressed by two recent ORRUBA/GODDESS experiments, as detailed in Sections 6.6.1 and 6.6.2.

6.6.1 Constraining ^{38}K(p,γ)^{39}Ca reaction via the ^{40}Ca(^{3}He,$\alpha\gamma$)^{39}Ca reaction

GODDESS was deployed at ATLAS to search for resonances in ^{39}Ca, utilizing the ^{40}Ca(^{3}He,$\alpha\gamma$)^{39}Ca reaction [118], and in particular to better constrain the energies of these three $5/2^+$ states. The (^{3}He,α) reaction channel was cleanly selected by particle-identification and two-body reaction kinematics of outgoing α particles in ORRUBA. The coincident de-excitation γ rays were used to determine 23 new transitions, corresponding to three $5/2^+$ states in ^{39}Ca. The γ decay of the 386-keV $5/2^+$ resonance was observe via a direct ground-state transition of 6156.7 (16) keV. This level had previously been measured via the same ^{40}Ca(^{3}He,α)^{39}Ca reaction, detecting the alphas in a split-pole spectrograph, as 6154 (5) keV [119]. Reducing the uncertainty on this resonance energy alone reduced the uncertainty on this resonance contribution from a factor of ~3 to ~1.6.

The second of these resonances was first reported in 1993 to be at 6286 (10) keV by a spectrograph measurement of the ^{40}Ca(p,d)^{39}Ca reaction at 65 MeV [120], giving a resonance energy of 515 (13) keV. This state was not been confirmed in subsequent measurements, such as the ^{40}Ca(^{3}He,α)^{39}Ca measurement of [119], and was non-observed (i.e., an upper limit reported) in the direct ^{38g}K(p,γ)^{39}Ca [112, 117]. In the GODDESS experiment, a direct to ground-state transition of 6268.8 (22) keV was observed, giving a resonance energy of 498 (2) keV - barely over 1σ away from the energy of [120]. If this is the same state, not only does this energy difference impact the reaction rate, it also impacts the interpretation of the direct ^{38g}K(p,γ)^{39}Ca experiment of [112, 117], in which the gas target covered resonance energies of 515±13 keV; a 498 (2) keV would not have been located in the gas target.

The third resonance, placed at 679 (2) keV in the ^{38g}K(p,γ)^{39}Ca, likely corresponds to previous observations at 6450 (30) keV [121] and 6467 (10) keV [120]. However, the ^{40}Ca(^{3}He,α)^{39}Ca experiment of [119] placed this state at 6472.2 (24) keV. The GODDESS experiment measured a ground-state transition of 6470.8 (19) keV, in agreement with [119]. This would place this resonance even higher in energy, at 701 (2) keV, which would have been located at the entrance (rather than the center) of the target, which covered 689±13 keV. This leads to questions as the absolute normalization of the yields from this experiment if these are the same resonance. It is noteworthy that capture at this beam energy on the 0^+ isomer (which comprised ~5% of the beam composition [112, 117]), corresponds exactly to a known state at 6580 keV [120].

In total, from this experiment, by locating the energies of states more precisely, the upper limit on the ^{38}K(p,γ)^{39}Ca was reduced over the temperature range of novae [118]. Furthermore, such experiments highlight the importance of high-resolution experiments, such as γ-ray spectroscopy, for precise determination of resonance energies, which are crucial to guiding the planning and interpretation of direct (p,γ) measurements with radioactive beams.

6.6.2 Constraining ^{38}K(p,γ)^{39}Ca reaction via the ^{38}K (d,p)^{39}K reaction

Despite substantial progress, many open questions remain pertaining to the ^{38}K(p,γ)^{39}Ca reaction rate. Firstly, these direct measurements provided no explicit constraint on proton capture on ^{38m}K. Furthermore, in addition to the $\ell_p = 0$ resonances that have been the subject of much focus, important $\ell_p = 1$ resonances are anticipated in this region, as the $2p$ orbitals are mostly vacant in ^{38}K, the $2s$ orbital is full, and the $3s$ orbital lies much higher in energy. No information constraining the precise location and strength of these resonances currently exists. Proton capture through higher-ℓ orbitals is suppressed due to the larger barrier (Section 4.3).

Indeed, there are two known $3/2^-$ states in ^{39}Ca that are just above the ^{38}K + p threshold at 5.771 MeV, and there are several levels in ^{39}K in the same region that are potential mirrors to these ^{39}Ca states [122]. One or both of these states might be formed with a $2p_{3/2}$ proton coupled to either the 3^+ $^{38\text{g}}$K or the 0^+ $^{38\text{m}}$K(130.4 keV), but those structures have not been studied. Determining the location, spins and strengths of these resonances is crucial for an accurate and robust description of the ^{38}K(p,γ) rate, and to identify the most important resonances to be targeted with direct measurements.

To inform the properties of the relevant proton resonances near the ^{38}K + p threshold, a proton transfer reaction, such as ^{38}K(^{3}He,d)^{39}Ca or ^{38}K(d,n)^{39}Ca, would ideally be performed on both ground and isomeric states of ^{38}K. However, as ^{39}K and ^{39}Ca are mirror nuclei, the technique of measuring the mirror ^{38}K(d,p)^{39}K reaction can be applied. Furthermore, due to the advances in delivering beams of nuclides in their ground and isomeric states, and controlling their ratio (as described in Section 5), a simultaneous measurement of $^{38\text{g,m}}$K (d,p)^{39}K was undertaken at the ReA facility.

The 4.57 MeV/u beam, at a total intensity of ~50k ions/second, comprised a 60:40 composition of ^{38}K and ^{38}Ar. The beam was delivered to a 420 μg/cm^2 C_2D_4 target. Proton ejectiles following the (d,p) reaction were measured between ~ 45° and ~ 175° using ORRUBA. The GODDESS position-sensitive fast ionization chamber MAGIC (Pain et al., forthcoming) was used to identify events corresponding to K or Ar induced reactions. Two charge-breeding settings were employed for the experiment to manipulate the ^{38}K GS:IS content of the beam. A short setting of 150 ms charge-breeding time (corresponding to a total hold-up time of ~ 300 ms) produced a^{38}K GS:IS composition of ~5:4. A long setting, allowing most of the IS to decay, resulted in a GS:IS composition of ~9:1.

The reactions on the GS and isomer are deconvolved by scaling the data with the long holdup time to the short-holdup-time data by the number of incident GS ions. The difference between the two spectra therefore results entirely from reactions on the isomer. This deconvolution is straightforward, as the beam, target and detector properties, and hence experimental response, are identical for the two data sets. These data are currently under analysis to extract angular distributions, J^π assignments and spectroscopic factors for states built on both $^{38\text{g}}$K and $^{38\text{m}}$K.

7 Conclusion and outlook

Recent years have seen substantial investments in radioactive beam production, in the US (with the nascent US flagship facility, FRIB, and nuCARIBU at ATLAS at Argonne National Laboratory), and globally. With these investments come opportunities for constraining radiative-capture cross sections via direct measurements of resonance strengths, consequently spurring the development of new instrumentation, such as recoil separators such as SECAR at FRIB, and the JENSA gas-jet target.

However, to make use of these advances, indirect techniques, including various direct reactions (such as (d,p), (^{3}He,t) and (^{3}He,α) reactions highlighted herein) using stable and radioactive beams, are crucial in guiding the direct measurements. Techniques for constraining astrophysically-important proton-capture reactions via direct reactions has been a major focus of the ORRUBA program for approaching two decades. To this end, new developments in instrumentation have been undertaken, such as the GODDESS coupling to the flagship HPGe arrays (Gammasphere, GRETINA and GRETA), and improved recoil detectors, to improve the sensitivity and resolution of direct reaction measurements.

With the increased complexity of RIB facilities, and competition for beam time, such indirect measurements will be increasingly critical for guiding direct measurements of radiative capture reactions, and in some cases remain the only way of constraining lower-lying resonances that are too weak for direct measurements with radioactive beams in the foreseeable future.

Author contributions

SP: Writing – original draft, Writing – review and editing.

Funding

The author(s) declare that financial support was received for the research and/or publication of this article. This work was supported by the U.S. Department of Energy, Office of Science, Office of Nuclear Physics under Contract No. DE-AC05-00OR22725 (ORNL).

Acknowledgments

Thanks are owed to the members of the ORRUBA and GODDESS collaborations, and the operations staff at the HRIBF, ATLAS and ReA (NSCL/FRIB). The mentorship, friendship, collaboration, and pioneering contributions of the late Ray Kozub to the (d,p) experimental program discussed herein, stemming from the ^{18}F(d,p) experiment, are remembered with fondness and gratitude.

Conflict of interest

Generative AI statement

Publisher’s note

References

1. Bardayan DW. Transfer reactions in nuclear astrophysics. *J.Phys.(London)* (2016) G43:043001. doi:10.1088/0954-3899/43/4/043001

2. Brune CR, Davids B. Radiative capture reactions in astrophysics. *Annu Rev Nucl Part Sci* (2015) 65:87–112. doi:10.1146/annurev-nucl-102014-022027

3. Hammache F, de Séréville N. Transfer reactions as a tool in nuclear astrophysics. *Front Phys* (2021) 8. doi:10.3389/fphy.2020.602920

4. Catford WN. *What can we learn from transfer, and how is best to do it?* Berlin, Heidelberg: Springer Berlin Heidelberg (2014). 67–122. doi:10.1007/978-3-642-45141-6_3

5. Bardayan DW, Blackmon JC, Brune CR, Champagne AE, Chen AA, Cox JM, et al. Observation of the astrophysically important 3^+ state in^{18}*ne* via elastic scattering of a radioactive^{17}*f* beam from^{1}*h*. *Phys Rev Lett* (1999) 83:45–8. doi:10.1103/PhysRevLett.83.45

6. Davinson T, Bradfield-Smith W, Cherubini S, DiPietro A, Galster W, Laird A, et al. Louvain–edinburgh detector array (leda): a silicon detector array for use with radioactive nuclear beams. *Nucl Instr Methods Phys Res Section A: Acc Spectrometers, Detectors Associated Equipment* (2000) 454:350–8. doi:10.1016/S0168-9002(00)00479-4

7. Pain SD, Cizewski JA, Hatarik R, Jones KL, Thomas JS, Bardayan DW, et al. Development of a high solid-angle silicon detector array for measurement of transfer reactions in inverse kinematics. *Nuclear Instruments and Methods in Physics Research Section B: Beam Interactions with Materials and Atoms* (2007). 261:1122–1125. doi:10.1016/j.nimb.2007.04.289

8. Pain SD. Advances in instrumentation for nuclear astrophysics. *AIP Adv* (2014) 4:041015. doi:10.1063/1.4874116

9. Chae K, Ahn S, Bardayan D, Chipps K, Manning B, Pain S, et al. Construction of a fast ionization chamber for high-rate particle identification. *Nucl Instr Methods Phys Res Section A: Acc Spectrometers, Detectors Associated Equipment* (2014) 751:6–10. doi:10.1016/j.nima.2014.03.016

10. Hall MR, Bardayan DW, Baugher T, Lepailleur A, Pain SD, Ratkiewicz A, et al. ^{19}Ne level structure for explosive nucleosynthesis. *Phys Rev C* (2020) 102:045802. doi:10.1103/PhysRevC.102.045802

11. Chipps K, Greife U, Bardayan D, Blackmon J, Kontos A, Linhardt L, et al. The jet experiments in nuclear structure and astrophysics (jensa) gas jet target. *Nucl Instr Methods Phys Res Section A: Acc Spectrometers, Detectors Associated Equipment* (2014) 763:553–64. doi:10.1016/j.nima.2014.06.042

12. Schmidt K, Chipps KA, Ahn S, Bardayan DW, Browne J, Greife U, et al.Status of the JENSA gas-jet target for experiments with rare isotope beams. *Nucl Inst.s Meth.in Phys Res A* (2018). 911:1–9. doi:10.1016/j.nima.2018.09.052

13. Labiche M, Catford W, Lemmon R, Timis C, Chapman R, Orr N, et al. Tiara: a large solid angle silicon array for direct reaction studies with radioactive beams. *Nucl Instr Methods Phys Res Section A: Acc Spectrometers, Detectors Associated Equipment* (2010) 614:439–48. doi:10.1016/j.nima.2010.01.009

14. Diget CA, Fox SP, Smith A, Williams S, Porter-Peden M, Achouri L, et al. SHARC: silicon highly-segmented array for reactions and coulex used in conjunction with the tigress γ-ray spectrometer. *J Instrumentation* (2011) 6:P02005. doi:10.1088/1748-0221/6/02/p02005

15. Bildstein V, Gernhauser R, Kroll T, Krucken P, Wimmer P, Van Duppen P, et al. T-rex a new setup for transfer experiments at rex-isolde. *Eur.Phys.J.* (2012) 48:85. doi:10.1140/epja/i2012-12085-6

16. Berner C, Werner L, Gernhäuser R, Kröll T. Hi-trex—a highly integrated transfer setup at rex-(hie)isolde. *Nucl Instr Methods Phys Res Section A: Acc Spectrometers, Detectors Associated Equipment* (2021) 987:164827. doi:10.1016/j.nima.2020.164827

17. Assié M, Clément E, Lemasson A, Ramos D, Raggio A, Zanon I, et al. The mugast-agata-vamos campaign: set-up and performances. *Nucl Instr Methods Phys Res Section A: Acc Spectrometers, Detectors Associated Equipment* (2021) 1014:165743. doi:10.1016/j.nima.2021.165743

18. Pain SD, Ratkiewicz A, Baugher T, Febbraro M, Lepailleur A, Ayangeakaa AD, et al. Direct reaction measurements using GODDESS. *Phys Proc* (2017) 90:455. doi:10.1016/j.phpro.2017.09.051

19. Lee IY. The gammasphere. *Nucl Struct Nineties* 520 (1990) c641–55. doi:10.1016/0375-9474(90)91181-P

20. Vetter K, Kuhn A, Lee I, Clark R, Cromaz M, Deleplanque M, et al. Performance of the greta prototype detectors. *Nucl Instr Methods Phys Res Section A: Acc Spectrometers, Detectors Associated Equipment* (2000) 452:105–14. doi:10.1016/S0168-9002(00)00431-9

21. Descovich M, Lee I, Cromaz M, Clark R, Deleplanque M, Diamond R, et al. GRETINA status and recent progress: The effect of neutron damage on energy and position resolution of the GRETINA detector. *Nucl Instr Methods Phys Res Section B: Beam Interactions Mater Atoms* (2005) 241:931–4. doi:10.1016/j.nimb.2005.07.150

22. Paschalis S, Lee I, Macchiavelli A, Campbell C, Cromaz M, Gros S, et al. The performance of the gamma-ray energy tracking in-beam nuclear array GRETINA. *Nucl Instr Methods Phys Res Section A: Acc Spectrometers, Detectors Associated Equipment* (2013) 709:44–55. doi:10.1016/j.nima.2013.01.009

23. Fallon P, Gade A, Lee IY. GRETINA and its early science. *Annu Rev Nucl Part Sci* (2016) 66:321–39. doi:10.1146/annurev-nucl-102115-044834

24. Weisshaar D, Bazin D, Bender P, Campbell C, Recchia F, Bader V, et al. The performance of the γ -ray tracking array GRETINA for γ -ray spectroscopy with fast beams of rare isotopes. *Nucl Instr Methods Phys Res Section A: Acc Spectrometers, Detectors Associated Equipment* (2017) 847:187–98. doi:10.1016/j.nima.2016.12.001

25. *GRETA final design report*. Lawrence Berkeley National Laboratory (2020).

26. Thomas JS, Bardayan DW, Blackmon JC, Cizewski JA, Greife U, Gross CJ, et al. First study of the level structure of the r-process nucleus ^{83}Ge. *Phys Rev C* (2005) 71:021302. doi:10.1103/PhysRevC.71.021302

27. Kimura K, Izumikawa T, Koyama R, Ohnishi T, Ohtsubo T, Ozawa A, et al. High-rate particle identification of high-energy heavy ions using a tilted electrode gas ionization chamber. *Nucl Instr Methods Phys Res Section A: Acc Spectrometers, Detectors Associated Equipment* (2005) 538:608–14. doi:10.1016/j.nima.2004.08.100

28. Koshchiy E, Blackmon J, Rogachev G, Wiedenhöver I, Baby L, Barber P, et al. Anasen: the array for nuclear astrophysics and structure with exotic nuclei. *Nucl Instr Methods Phys Res Section A: Acc Spectrometers, Detectors Associated Equipment* (2017) 870:1–11. doi:10.1016/j.nima.2017.07.030

29. Lai J, Afanasieva L, Blackmon J, Deibel C, Gardiner H, Lauer A, et al. Position-sensitive, fast ionization chambers. *Nucl Instr Methods Phys Res Section A: Acc Spectrometers, Detectors Associated Equipment* (2018) 890:119–125. doi:10.1016/j.nima.2018.01.010

30. Chester A, Smallcombe J, Henderson J, Berean-Dutcher J, Bernier N, Bhattacharjee S, et al. Trific: the triumf fast ion counter. *Nucl Instr Methods Phys Res Section A: Acc Spectrometers, Detectors Associated Equipment* (2019) 930:1–7. doi:10.1016/j.nima.2019.03.075

31. Woods RD, Saxon DS. Diffuse surface optical model for nucleon-nuclei scattering. *Phys Rev* (1954) 95:577–578. doi:10.1103/PhysRev.95.577

32. Schiffer JP. Proton widths in a diffuse well. *Nucl Phys* (1963) 46:246–250. doi:10.1016/0029-5582(63)90586-8

33. Iliadis C. Proton single-particle reduced widths for unbound states. *Nucl Phys A* (1997) 618:166. doi:10.1016/s0375-9474(97)00065-1

34. Author anonymous (2024). Available online at: https://orruba.org/software (Accessed December 2024).

35. Author anonymous (2024). Available online at: https://people.frib.msu.edu/brown/reaction-codes (Accessed December 2024).

36. Iliadis C, Wiescher M. Spectroscopic factors from direct proton capture. *Phys Rev C* (2004) 69:064305. doi:10.1103/PhysRevC.69.064305

37. Iliadis C, Endt PM, Prantzos N, Thompson WJ. Explosive hydrogen burning of 27si, 31s, 35ar, and 39ca in novae and x-ray bursts. *Astrophysical J* (1999) 524:434–53. doi:10.1086/307778

38. Iliadis C. *Nuclear Physics of Stars*. Wiley-VCH (2007).

39. Kozub RL, Youngblood DH. Single-particle strengths for quasibound levels in ^{33}Cl. *Phys Rev C* (1972) 5:413–9. doi:10.1103/PhysRevC.5.413

40. Hale SE, Champagne AE, Iliadis C, Hansper VY, Powell DC, Blackmon JC. Investigation of the $^{22}\mathrm{Ne}(p,\gamma)^{23}\mathrm{Na}$ reaction via (^{3}He, *d*) spectroscopy. *Phys Rev C* (2001) 65:015801. doi:10.1103/PhysRevC.65.015801

41. Harrouz DS, de Séréville N, Adsley P, Hammache F, Longland R, Bastin B, et al. Experimental study of the $^{30}\mathrm{Si}(^{3}\mathrm{He},\, d)^{31}\mathrm{P}$ reaction and thermonuclear reaction rate of $^{30}\mathrm{Si}(p,\gamma)^{31}\mathrm{P}$. *Phys Rev C* (2022) 105:015805. doi:10.1103/PhysRevC.105.015805

42. Kankainen A, Woods PJ, Nunes F, Langer C, Schatz H, Bader V, et al. Angle-integrated measurements of the ^{26}Al (d, n)^{27}Si reaction cross section: a probe of spectroscopic factors and astrophysical resonance strengths. *Eur Phys J* (2016). 52:6. doi:10.1140/epja/i2016-16006-5

43. Kankainen A, Woods PJ, Schatz H, Poxon-Pearson T, Doherty DT, Bader V, et al. Measurement of key resonance states for the $^{30}\mathrm{p}(\mathrm{p},\gamma)^{31}\mathrm{s}$ reaction rate, and the

production of intermediate-mass elements in nova explosions. *Phys Lett B* (2017) 769:549. doi:10.1016/j.physletb.2017.01.084

44. Hallam S, Lotay G, Gade A, Doherty DT, Belarge J, Bender PC, et al. Exploiting isospin symmetry to study the role of isomers in stellar environments. *Phys Rev Lett* (2021) 126:042701. doi:10.1103/physrevlett.126.042701

45. Lotay G, Henderson J, Catford WN, Ali FA, Berean J, Bernier N, et al. Single neutron transfer on ^{23}ne and its relevance for the pathway of nucleosynthesis in astrophysical x-ray bursts. *Phys Lett B* (2022) 833:137361. doi:10.1016/j.physletb.2022.137361

46. Laird AM, Lugaro M, Kankainen A, Adsley P, Bardayan DW, Brinkman HE, et al. Progress on nuclear reaction rates affecting the stellar production of ^{26}al. *J.Phys.(London)* (2023). G50:033002. doi:10.1088/1361-6471/ac9cf8

47. Vogelaar RB. The ^{26}Al(p,γ) ^{27}Si reaction: stellar origins of galactic ^{26}Al. Pasadena, CA: California insitute of Technology. Ph.D Thesis (1989).

48. Ruiz C, Parikh A, José J, Buchmann L, Caggiano JA, Chen AA, et al. Measurement of the Ec.m. = 184 keV resonance strength in the 26gAl (p, gamma)27 Si reaction. *Phys Rev Lett* (2006) 96:252501. doi:10.1103/PhysRevLett.96.252501

49. Vogelaar RB, Mitchell LW, Kavanagh RW, Champagne AE, Magnus PV, Smith MS, et al. *Phys Rev C* (1996). 53:1945–9. doi:10.1103/PhysRevC.53.1945

50. Pain SD, Bardayan DW, Blackmon JC, Brown SM, Chae KY, Chipps KA, et al. Constraint of the astrophysical ^{26g}Al(p,γ)^{27} Si destruction rate at stellar temperatures. *Phys Rev Lett* (2015) 114:212501. doi:10.1103/PhysRevLett.114.212501

51. Margerin V, Lotay G, Woods PJ, Aliotta M, Christian G, Davids B, et al. Inverse kinematic study of the (26g)Al(d,p)(27)Al reaction and implications for destruction of (26)Al in wolf-rayet and asymptotic giant branch stars. *Phys Rev Lett* (2015) 115:062701. doi:10.1103/PhysRevLett.115.062701

52. Lotay G, Woods PJ, Moukaddam M, Aliotta M, Christian G, Davids B, et al. High-resolution radioactive beam study of the ^{26}al(d, p) reaction and measurements of single-particle spectroscopic factors. *Eur Phys J* (2020) A 56:3. doi:10.1140/epja/s10050-019-00008-8

53. Okołowicz J, Płoszajczak M, Rotter I. Dynamics of quantum systems embedded in a continuum. *Phys Rep* (2003) 374:271–383. doi:10.1016/S0370-1573(02)00366-6

54. Okołowicz J, Michel N, Nazarewicz W, Płoszajczak M. Asymptotic normalization coefficients and continuum coupling in mirror nuclei. *Phys Rev C* (2012) 85:064320. doi:10.1103/PhysRevC.85.064320

55. Brown BA, Richter WA. New usd Hamiltonians for the sd shell. *Phys Rev C* (2006) 74:034315. doi:10.1103/physrevc.74.034315

56. Ward R, Fowler WA. Thermalization of long-lived nuclear isomeric states under stellar conditions. *Astrophys J* (1980) 238:266–86. doi:10.1086/157983

57. Coc A, Porquet MG, Nowacki F Lifetimes of ^{26}Al and ^{34}Cl in an astrophysical plasma. *Phys Rev C* (1999) 61:015801. doi:10.1103/PhysRevC.61.015801

58. Gupta SS, Meyer BS. Internal equilibration of a nucleus with metastable states: ^{26}Al as an example. *Phys Rev C* (2001) 64:025805. doi:10.1103/PhysRevC.64.025805

59. Misch GW, Ghorui SK, Banerjee P, Sun Y, Mumpower MR. Astromers: nuclear isomers in astrophysics*. *Astrophysical J Suppl Ser* (2020) 252:2. doi:10.3847/1538-4365/abc41d

60. Misch GW, Sprouse TM, Mumpower MR. Astromers in the radioactive decay of r-process nuclei. *Astrophysical J Lett* (2021) 913:L2. doi:10.3847/2041-8213/abfb74

61. Misch GW, Sprouse TM, Mumpower MR, Couture AJ, Fryer CL, Meyer BS, et al. Sensitivity of neutron-rich nuclear isomer behavior to uncertainties in direct transitions. *Symmetry* (2021) 13:1831. doi:10.3390/sym13101831

62. Misch GW, Mumpower MR Astromers: status and prospects. *Eur Phys J Spec Top* (2024) 233:1075–99. doi:10.1140/epjs/s11734-024-01136-z

63. Lotay G, et al. Radiative Capture on Nuclear Isomers: Direct Measurement of the ^{26m}Al(p, γ) ^{27}Si Reaction. *Phys Rev Lett* (2022). 128:042701. doi:10.1103/PhysRevLett.128.042701

64. Almaraz-Calderon S, Rehm KE, Gerken N, Avila ML, Kay BP, Talwar R, et al. Study of the ^{26}Al$^{m(d,p)}{}_{27AI}$ reaction and the influence of the ^{26}Al 0^{+} isomer on the destruction of ^{26}Al in the galaxy. *Phys Rev Lett* (2017) 119:072701. doi:10.1103/PhysRevLett.119.072701

65. Chipps KA, Kozub RL, Sumithrarachchi C, Ginter T, Baumann T, Lund K K 38 isomer production via fast fragmentation. *Phys Rev Accel Beams* (2018). 21:121301. doi:10.1103/PhysRevAccelBeams.21.121301

66. Shehu OA, Crider BP, Ginter T, Hoffman CR, Ogunbeku TH, Xiao Y, et al. Experimental study of the ^{34m}Cl beam production at intermediate energies. *Nuclear Instruments and Methods in Physics Research Section A: Accelerators, Spectrometers, Detectors and Associated Equipment* (2022). 1035:166789. doi:10.1016/j.nima.2022.166789

67. Pain S. FRIB Proposal 23079 Approved; awaiting scheduling (2023).

68. Mahoney WA, Ling JC, Jacobson AS, Lingenfelter RE. Diffuse galactic gamma-ray line emission from nucleosynthetic Fe-60, Al-26, and Na-22 - preliminary limits from HEAO 3. *Astrophys J* (1982) 262:742. doi:10.1086/160469

69. Share GH, Kinzer RL, Kurfess JD, Forrest DJ, Chupp EL, Rieger E. Detection of galactic Al-26 gamma radiation by the SMM spectrometer. *Astrophys J* (1985) 292:L61–L65. doi:10.1086/184473

70. Schoenfelder V, Aarts H, Bennett K, de Boer H, Clear J, Collmar W, et al. Instrument description and performance of the imaging gamma-ray telescope COMPTEL aboard the Compton gamma-ray observatory. *Astrophys J Supp Ser* (1993) 86:657–92. doi:10.1086/191794

71. Diehl R, Dupraz C, Bennett K, Bloemen H, de Boer H, Hermsen W, et al. *COMPTEL observations of the 1.809 MeV gamma-ray line from galactic Al* (1994). 26:429–32. doi:10.1086/191990

72. Diehl R, Halloin H, Kretschmer K, Lichti GG, Schönfelder V, Strong AW, et al. Radioactive ^{26}Al from massive stars in the Galaxy. *Nature* (2006) 439:45–7. doi:10.1038/nature04364

73. Diehl R, Lang M, Kretschmer K, Wang W. ^{26}Al emission throughout the galaxy. *New Astron Rev* 52 (2008). 440–4. doi:10.1016/j.newar.2008.06.024

74. Voss R, Diehl R, Hartmann D, Kretschmer K. Population synthesis models for 26al production in starforming regions. *New Astron Rev* (2008) 52:436–9. doi:10.1016/j.newar.2008.06.022

75. Banerjee P, Misch GW, Ghorui SK, Sun Y Effective stellar β-decay rates of nuclei with long-lived isomers: ^{26}Al and ^{34}Cl. *Phys Rev C* (2018) 97:065807. doi:10.1103/PhysRevC.97.065807

76. Kozub RL, Bardayan DW, Batchelder JC, Blackmon JC, Brune CR, Champagne AE, et al. New constraints on the^{18}F(p,α)^{15}O rate in novae from the (d, p) reaction. *Phys Rev C* (2005) 71:032801. doi:10.1103/PhysRevC.71.032801

77. Kozub RL, Bardayan DW, Batchelder JC, Blackmon JC, Brune CR, Champagne AE, et al. Neutron single particle strengths from the reaction on ^{18}F. *Phys Rev C* 73 (2006) 044307. doi:10.1103/PhysRevC.73.044307

78. Hall MR, Bardayan DW, Baugher T, Lepailleur A, Pain SD, Ratkiewicz A, et al. Key^{19}Ne states identified affecting γ-ray emission from^{18}F in novae. *Phys Rev Lett* (2019) 122:052701. doi:10.1103/PhysRevLett.122.052701

79. Iyudin AF, Bennett K, Bloemen H, Diehl R, Hermsen W, Lichti GG, et al. COMPTEL search for 22Na line emission from recent novae. *Astron Astrophys* (1995) 300:422.

80. Jean P, Hernanz M, Gomez-Gomar J, Jose J. Galactic 1.275-MeV emission from ONe novae and its detectability by INTEGRAL/SPI. *Mon Not R Astron Soc* (2000) 319:350–64. doi:10.1046/j.1365-8711.2000.03587.x

81. Siegert T, Coc A, Delgado LG, Diehl R, Greiner J, Hernanz M, et al. *Gamma-ray observations of nova sgr 2015 no. 2 with integral*, 292 (2018).

82. Siegert T, Coc A, Delgado LG, Diehl R, Greiner J, Hernanz M, et al. Gamma-ray observations of nova sgr 2015 no. 2 with integral. *Astron Astrophys* (2018) 615:A107. doi:10.1051/0004-6361/201732514

83. Fryer CL, Timmes F, Hungerford AL, Couture A, Adams F, Aoki W, et al. Catching element formation in the act (2019).

84. Seuthe S, Rolfs C, Schroder U, Schulte W, Somorjai E, Trautvetter H, et al. Resonances in the 22Na(p,γ)23mg reaction. *Nucl Phys A* (1990) 514:471–502. doi:10.1016/0375-9474(90)90153-D

85. Sallaska AL, Wrede C, García A, Storm DW, Brown TAD, Ruiz C, et al. Direct measurements of ^{22}Na(p,γ) ^{23}Mg resonances and consequences for ^{22}Na production in classical novae. *Phys Rev Lett* (2010) 105:152501. doi:10.1103/PhysRevLett.105.152501

86. Sallaska AL, Wrede C, García A, Storm DW, Brown TAD, Ruiz C, et al. Absolute determination of the^{22}Na(p, γ)^{23}Mg reaction rate in novae. *Phys Rev C* (2011) 83:034611. doi:10.1103/PhysRevC.83.034611

87. Stegmüller F, Rolfs C, Schmidt S, Schulte WH, Trautvetter HP, Kavanagh RW. ^{22}Na(p,γ) ^{23}Mg resonant reaction at low energies. *Nucl Phys A* (1996) 601:168–80. doi:10.1016/0375-9474(96)00084-X

88. Friedman M, Budner T, Pérez-Loureiro D, Pollacco E, Wrede C, José J, et al. Low-energy ^{23}-delayed proton decay and ^{22}Na destruction in novae. *Phys Rev C* 101 (2020) 052802. doi:10.1103/PhysRevC.101.052802

89. Friedman M, Perez-Loureiro D, Budner T, Pollacco E, Wrede C, Cortesi M, et al. Gadget: a gaseous detector with germanium tagging. *Nucl Instr Methods Phys Res Section A: Acc Spectrometers, Detectors Associated Equipment* (2019) 940:93–102. doi:10.1016/j.nima.2019.05.100

90. Saastamoinen A, Trache L, Banu A, Bentley MA, Davinson T, Hardy JC, et al. Experimental study of β-delayed proton decay of ^{23}Al for nucleosynthesis in novae. *Phys Rev C* (2011) 83:045808. doi:10.1103/PhysRevC.83.045808

91. Friedman M, Budner T, Perez-Loureiro D, Pollacco E, Wrede C, Jose J, et al. Low-energy ^{23}Al β-delayed proton decay and ^{22}Na destruction in novae. *arXiv* (2019).

92. Jenkins DG, Lister CJ, Janssens RVF, Khoo TL, Moore EF, Rehm KE, et al. Reevaluation of the ^{22}Na(p, γ) reaction rate: implications for the detection of ^{22}Na gamma rays from novae. *Phys Rev Lett* (2004) 92:031101. doi:10.1103/PhysRevLett.92.031101

93. Jenkins DG, Bouhelal M, Courtin S, Freer M, Fulton BR, Haas F, et al. γ-ray spectroscopy of the a = 23, t = 1/2 nuclei ^{23}Na and ^{23}Mg: high-spin states, mirror

symmetry, and applications to nuclear astrophysical reaction rates. *Phys Rev C* (2013) 87:064301. doi:10.1103/PhysRevC.87.064301

94. Kirsebom OS, Bender P, Cheeseman A, Christian G, Churchman R, Cross DS, et al. Measurement of lifetimes in ^{23}Mg. *Phys Rev C* (2016) 93:025802. doi:10.1103/PhysRevC.93.025802

95. Jin SJ, Wang YB, Su J, Yan SQ, Li YJ, Guo B, et al. Resonant scattering of ^{22}na + *p* studied by the thick-target inverse-kinematic method. *Phys Rev C* (2013) 88:035801. doi:10.1103/PhysRevC.88.035801

96. Schmidt S, Rolfs C, Schulte WH, Trautvetter HP, Kavanagh RW, Hategan C, et al. ^{22}Na(^{3}He,d)^{23}Mg reaction studies of states near the proton threshold and hydrogen burning of ^{22}Na. *Nucl Phys A* (1995). 591:227. doi:10.1016/0375-9474(95)00164-V

97. Knödlseder J, Bennett K, Bloemen H, Diehl R, Hermsen W, Oberlack U, et al. *A multiwavelength comparison of COMPTEL 1.8 MeV {(26)} line data*, 344 (1999). 68–82.

98. Knödlseder J. On the origin of galactic ^{26}AL. *Astrophys Lett Comm* (1999) 38:379. doi:10.48550/arXiv.astro-ph/9902281

99. Wrede C. The ^{30}P(p,γ)^{31}S reaction in classical novae: progress and prospects. *A.I.P Adv* (2014) 4:041004. doi:10.1063/1.4864193

100. Iliadis C, Champagne A, José J, Starrfield S, Tupper P. *Ap J Suppl Ser* (2002) 142:105. doi:10.1086/341400

101. José J, Hernanz M, Amari S, Lodders K, Zinner E. The Imprint of Nova Nucleosynthesis in Presolar Grains. *Astrophys J* (2004) 612:414. doi:10.1086/422569

102. Downen LN, Iliadis C, Josè J, Starrfield S. Nuclear Thermometers for Classical Novae. *Astrophys J* (2013) 762:105. doi:10.1088/0004-637X/762/2/105

103. Hynes K, Gyngard F. The presolar grain database. *Lunar Planet Sci* (2009) 40:1198.

104. Fry C, Wrede C, Bishop S, Brown BA, Chen AA, Faestermann T, et al. Discovery of ^{34g,m}Cl(p,γ)^{35}Ar resonances activated at classical nova temperatures. *Phys Rev C* (2015) 91:015803. doi:10.1103/PhysRevC.91.015803

105. Grineviciute J, Brown BA, Schatz H. The role of excited states in rp-process for sd shell nuclei. *arXiv [Preprint]. arXiv:1404.7268* (2014). Available online at: https://arxiv.org/abs/1404.7268 (Accessed April 29, 2025).

106. Brown BA, Wildenthal WDM. Status of the nuclear shell model. *Ann Rev Nucl Part Sci* (1988) 38:29–66. doi:10.1146/annurev.ns.38.120188.000333

107. Richter WA, Brown BA, Longland R, Wrede C, Denissenkov P, Fry C, et al. Shell-model studies of the astrophysical *rp*-process reactions ^{34}S(p,γ)^{35}Cl and ^{34g,m}Cl(p,γ)^{35}Ar. *Phys Rev C* (2020) 102:025801. doi:10.1103/PhysRevC.102.025801

108. Brown BA, Richter WA, Wrede C. Shell-model studies of the astrophysical rapid-proton-capture reaction ^{30}P(p,γ)^{31}S. *Phys Rev C* (2014) 89:062801R. doi:10.1103/physrevc.89.062801

109. Pain SD (2018). Proposal to the NSCL PAC, e18037.

110. Utsuno Y, Otsuka T, Brown BA, Honma M, Mizusaki T, Shimizu N. Shape transitions in exotic si and s isotopes and tensor-force-driven jahn-teller effect. *Phys Rev C* (2012) 86:051301. doi:10.1103/PhysRevC.86.051301

111. Pain S. FRIB Proposal 21067 (2021). Approved; awaiting scheduling.

112. Lotay G, Christian G, Ruiz C, Akers C, Burke DS, Catford WN, et al. Direct measurement of the astrophysical ^{38}K(p,γ)^{39}Ca reaction and its influence on the production of nuclides toward the end point of nova nucleosynthesis. *Phys Rev Lett* (2016) 116:132701. doi:10.1103/PhysRevLett.116.132701

113. Fisker JL, Brown EF, Liebendörfer M, Thielemann FK, Wiescher M, et al. The reactions and ashes of thermonuclear explosions on neutron stars. *Nucl.Phys.* (2005). A752:604c. doi:10.1016/j.nuclphysa.2005.02.063

114. Fisker JL, Schatz H, Thielemann FK. Explosive hydrogen burning during type I X-ray bursts. *Astrophys J Supp Ser* (2008) 174:261–76. doi:10.1086/521104

115. Cyburt RH, Amthor AM, Ferguson R, Meisel Z, Smith K, Warren S, et al. The jina reaclib database: its recent updates and impact on type-i x-ray bursts. *Astrophysical J Suppl Ser* (2010) 189:240–52. doi:10.1088/0067-0049/189/1/240

116. Cameron JA, Singh B. Nuclear data sheets for a = 38. *Nucl Data Sheets* (2008) 109:1–170. doi:10.1016/j.nds.2007.12.001

117. Christian G, Lotay G, Ruiz C, Akers C, Burke DS, Catford WN, et al. Direct measurement of astrophysically important resonances in ^{38}K(p,γ)^{39}Ca. *Phys Rev C* (2018) 97:025802. doi:10.1103/PhysRevC.97.025802

118. Hall MR, Bardayan DW, Baugher T, Lepailleur A, Pain SD, Ratkiewicz A, et al. γ-ray spectroscopy of astrophysically important states in ^{39}Ca. *Phys Rev C* (2020) 101:015804. doi:10.1103/PhysRevC.101.015804

119. Setoodehnia K, Marshall C, Kelley JH, Liang J, Portillo Chaves F, Longland R. Excited states of ^{39}Ca and their significance in nova nucleosynthesis. *Phys Rev C* (2018) 98:055804. doi:10.1103/PhysRevC.98.055804

120. Matoba M, Iwamoto O, Uozumi Y, Sakae T, Koori N, Fujiki T, et al. ^{40}Ca(p,d)^{39}ca reaction at 65 mev. *Phys Rev C* (1993) 48:95–104. doi:10.1103/PhysRevC.48.95

121. Doll P, Wagner G, Knöpfle K, Mairle G. The quasihole aspect of hole strength distributions in odd potassium and calcium isotopes. *Nucl Phys A* (1976) 263:210–36. doi:10.1016/0375-9474(76)90169-X

122. Singh B, Cameron JA. Nuclear data sheets for a = 39. *Nucl Data Sheets* (2006) 107:225–354. doi:10.1016/j.nds.2006.01.001

Frontiers in
Physics

Investigates complex questions in physics to understand the nature of the physical world

Addresses the biggest questions in physics, from macro to micro, and from theoretical to experimental and applied physics.

Discover the latest Research Topics

See more →

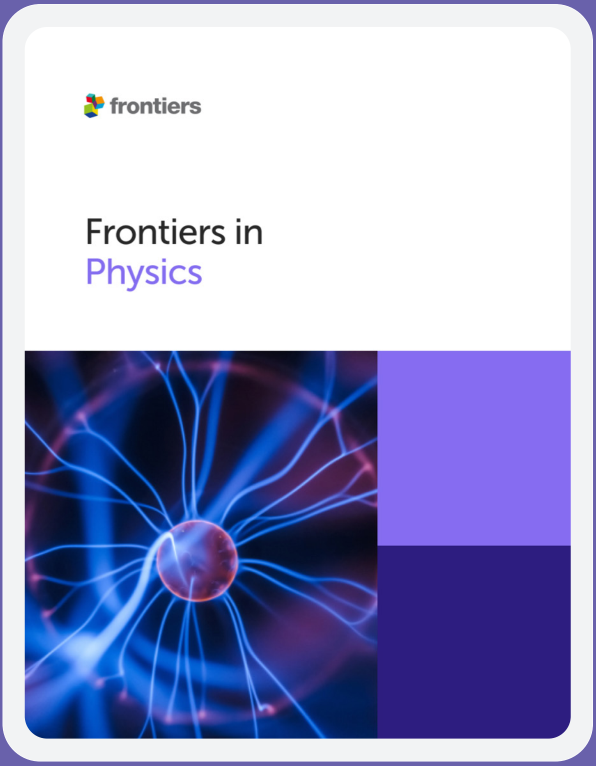

Frontiers

Avenue du Tribunal-Fédéral 34
1005 Lausanne, Switzerland
frontiersin.org

Contact us

+41 (0)21 510 17 00
frontiersin.org/about/contact